ISSN-Printed: 2536-5010
ISSN-Online: 2536-5134

Volume 12, No 1, 2022

EJT

EUROPEAN JOURNAL OF TECHNIC

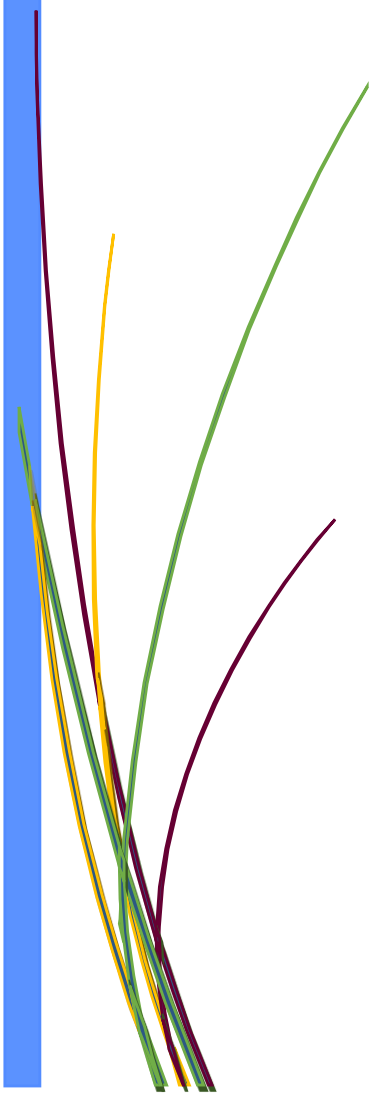

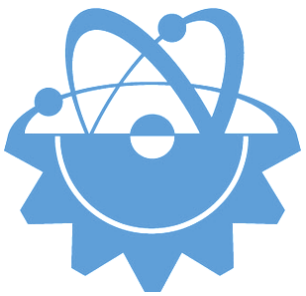

Email (for orders and customer services enquiries): info@ineseg.org, ejt@ineseg.org
Visit our home page on www.ineseg.org

EUROPEAN JOURNAL OF TECHNIQUE (EJT)
ISSN-Printed: 2536-5010
ISSN-Online: 2536-5134

Scope: European Journal of Technique (EJT) established in 2010. It is a peer –reviewed international journal to be of interest and use to all those concerned with research in various fields of, or closely related to, Engineering disciplines. European Journal of Technique (EJT) aims to provide a highly readable and valuable addition to the literature which will serve as an indispensable reference tool for years to come. The coverage of the journal includes all new theoretical and experimental findings in the fields of Engineering or any closely related fields. The journal also encourages the submission of critical review articles covering advances in recent research of such fields as well as technical notes.

The scopes include:

- Mechanical Engineering
- Textile Engineering
- Electrical-Electronics Engineering
- Computer and Informatics Engineering
- Civil and Architecture Engineering
- Mining Engineering
- Chemical Engineering
- Metallurgical and Materials Engineering
- Environmental Engineering
- Food Engineering
- Geological Engineering
- Industrial Engineering
- Renewable Energy

EDITORIAL BOARD MEMBERS

Editor-in-Chief

- Musa YILMAZ

Publisher Of Journal

- Heybet KILIÇ

ETHICS and POLICIES

European Journal of Technique (EJT) is committed to following the Code of Conduct and Best Practice Guidelines of COPE (Committee on Publication Ethics). It is a duty of our editors to follow Cope Guidance for Editors and our peer-reviewers must follow COPE Ethical Guidelines for Peer Reviewers We expect all prospective authors to read and understand our Ethics Policy before submitting any manuscripts to our journals.

Please note that submitted manuscripts may be subject to checks using the iThenticate service, in conjunction with CrossCheck, in order to detect instances of overlapping and similar text.

The iThenticate software checks submissions against millions of published research papers, documents on the web, and other relevant sources. If plagiarism or misconduct is found, consequences are detailed in the policy.

The chief goal of our policy is threefold: to provide advice for our authors, to maintain the scholarly integrity of our journals and their content, and to detail the ethical responsibilities of EJT, our editors and authors.

We expect all authors to read and understand our ethics policy before submitting to any of our journals. This is in accordance with our commitment to the prevention of ethical misconduct, which we recognise to be a growing problem in academic and professional publications. It is important to note that most incidents of plagiarism, redundant publication, copyright infringement or similar occur because of a lack of understanding, and not through fraudulent intent. Our policy is one of prevention and not persecution.

If you have any questions, please contact the relevant editorial office, or European Journal of Technique (EJT)' ethics representative: ejtineseg@gmail.com

Download a PDF version of the Ethics and Policies [PDF,392KB].

Authors' Responsibilities

Authors should:

- Ensure that all researched work submitted is original, fully referenced and that all authors are represented accurately. The submission must be exclusive and not under consideration elsewhere.
- Provide accurate contact details for a designated corresponding author, who shall be deemed by the publisher and editor as fully responsible for the authorship of the paper and all communications concerning the ethical status and originality of the paper. This includes any queries or investigations that may arise, pre- or post publication.
- Openly disclose the source of all data and third party material, including previously unpublished work by the authors themselves. Anything that could compromise the originality of the submission should be expressly avoided and/or discussed with the editorial office in the first instance.
- Identify any third party material that they intend to include in their article, and obtain written permission for re-use in each instance from the relevant copyright holders. Such permissions should be submitted once the manuscript is accepted, or requires small changes to be accepted. For further guidance on seeking permission to use 3rd party material please see the Rights and Permissions section.
- Openly disclose any conflict of interest - for example, if publication were to benefit a company or services in which the author(s) has a vested interest.

- Expect to formally agree publication terms which defines the author and the publishers rights for the work. Visit our website for further information.
- Expect the editor to scan submissions using plagiarism detection software at iThenticate to check a paper's originality before sending out for review.
- Fully correspond and comply with the editor and publisher in any requests for source data, proof of authorship or originality in a timely manner, providing reasonable explanation for discrepancies or failures to disclose vital information.
- Fully co-operate with any consequent investigations if the editor and/or publisher are dissatisfied with the evidence available or the explanations provided.
- Expect transparency, efficiency and respect from the publisher and the editor during the submissions process.
- Remain in good communication with both the publisher and the editor.
- When necessary, submit corrigenda in a timely and responsible fashion.
- Co-operate fully with the publication of errata and with the retraction of articles found to be unethical, misleading or damaging.
- Remain in good communication with the editor(s), the publisher and any co-authors.

Editors' Responsibilities

Editors should:

- Read and understand COPE guidelines as well as EJT's ethics policy, and follow them during all editorial processes.
- Protect the reputation of their journal(s) and published work by only publishing content of the highest quality and relevance in a timely and responsible manner.
- Carry out thorough, objective and confidential peer review for original article submissions that pass the initial quality check and editorial assessment, in adherence with COPE guidelines and EJT' ethics policy.
- Detail and justify any article types which will not be peer reviewed (e.g. editorials, opinion pieces etc.).
- Provide a transparent review and publication process as far as is possible, with full respect and care paid to the author(s).
- Provide advice and give reasonable explanation and updates to authors during the submissions process and once a decision has been made.
- Allow authors the right to appeal any editorial decision.
- Only accept papers based on the original merit, quality and relevance of their content.
- Support authors in queries concerning the originality of their submissions and request the support of EJT if necessary.
- Advise the publisher of any third party material which has been included for which they do not believe sufficient permission has been cleared.

- Be ready and prepared to publish corrections, corrigenda, errata when necessary, as well as retract articles that (the editor and EJT) deem unethical, misleading or damaging.
- Remain in good communication with both the publisher and the author(s).

Reviewers' Responsibilities

Reviewers should:

- Adhere to EJT's policy of confidential peer review of their journals. This includes, but is not restricted to, keeping their identity hidden from authors and not externally distributing any work that is passed to them for their eyes only.
- Only accept invitations to review work that is relevant to their own expertise and speciality.
- Review submitted work in a responsible, impartial and timely manner.
- Report any suspected ethical misconduct as part of a thorough and honest review of the work.
- Avoid the use of unnecessarily inflammatory or offensive language in their appraisal of the work.
- Accept the commitment to review future versions of the work and provide 'follow up' advice to the editor(s), if requested.
- Seek advice from the editor if anything is unclear at the time of invitation.
- Remain in good communication with both the publisher and the editor.

EJT's Responsibilities

EJT will:

- Protect the reputation of our journals and published work by only publishing content of the highest quality and relevance in a timely and responsible manner.
- Provide detailed information concerning both our understanding of publication ethics and our implementation of the same. Emphasise a desire for prevention, not eventual detection, of ethical misconduct.
- Uphold our COPE membership (or of such similar organisations) and keep our editorial offices, publishing staff and society partners up-to-date with their guidelines and policies, adapting our own where appropriate (and publicising any update).
- When necessary, request proof of originality/accuracy from the corresponding author of any work submitted to any of our journals.
- Use plagiarism detection software when necessary for any submission to any journal at any stage of the submissions and publication process.
- Provide a transparent submissions and publication process, with full respect and care paid to the author. This includes detailed and dedicated instructions to authors for each journal, outlining referencing style, accepted article types and submission processes.
- Investigate thoroughly any suggestion of ethical misconduct detected during any stage of the submissions process. This can include, but is not restricted to, the following: plagiarism, redundant publication, fabrication or misuse of data and authorial disputes.

- When necessary, retract articles that we deem to be unethical, misleading or damaging.
- When necessary, publish errata, corrigenda and retractions in a timely and responsible fashion, detailing the decision online in an open access format and publishing in print as soon as possible.
- Remain in good communication with editors, authors, reviewers and society partners (where applicable).

Further reading

- Authorship of the paper: Authorship should be limited to those who have made a significant contribution to the conception, design, execution, or interpretation of the reported study.
- Originality and plagiarism: The authors should ensure that they have written entirely original works, and if the authors have used the work and/or words of others that this has been appropriately cited or quoted.
- Data access and retention: Authors may be asked to provide the raw data in connection with a paper for editorial review, and should be prepared to provide public access to such data.
- Multiple, redundant or concurrent publication: An author should not in general publish manuscripts describing essentially the same research in more than one journal or primary publication. EJT do not view the following uses of a work as prior publication: publication in the form of an abstract; publication as an academic thesis; publication as an electronic preprint. Information on prior publication is included within each EJT and its journal Guideline for Authors.
- Acknowledgement of sources: Proper acknowledgment.
- Disclosure and conflicts of interest: All submissions must include disclosure of all relationships that could be viewed as presenting a potential conflict of interest.
- Fundamental errors in published works: When an author discovers a significant error or inaccuracy in his/her own published work, it is the author's obligation to promptly notify the journal editor or publisher and cooperate with the editor to retract or correct the paper.
- Reporting standards: Authors of reports of original research should present an accurate account of the work performed as well as an objective discussion of its significance.
- Hazards and human or animal subjects: Statements of compliance are required if the work involves chemicals, procedures or equipment that have any unusual hazards inherent in their use, or if it involves the use of animal or human subjects.
- Use of patient images or case details: Studies on patients or volunteers require ethics committee approval and informed consent, which should be documented in the paper.

EJT has also accessed and learned from the existing policies of other publishers and leading experts as well as open access articles that detail and define ethical misconduct.

- 'Plagiarism and the law', Joss Saunders, Learned Publishing, 23:279-202: http://www.ingentaconnect.com/content/alpsp/lp/2010/00000023/00000004/art00002
- iThenticate Plagiarism Resources: http://www.ithenticate.com/resources/6-consequences-of-plagiarism

Vol 12, Number 1, 2022
European Journal of Technique (EJT)
ISSN: 2536-5134

CONTENTS

European Journal of Technique

journal homepage: https://dergipark.org.tr/en/pub/ejt

Vol.12, No.1, 2022

A Survey on Traction System Development of Automated Guided Vehicles

Mustafa Karamuk[1*], Ismail Hakki Savci[1], Hakan Ocakli[1]

[1*]Ford Otosan R&D Center, 34885, Sancaktepe, Istanbul, Turkey. (e-mail: mkaramuk@ford.com.tr, isavci@ford.com.tr, hocakli@ford.com.tr).

ARTICLE INFO

Received: Jan., 04. 2021
Revised: Dec., 05. 2021
Accepted: Mar, 17. 2022

Keywords:
Automated Guided Vehicles (AGV)
Traction system topologies
Energy efficiency
AGV motors, inverters

Corresponding author: *Mustafa Karamuk*

ISSN: *2536-5010* | e-ISSN: *2536-5134*

DOI: https://doi.org/10.36222/ejt.1002554

ABSTRACT

Abstract—Automated guided vehicles have been part of all production and logistic systems. Industry 4.0 technologies have also increased the applications of AGVs because of the demand for autonomous operations with minimum human power. In parallel to the growth of AGV market, researchers and application engineers need a holistic approach considering all aspects of development and application of AGVs.

Objective of this study is to provide guidelines for AGV development with focus on traction systems. Traction topologies, motor and inverter specifications, energy efficiency solutions, failure risks of AGV motors, and electrical system development issues are reviewed.

1. INTRODUCTION

Automated guided vehicles (AGVs) have been part of all production plants for the last 20 years. It is also one of the fastest-growing markets [1], as the demand for logistics and robot-operated automation systems are increasing. First generation of AGVs were developed as standalone vehicles. Second and third-generation AGVs have evolved into decentral control in terms of path planning, localization, and traffic management [2-5]. This evolution has been accelerated by the development of smart factories using the industry 4.0 technologies. The historical evolution of AGVs for different applications is given in [5].

In AGV literature, majority of the publications are on AGV control system software [2-4]. There are a few studies on traction and electrical system development. Therefore, the objective of this study is to review the conceptual development phases, integration and application aspects of the traction and electrical system of an AGV.

According to the market analysis reported in [6], the most common types of AGVs in the global market in 2020 are listed as below:

- Unit load carriers
- Automated forklift trucks
- Tow vehicles
- Assembly line vehicles
- Underride tunneling vehicles

Due to the variety of these applications, power components market can be expected to grow further in order to provide solutions at higher power levels. Power components of an AGV includes traction motor, inverter (motor control unit), gearbox, lithium based batteries, cabled or wireless (inductive) chargers and DC-DC converters.

48 V electrical system is commonly used in AGVs. There are AGV motor controllers rated at 1500 A current at 48 V DC input supply [7].

Contrary to the past use of 48 V supply for auxiliary systems in automotive applications, 48 V supplied motors, motor controllers and chargers are expected to have higher currents ratings in near future.

2. CONCEPTUAL DEVELOPMENT STEPS OF AN AGV PROJECT

2.1. Specifications and system configuration

The list given below refers to an AGV applied in automotive production and can be expanded into other AGV applications as well:

Step-1: Specifications and tasks related to the AGV operation environment

- Type of AGV
- Central or decentral control
- Localization and mapping method

- Positioning accuracy of AGV
- AGV speed
- Maximum inclination angle at the operation floor
- Maximum payload at maximum acceleration
- Safety and certification requirements

Step-2: Specifications and tasks related to the software development

- Configuration of the safety PLC software operating according to the outputs of the safety sensors
- Sensor selection and integration of drivers into the ROS (Robot Operating System).
- Configuration of task manager and path planner according to the operation environment
- Configuration of the traffic management system according to the operation environment

Step-3: Load related specifications

- Traction system topology
- Sizing of motors, gearbox and battery Ah capacity
- Radial forces per wheel at maximum payload

In this study, steps 1 and 2 are reviewed briefly. Step-3 and its relationship with step-1 and 2 is analyzed in detail.

3. INTEGRATION of AGV into FACTORY AUTOMATION

3.1. Compatibility with Industry 4.0

In this section, an overview of AGV technologies and technology selection criteria will be studied. Technology selection has a decisive impact on AGV lifetime and performance in the target application.

Industry 4.0 is a broad term specifying features of an intelligent factory environment where process efficiency and production outputs can be increased by software tools such as data processing, connectivity of process components, predictive maintenance, remote control etc.

In order to integrate an AGV into an industry 4.0 compatible factory, technological transformation is required as listed below:

1) Decentral control of AGVs

In decentral control, AGVs can autonomously plan their path and make decisions about their motions. Decentralized control methods are practical and scalable solution for large AGV fleet operations [2-4].

In [2], solution models for centralized and decentralized control are studied and importance of decentralized algorithms are emphasized as they provide open architecture, configurability, scalability, and robustness.

In decentralized architecture, AGVs can navigate independently within the defined AGV control tasks [3]. If the process requires a higher number of AGVs and complex tasks, the central control of AGV is not suitable as the central controller needs to re-define the path in case of a deviation from the planned path for each of the AGVs [2-4].

2) Use of digital twin modelling in AGV control

Digital twin (DT) a virtual model of a physical system. It has been studied recently in manufacturing systems for industry 4.0 compatibility. DT enables simulation and optimization of manufacturing system in a digital platform [8]. In development of AGVs, DT can be used to model the physical operation environment to develop navigation and localization software and test of operation safety as well [9-10].

3) Remote monitoring of AGV data

AGV control can be improved if operational states of AGV, faults and variables like energy consumption, battery state of charge (SOC) can be monitored remotely. Monitored data can be used to improve the task management, predictive maintenance and energy efficiency. DT modeling is an effective tool for AGV performance monitoring and optimization. Modeling and application examples from a smart factory model is studied in [11].

4) Charging method

Wireless charging technology, known as also inductive charging, enables charging of AGV at any location where transmitter pad of wireless charger is installed and thus eliminates cable and connector [5,12-13]. If charging and operation duty cycle times can be optimized, wireless charging can enable operation of AGV continuously without need for a cabled charging.

5) Cyber security of AGV

Despite the advantages of industry 4.0, the connectivity of components increases the risks of cyber-attacks which can cause uncontrolled stops. Case studies and solutions are studied in [14-16]. Use of 5G private network enables higher system security [17]. Digital twin modeling can also detect normal and cyber attacted operations in a smart factory [18].

6) 5G wireless network

Use of 5G wireless network (WN) for AGV control and fleet management is expected be the future trend [5,17]. 5G WN enables faster control of AGV and increase of production throughput as studied in [19].

3.2. Relationship between AGV subsystems

Overall Equipment Efficiency (OEE) is a production performance metric and studied in [20].

Fig.1 illustrates how the conceptual development phase can improve the overall performance of an AGV and key performance index (KPI) of the production as well.

Fig.2 illustrates the multidisciplinary engineering works for an AGV development. For an optimum development of an AGV, relationship between these engineering works should be carefully analysed at the conceptual development phase.

The following issues are listed to highlight the relationship between AGV subsystems:

1) Navigation methods, path planning and motor duty cycle:

The selected navigation method, path planning and operation environment will significantly influence the motor and battery duty cycle. Critical issue is to operate the motor at efficient operating points. For this purpose, the number of start and stop cycles can be reduced. Because every start needs an acceleration torque and causes higher power consumption than constant speed operation. If AGV path plan can enable operation at higher speed, this will also improve the AGV traction system efficiency. Therefore, navigation method, path plan and permissible motor duty cycle given in motor datasheet should be analysed together.

2) Importance of EMC/EMI in an AGV Fleet

The minimum distance between AGVs for collision avoidance is a design parameter for path planning algorithm. Additionally, when developing the path planning, potential EMI (electromagnetic interference) problems between AGVs should also be considered to avoid the EMI problems as well.

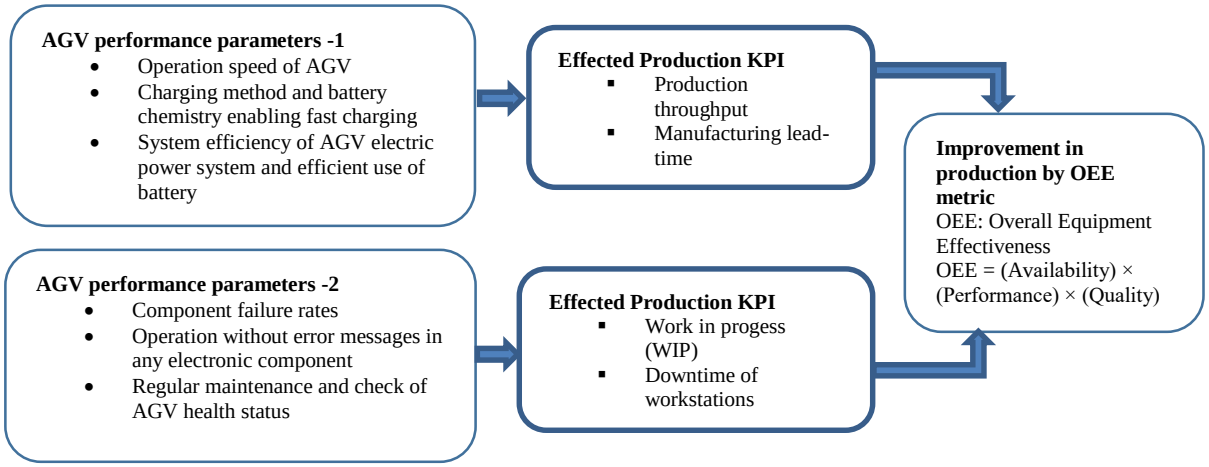

Figure 1. AGV performance parameters and improvement possibilities on process KPI (Key Performance Index)

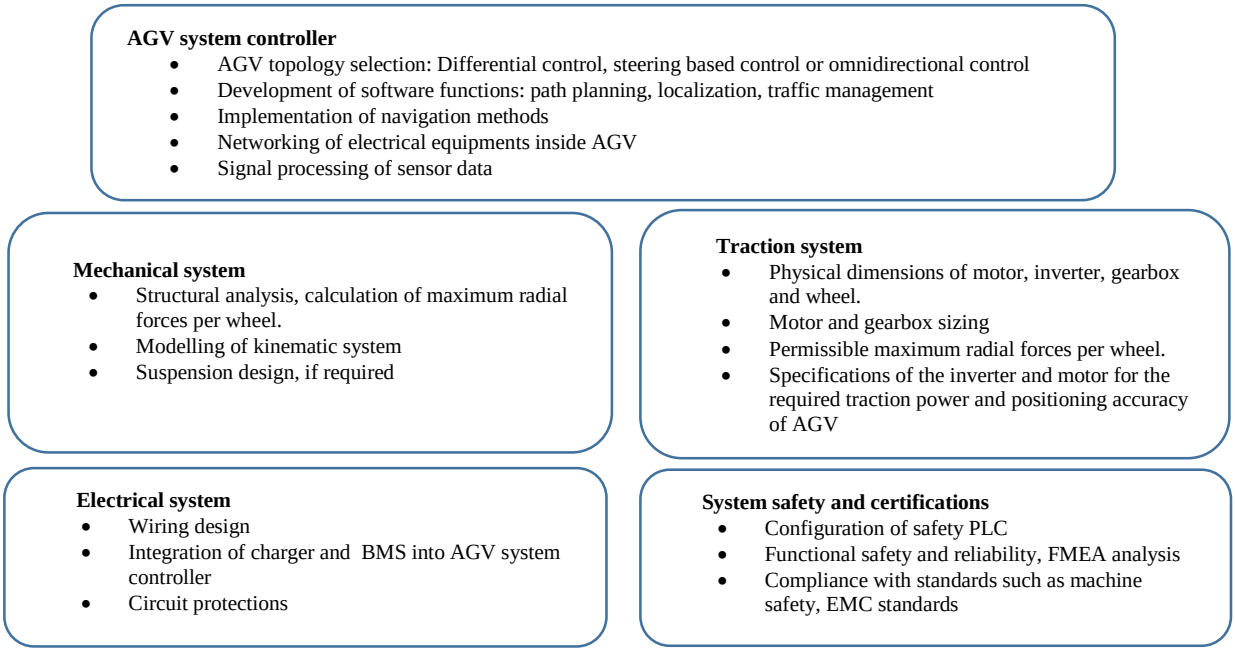

Figure 2. Main development steps of subsystems of an AGV

In [21], EMI risks and analysis is studied for battery electric vehicle in traffic that can create interference to vehicles nearby. Same risks are valid for AGVs.

3) Available battery energy and payload

AGV payload capacity for a predefined task can be estimated depending on the available battery energy. This type of estimation can prevent deep discharge of the battery and also prevent undesired stops of AGV during the operation.

4. CONCEPTUAL DEVELOPMENT OF AGV TRACTION SYSTEM

4.1. Relationship between traction topology and traction system specifications

Steering of an AGV can be realized either by differential control or steerable drive system. Steerable motor drive systems are commonly used if AGV has longer length (> 2m) and smaller turning radius is required. Some examples of commercially available steerable systems are given in [22-24]. Total system efficiency and maintenance requirements of steerable drive system should be discussed with the suppliers. The most common topologies and steered drive systems are listed below [22-25].

1. Two-wheels active steered, two wheels passive driven systems.
2. Steering system with two steered wheels and rotating 180 º or 360 º.
3. Steerable drives designed as a compact system including one motor for steering and one motor for traction system.
4. Omnidirectional AGV which can move in all directions and rotate 360º. The number of wheels can be four or six.

Most of the AGVs used in automotive production plants can have a payload capacity between 600 kg and 3000 kg.

When selecting the AGV traction topology, the requirements for the following operation conditions should be defined:

1) Minimum radius for cornering
2) AGV length
3) Type of operations of AGV such as AGV carrying robot arms or an AGV carrying a payload is a critical parameter for the positioning accuracy
4) Maximum inclination
5) Irregularities of operation floor that can cause vibration.
6) Minimum required AGV speed during cornering
7) The selected motor and inverter combination should produce the required torque at the requested minimum speed operation. The second issue is the motor position accuracy at the requested minimum speed.
8) If required, design of suspension for each wheel
9) Physical dimensions and available space for the selected topology

In [25], AGV topologies shown in Fig.3 is studied considering three design parameters: maneuverability, stability, and controllability. As stated in [25], in order to maintain AGV stability at least three wheels should be in ground contact. Four and more wheels can improve stability and in this case flexible suspension system is required in order to maintain contact of each wheel to the ground [25].

In [26], AGV suspension design is studied. A suspension system acts as a mechanical filter and maintains the stability of AGV [26].

The suspension also provides mechanical protection to the motor and its bearings against vibration at imperfect floors.

Based on the evaluation of these topologies, the decision can be given to use the steerable drive, differential drive or Omnidirectional system. Steered drive includes the motor, inverter, gearbox of traction system and steering mechanism driven by a separate motor and inverter as well.

The type of vehicle wheel and wheel material should also be selected in conjunction with the traction topology. For example, in Omnidirectional AGVs, Swedish type or Mecanum type wheels provide an extra degree of mobility with respect to conventional rolling wheels. An AGV design example with Mecanum wheels is given in [27] **.** On the other hand, polyurethane wheels are primarily used in steerable and differentially controlled AGVs because of their advantages such as noise reduction, load-bearing capability, improved traction properties and resistance to corrosion [28]. Detailed datasheets are available in [28-30].

The design of Omnidirectional AGVs has been studied in [31-35].The steerable wheel has a rotating mechanism, including the traction motor and gearbox. Based on the received position reference, steerable wheel system can change its steering angle actively. Omni-directional wheels use a special wheel structure for movement in any direction. Swedish type wheels have been widely used in narrow maneuvers. Robot soccers is one of the typical applications [31].

In [33-34], a novel MY3 type wheel is developed. MY3 wheel is insensitive to dirt and any particles on the floor in any production environment. In [35], Omnidirectional AGV having 740 kg payload and driven by Mecanum wheels has been studied, including the design details such as finite element analysis, calculation of radial forces, mecanum wheel design, motor sizing, electric schematics and test bench. Design schematics in [35] indicate that an additional ball bearing and coupling are installed between gearbox and wheel are mounted for each wheel. In case the radial force limits of motor and gearbox per wheel can not handle the design limits, an external bearing system can be designed as shown in [35].Therefore, radial force limits of motor, gearbox and wheel should be analyzed in detail in datasheets. Assuming an equal distribution of total force per wheel, basic calculation of radial force per wheel is given as

$$F_{rad} = m/(N_{dr} + N_s) \qquad (1)$$
$$m = (m_p + m_{agv})$$

Where: F_{rad} : is the radial force per wheel [N];
m : total weight of AGV including payload
m_p : payload [kg]
m_{agv} : mass of AGV [kg]
N_{dr} : number of the motor driven wheels [-]
N_s : number of supporting wheels [-]

However, this calculation assumes that all of the wheels are always in contact with the ground. In case of irregularities on the floor, one wheel may not be in contact with the floor. In this case, the radial force per wheel will be higher than the calculated radial force in (1). Such worst cases should be included in the calculations.

4.2. Motion control loops in an AGV

As depicted in Fig.4, AGV system controller calculates the position reference based on the target trajectory planning algorithm (TPA). Inverters (motor controllers) run in speed control mode following the output of the TPA. Similar control configuration is also studied in [27,36-37].

Motion control accuracy is very much dependent on the odometry system and its accuracy. Odometry is the calculation method of relative position of AGV. Odometry errors are due to the changes of the wheel elasticity at load variation and wheel slip.

In [38], it is proposed that encoder mounted on the non-driven wheel axle can eliminate errors caused by the wheel slip while applying the braking or driving torque by the motor. Odometry errors and solution proposals are studied in detail in [38].

4.3. Definition of specifications of AGV traction system components

Basic components of the traction torque are acceleration, friction and inclination torques as expressed by equation 2,3,4 respectively.

A template for motor sizing of an AGV are given [39-40]. In addition to the calculation methods in [39-40], RMS (root mean square) torque over a given period of operation should also be calculated to verify that RMS torque representing the load torque is equal to or less than the rated torque [41].

RMS torque can be calculated as given in equation (6). A detailed motor datasheet is available in [42].

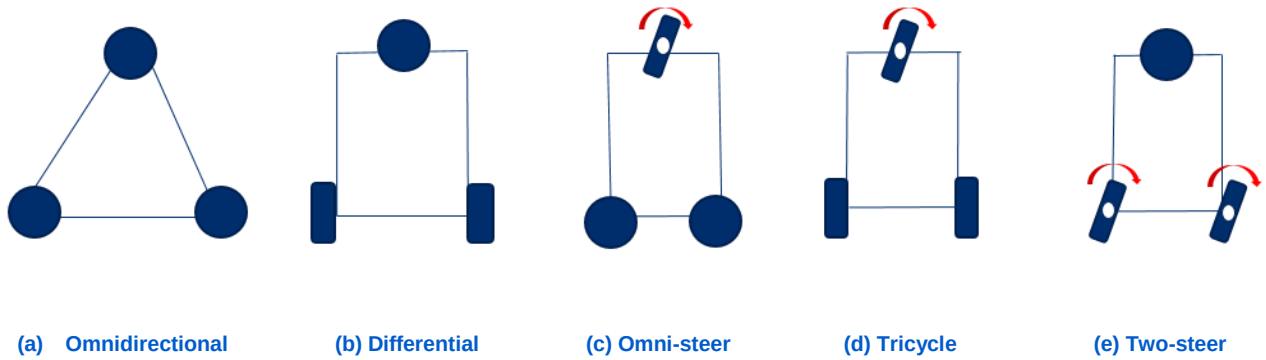

Figure 3. AGV traction system topologies [25]

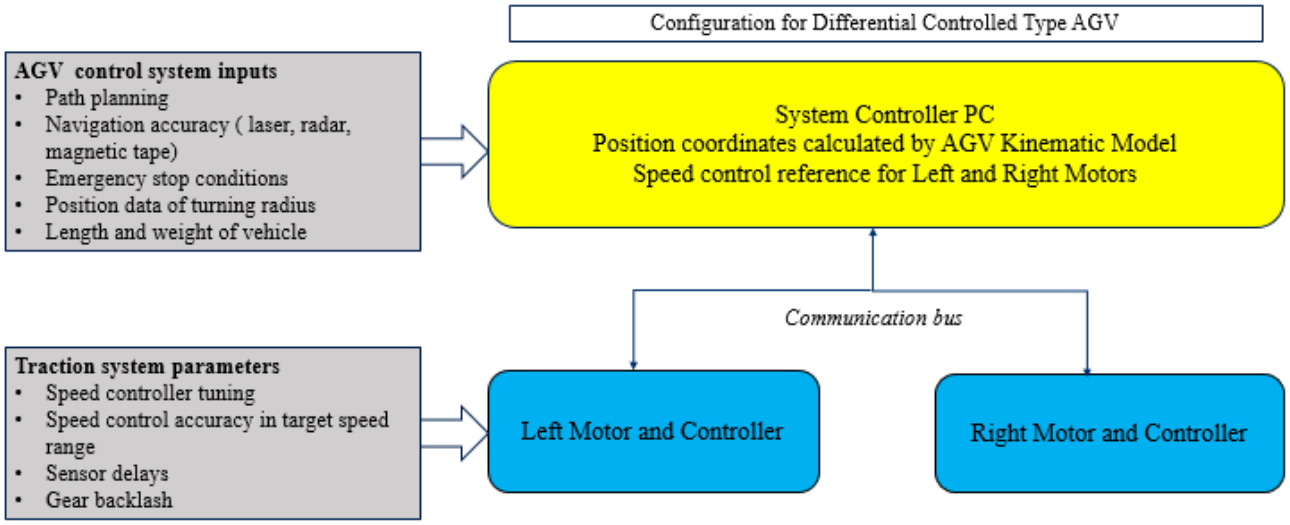

Figure 4. Basic schematics of AGV motion control and critical system parameters

$$M_{acc} = m\frac{dV}{dt}. \quad (2)$$

$$M_{rr} = mgf_r. \quad (3)$$

$$M_{gr} = mgsin(\theta). \quad (4)$$

$$M_{tract} = M_{acc} + M_{rr} + M_{gr}. \quad (5)$$

$$M_{rms} = \sqrt{\frac{M_1^2t_1 + M_2^2t_2 + M_3^2t_3 + M_4^2t_4 + M_5^2t_5}{t_1 + t_2 + t_3 + t_4 + t_5}}. \quad (6)$$

m is the total weight of AGV as given in (1) ,f_r is the rolling friction coefficient of the AGV wheels, and θ is the inclination angle of the operation floor.

In fig.5, change of traction torque is given for an example duty cycle. It is assumed that AGV operates based on the operations as described below:

M_1: Acceleration torque at maximum payload.

M_2: Torque at constant speed operation. Payload is maximum.

M_3: Deceleration torque to lower speed.

(short resting period can be applied at the end of t_3)

M_4: Acceleration torque at reduced payload.

M_5: Torque at constant speed operation at reduced payload.

Durations of operations for each of the torques M_1, M_2, M_3, M_4, M_5 corresponds to t_1, t_2, t_3, t_4, t_5 respectively.

A sample duty cycle of AGV can be recorded during a test operation including the frequent start-stop operations at peak loads and possible inclination angles. Recorded duty cycle can be used for calculation of RMS torque.

Most of the motor and inverter suppliers have available products designed for 48 V DC input.

PWM frequency of inverters used in AGVs can be in the range of 12-24 kHz. Higher PWM frequency, in principle, increases inverter switching losses and motor core losses as well. Therefore, combined efficiency of the motor and inverter is necessary for energy consumption and energy management as well.

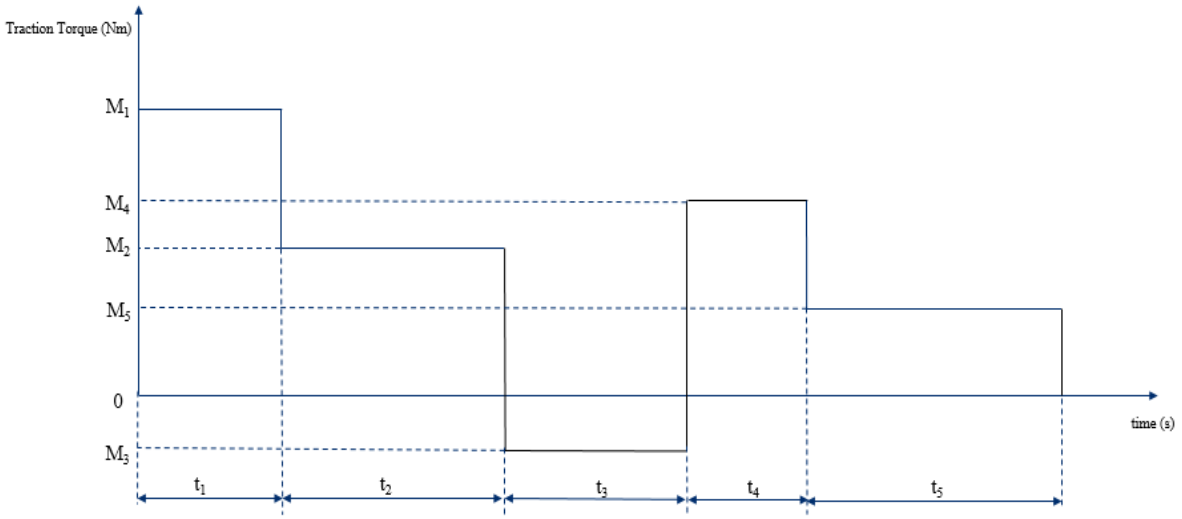

Figure 5. An AGV duty cycle example for RMS torque calculation

In case of a combination of motor and inverter from different suppliers, a combined efficiency map of motor and inverter can be derived by performing an efficiency test on a dynamometer test bench. In this way, efficient operation points on the motor efficiency map can be chosen for the target duty cycle.

Important details on component selection and application of AGV traction system are summarized below:

Inverter

- Speed control performance, available peak torque and speed accuracy below 200 rpm should fulfil the low speed AGV performance requirements (i.e. Vx < 0.1m/s) at maximum loads.
- The setting of the S-ramp profile in the inverter enables smooth start and stop, and can improve the positioning accuracy during stops.
- Safe torque OFF function, compliance with safety standards EN61800-5-2, PL e CAT3 EN ISO 13849-1:2015, SIL3 EN 61800-5-2:2017 [43].
- Use of brake resistors at the DC input terminals of the inverters provides overvoltage protection of battery and inverter in case of rapid deceleration and emergency stop conditions at maximum payloads.

Motor

- Cogging torque in permanent magnet motors causes speed and torque ripples, especially at speeds below 200 rpm. Cogging torque should be minimum in order to improve the AGV positioning accuracy [44].
- Maximum requested torque at the maximum ambient temperature should be verified by the motor datasheets.
- Efficient motor operation will reduce the motor thermal load, and provide longer duration of operation due to the efficient use of the battery energy. Efficient operation of the motor can be realized if the combination of gear ratio and motor speed reference yields an efficient operation point on the motor efficiency map. Speed ranges between 0-300 rpm is typically not an efficient operating point for a motor having 3000 rpm rated speed.

Motor and Gearbox

- Radial force limit (RFL) at maximum load is the critical mechanical limits the maximum payload capacity. RFL is also a critical regarding the lifetime of motor bearings and gearbox.

Gearbox

- Lower backlash reduces positioning errors.
- Higher gear ratios reduces the load inertia reflected at the motor shaft, and hence enables easier tuning of the speed controller of the inverter.
- For the same power requirement, choosing a high gear ratio enables shifting the motor's operating point to the high-efficiency region, which can be greater than 85 % and energy saving as well.

Battery

When operating at maximum levels of inclination, operation at maximums of speed, load, and acceleration should be avoided. Because this is the worst case for the energy consumption and causes rapid discharge of the battery.

5. INTEGRATION AND APPLICATION ASPECTS OF AGV TRACTION SYSTEM

5.1. Preventive measures against the failure of AGV traction motors

AGV is an enclosed vehicle without any airflow inside. Most of the traction motors of AGVs are naturally cooled and can be exposed to overload cyclically because the operator can exceed the payload limits. If the specifications at conceptual development does not consider real-life operation conditions, motor premature failures such as winding and bearing failures can occur. As a consequence of this, undesired shutdown can occur.

Due to the lack of studies on motor and inverter failures specific to the AGV applications, relevant studies from industrial and electric vehicle applications are reviewed which can provide also input to the AGV applications.

In order to prevent component failures, as a general rule, the unsymmetrical distribution of payload placed on AGV should be avoided as it can cause electrical and mechanical overloading of motors and gearboxes either on left or right side of AGV. It can also cause exceeding the radial force limits of bearings and gearboxes.

In [45], it is stated that thermal stresses, mechanical vibrations and humidity are the first three causes of inverter failures caused by long-term wear-out. Inverter manufacturer's test conditions in the production phase may not match the field operation. Considering the cyclic overload conditions, ambient temperature variations, and mechanical vibrations due to the floor imperfections, inverters used in AGVs can easily be exposed to the failure risks analyzed in [45].

In order to prevent failure of AGV during the operation, a list of possible motor failures are briefly given here, and possible solutions are discussed. Most typical motor faults occur in stator, rotor and bearings. Common stator faults are due to thermal overload or short circuited turns inside the stator windings. Bearing faults can be caused by thermal overload, mechanical overload, and shaft misalignment. In induction motors, broken rotor bar failures can occur due to prolonged and frequent acceleration at high torque applications.The causes of motor failures and solutions are studied in [46-50].

These problems have a slowly progressing nature, and therefore may not activate a protection function instantly. However, they can cause instant failure anytime, which can cause production stops. In [47], it is stated that almost 50 % of all motor failures are related to mechanical faults. Electrical faults of the motors can also increase noise and vibration. Consequently, noise, vibrations, and finally, the total damage to the machine and the mechanics can occur if the failure is not detected and isolated.

The list of proposed preventive measures are given below:

- Road imperfections should not cause violation of permissible vibration at the motor shafts and gearboxes. Suspension design can be considered as a solution.
- The inverter's current and torque limits should be set to limit the requested maximum torque, protecting the motor against overloading.
- In order to prevent any premature failure and detect the design problems at the earlier stage, AGV motors, bearings and gearbox should be tested periodically. Tests can be categorized as electrical faults and mechanical noises from shafts, bearings and gearboxes. Motor condition monitoring modules available in the market are not cost-effective for an AGV. An alternative solution can be use of motor and inverter test equipment [51] for periodic diagnosis.

Thermal failure risks of AGV traction motors and inverters

- Frequent acceleration at maximum payload.
- Limited resting period for cooling of the motor and inverter.
- For under-drive type AGVs, payload between left and right motors should be symmetrically placed. Otherwise, overheating risks of motor and inverter can also occur.
- Exceeding the RMS torque limits during the operation periods.

Proposed practical solutions

- Use of motor temperature sensor. Statistical evaluation of motor temperature sensor to track the overheating risks through the operations.
- Periodical temperature measurement of motor and inverters by thermal camera.
- Correct settings of current and torque limits for the inverters.
- Comparing RMS motor currents and motor temperature of all traction motors installed on left and right side of AGV for a given duty cycle. This can be helpful to evaluate the load share between left and right side motors.

5.2. Energy-Efficient Operation of AGV

Electrical supply of AGVs up to 3000 kg payload are typically lithium-based batteries. However, energy storage of heavier AGVs (> 3000 kg) can be designed as hybrid systems such as battery and supercapacitor, or fuel cell and ultracapacitors [52]. Energy management of an AGV is required to predict if the next operation can be completed with the available battery energy.

The tasks of energy management and efficiency optimization of an AGV can be categorized into six different levels, covering the software development at a higher level and optimizing the component specifications and efficient operation of the traction system at the lower level. A summary from the state of the art is given below:

1) Energy consumption and prediction models for a given load and speed profile: In [52], variation of power and SOC of the AGV energy storage system is simulated for different operation conditions.

2) *Path planning minimizing the distance*: In [53], using the linearized AGV model, path planning control is implemented using the constraint of minimum energy consumption.

3) Energy-efficient design of traction system considering the most efficient operating points: Detailed analysis of power and energy consumption of AGV is studied in [54-55]. In [54], it is reported that the higher AGV speeds yield higher efficiency and less battery energy consumption. This is due to the operation of motors at higher efficiency points. On the other hand, in [55], 2 m/s AGV speed yields rather higher energy consumption such as 0.423 kWh whereas reducing the AGV speeds to 0.7 m/s reduces the energy consumption to 0.305 kWh in one of the test cases. One reason can be increase of friction of mechanical components at higher AGV speeds. Complete model on losses of mechanical and electrical components and efficiency map of traction system is required for evaluation of energy efficiency measurements of AGVs.

4) *Flux optimized induction motor control:* Optimized flux operation of an induction motor at no-load and partial load of AGV can be potentially effective function for energy saving. This function is available in industrial applications like pumps and HVAC and it stills needs to be developed for AGV inverters. In [56], the flux-optimized induction motor is studied for an electric vehicle.

5) Utilization of regenerative energy: Regeneration can occur mostly while decelerating from high speed (i.e. from

2000 rpm motor speed) to standstill or low speed (i.e. 200 rpm range). In order to utilize the benefits of regeneration, AGV duty cycle can be planned to operate at high speed range.

6) *Optimization of operation variables by data analytic tools:* Operation variables involving in energy consumption can be optimized using the data analytic tools as given in [57]. These variables can be AGV speed, path plan, acceleration time, maximum load, periods and speed of charging time.

In Fig.6 and Fig.7, power and energy consumption from the battery terminals of an AGV used in automotive production has been given at 0.087 m/s, 0.174 m/s, 0.349 m/s, 0.698 m/s longitudinal vehicle speeds for 10 m distance for each speed. Tests are performed without any payload. The results are in parallel to the results reported in [54]. Energy consumption of an AGV is higher at lower speeds and lower at higher speeds for the same distance. Because, motor efficiency is increasing as the speed goes higher.

Best efficiency can be around 96% for permanent magnet synchronous motors.

In case of an energy efficient control of an AGV, energy management software module can select the speed which can yield most efficient point corresponding to the actual payload.

6. ELECTRICAL SYSTEM DESIGN OF AGV

AGV inverters operate at high PWM switching frequency (12 kHz-24 kHz range) and high current ratings (ranging from 50 A up to 450 A peak motor currents) at 48 V DC input. High current power cables and low current signal cables and sensors are installed in the same limited space in an AGV. Therefore, it is critical to apply all basic EMC /EMI design rules. EMC guidelines are given in [58-59]. Shielding of power and signal cables and minimizing the length of the cables between the battery and inverters are the basic and critical rules.

Operation of inverters at high PWM frequency and at high current can increase the risk of interference to signal cables of system controller, PLC and sensors. EMC/EMI issues should be considered during the layout design and can be minimized by performing a precompliance test during the prototype phases. In this way, on-going problems can be detected at the earlier phases of the development.

6.1. EMC compliance of an AGV

EMC test compliance of all electrical components referring to the EN 61000-6-4 standard should be verified at the design phase. A list of EMC and machine safety standards for AGV is given in [60].

Charger should unit should fulfil the conducted emission standard for the grid.

When the AGV fleet operates in a given zone, each AGV can radiate noise to each other and other electrical components in the same operating zone. In [21,61], analysis and solutions are studied for battery electric vehicles considering the EMI (electromagnetic interference) risks in traffic, which also provides inputs for EMC/EMI issues of AGVs.

The root causes of EMI problems in electric vehicles are the same in AGVs as power electronics components can cause interference to the electronic control modules and sensors inside AGV.

Component selection with the relevant EMC certificates and design and layout of electrical cabling considering basic EMC rules should be included in the conceptual development phase.

6.2 Common mode currents in AGV motor and inverter

In this section, possible interactions between common mode currents created by inverter and EMC/EMI related problems of an AGV is discussed briefly. Common mode currents (CMC) induced by common-mode voltages of inverter and its effect on bearing failures have been studied extensively in industrial applications and recently realized as a design and application problem in electric vehicles [62-71].

CMC currents flowing through the motor bearings are also called as bearing currents.

Schematics given in [62] can be used to analyze the problem for an AGV as well.

As stated in [62], some part of CMC can follow a return path to the inverter through the vehicle body causing large EMI problems. Same risks are valid for AGVs. Moreover, AGVs can have two, four or six motors which can amplify the EMI problems. Considering the high frequency content of CMCs, it can increase the interference risks to the AGVs nearby and electrical equipments inside and outside of AGV.

Unlike an electric vehicle, AGVs carry a payload based on their loading profile and bearings are exposed to load most of the time. Therefore, bearing currents caused by the inverter can potantially accelerate the failure of bearings in AGVs.

Further researches are needed to analyze the risks of bearing currents at 48 V operation and inverter PWM frequency range between 10 kHz-24 kHz.

A solution on the motor side is to apply specially designed insulated bearings [69]. Another solution is using a common mode filter that is not as effective as the insulated bearing; however, it can mitigate the problem. Measurement of shaft voltages by measurement instruments like in [51] is the practical way to evaluate the risks of bearing currents and potential EMI risks as well. Detailed analysis and solution proposals on CMC are studied in [62-71].

6.3. Electrical safety against electrical arc

It is known that 48 V systems draw a higher current than 400 V supplied electrical systems at the same electrical power.

An electric arc can occur at voltages higher than 16 V DC [72]. Although 48 V is electrically safe to the human body,electrical arc in a broken cable or loose contacts can cause the burning of components and fire [72-75].

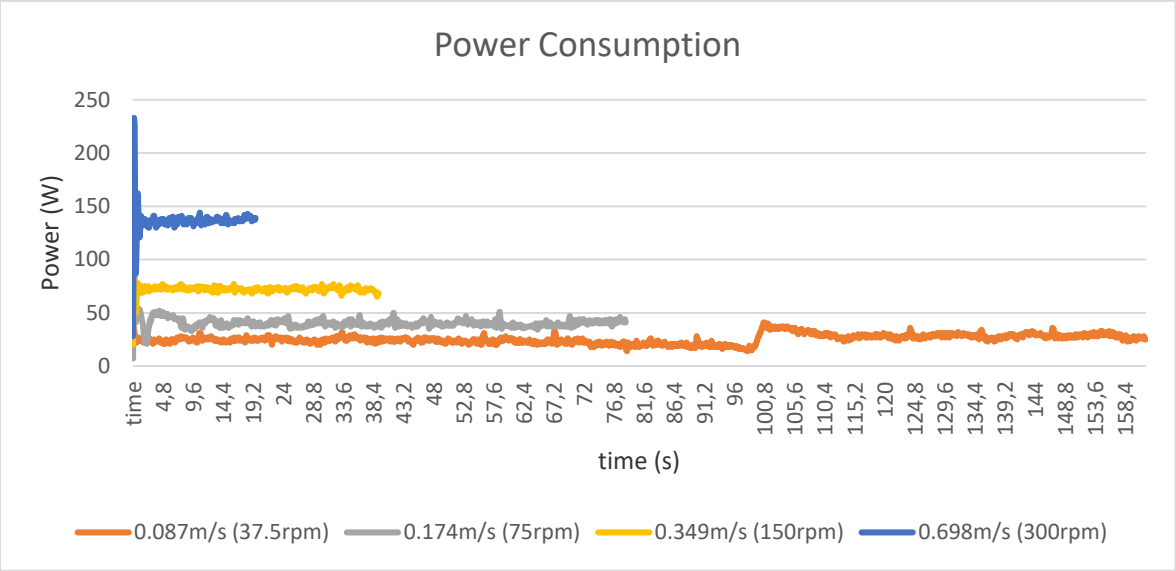

Figure 6. Electrical power consumption of an AGV at four different speeds. Payload is set to zero.

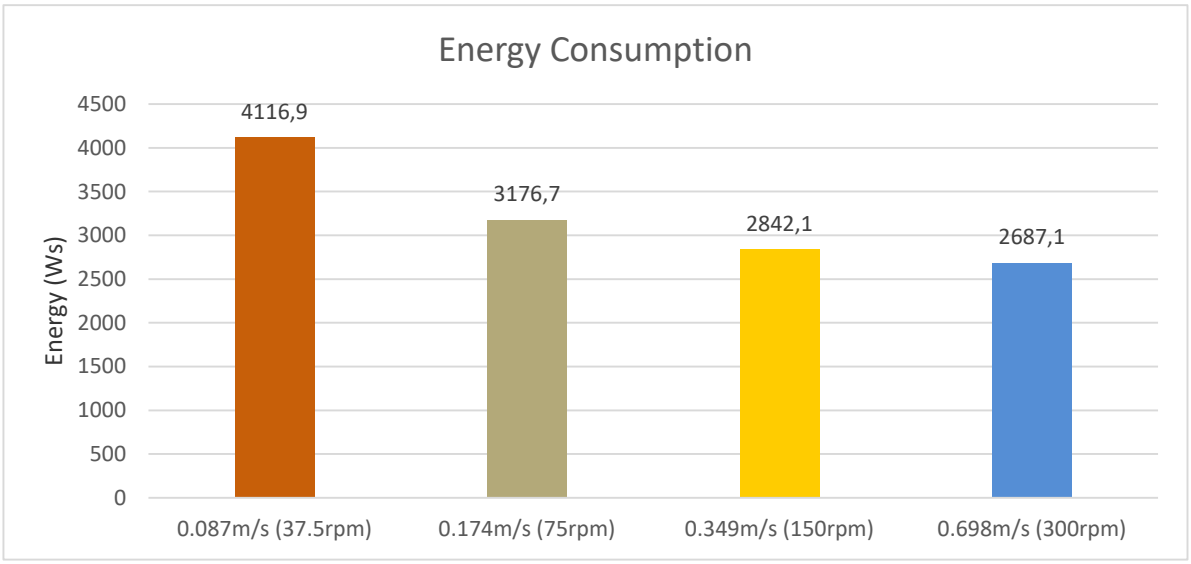

Figure 7. Energy consumption for the condition given in fig.6.

Due to exposure to vibration at surface imperfections, temperature variations, dust and humidity in the operation environment, electric arc due to the loose connections can occur inside AGV.

Therefore, any arc inside the AGV should be detected, and an emergency stop should be activated immediately.

In [75], arc occurrence and hazards in battery-supplied DC and AC supplied systems have been analyzed.

Occurance of an arc is a safety-critical situation considering the space limited layout of AGV components and lithium based batteries used as energy storage of AGV. Moreover, if AGV should carry a payload like a lithium battery in an electric vehicle production, electrical safety of the battery inside the AGV is even more critical.

As stated in [73], the consequences of an arcing short-circuit or earth-fault inside a low voltage panel can be very disastrous. The extremely hot electric arc can destroy valuable equipment causing prolonged and costly downtimes.

Protection solution for 48 V automotive systems is given in [72].

Arc flash detectors in medium and low-voltage switchgear systems given in [74,76] can be also used in AGVs designed at high power levels. Because the arc flash sensors operate based on the light occurred by the arc.

6.4. Regeneration and use of brake resistor

AGV traction system can regenerate when decelerating from maximum speed to standstill or low speeds.

Inverter overvoltage failure can occur in case of rapid deceleration or emergency stops at maximum payload condition.

A brake resistor connected to the DC input terminals of inverter can protect the battery and inverter against overvoltage.

Detailed electrical design guidelines for an AGV motor-inverter application can also be found in [77].

7. FUTURE TRENDS FOR AGV TRACTION MOTOR AND INVERTERS

Estimated future trends for the optimized AGV traction system are summarized below:

1) Integrated motor and inverters

The availability of integrated motors and inverters (IMI) are limited for AGVs. However, the IMI provides tested performance and preset tuning by the supplier. As the cable between the motor and inverter is eliminated, IMI can mitigate dV/dt voltage stress at the stator terminals of the motor and reduce EMI problems as well. Because of the electrical benefits and compact dimensions of IMIs, AGV applications need IMI solutions.

2) *48 V Induction motor as an alternative to PM motor:*

Due to the rapid growth of electromobility and AGV market, supply problems and price increase of rare earth elements has been discussed more than a decade and problem will be even more dramatic as the market for AGV and electromobility applications grow very fast. Induction motors are the best alternative to permanent magnet synchronous motors (PMSM) in AGV applications both technically and for cost reduction purposes. There are 48 V induction motor solutions in the market for AGVs [24,78].

3) 48 V Induction motor drives with optimized flux control at light loads:

For pump and HVAC loads, this function is available in industrial induction motor drives [79]. Basic principle is to optimize the induction motor efficiency by optimizing the motor flux and minimizing the motor losses at light loads. This function is currently at the research level for electric vehicles [56,80] and a research is not available on AGV. It is difficult to develop it in a battery electric vehicle where the drive cycle and inclination angle can be highly variable which means motor load is highly variable. AGVs operate at predetermined speeds and loads. Therefore, induction motor flux optimization can be adapted to AGVs easier than electric vehicle applications.

4) Temperature related power derating:

New thermal concepts are required to mitigate the thermal de-ratings of all power components at high ambient temperatures. On the other hand, minus temperatures will decrease available AGV battery capacity and hence reduce the payload capacity as well. Unlike an electric vehicle, AGVs do not have a cooling system for motors, inverters and batteries. Derating behavior of both induction motor and PM motor should be compared above 40 º for an AGV duty cycle in real conditions.

A possible remedy could be injecting cooled air into the motors by installing a cooling pipe when the AGV is parked while docking or charging. This will be a similar to plugging the charging cable of an electric vehicle during the parking. Extra housing is needed for the motors so that the cooled air will only be injected into the motor and will not cause an increase of humidity to the other electrical components inside the AGV.

At minus temperatures, payload capacity will be limited because of the limited battery discharge current. Therefore, temperature of the operation environment should comply with the allowable operation temperature of AGV battery.

Energy management strategies of an AGV has not been studied in detail in state of art. However, an energy management control module in AGV software, thermally optimized traction system and battery are mandatory for energy efficiency improvement at system level.

5) SiC and GaN semiconductors:

48 V supplied PM and induction motors and inverters are available at various current ranges [24,78,81].

SiC and GaN technology will enable thermal and efficiency improvements in inverter hardware. For example, Texas Instruments has developed a 48 V 10 A inverter with GaN (Gallium Nitride) transistors [82].

As stated in [82], advantages of GaN FET over Silicon FET can be described as having lower conduction losses, lower gate driver losses enabling faster switching, lower switching and conduction losses. All these improvements will increase the total system efficiency of the AGV.

Considering the demand for higher traction power for AGVs at 48 V, SiC and GaN technology is expected to be applied in AGVs in the near future.

6) Motor control functions:

- Motor parameter identification: Combinations from different motor and inverter suppliers can be implemented if motor electrical parameters can be identified by the inverter. This is not a common function in AGV inverter.
- Duty cycle estimation for a given AGV operation: Estimated motor shaft torque as a function of time can be logged in inverter. Based on the logged data, motor power sizing and RMS torque calculation can be done based on a defined duty cycle.
- Motor condition monitoring algorithms embedded in inverter can increase the reliability of AGV operation.

7) Monitoring functions to support cyber security:

- Suspicious and irregular acceleration patterns can be detected by tracking the motor current and speed by the inverter and reported to system operator. Emergency stop against a suspected cyber attack can be performed in such a case.

8) Inverter communication interface:

- ROS systems enables practical implementation of communication between the electronic modules. There is a growing need for ROS compatible inverters.
- In order to facilitate the system integration, AGV inverters should be designed to have optional communication interface modules supporting the most commonly used communication protocols such as Profinet, EtherCAT, CANopen, Modbus RTU, and USB.

8. CONCLUSION

In this paper, the AGV traction system, critical development and integration parameters have been studied. It is concluded that all subsystems of an AGV have interaction with each other. Each phase of conceptual development has impact on performance of AGV in the operation environment. New generation AGV traction systems should be optimized for higher efficiency. Thermal optimization is also required for improvement of available motor power. Energy management algorithms should be developed specific to AGVs. Energy efficiency of AGVs at system level will be critical performance indicator for the plant's energy efficiency as well.

REFERENCES

[1] https://www.fortunebusinessinsights.com/automated-guided-vehicle-agv-market-101966

[2] M. De Ryck, M. Versteyhe, "Automated Guided Vehicle Systems, State-Of-The-Art Control Algorithms and Techniques," Journal of Manufacturing Systems , vol.4, pp.152-173, Jan.2020.

[3] M. De Ryck, M. Versteyhe, K. Shariatmadar, "Methodology for a Gradual Migration from a Centralized towards a Decentralized Control in AGV Systems," 6th Int. Conf. on Mechatronics and Robotics Engineering, Feb.2020.

[4] I.Draganjac et.al. "Decentralized Control of Multi-AGV Systems in Autonomous Warehousing Applications," IEEE Transactions on Automation Science and Engineering, vol. 13, No. 4, October 2016.

[5] E. Oyekanlu et al., "A Review of Recent Advances in Automated Guided Vehicle Technologies: Integration Challenges and Research Areas for 5G-Based Smart Manufacturing Applications,",IEEE*Acces*, Nov. 2020.

[6] https://www.fortunebusinessinsights.com/automated-guided-vehicle- agv-market-101966

[7] https://scottautomation.com/en/products/agv/custom-agvs/heavy-load- agv

[8] Q. Fi, T. Tao, "Digital Twin and Big Data Towards Smart Manufacturing and Industry 4.0: 360 Degree Comparison," IEEE *Access*, Jan. 2018.

[9] M. Azangoo, A. Taherkordi, J.O. Blech and V. Vyatkin, "Digital Twin-Assisted Controlling of AGVs in Flexible Manufacturing Environments," IEEE 30th International Symposium on Industrial Electronics (ISIE).

[10] Staczek, P.; Pizon´ , J.; Danilczuk,W.; Gola, A. "A Digital Twin Approach for the Improvement of an Autonomous Mobile Robots (AMR's) Operating Environment—A Case Study," Sensors **2021**, 21, 7830. https://doi.org/10.3390/s21237830.

[11] Y. Bai , J-B. You , and Il-K. Lee, "Design and Optimization of Smart Factory Control System Based on Digital System Model," August 2021, Hindawi, https://doi.org/10.1155/2021/2596946.

[12] www.wiferion.com

[13] www.in2power.com

[14] R. French, V. Degeler, and Kevin Jones, "A Model of a Malware Infected Automated Guided Vehicle for Experimental Cyber-Physical Security, Proceedings of SAI Intelligent Systems Conference," Sept. 2018.

[15] MD. Sarder, M. Haschak, "Cyber Security and Its Implication on Material Handling and Logistics," Feb. 2019, available at https://www.mhi.org/downloads/industrygroups/solutions-community/white-papers/cyber-security.pdf

[16] https://www2.deloitte.com/cn/en/pages/consumer-industrial-products/articles/industry-4-0-and-cyber-security.html

[17] "Connected manufacturing, a guide to industry 4.0 transformation with private cellular technology", available at https://www.ericsson.com/en/internet-of-things/audience-page/connected-manufacturing-report

[18] Bécue et al., "CyberFactory#1– Securing the Industry 4.0 with cyber-ranges and digital twins," 2018 14th IEEE International Workshop on Factory Communication Systems.

[19] R. Kiesel, "Quantification of Influence of 5G Technology Implementation on Process Performance in Production", ScienceDirect, 54th CIRP Conference on Manufacturing Systems, 2021.

[20] K. Foit, G. Golda, A. Kampa, "Integration and Evaluation of Intra Logistics Processes in Flexible Production Systems Based on OEE Metrics, with the Use of Computer Modelling and Simulation of AGVs,", Processes, vol.8., issue 12, Nov. 2020.

[21] N. Mutoh, M. Nakanishi, M. Kanesaki, and J. Nakashima, "EMI Noise Control Methods Suitable for Electric Vehicle Drive Systems," IEEE Transactions on Electromagnetic Compatibility vol.47, No.4, Nov. 2005

[22] www.alliedmotion.com

[23] www.metalrota.it

[24] www.tekno-mp.com

[25] Legius, M. J. E., Nijmeijer, H., & Rodriguez Angeles, A. "Simulating the dynamical behavior of an AGV," D&C vol. 2014.012 Eindhoven University of Technology, 2014.

[26] A. Carvalho, "Improvement Project of an AGV's Suspension System in order to Reduce Manufacturing Costs," Instituto Superior Tecnico, Lisboa, Portugal, Nov. 2019.

[27] M. Braverman, Y. Danino, H. Lepak, Y. Mordecai, "AGV Testing and performance," Nov. 2016, available at www.etc.europa.eu

[28] https://www.casterconcepts.com/solutions/polyurethane-casters/polyurethane-tires-advantages/

[29] https://www.hamiltoncaster.com/wheels

[30] https://www.blickle.com/

[31] G. Indiveri, "Swedish Wheeled Omnidirectional Mobile Robots: Kinematics Analysis and Control," IEEE Transactions on Robotics vol.: 25, Issue: 1, Feb. 2009

[32] J. Qian et al., "The Design and Development of an Omni-Directional Mobile Robot Oriented to an Intelligent Manufacturing System," Sensors, Sept. 2017.

[33] S. Yu, C. Ye, H. Liu, J. Chen, "Development of an omnidirectional Automated Guided Vehicle with MY3 wheels", Dec. 2015, Elsevier.

[34] Wang, W. Cui, X. Xu, C. Ye, "Research on an Omni-directional AGV with Differential Wheels," Proceedings of 2016 IEEE International Conference on Mechatronics and Automation Aug.2016.

[35] ZY. Chen, PR Liaw, V. Nguyen, P. Lin, "Design of a high-payload Mecanum-wheel ground vehicle (MWGV)", JVE Journals, Robotic Systems and Applications, vol. 1, Issue 1, 2021, p. 24-34.

[36] H. Zhang, D. Wu and T. Yao, "Research on AGV trajectory tracking control based on double closed-loop and PID control", Journal of Physics Conference Series, September 2018.

[37] Y. Han, Y. Cheng, and G. Xu, Trajectory Tracking Control of AGV Based on Sliding Mode Control With the Improved Reaching Law, IEEE *Access*, vol.7, Feb.2019

[38] M. Smieszek, M. Dobrzanska, P. Dobrzanski, "The impact of load on the wheel rolling radius and slip in a small mobile platform," Auton Robot 43, 2095–2109, 2019 https://doi.org/10.1007/s10514-019-09857-0

[39] https://www.orientalmotor.com/motor-sizing/agv-sizing.html

[40] M.Cheira, "Design of an Automated Guided Vehicle for Material Handling," Master Thesis, Technical University of Lisbon, July 2019.

[41] https://www.hmkdirect.com/downloads/knowledge_base/drive_sizing_v2.pdf

[42] Nidec Servo Motor Series Unimotor HD ultra low voltage (24V-48V) , available at https://acim.nidec.com/

[43] https://www.roboteq.com/docman-list/motor-controllers-documents-and-files/documentation/application-notes/documentsareports/917-sto-certification/file

[44] https://www.baumueller.com en/insights/basics/ /what-is-the-cogging-torque

[45] A.Abuelnaga, M. Narimani, and A. Bahman, "A Review on IGBT Module Failure modes and Lifetime Testing," Jan. 2021, IEEE Access

[46] https://www.emerson.com/documents/automation/brochure-electric-motor-problems-diagnostic-techniques-ams-en-6652274.pdf

[47] S. Anchehpoli, "Analysis and diagnosis of faults in the PMSM drivetrains for series hybrid electrical vehicles (SHEVs)," Electric power. Université de Technologie de Belfort-Montbeliard, 2013.

[48] E. Ayaz, "A Review Study on Mathematical Methods for Fault Detection Problems in Induction Motors," Balkan Journal Of Electrical & Computer Engineering, 2014, vol.2, No.3

[49] R. Selcuk, R. Dogan, "A Diagnosis Of Stator Winding Fault Based on Empirical Mode Decomposition in PMSMs," Balkan Journal Of Electrical & Computer Engineering vol. 8, No. 1, January 2020

[50] M. Seker, D.B.Kara, "Dynamic Investigation of a Permanent Magnet Synchronous Motor for Faulty Operations," European Journal of Technique, vol.11, No.1, 2021

[51] https://www.fluke-direct.com/product/fluke-mda-550-motor-drive-analyzer-with-motor-shaft-and-harmonics-4-channel-500-mhz

[52] R. Niestrój, T. Rogala and W. Skarka, "An Energy Consumption Model for Designing an AGV Energy Storage System with a PEMFC Stack," Energies, July 2020.

[53] I. Holovatenko, A. Pysarenko, "Energy-Efficient Path-Following Control System of Automated Guided Vehicles," Journal of Control, Automation, and Electrical Systems, Nov. 2020.

[54] M. Meißner , L. Massalski, "Modeling the electrical power and energy consumption of automated guided vehicles to improve the energy efficiency of production systems," The International Journal of Advanced Manufacturing Technology, April 2020.

[55] S. Riazi, K. Bengtsson, B. Lennartson, "Energy Optimization of Large-Scale AGV Systems," IEEE Transactions on Automation Science and Engineering (vol.: 18, Issue: 2, April 2021)

[56] D. Casadei et al. "Energy-Efficient Control of Induction Motors for Automotive Applications," XIX International Conference on Electrical Machines - ICEM 2010, Rome.

[57] https://www.ge.com/digital/lp/free-proficy-csense-software-trial

[58] https://dl.mitsubishielectric.com/dl/fa/document/manual/plc/bqn-p0e100083e/bqnp0e100083e.pdf

[59] https://download.sew-eurodrive.com/download/pdf/11535814.pdf

[60] https://www.sgs.com/en/news/2017/01/market-access-requirements-for-automated-guided-vehicles-agvs

[61] F. Corbett, " EMC Challenges in connected cars," White Paper, available at https://www.ttieurope.com/content/dam/tti-europe/about/distribution-center/TTI_Whitepaper-EMC-challenges-in-connected-cars.pdf

[62] S. Hatsukade, M. Nagata, "Reduction of EMI from Traction Circuits using Shielded Cable," Quarterly Report of RTRI 49(1):20-25, Feb.2008.

[63] Turzynski, M. ; Musznicki, P. A Review of Reduction Methods of Impact of Common-Mode Voltage on Electric Drives. Energies 2021, 14, 4003. https://doi.org/10.3390/en14134003

[64] T.G.Arora, M.M.Renge, M.V.Aware, "Effects of Switching Frequency and Motor Speed on Common Mode Voltage, Common Mode Current and Shaft Voltage in PWM Inverter-fed Induction Motors", 12th IEEE Conference on Industrial Electronics and Applications (ICIEA), 2017.

[65] Y. Xu et al., "Experimental Assessment of High Frequency Bearing Currents in an Induction Motor Driven by a SiC Inverter", March 2021, IEEE*Access.*

[66] Y. Yang, H. Peng, Q. Wang, "Common Model EMI Prediction in Motor Drive System for Electric Vehicle Application"

[67] https://library.e.abb.com/public/8c253c2417ed0238c125788f003cca8e/ABB_Technical_guide_No5_RevC.pdf

[68] https://est-aegis.com/bearing

[69] https://www.skf.com/binaries/pub12/Images/0901d1968019754c-6815EN_tcm_12-57716.pdf

[70] M. Turzynski, P. Musznicki, "A Review of Reduction Methods of Impact of Common-Mode Voltage on Electric Drives," Energies, July 2021.

[71] A Muetze, A. Binder, "Practical Rules for Assessment of Inverter-Induced Bearing Currents in Inverter-Fed AC Motors up to 500 kW", IEEE Transactions On Industrial Electronics, vol. 54, No. 3, June 2007

[72] https://blog.leoni.com/what-opportunities-and-risks-will-48-volt-wiring-systems-provide/

[73] https://www.fluke.com/en-us/learn/blog/safety/arc-flash-vs-arc-blast

[74] https://new.abb.com/medium-voltage/digital-substations/arc-fault-protection/arc-fault-protection-system-rea/rea-101

[75] H. Schau, "Risk parameters of DC fault arcs – research work on DC arcs in LV systems," 12th International Conference on Live Maintenance (ICOLIM), April 2017.

[76] https://new.siemens.com/global/en/products/energy/energy-automation-and-smart-grid/protection-relays-and-control/general-protection/arc-protection.html

[77] https://www.roboteq.com/docman-list/motor-controllers-documents-and-files/documentation/user-manual/272-roboteq-controllers-user-manual-v21/file

[78] https://www.benevelli-group.com/

[79] K. Lee at al., "Optimal Energy Efficiency Evaluation in Induction Machines Driven by Adjustable Speed Drives under EN 50598-2 and IEC 61800-9-1 Standards," IEEE Energy Conversion Congress and Exposition (ECCE), Sept 2018.

[80] Pedro Melo, Ricardo de Castro and Rui Esteves Araújo (November 14th 2012). Evaluation of an Energy Loss-Minimization Algorithm for EVs Based on Induction Motor, Induction Motors - Modelling and Control, Prof. Rui Esteves Araújo, IntechOpen, DOI: 10.5772/52280. available at: https://www.intechopen.com/chapters/40909

[81] https://www.elmomc.com/

[82] TI Designs,"48-V, 10-A, High-FrequencyPWM,3-Phase GaN Inverter Reference Design for High-Speed Motor Drives," available at https://www.ti.com/lit/ug/tiduce7b/tiduce7b.pdf?ts=1628842395816&ref_url=https%253A%252F%252Fwww.google.com%252F

BIOGRAPHIES

Mustafa Karamuk obtained his BS and MS degrees in electrical engineering from Istanbul Technical University in 1994 and 1998, respectively. He is studying towards Ph.D. at Istanbul Okan University in Mechatronics Engineering Department. He worked as application engineer in Siemens Istanbul, and R&D engineer in Danfoss Drives in Denmark, IAV GmbH in Germany, Tofaş-FIAT and Arcelik. Currently, he is working as Senior R&D Engineer in Ford Otosan R&D Center in Istanbul. He is the author of 7 articles. His research interests include control of motor drives in industrial automation and electric vehicle applications, electric powertrain development and automotive mechatronics.

Ismail Hakki Savci obtained his BS in mechanical engineering from Istanbul Technical University and a Ph.D. degree in mechanical engineering in 2015. He has been a technical manager in Ford Otosan. He published more than 20 articles and more than 10 inventions. His research interests include thermal systems, measurement techniques and autonomous vehicles.

Hakan Ocakli obtained his BS degree in Mechatronics engineering from the University of Kocaeli in 2012. He worked as a Test and Validation Engineer at Ford Otosan Engine Development and Test Laboratory from 2014 to 2019. He worked on heavy-duty engines projects used in Ford trucks. He has been working as an autonomous mobile robot software development engineer in the Ford Otosan Product Development department since 2019. In this role, he works on the development of indoor localization software for autonomous mobile robots

.

European Journal of Technique

journal homepage: https://dergipark.org.tr/en/pub/ejt

Vol.12, No.1, 2022

Dynamic Performance Comparison of the Different PV Modules with Real Data

Onur ELMA[1*],

[1*]Çanakkale Onsekiz Mart University, Electrical and Electronics Engineering Department, Çanakkale, Turkey. (e-mail: onurelma@comu.edu.tr).

ARTICLE INFO

Received: Nov., 28. 2021
Revised: Feb., 02. 2022
Accepted: Apr, 21. 2022

Keywords:
PV systems
Renewable resources
Performance analysis
Modeling
Dynamic weather data

Corresponding author: *Onur Elma*

ISSN: *2536-5010* | e-ISSN: *2536-5134*

DOI: https://doi.org/10.36222/ejt.1029684

ABSTRACT

Nowadays, photovoltaic panels are an important source of electricity production and one of the preferable renewable resources. Many companies have started to produce because of increasing PV panel demand. It is a fact that the performance of PV panels under real environmental conditions in the application area will affect the benefit to be obtained from the application and the investment to be made. In this study, MATLAB/Simulink models of the PV panels are used for performance comparison with measured weather data in Istanbul, Turkey. The parameters of five different PV panels in the market are used for analysing the total energy generation performances under different weather conditions. Thus, the effects of using dynamic analysis to be obtained from more detailed simulation studies have been revealed instead of feasibility calculations to be made using only the data specified in the technical document.

1. INTRODUCTION

Today, where humanity's energy needs are increasing day by day, renewable energy sources have become an important alternative to meet this need and reduce the dependence on fossil fuels. Photovoltaic (PV) systems, which produce electricity, especially from solar energy, are the most preferred renewable energy sources. In addition, PV panels have an important effect on the spread of these systems with the incentives given to the electrical energy produced by them. The interest in PV systems helps decrease production costs, and also, this system becomes more advantageous as a cheaper energy source. PV systems have important advantages in grid-connected and off-grid systems in modular structures, accessible design, and hybrid operation with different sources. These systems allow electricity production in a wide range, from a small system that can meet the needs of a house to a large power plant that can meet the energy needs of a region. For this reason, it is an energy source that can be used by both end consumers and large energy investors.

Many studies focus on the ability of PV systems to produce more efficiently in this wide production range, their integration with the existing grid, proper positioning, and operation in hybrid systems [1-4]. In one of these studies, the advantages of positioning the PV panels at the appropriate angle were analyzed [4,5]. In addition, the effect of data resolution on the sizing of the hybrid energy system supplied with off-grid PV panels and wind turbines has been investigated [2]. Another study examined the economic analysis of solar tracking systems in a hybrid pumping system with PV panels [6]. The experimental setup has been done for analysis of the PV performance [7]. Also, performance comparisons of PV panel types with different production structures under real environmental conditions have also been carried out [8, 9].

These studies provide important information for more efficient operation of the systems in which PV panels will be used. Especially, general weather data of the region and efficiency parameters for the PV panels are used in the calculations made during the investment and projecting phase of large-scale solar farms [10]. In another study, the performances of monocrystalline and polycrystalline panels were compared under the same ambient conditions [11]. In one project in Morocco, different PV panel technologies were installed in 20 other cities, and the energy performance of the system was tested [12]. In addition, the long-term performance of PV panels in tropical climate conditions was also investigated [13]. The performance of PV panels is affected by environmental conditions directly. In one of the related studies, the performances of different PV modules have been compared under Australian climate conditions. [14]. Most studies aim to determine the factors affecting the performance of PV panels in real application conditions. Most of them use more general data (hourly and/or daily measurements) to do this. However,

more dynamic data should be used for better results and accurate calculations.

PV panels are formed by combining PV cells with different sizes and power values. It is a fact that the efficiency and performance of the PV panels in the real system will directly affect the depreciation period and the profit to be obtained from installing the solar power plant. Generally, during the projecting phase of solar power plants, a general installation power analysis is made based on technical document data. For this reason, analyzes made only on the price or public values of the panels cannot obtain sufficient dynamic results. However, with the widespread use of dynamic pricing in energy markets, the importance of instantaneous power generation from power plants will emerge.

In this study, the situation of the PV panel manufacturers in the market to create 100kW solar power plants using five different PV modules in the same power band has been taken into account. The performances of five different PV systems with the same power have been analyzed in the simulation environment with the measured data at the exact location and weather conditions. PV models created in the MATLAB/Simulink program were used.

This study is organized as follows; in section 2, mathematical description of PV panel and electrical modeling are explained. In addition, the modeling of the PVs is given detailed. In section 3, the performances of different PV panels under the same conditions are analyzed with the case study. Finally, the outputs obtained in the results section were evaluated, and suggestions and conclusions were stated.

2. MODELING OF THE PV SYSTEMS

First of all, PV panels must be modeled in order to analyze the proposed system structure. A detailed description of the model used for this purpose is given below.

The five parameters used in the modeling of the PV cell are determined respectively as; a current source (I_L), a diode (I_0 and D_0), a series resistor (R_s), and a parallel resistor (R_{sh}). The current-voltage characteristics of the PV cell have been determined by using the relevant parameters. Accordingly, the mathematical definition of a single PV cell can be made with the equations given below;

$$I_d = I_0 + \left[\exp\left(\frac{V_d}{V_T}\right) - 1\right] \quad (1)$$

where I_d is the diode current (A), V_d is the diode voltage (V), and I_0 is the diode saturation current (A).

$$V_T = \frac{KT}{q} \times D_I \times N_{cell}. \quad (2)$$

where k is the Boltzmann constant (1.3806e-23), T is the temperature of the cell (K), q is the magnitude of the charge of an electron (1.6022e-19) and D_I is ideality factor of the diode. N_{cell} is the number of cells that are connected parallel and series in the PV module.

The electrical model of the PV cell, which has been modeled with related parameters, has been given in Figure 1. In the literature, the electrical model of the PV cell has been used as a single-diode model and a double-diode model. In this study, a single-diode electrical model of the PV has been chosen.

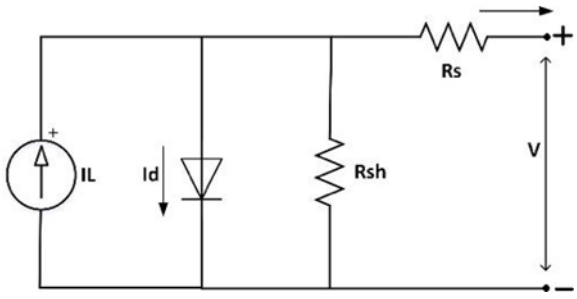

Figure 1. Electrical model of a PV cell

PV module is constructed by making a N_{cell} number of connections between PV cells. The serial and parallel connections of PV modules and the formation of PV panels' phases are given in Figure 2.

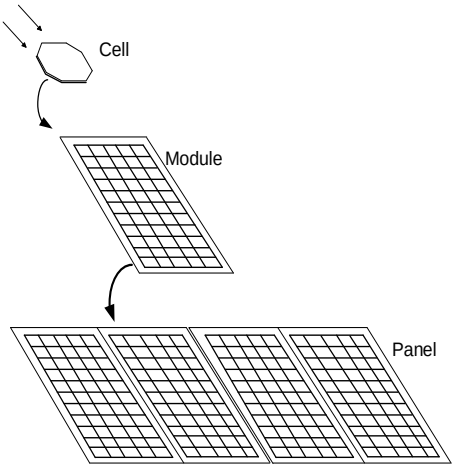

Figure 2. The transition from PV cells to panels

The PV model explained electrically and mathematically above is found as a ready model on MATLAB/Simulink setting [15]. Some panels' information is already included in this model, and new panel data can be defined manually. The information required to prepare the PV model on MATLAB/Simulink media is given in Table 1.

TABLE I
TECHNICAL DATA OF PV PANELS

Symbol	Parameter
Voc (V)	Open circuit voltage
Vmp (V)	Opt. operating voltage
TCOC (%/deg.C)	Temp. coefficient of P_{max}
Isc (A)	Short circuit current
Imp (A)	Opt. Operating current
TCSC (%/deg.C)	Temp. coefficient of short circuit current
Ncell	Number of cells

3. CASE STUDY

Five different PV models are obtained using the data given in Table 1, which are sold in Turkey. The measured radiation and temperature values of each model are defined, and the expected

current and voltage values are determined. Each one of the PV modules has the same output power. In order to obtain the same output power with suitable voltage and current values, the PV modules are brought together with 100 parallel and 10 serial connections. In this way, five separate solar farms are formed with 300kW power values.

The radiation and temperature values used in the analysis are acquired through the Vantage Pro2 weather station measurements in Istanbul, Turkey. This weather station is connected to an interface monitor in the main station where the data is collected with wireless communication. The data is saved to a computer system through the interface. The measured data is saved in minute intervals for better demonstrations of the dynamic performances of PV panels. So that the effects of dynamic radiation and temperature variables on PV performances can be observed clearly. In addition, the newest models of 5 different PV brands in Turkey market are chosen, which have 300 W power output and monocrystalline structure. The parameters of the determined PV panels modules (Under Standard Test Conditions; 1000 W/m2 radiation, spectrum value AM 1.5, and cell temperature 250C) are given in Table II [16-20].

TABLE II
PARAMETERS OF DIFFERENT BRAND PV PANELS

Parameter	PV1	PV2	PV3	PV4	PV5
P_{max} *(W)*	300	300	300	300	300
V_{oc} *(V)*	39.9	39.7	39.4	39.8	40.1
V_{mp} *(V)*	32.6	32.5	32.4	32.6	32.7
TC_{OC} *(%/deg.C)*	-0.34	-0.29	-0.29	-0.29	-0.30
I_{sc} *(A)*	9.65	9.83	9.76	9.77	9.66
I_{mp} *(A)*	9.21	9.24	9.26	9.19	9.16
TC_{SC} *(%/deg.C)*	0.06	0.05	0.05	0.05	0.04
N_{cell}	60	60	60	60	60

According to the parameters given in Table II, current-voltage and power-voltage graphs of selected PV panels are shown in Figure 3.

The view of the system created in MATLAB/Simulink environment for performance analysis of PV modules is given in Figure 5. The panels are connected in series and parallel so that the nominal output power of each PV system is 300 kW. The DC bus voltage (output voltage) of the system is selected as 400V. For this reason, each model module is connected as 10 serial and 100 parallel cells.

Since the study aims to obtain dynamically how the output power of the five different PV panel systems change when using dynamic radiation and temperature data, if only DC output power has been considered. Maximum power point trackers (MPPT) and converter and/or inverter structures used are in the practical applications of PV systems. However, these parts have not been taken into consideration for this study. One of the reasons the related power electronics systems are not included in the simulation study is that the modeling of the related systems is carried out at high-frequency values, so long-term (weekly) simulation analysis is not possible with existing computer hardware.

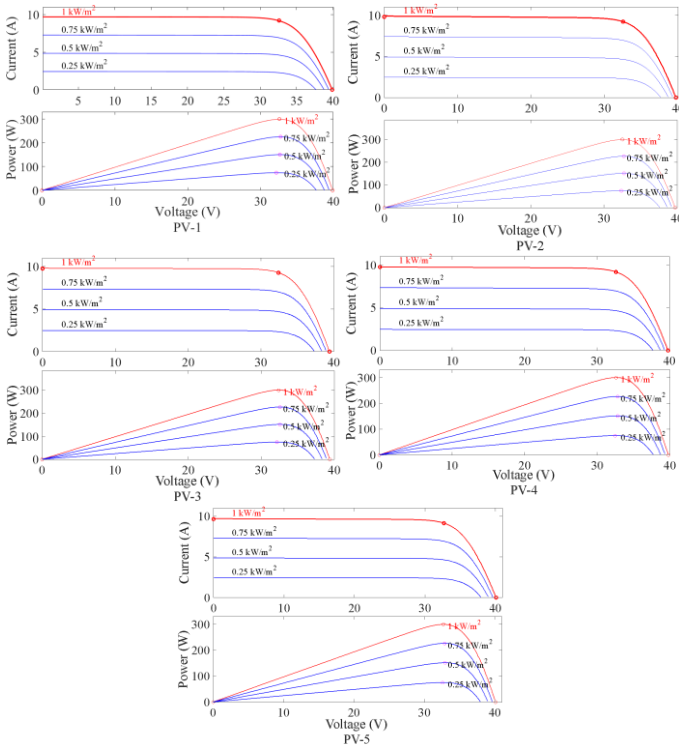

Figure 3. Current-voltage and power-voltage graphs of selected PV modules

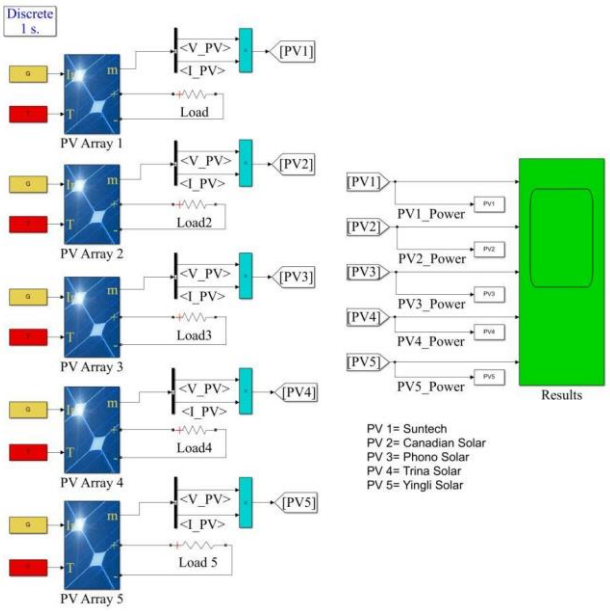

Figure 4. MATLAB/Simulink comparative model of PV panels

For the analysis study, seven days (a week) real radiation and temperature data are used as given and explained in Figure 5.

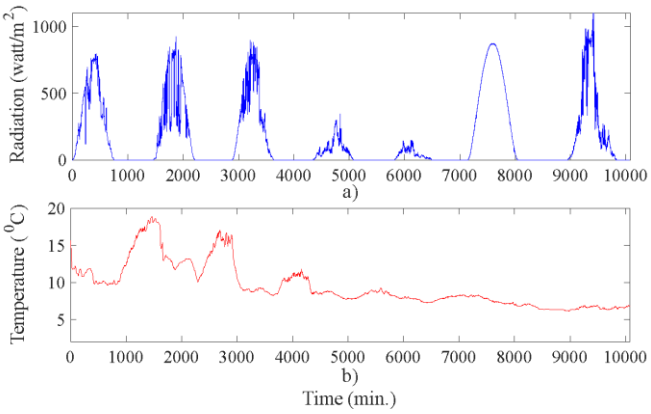

Figure 5. Measured weather data for one week
a) Radiation b) Temperature

The related real-life data is gained through a weather station located in Istanbul, the European side, in which various weather conditions are chosen for each day. So, it is aimed to examine different real-life conditions of PV panel performances that can come upon a sunny day, partly cloudy day, and cloudy day. Depending on the compare/ contrast study of the data, the power value differences of the PVs are given in Figure 6.

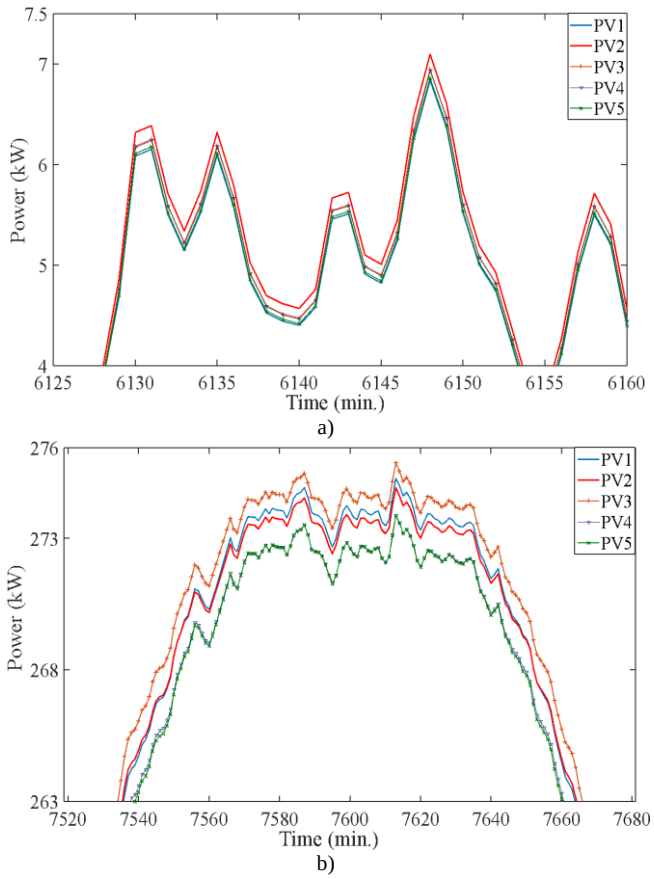

Figure 6. Generated powers of the different PVs
a) Cloudy day
b) Sunny day

In Figure 6, the dynamic performances of five different PV panels are given for the sunny day and cloudy day conditions. In order to observe the dynamic variations better, the time interval is limited for power value differences in Figure 7. In addition, the total energy production of PV panels is a critical criterion for massive PV farm performances, which directly affects the investment feedback and system profits.

Depending on the performance examination, the total energy production of the PV systems with the same power values and different weather conditions are calculated for one week time interval. Based on the survey above, weekly and yearly calculated energy values are given in Table III.

TABLE III
ENERGY PRODUCTION OF DIFFERENT PV PANELS

Parameter	PV1	PV2	PV3	PV4	PV5
Generated energy (week)	56620 MWh	57168 MWh	57113 MWh	56600 MWh	56386 MWh
Generated energy (annual)	2944 GWh	2972 GWh	2970 GWh	2943 GWh	2932 GWh

When the data in Table III is analyzed, the PV2 system provides; 28496 MWh higher than PV1, 2869 MWh higher than PV3, 29536 MWh higher than PV4, and 40664 MWh higher than PV5 in terms of the energy production performances. That is because PV2 has better performance than others on cloudy days. Based on that, PV2 has generated more energy than others. Hence, the PV panel's dynamic performance is critical, which should be analyzed before choosing a PV panel product for investment.

4. CONCLUSION

PV panels are making rapid progress in terms of being an important energy source of the future. In this study, the performances of panels produced by different brands with the same power output in real weather conditions were compared over the simulation model. In the relevant model, the technical parameters of each PV panel are taken into account. The performance study was examined with the measured dynamic radiation and temperature data in this comparison. The calculation error because of using only the label power values is analyzed. It turns out that a general calculation based on the label value and the sunshine duration causes more errors than the calculation with dynamic data. In addition, it is seen that considering only the panel price is not sufficient for the total benefit to be obtained from the panels. Each of the PV panels has different energy generation under the same conditions. PV2 has the best energy generation performance. Annually the best-performance PV panels generate 40 GWh more than the lowest-performance PV panels.

The improvements to be made in the unit efficiency of PV panels will contribute to the generation of more electrical energy in smaller areas. Thus, it is certain that PV panels will consolidate their place in human life as an indispensable energy source in the future. In this way, PV panels, one of the most environmentally friendly and renewable energy sources, will also provide solutions for global warming and other environmental problems.

REFERENCES

[1] O. O. Amusat, P. R. Shearing, and E. S. Fraga, "Optimal design of hybrid energy systems incorporating stochastic renewable resources fluctuations," J. Energy Storage, 2018, doi: 10.1016/j.est.2017.12.003.

[2] O. Elma and U. S. Selamogullari, "A comparative sizing analysis of a renewable energy supplied stand-alone house considering both demand

side and source side dynamics," Appl. Energy, 2012, doi: 10.1016/j.apenergy.2012.02.080.

[3] A. Kaabeche, M. Belhamel, and R. Ibtiouen, "Sizing optimization of grid-independent hybrid photovoltaic/wind power generation system," energy, 2011, doi: 10.1016/j.energy.2010.11.024.

[4] O. Erdinc, O. Elma, M. Uzunoglu, and U. S. Selamogullari, "Real-time performance analysis of an optimally sized hybrid renewable energy conversion unit," Energy Build., 2014, doi: 10.1016/j.enbuild.2014.01.052.

[5] Durusu, A., Erduman, A. & Yıldız, F. 'Comparative Study of Photovoltaic Array Optimum Tilt Angle and Orientation with Multi-Objective Consideration,' Mühendislik Bilimleri ve Tasarım Dergisi , 8 (4) , 1031-1041, 2020, DOI: 10.21923/jesd.745835.

[6] M. Shabani and J. Mahmoudimehr, "Techno-economic role of PV tracking technology in a hybrid PV-hydroelectric standalone power system," Appl. Energy, vol. 212, no. December 2017, pp. 84–108, 2018, doi: 10.1016/j.apenergy.2017.12.030.

[7] A. Durusu and A. Erduman , "Design of an Experimental Test Bench to Obtain I-V Curve and to Track Maximum Power Point of PV Modules under Different Conditions", Bitlis Eren Üniversitesi Fen Bilimleri Dergisi, vol. 9, no. 3, pp. 1242-1250, Sep. 2020, doi:10.17798/bitlisfen.618600.

[8] E. Elibol, Ö. T. Özmen, N. Tutkun, and O. Köysal, "Outdoor performance analysis of different PV panel types," Renewable and Sustainable Energy Reviews. 2017, doi: 10.1016/j.rser.2016.09.051.

[9] A. Guenounou, A. Malek, and M. Aillerie, "Comparative performance of PV panels of different technologies over one year of exposure: Application to a coastal Mediterranean region of Algeria," Energy Convers. Manag., 2016, doi: 10.1016/j.enconman.2016.02.044.

[10] U. F. and E. O. Kayhan V. A, "Photovoltaic system design, feasibility and financial outcomes for different regions in Turkey," in 4th International Conference on Electric Power and Energy Conversion Systems (EPECS), 2015, no. I, doi: 10.1109/MCOM.2016.7786133.

[11] U. S. Elma O, Selamogullari, "Performance Evaluation Of Monocrystalline And Polycrystalline PV Modules-A Case Study For Istanbul," in 10th International Conference on Sustainable Energy Technologies, 2011, pp. 1–5.

[12] A. Bennouna et al., "Energy performance of 3 silicon-based PV module technologies in 20 sites of Morocco," Energy Sustain. Dev., 2019, doi: 10.1016/j.esd.2019.09.002.

[13] D. Atsu, I. Seres, M. Aghaei, and I. Farkas, "Analysis of long-term performance and reliability of PV modules under tropical climatic conditions in sub-Saharan," Renew. Energy, 2020, doi: 10.1016/j.renene.2020.08.021.

[14] A. J. Carr and T. L. Pryor, "A comparison of the performance of different PV module types in temperate climates," Sol. Energy, 2004, doi: 10.1016/j.solener.2003.07.026.

[15] MATLAB, "Implement PV array modules." [Online]. Available: https://www.mathworks.com/help/physmod/sps/powersys/ref/pvarray.html. [Accessed: 20-Sep-2021].

[16] Canadian Solar, "Superpower 290|295|300|305ms," 2018.

[17] Yingli Solar, "Panda 60 solar panel." [Online]. Available: https://d9no22y7yqre8.cloudfront.net/assets/uploads/products/downloads/PANDA 60 TUR-NEW- 2016.pdf. [Accessed: 30-Jul-2020].

[18] T. Solar, "60-Cell Module." [Online]. Available: http://static.trinasolar.com/sites/default/files/PS-M-0421 Datasheet_Allmax M Plus_US_B Feb2018_TS4.pdf. [Accessed: 29-Jul-2020].

[19] P. Solar, "MWT Module 275-300W." [Online]. Available: http://www.phonosolar.com/files/20171130/EN-MWT.pdf. [Accessed: 30-Jul-2020].

[20] Suntech, "HyPro PV model," 2017. [Online]. Available: http://www.mpptsolar.com/en/pdf/best-solar-panel-manufacturers/suntech-hypro-stp300s.pdf. [Accessed: 28-Jul-2020].

BIOGRAPHY

Onur ELMA obtained his BSc degree in electrical engineering from Yildiz Technical University (YTU) Istanbul, Turkiye, in 2009. Onur Elma received his M.S. and Ph.D. degrees in Electrical engineering from YTU, in 2011 and 2016 respectively. He worked as a project engineer in the industry between 2009 and 2011. He has been employed as a research assistant in the Electrical Engineering Department at YTU from 2011 to 2017. He has been in the Smart Energy Research Center (SMERC) at the University of California, Los Angeles (UCLA) as a visiting researcher from 2014 to 2015. Also, he has worked as a post-doc researcher at the Ontario Tech University (ONTechU) from 2017 to 2020. He has worked as an Assistant Professor in the Department of Electrical Engineering at YTU between January and September 2021. He is currently working as an Assistant Professor in the Department of Electrical and Electronics Engineering at Canakkale 18 Mart University (COMU). He participates in many national and international projects also has more than 40 papers. He has national and international patents. His research interests include smart grid, electric vehicles, home energy management systems, energy storage, and renewable energy systems.

European Journal of Technique

journal homepage: https://dergipark.org.tr/en/pub/ejt

Vol.12, No.1, 2022

Investigation of the Gelation Potential of Low Molecular Weight Organogelator

Deniz BARIŞ CEBE[1*], **Murat SUNKUR**[2]

[1*] Batman University, Faculty of Science and Letters, Department of Chemistry, Batman, Turkey. (e-mail: deniz.baris@batman.edu.tr).

[2] Batman University, Faculty of Science and Letters, Department of Chemistry, Batman, Turkey. (e-mail: murat.sunkur@batman.edu.tr).

ARTICLE INFO

Received: Feb., 10. 2022
Revised: April., 20. 2022
Accepted: May., 09. 2022

Keywords:
Gelation
Tetraamide compounds
Low Molecular Weight Organogelator

Corresponding author: *D. Barış Cebe*

ISSN: *2536-5010* | e-ISSN: *2536-5134*

DOI: https://doi.org/10.36222/ejt.1106639

ABSTRACT

In this study, low molecular weight amide compound was employed as the organogelator and its gelation potential was investigated with various solvents. The morphological properties of the obtained gels were investigated. The network structure of the obtained gel was determined by scanning electron microscopy (SEM). Fatty acid esters used in the cosmetic and pharmaceutical industries and also solvents commonly used in the laboratory were employed for gelation. According to this process, the organogelator formed a gel with all the fatty acid esters at very low concentrations and with only anisole, xylene, liquid paraffin and n-dodecane of common organic solvents. Among the gels obtained, those with the lowest concentration were made with isopropyl laurate and isopropyl myristate. It was determined that the melting temperature of the gels prepared with fatty acid esters was higher than those prepared in common solvents. The organogel with the highest melting temperature is the gels made with isopropyl myristate and isopropyl palmitate. In addition, gelation enthalpy values ΔH_g were found. According to the results obtained, it was determined that the highest ΔH_g value belonged to the gel prepared with isopropyl laurate.

1. INTRODUCTION

Gels can be defined as a semi-solid formulation with a solvent phase. They are located in a three-dimensional network structure, either nonpolar or polar [1]. Gels can be classified according to the bonds that hold the existing molecules together in the gelator network. In chemical gels, molecules are held together by covalent bonds while physical gels are joined by weaker physical forces of attraction, such as van der Waals interactions and hydrogen bonds. In many studies, it has been reported that non-polymeric, low molecular weight compounds called organogelators can form networks in hydrophobic solvents as a result of non-covalent interactions [2].

Although a wide variety of gelators have been identified in the gelation process, it is difficult to predict the molecular structure of a potential gelator [3]. Besides that, it may not be possible to predict in advance with which solvent it will form a gel. Currently, the discovery of gelators is still going on by chance. This is followed by screening research, testing different solvents which potentially compatible with the gelator. Estimation of the gelation potential of a molecule may seem possible by investigating its tendency for chemical or physical intermolecular interactions. However, it has not been possible to make generalizations so far. Many factors such as steric effects, stiffness and polarity can inhibit the aggregation tendency of the molecule [4].

In recent years, numerous examples of low molecular weight gels that are very useful as a new drug delivery tool have been shown in the literature [5, 6]. However, until now low molecular weight gels have been used to form gel from organic solvents and to examine the relationship between gelator structure and gelation abilities [7-9]. Organogels can be used in pharmacy, drug and vaccine applications. Low molecular weight gels provide an environment that increases the stability of encapsulated drug molecules, and helps to prevent enzymatic degradation during drug administration. Another benefit of use is that the spontaneous formation of gels takes place during formulation of the drug-loaded material [10]. Organogelator has not been studied much as drug carrier. However, organogels have some advantages as a drug delivery system [11]. Organogels are not affected by moisture and accelerate the penetration to the skin. Due to their organic character, they are also resistant to microbial pollution. The gelation and entrapment procedure as a drug carrier is quite simple and easy to use. Its biocompatibility, biodegradability and non-immunogenic properties eliminate harmful drug effects in long-term applications [12, 13].

2. MATERIALS AND METHODS

2.1. Reagents and materials

The organogelator was synthesized according to the procedure described in the related reference [14] (Figure 1). Fatty acid esters and common organic solvents were chosen as solvents. Ethyl laurate (LEE), ethyl palmitiate (PEE), ethyl myristate (MEE), isopropyl laurate (LIE), isopropyl palmitate (PIE) and isopropyl myristate (MIE) were selected as fatty acids and supplied from Merck Chemical Company. Anisole, xylene, liquid paraffin, n-dodecane, diethylene glycol, 1-decanol, toluene, chloroform was chosen as common organic solvents, and supplied from Merck Chemical Company or Sigma Aldrich Chemical Companies.

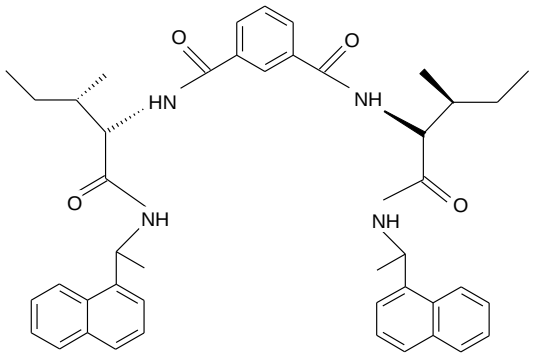

Figure 1. Structure of the organogelator

2.2. Determination of minimum gel concentration (MGC)

1 mg of organogelator was placed in a tube with a 1 cm inner diameter and 1 mL solvent was added. This solution was heated to 20°C below the boiling point of the gelation liquid until the organogelator was completely dissolved. It was then cooled in a thermostated water bath at 25 °C. After about 15 minutes, it was checked whether the solution formed a gel or not. If no gel was formed, 1 mg additional gelator was added and this process was continued until gelation was occurred. The concentration at which gelation occurred was determined as the minimum gelation concentration (MGC mg/mL) [15].

2.3. Determination of melting point of gels (T_g)

A steel ball weighting 0.25 g was carefully placed on the surface of the gels prepared at the minimum gelation concentration. In a temperature-controlled oil bath, the temperature was increased at 1°C intervals until the steel ball dropped to the bottom of the tube. The temperature at which the ball started to fall was determined as the melting point (T_g) of the gelator. This method was repeated with gels prepared at increasing concentrations [16].

2.4. Determination of gelation enthalpy (ΔH_g)

Gelation enthalpy values were calculated via the van't Hoff equation (Equation 1) [17, 18]. The gelation enthalpy values of the organogelator were determined from the slope of the lines found by plotting the $1/T_g$ value against $\ln\%C_g$ (gelator concentration in w%). Here, C_g is the gelator concentration in mol L^{-1}, T_g is the phase transition temperature, and R is the Rydberg gas constant (R = 8.314 J mol^{-1} K^{-1}).

$$d\ln[Cg]/d(1/Tg) = -\Delta Hg/R \quad (1)$$

2.5. Characterization of gel structure by SEM

Gels are formed as a result of the three-dimensional network structure formed by organogelators with solvents [19]. These structures can be characterised by a SEM. Due to the high boiling points of the solvents used in current study, the reprecipitation method was applied while preparing the xerogel [20]. The gels were quickly precipitated in hexane because of insolubility in room temperature. In this way, solvents with high boiling points were transferred to the hexane phase. After the solvents were removed from the gel, the excess hexane was removed by freeze drying process. Thus, the gels were made suitable for SEM analysis.

3. RESULTS AND DISCUSSION

3.1. Determination of the minimum gel concentration

The minimum gelation concentration (MGC) values of the organogelator were determined by performing gelation experiments in ethyl and isopropyl laurate, ethyl and isopropyl myristate, ethyl and isopropyl palmitate, anisole, xylene, liquid paraffin, n-dodecane, diethylene glycol, 1-decanol, toluene and chloroform. Accordingly, the organogelator has a better gel-forming capacity with fatty acid esters than common solvents. It formed a gel with all fatty acid esters at low concentration values. The gels with the lowest minimum gelation concentration are those formed by LIE and MIE. It formed gel with anisole, xylene, liquid paraffin, n-dodecane, which are common solvents (Table I, Figure 2). It did not form gels with diethylene glycol, 1-decanol, toluene and chloroform.

TABLE I
MGC VALUES OF THE ORGANOGELATOR (MG/ML)

Solvents	MGC
Ethyl Laurate	2
Isopropyl Laurate	1
Ethyl Myristate	2
Isopropyl Myristate	1
Ethyl Palmitate	2
Isopropyl Palmitate	2
Anisole	3
Xylene	2
Liquid Paraffin	3
n-dodecane	2
Diethylene glycol	no gelation
1-decanol	no gelation
Toluene	no gelation
Chloroform	no gelation

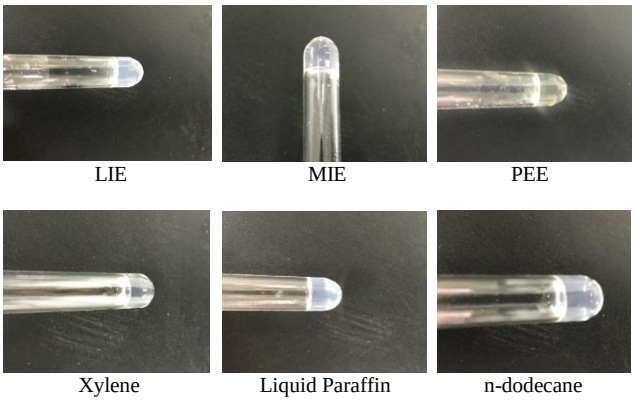

Figure 2. Photographs of gels formed by organogelator with various solvents in MGC

3.2. Determination of melting point of gels (T_g)

The graphs of the melting point (T_g) change values of the gelator against the weight % (C_g) in the gel of the obtained gels are shown in Figures 3 and 4. The T_g values of the gels obtained with fatty acid esters were higher than the gels obtained with common solvents. Accordingly, the organogels with the highest T_g values are the gels made with isopropyl myristate and isopropyl palmitate. The organogel with the lowest T_g value is the gel obtained with n-dodecane. Additionally it was determined that T_g values increased with the concentration of the gel.

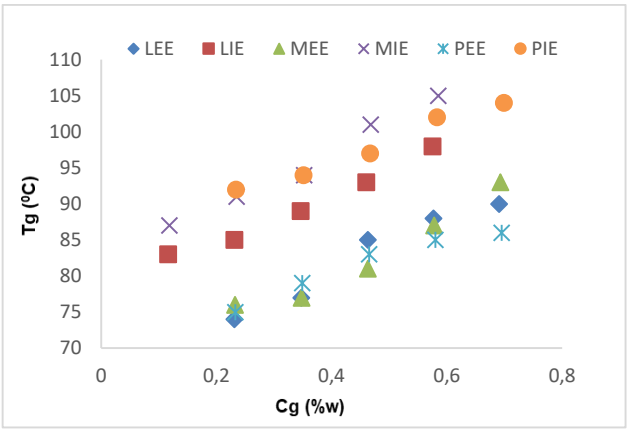

Figure 3. Plot of *Tg* versus the concentration of the organogelator C_g (% w) in fatty acid esters

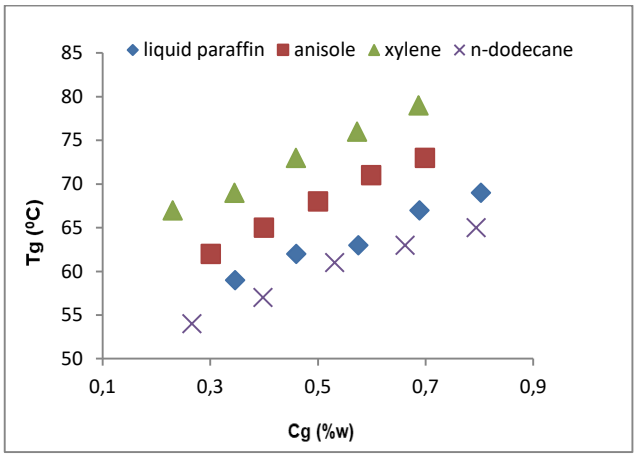

Figure 4. Plot of *Tg* versus the concentration of the organogelator C_g (% w) in common solvents

3.3. Calculation of enthalpy of gelation (ΔH_g)

The graphs of the $1/T_g$ change values of the obtained gels against In C_g are given in Figures 5 and 6. The gelation enthalpy value ΔH_g derived from the slopes of the drawn lines via van't Hoff equation is given in Table II. The high ΔH_g (gel-sol transition enthalpy) indicates that it gives a stable network structure. According to the values shown in Table II, it could be seen that the highest ΔH_g value in fatty acid esters is LIE with 106.91 kj mol^{-1}, and the lowest is MEE with 59.25 kj mol^{-1}. Furthermore it could be seen that the highest ΔH_g value is n-dodecane with 88.61 kj mol^{-1} and the lowest is anisole with 71.92 kj mol^{-1} among common solvents.

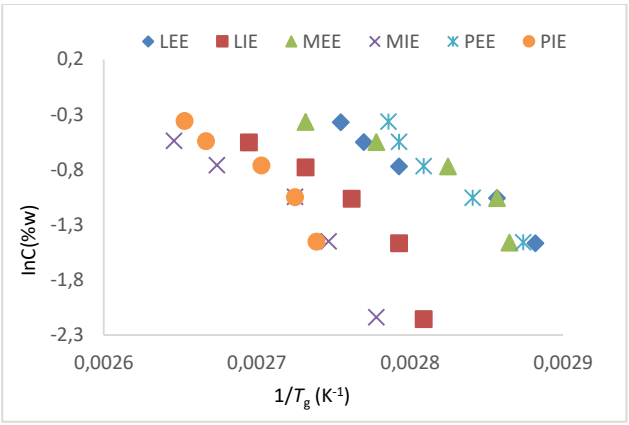

Figure 5. van't Hoff plots of organogelator in fatty acid esters

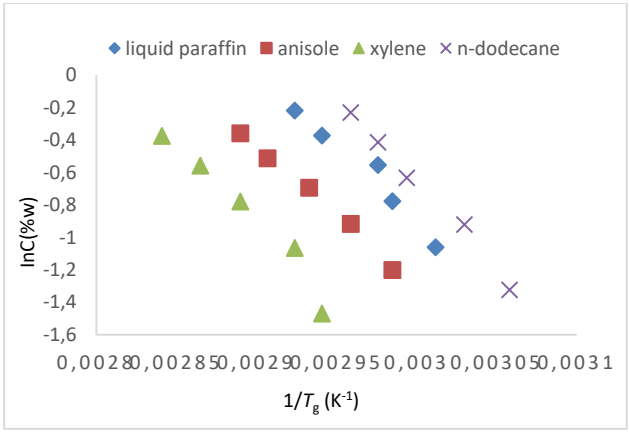

Figure 6. van't Hoff plots of organogelator in common solvents

TABLE II
SOL-GEL TRANSITION ENTHALPY ΔH_g (KJ MOL^{-1}) VALUES FOUND USING VAN'T HOFF PLOTS OF THE ORGANOGELATOR

Solvents	ΔH_G (KJ MOL^{-1})
LEE	63.46
LIE	106.91
MEE	59.25
MIE	93.18
PEE	97.33
PIE	94.01
Anisole	71.92
Xylene	85.44
Liquid Paraffin	76.88
n-dodecane	88.61

3.4. Characterization of gel structure by SEM

Xerogel was created to display the network structures formed by the gels. The solvent was removed by hexane extraction from the gel structure prepared in 1 mL LIE of the organogelator. While doing this, hexane was added and the gels were stirred vigorously, then white precipitate was filtered and washed with hexane. It has been waited for 24 hours under vacuum via freze-dry technique, and xerogel was obtained. The image of xerogel structure is shown in Figure 7. The network structure required for the formation of gels is visible in the photograph.

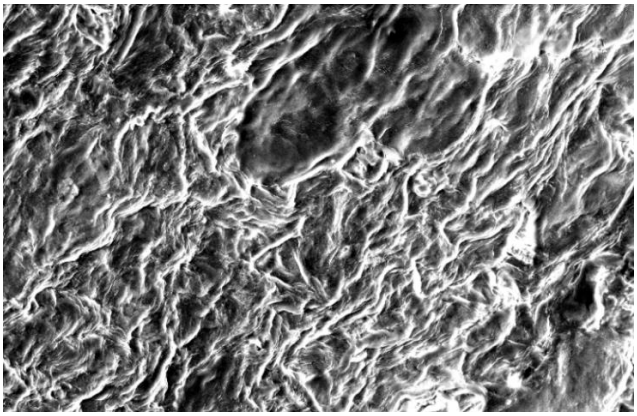

Figure 7. SEM image of gel prepared in LIE of organogelator

4. CONCLUSION AND DISCUSSION

The low molecular weight organogelator that we employed in gelation experiments formed gel with all fatty acid esters. However it formed gel with some of the common solvents. When the investigated organogelator is compared with similar structures in the literature, it could be seen that the gelation potential is good for fatty acid esters. The minimum gelation concentration values of the gels were also found to be quite low. This shows that even a very low amount of organogelator can form the gels while the solvents are fatty acids. In addition, it was determined that the melting temperatures of the gels increased as the concentrations of the prepared gels increased. When we look at the ΔH_g values found using the van't Hoff graphs of the organogelator, it could be seen that the highest result belongs to the LIE fatty acid ester. The solvents employed in this study are liquids used in the pharmaceutical industry such as fatty acid esters and liquid paraffin. Moreover, the organogelator structure contains biocompatible material such as *L*-isoleucine amino acid. Prepared organogels with low MGC values can be used as potential drug carriers.

REFERENCES

[1] Vintiloiu, A., Leroux, J. C., Organogels and Their Use in Drug Delivery–A review, *J. Control. Release*, *125* (2008), pp. 179-192.

[2] Terech, P., Weiss, R. G., Low Molecular Mass Gelators of Organic Liquids and the Properties of Their Gels, *Chem. Rev.*, *97* (1997), pp. 3133-3159.

[3] Van Esch, J., Feringa, B. L., New Functional Materials Based on Self-Assembling Organogels: from Serendipity Towards Design, *Angew. Chem. Int. Ed.*, *13* (2000), pp. 2263-2265.

[4] Murdan, S., Organogels in Drug Delivery, *Expert Opin. Drug Deliv.*, *2* (2005), pp. 489-505.

[5] Heeres, A., Pol, C. van der, Stuart, M., Friggeri, A., Feringa, B. L., Esch, J. van, Orthogonal Self-Assembly of Low Molecular Weight Hydrogelators and Surfactants, *J. Am. Chem. Soc.*, *125* (2003), pp. 14252-14253.

[6] Kobayashi, H., Friggeri, A., Koumoto, K., Amaike, M., Shinkai, S., Reinhoudt, D. N., Molecular Design of ‘‘Super’’ Hydrogelators: Understanding the Gelation Process of Azobenzene-Based Sugar Derivatives in Water, *Org. Lett.*, *4* (2002), pp. 1423-1426.

[7] Abdallah, D. J., Weiss, R. G., Organogels and Low Molecular Mass Organic Gelators, *Adv. Mater.*, *12* (2000), pp. 1237-1247.

[8] Gronwald, O., Shinkai, S., Sugar-Integrated Gelators of Organic Solvents, *Chem. Eur. J.*, *7* (2001), pp. 4328-4334.

[9] Baris Cebe D., Ekmen M., Investigation of the Gelation Properties of *L*-Isoleucine Derivative Tetraamide Compounds, *Fresenius Environ. Bull.*, *31* (2022), 03A, pp. 3819-3827.

[10] Branco, M. C., Pochan, D. J., Wagner, N. J., Schneider, J. P., Macromolecular Diffusion and Release from Self-Assembled β-hairpin Peptide Hydrogels, *Biomaterials*, *30* (2009), pp. 1339-1347.

[11] Murdan, S., Bergh, V. D., Gregoriadis, G., Florence, A. T., Water-in-Sorbitan Monostearate Organogels (Water-in-Oil Gels), *J. Pharm. Sci.*, *88* (1999), pp. 615-619.

[12] Zhou, S. L., Matsumoto, S., Tian, H. D., Yamane, H., Ojida, A., Kiyonaka, S., Hamachi, I., pH-Responsive Shrinkage/Swelling of A Supramolecular Hydrogel Composed of Two Small Amphiphilic, *Chem. Eur. J.*, *11* (2005), pp. 1130-1136.

[13] Zhang, Y., Gu, H., Yang, Z., Xu, B., Supramolecular Hydrogels Respond to Ligand−Receptor Interaction, *J. Am. Chem. Soc.*, *125* (2003), 45, pp. 13680-13681.

[14] Sunkur, M., Aydın, S., Aral, T., Dağ, B., Erenler, R., Preparation of New Mono- and Bis-Amide Derivatives of *L*-isoleucine via Amidation of Carboxyl and Amino Groups, *Org. Commun.*, *14* (2021), 3, pp. 294-299.

[15] Hanabusa, K., Yamada, M., Kimura, M., Shirai, H., Prominent Gelation and Chiral Aggregation of Alkylamides Derived from trans-1,2-diaminocyclohexane, *Angew. Chem. Int. Ed.*, *35* (1996), pp. 1949-1951.

[16] Xudong, Y., Li, Y., Yin, Y., Yu, D., A Simple and Colorimetric Fluoride Receptor and its Fluoride-Responsive Organogel, *Mater. Sci. Eng. C*, *32* (2012), pp. 1695-1698.

[17] Seo, S. H., Chang, J. Y., Organogels from ^{1}H-imidazole Amphiphiles: Entrapment of a Hydrophilic Drug into Strands of the Self-Assembled Amphiphiles, *Chem. Mater.*, *17* (2005), pp. 3249-325.

[18] Suzuki, M., Yumoto, M., Shirai, H., Hanabusa, K., Supramolecular Gels Formed by Amphiphilic Low-Molecular-Weight Gelators of N-alpha,N-epsilon-diacyl-L-lysine Derivatives, *Chem. Eur. J.*, *14* (2008), pp. 2133-2144.

[19] George, M., Weiss, R. G., Molecular Organogels. Soft Matter Comprised of Low-Molecular-Mass Organic Gelators and Organic Liquids, *Acc. Chem. Res.*, *39* (2006), pp. 489-497.

[20] Suzuki, M., Saito, H., Hanabusa, K., Two-Component Organogelators Based on Two L-Amino Acids: Effect of Combination of L-Amino Acids on Organogelation Behavior, *Langmuir*, *25* (2009), pp. 8579-8585.

BIOGRAPHIES

Deniz BARIŞ CEBE received the B.S., M.S., and Ph.D. degrees in Chemistry Department from Dicle University. She is currently an Assistant Professor of Chemistry Department with Batman University. Her research interests include molecular recognition, gelation, low molecular weight organogel.

Murat SUNKUR received the B.S. degree in chemistry teaching from Dicle University, Diyarbakır, in 1999. He received the M. S. and Ph. D. degrees in organic chemistry from Dicle University, Diyarbakır, in 2001 and 2008, respectively. He worked as a teacher from 1999 to 2004. Since 2008, he has been an Assistant Professor with the Chemistry Department, Batman University. His research interests include organic synthesis, enantiomeric recognition and HPLC.

European Journal of Technique

journal homepage: https://dergipark.org.tr/en/pub/ejt

Vol.12, No.1, 2022

Effects of Different Splicing Methods on Conveyor Belt Strength

Savaş Kirenli[1], **Recep Demirsöz**[2*]

[1]Karabük Demir Çelik Sanayi ve Ticaret A.Ş, 78170, Merkez, Karabük, Türkiye. (e-mail: skirenli@kardemir.com).

[2*]Karabuk University, Mechanical Engineering Department, Karabük, Türkiye (e-mail: recepdemirsoz@karabuk.edu.tr).

ARTICLE INFO

Received: Mar., 12. 2022
Revised: Apr., 02. 2021
Accepted: May, 05. 2021

Keywords:
Conveyor
Belt
Vulcanization
Mechanical splicing

Corresponding author: *Recep Demirsöz*

ISSN: *2536-5010* | e-ISSN: *2536-5134*

DOI: https://doi.org/10.36222/ejt.1086915

ABSTRACT

Belt conveyors are at the forefront of the systems that minimize the need for people in the transportation of materials. With the continuous development of today's technology, it develops in the improvements in belt conveyor systems. Owing to the innovations and improvements in the conveyor belts, it becomes possible to minimize the maintenance, repair, and undesired stoppages of the facilities. In this study, specimens were extracted from a conveyor belt with a width of 800 mm, with a tensile strength of 45 N/mm^2, 4 layers of polyester-polyamide blend cord fabric, 6 mm rubber bottom coating thickness, and 3 mm rubber top coating thickness were used. The specimens were taken in three different ways (from the unspliced belt, from the mechanically spliced belt, and the vulcanized belt). The specimens were subjected to the tensile test. The strength values of the belt specimens, from high to low, are in the form of unan spliced belts vulcanized belts, and mechanically spliced belts. It is found that there is a 28.2% decrease in tensile strength compared to the unspliced belt in the vulcanized belt, and a 49.8% decrease in the tensile strength compared to the unspliced belt in the mechanical spliced belt.

1. INTRODUCTION

With the development of technology, the factories and facilities being established have become more modern. The development of technology has led to an increase in production capacities in parallel with this situation. The use of raw materials and materials has increased in almost all production facilities, especially in iron and steel plants, and the need for them to be transported more easily, quickly, and reliably has arisen. Because of this need, transportation and transportation technology have also improved.

Today, one of the parameters affecting the operating costs in industrial facilities is material transportation. Belt conveyors are the first transport equipment that comes to mind in facilities such as iron and steel plants where raw material transport is of great importance. Belt conveyors are transmission mechanisms that are used to transport materials of various sizes and sizes to desired distances, and they are one of the most preferred transportation techniques for the continuous transportation of materials. High carrying capacities and the ability to transport to desired distances have made it inevitable to prefer belt conveyors. Moreover, features such as simple belt conveyor designs, light construction, and safe operation were also important factors in this choice. With belt conveyors, wet or dry materials are transported in general, as well as coarse-grained materials in whole or in pieces. In short, belt conveyor systems are the cheapest, most effective, and most efficient systems for transporting bulk materials today [1, 2]. These high-efficiency belt conveyors have become important equipment applied in industries such as power generation, iron, and steel production, manufacturing, metallurgy, mining [3].

Belt conveyors are frequently used especially in integrated iron and steel production facilities. In the industry, belt conveyors are mostly preferred for the transportation of bulk goods, but they are frequently used especially in integrated iron and steel production facilities. Along with the studies on conveyor belts in the world, innovative solutions are produced regarding the resistance of belts against burning, pressure, and tensile. In addition to all these, it is important to determine the splicing methods, which will ensure the belt serves for the maximum time. Repair of conveyor belts with hot vulcanization and mechanical splicing methods continues to be researched and developed today as in the past. Splicing points on belt conveyors are considered the weakest part of the conveyor belt and approximately 93.75% of belt failures occur at these points [1-5].

Hardygora et al. tried to explain the decrease in strength at the splice of conveyor belts with various test methods. They stated that systematic testing of conveyor belts and their splices is needed to achieve the high standards of safety and operational reliability required by belt conveyors. The strength of the conveyor belt splices determines the strength of the entire belt loop on a conveyor. They stated that the strength loss in a properly made splice can vary between 30% and 45% depending on the number of layers. The strongest splices are made between belts with the same strength characteristics and without damaging the ply fabric. Factors causing strength reduction at the belt splice are shown as construction defects in the splices, surface roughness between the layers, cutting of the layers, and improper vulcanization method. As the layer

surface roughness damages the structure of the layers, it causes a decrease in strength. It has been found that this defect usually occurs during the cleaning phase between the belt layers. It has been stated that incorrectly applied vulcanization failure is usually caused by insufficient or inappropriate vulcanization pressure and temperature [6].

Chuen-Shii et al. investigated the optimum conditions for vulcanizing a conveyor belt with better adhesion strength and less wear. They tried to achieve optimum conditions for the on-site curing of the conveyor belt and specified these conditions as a curing time of 25 minutes, a curing pressure of9 kg/cm^2, a stripping temperature of 30 °C, and an air cooling method. They then sought to determine the optimum conditions for on-site curing of a conveyor belt with less wear and specified these as a curing time of 15 minutes, a curing pressure of 9 kg/cm^2, a stripping temperature of 60 °C, and a water-cooling method. Accordingly, it takes a longer time to vulcanize the belt with better adhesion strength than vulcanizing the belt with less wear with a constant curing pressure. The percent contribution of each controllable factor within the current research range was also determined by the Taguchi method's analysis of variance ANOVA. Interestingly, among the four controllable factors, the curing time was found to be the most influential factor on both the bond strength of the bonded area (38.61%) and the wear of the patched and spliced areas (61.22%) [7].

Şahbaz discussed the cold vulcanized splicing method in his study. In the first stage of the study, the effects of factors such as time, temperature, and pressure in the application of cold vulcanized adhesives used in the market were determined and experimental working parameters were established. In the second stage of the study, experimental studies on the production of a new cold curing adhesive were carried out on a laboratory scale. During production, the effects of solvents, fillers, resins, metal oxides, and accelerators were investigated. As a result of the thesis study, A new product has been obtained that exhibits better adhesion than industrial products used in the market and shortens the application time [8].

Çankır applied the method of combining steel cord conveyor belts with the vulcanization method and examined the results. In this study, he investigated the methods and techniques that should be applied to add at least the breaking strength values of the belt and compiled the results obtained by applying them [9].

In his study, Soyubel explained the concept of elastomer and rubber by talking about the history of rubber, classified, and introduced important rubbers. He gave information about the components that make up the elastomer mixture and their effect on the properties of the elastomer. He gave information about the vulcanization temperature and time, which are the vulcanizing parameters of elastomers, and it was shown that curing at 140 ºC in 20 minutes is ideal [10].

Öztürk gave information about rubber and vulcanization in his study. He compared EPDM (Ethylene Propylene Diene Monomer) and NR (Natural Rubber) natural rubbers. In experiments, it was found that different accelerators not only shorten the curing time but also affect many physical properties. It has been concluded that changing the amount of accelerator affects the physical properties as well as the speed [11].

Vahapoğlu, on the other hand, mentioned in his study that the vulcanization temperature of rubber and rubber is generally applied between 140 °C and 180 °C, and quite good results are obtained in this temperature range [12].

2. EXPERIMENTAL STUDIES

2.1. Preparation of Specimens

In the hot vulcanized splicing method, TS EN ISO 283 Textile conveyor belts total belt tensile test standard is used. In the mechanical splicing method, the TS EN ISO 1120 standard for determining the strength of the mechanical connections of the conveyor belts is used. The belt was first cut in the form of a bow tie using the type B template selected according to the TS EN ISO 14890 standard, as it came from the manufacturer, without applying any splicing method. The conveyor belt combined with vulcanization was also cut to the same standard. Belt specimens are cut according to ISO 37 using the bow tie apparatus, which is shown in Figure 1 [13].

Figure 1. Image of bow tie specimen apparatus according to ISO 37 Standard [13]

The test specimens were kept at room temperature for 24 hours before being tested and were tested after this waiting period [14, 15].

2.1.1. Preparation of Hot Vulcanization Specimens

Before starting the belt splicing p, all the impurities and oils on the belt are cleaned. For the belt splicing process to be healthy and not be affected by adverse weather conditions (rain, wind, dust, etc.), the belt splicing process was carried out in a closed workshop environment. As a splicing technique, splicing by cutting perpendicular to the axis of the belt is not preferred, since there is a risk of opening the splice as a result of bending during the passage of the belt through the drums [16]. The two ends of the splice are connected at an angle to each other in the form of a right or left cross by the cross-cutting technique. In the studies, as shown in Figure 2, cross-cutting was applied by giving an angle of 0.3 x Belt width. This value corresponds to approximately 16.7º.

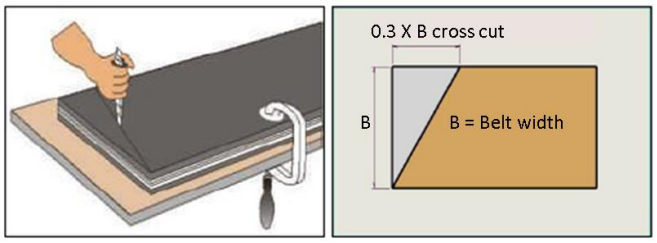

Figure 2. Belt angle cutting technique

Since the belt used in specimen preparation is a 600mm wide 4-layer belt, the number of layers was applied as 3 (Figure 3.a). In the site application, the belt splice determination is made according to the rotation (working) direction of the belt (Figure 3.b), the most important point to be considered is the prevention of damage that may occur due to the scraper. Since this study is experimental, the determination of the splice site is not important.

While L_v is the recommended total length of the splice, the required length for the curing length is shown in Figure 3.b.

$$L = L_v + L_a \quad (1)$$

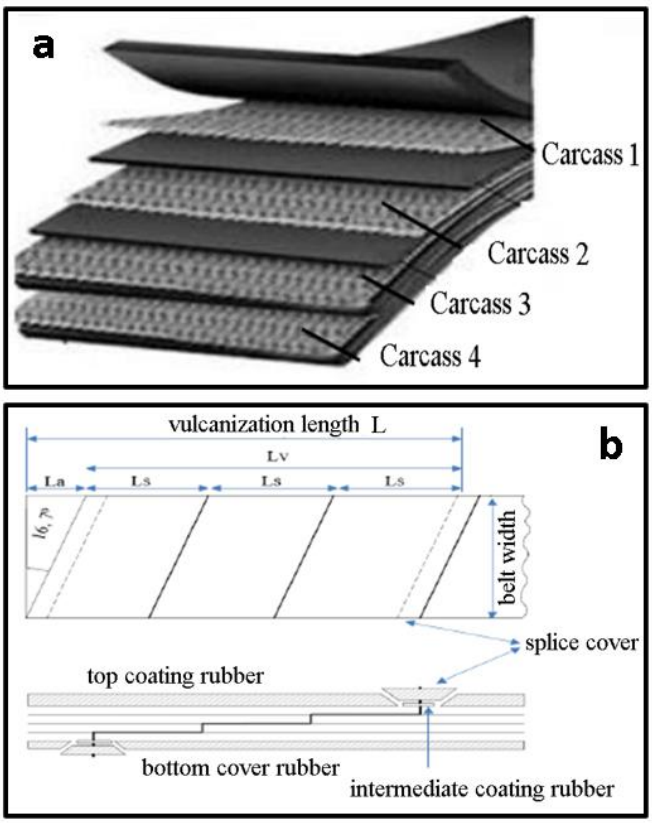

Figure 3. Schematic representation of four-layer carcass belt (a) and belt splice (b) [8, 17]

According to the fabric strength and the number of layers, the layer length value (Ls) and the additional length value (L_v) were chosen as 200mm and 600mm, respectively [8]. The distance La=0.3xB from the intersection of the reference line (LR) to the edge of the belt along the belt edge line was measured and marked. A line is drawn from the marked length La between the point where the reference point cuts the opposite edge. This line is called the coating cut line (LCO). The straight edge was used to draw this line and the square shape was adjusted and marked with a colored marker. This process was done at the end of the other belt in the same way. After the marking process, cross cuts were made (Figure 4) After the cross-cutting of the belt ends were completed, the upper splice rubber cover was peeled off with the belt scraper knife. Care should be taken that the blade does not injure the textile tissue while cutting the rubber cover of the upper splice. The end of the splice is vertical, the head (splice cheek) is cut with a 45° inclination. The cutting process was done up to the first court fabric. After the upper splice rubber cover was cut, the upper coating rubber of the belt was stripped. After the layers were opened and stripped on the belt, cleaning was carried out with a cleaning solvent to remove unwanted elements such as oil and pollution and to make an efficient addition.

All surfaces to be spliced were scraped. The scraping process was applied, including the rubber edges on all four sides of the joints and the beveled cut edges of the rubber cover. Textile tissue should not be damaged during scraping. In addition, during the scraping process, the angle grinder should not be pressed excessively on the belt, and the process should be done intermittently so that the temperature of the region does not increase more than 80°C and damage the belt.

Figure 4. Images of belt splice preparation stages

The lower and upper belt ends must be matched by taking into account their steps and axis adjustment. It is adhered to by mounting 15 to 20 mm wide edge rubber along with the belt splice. In the process of overlapping the belt ends, the bonding process should be done by pressing, starting from any direction, so that there is no gap and air at the splice. By controlling the centerline of the belt, the belt ends are fixed. The important thing in this process is that the axial adjustment of the belts is done well. The top cover closure rubber was cut at the upper splice of the belt and the filling and bonding process was applied (Figure 5).

Figure 5. Images of the bonding process

Figure 6 shows the vulcanizing machine and equipment. The vulcanization system in general; traverses, hydraulic pistons, vulcanized press tables (heat plates), hydraulic hand pump, hydraulic hoses, energy panel, resistances, and thermometer components.

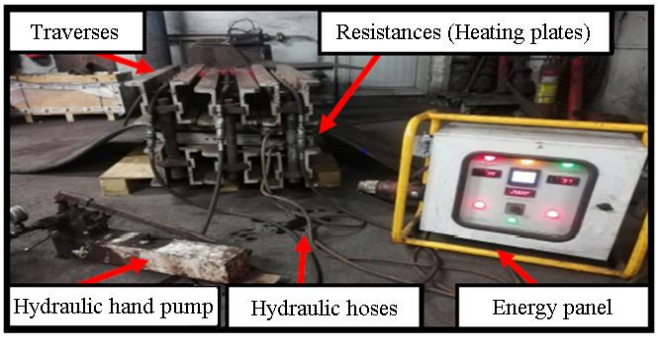

Figure 6. Vulcanization system equipment

When starting the loading process of the vulcanizing press machine, the important points are the heating time, temperature, and pressure. Generally, 50 bar pressure is applied at 0 ℃ when the system is idle. After this application, when the heater reaches 50 ℃ in the energy panel, it is increased to 100 bar pressure. When it reaches 100 ℃, 150 bar should be applied. In an average of 20-25 minutes, the temperature reaches 145 ℃, and cooking is continued by applying 150 bar pressure from 145 ℃ until the process ends. In this study, since the total belt thickness is 14 mm, it was left to bake for about 24 minutes after being seen from the energy panel at 145 ℃. Parallel to this, the pressure is adjusted as 150 bar on the hydraulic piston manometer screen. After the vulcanization process is finished, the system should be left to cool. The vulcanizing press machine is left to cool until the temperature drops to 60-80 ℃. After this process, the excess remaining on the splice surface and edges were trimmed and cleaned.

The test specimens were marked as 3 pieces in the longitudinal direction of the belt, and a minimum distance of 50 mm from the edges of the conveyor belt was cut from the inside (Figure 7).

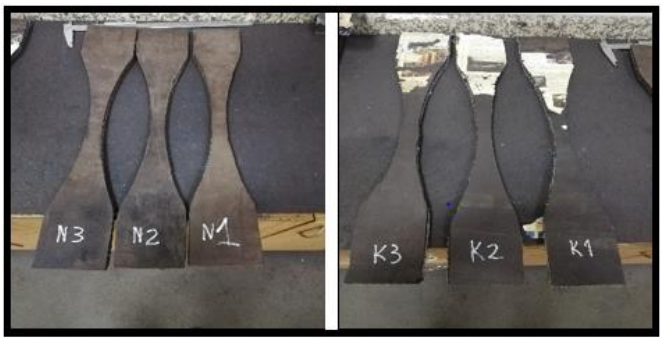

Figure 7. Bowtie-shaped specimens: Original unspliced (N coded) and vulcanized (K coded) belt specimens.

2.1.2. Preparation of Mechanical Splicing Specimens

The hole diameters of the fasteners used are 8 mm and the distance between the holes in the fasteners is 55 mm. The distance between the hole axes between the two fasteners is 40 mm, and it is applied by templating. 26 fasteners are used for the 1000 mm wide belt, 21 fasteners are used for the 800 mm wide belt, and 17 fasteners are used for the 650 mm wide belt according to the template. The number of fasteners to be used on the belt to be mechanically spliced is shown in Table 1 and recommended [19].

For the splicing to be made in the facility, firstly, the belt is fixed by tightening it with angle profiles from both ends and brought to the end with pullers. It is arranged by adjusting both ends with miter and gauge. In the mechanical splicing application, two different splicing methods are applied, which are performed in the form of angled (leveled) and straight splicing. One can be made as an angled cut and the other as a straight cut at 90º perpendicular to the movement direction of the belt. In this study, straight cut, which is mostly used in the facility, was preferred perpendicular to the movement direction of the belt (90º).

Table 1. Quantity of mechanical splicing fasteners [18]

Belt Width [mm]	Fasteners Qty.
300	8
400	10
500	13
650	17
800	21
1000	26
1200	31
1400	37
1600	42
1800	47
2000	53

To drill the fastener holes of the belt, the template supplied from the manufacturer was placed on the belt by using a gauge and a meter, and the hole centers were marked with a pencil (Figure 8). Likewise, the same procedure was applied to the opposite end. The 90º splice template facilitates the repair by allowing the holes to be drilled in the right places mutually. Since the diameter of the fasteners used is 8 mm, the holes were drilled with a 9, mm punch, and the application was made in the same way with the other belt end. After the drilling process on the belt was completed, the nuts and covers of the fasteners were removed and mounted on one side of the holes one by one. Rubber is placed between the fasteners to prevent dust spills in parallel. To ensure the alignment of the belt from the middle to the sides, the assembly of the upper fastener was started from the middle of the belt. After all the fasteners were mounted in the holes, the nuts were placed. Then tightening was done with the help of a nut tightening machine. The nut tightening process was carried out until the belt aligned with the upper surface of the upper coating rubber. After the tightening process was completed, the long bolt ends were broken with the help of a pipe and straightened. Finally, the protrusions on the bolt were removed with help of an angle grinder, to minimize the possible damage that the belt splice may cause while passing through the drums, scrapers, and belt carrier rollers, and the process was completed.

Figure 8. Images of the mechanical splicing application

Mechanically spliced conveyor belt specimens were cut in 3 pieces, parallel to the conveyor belt axis and at a distance of at least 50 mm from the belt edge, according to the TS EN ISO 1120 standard (Figure 9). The test specimens consist of a full-length longitudinal piece of a conveyor belt. The test specimen was taken with mechanical fasteners and the belt specimen was taken with a splicing width of at least 100 mm.

Figure 9. Image of belt specimens with mechanical splicing

2.2. Tensile Tests

A test piece cut from the full thickness of the conveyor belt is elongated under certain conditions using a tensile testing machine until rupture occurs. In the test, a test device that can apply a continuous and smooth tensile force is used. The testing speed of the device should be 100 mm/min [14, 20]. Experiments were carried out in the Mechanical Physics and Test Laboratory of Kardemir A.Ş, Quality Metallurgy and Laboratories Directorate, on a 200-ton SP1200 Zwick brand extensometer tensile testing device (Figure 10).

Figure 10. Image of the tensile tester

The extensometer tensile tester must have a measuring length of at least 100 mm and an accuracy of 0.1 mm or better, and be capable of measuring the elongation of the gauge length marked on the test pieces. It is also preferable to use a device that creates a graphical diagram throughout the test. Holders are required to prevent the test piece from slipping during the tensile test. It is recommended to use transverse serrated jaws as in Figure 11 [20]. To hold the test piece, the jaws to be attached to the device must be movable without slipping and causing excessive friction.

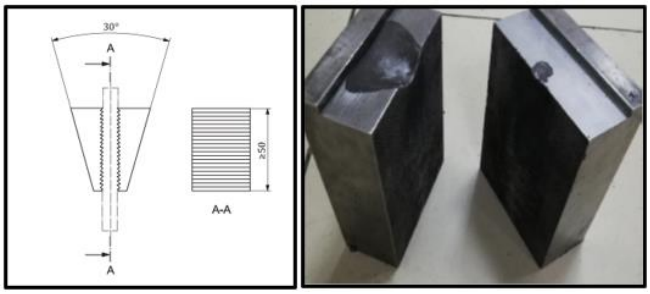

Figure 11. Technical drawing and image of the holding jaws

Conveyor belts spliced in the vulcanization splicing method were subjected to a full-thickness tensile strength test according to TS EN ISO 283 standard. The TS ISO 283 standard applied in the experiment explains how to perform the full-thickness tensile strength test of textile conveyor belts. A test piece cut from the full thickness of the conveyor belt is elongated under certain conditions using a tensile testing machine until rupture occurs. The force at the break of the test specimens gives the maximum value. In the experiment, a test device that can apply a continuous and uniform tension was used. The tensile strength is obtained by dividing the greatest force measured during the tensile test by the width of the test piece. It is expressed in N/mm or kg/cm. The test specimens are placed symmetrically between the serrated jaws of the testing device. Thus, the longitudinal axis of the test specimen, the centerline of the jaws, and the line of action of the tensile force are adjusted. At the beginning of the test, the distance between the inner surfaces of the jaws is applied as 415 ± 10 mm for type B test pieces.

Conveyor belts spliced by the mechanical method are subjected to a strength test according to the TS EN ISO 1120 standard and a static test method is provided according to this standard to determine the mechanical strength of the conveyor belt according to the operating conditions in the facility. The mechanical splice connection of a conveyor belt can be fixed or movable. Fixed fastener-type mechanical attachments were used in this study. The extensometer is tested by applying an increasing tensile force to the test device until the mechanical splice or piece of belt breaks, and the sample is divided into two parts. The ends of the test specimen body are fixed to the jaws of the tensile testing machine. The prepared test specimens were placed symmetrically between the jaws of the tensile test device. In Figures 12 and 13, the tensile test images of the unspliced specimen and mechanically attached specimens are given, respectively. The distance between the inner surfaces of the jaws is set as 415±10 mm for the type B template according to the standard. The width and thickness of the bow tie sample were measured from the narrowest part with the help of a caliper. The bow tie is placed on the device to cover the jaws. The tensile device was activated and the test specimen was extended steadily and uninterruptedly until it ruptured at a rate of 100±10 mm/min. The test was continued until the test piece broke, and when the belt specimen broke, the tensile device stopped. The maximum force F (tensile force N or kg) recorded for each test specimen was read.

Figure 12. Tensile test image of the unspliced belt

Figure 13. Tensile test images of the belt joined by mechanical splicing method

3. EXPERIMENTAL RESULTS AND DISCUSSION

The maximum force recorded during testing for each test specimen is divided by the width of the test piece and its value is recorded in N/mm or kg/cm. The tensile strength value in N/mm^2 is calculated using the belt thickness value. These processes were repeated as 3 samples for each, as the normal unspliced belt, the vulcanized belt, and the mechanical jointed belt, and the arithmetic average of the obtained values was taken. The results of the unspliced belt samples are given graphically in Figure 14 and as values in Table 2.

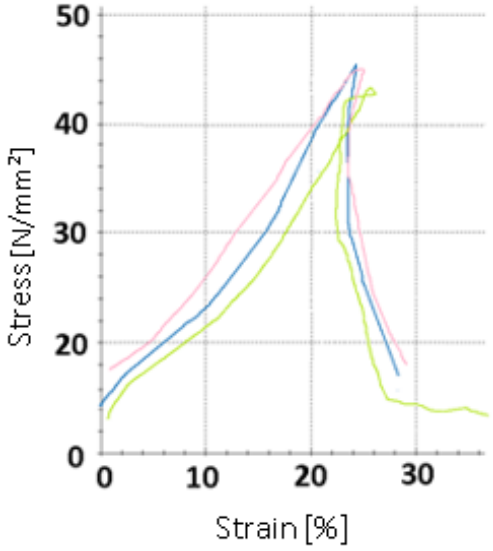

Figure 14. Tensile testing graph of unspliced belt specimens

Table 2. Tensile strength test results of unspliced belt samples

Specimen No	Thickness [mm]	Section [mm]	Sectional Area [mm^2]	Fmax - Tensile Force [kg]	Tensile Strength [N/mm^2]	Average Tensile Strength [N/mm^2]
1	14	25.5	357	1650	46.219	46.312 ±0.127
2	14	25.8	361.2	1678	46.456	
3	14	25.4	355.6	1645	46.260	

It has been observed that the normal belt specimen is above the minimum tensile strength of 630 N/mm (45 N/mm^2) specified in the standard and required to be provided.

The results of the belt specimens spliced by using the vulcanization method are given graphically in Figure 15 and values in Table 3, and the tag of the method is given in Table 4.

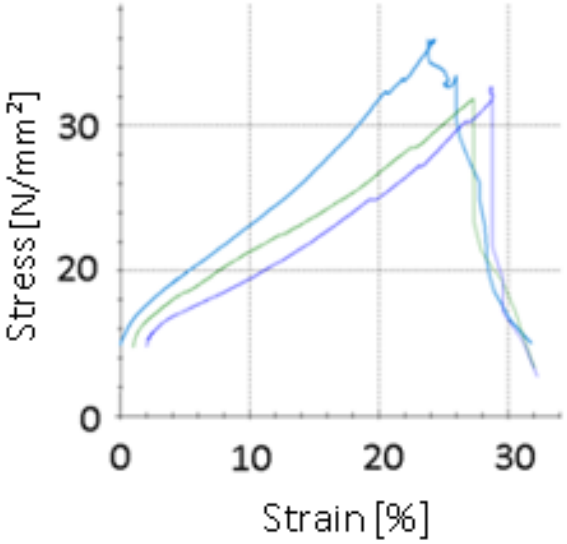

Figure 15. Tensile testing graphs of vulcanized bonded belt specimens

Table 3. Tensile test results of vulcanized belt specimens

Specimen No	Thickness [mm]	Section [mm]	Sectional Area [mm^2]	Fmax - Tensile Force [kg]	Tensile Strength [N/mm^2]	Average Tensile Strength [N/mm^2]
1	14	25.8	361.2	1205	33.361	33.268 ±0.082
2	14	25.6	358.4	1190	33.203	
3	14	26.0	364	1210	33.241	

Table 4. Identification table of the vulcanized splicing method

Features	Value
Width[mm]	800
Fabric quantity	4
Top coating thickness [mm]	6
Bottom coating thickness [mm]	3
Total thickness [mm]	14
Average tensile strength [N/mm^2]	33.268 ±0.082
Strength value compared to unspliced belt [%]	71.8

It has been revealed that the conveyor belt. which is spliced according to the vulcanized hot splicing method. has lost 28.2% of strength compared to the unspliced belt.

The results of the belt specimens spliced by the mechanical splicing method are given graphically in Figure 16 and as values in Table 5. and the tag of the method is given in Table 6.

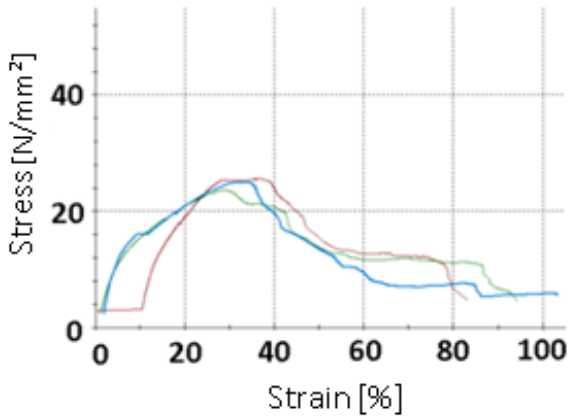

Figure 16. Tensile testing graphs of mechanically spliced belt specimens

Table 5. Tensile test results of mechanically spliced belt specimens

Specimen No	Thickness [mm]	Section [mm]	Sectional Area [mm²]	Fmax - Tensile Force [kg]	Tensile Strength [N/mm²]	Average Tensile Strength [N/mm²]
1	14	106.4	1489.6	3450	23.161	23.241 ±0.206
2	14	105.5	1477.0	3410	23.087	
3	14	107.1	1499.4	3520	23.467	

Table 6. Identification table of the Mechanical splicing method

Özellik	Değerler
Width[mm]	800
Fabric quantity	4
Top coating thickness [mm]	6
Bottom coating thickness [mm]	3
Total thickness [mm]	14
Average tensile strength [N/mm²]	23.241 ±0.206
Strength value compared to unspliced belt [%]	50.2

It has been revealed that the conveyor belt. which is spliced by using mechanical fasteners. has a 49.8% strength loss compared to the unspliced belt.

The strength values of unspliced. vulcanized and mechanically spliced belts are given in Table 7 as a table and in Figure 17 graphically. In Table 8. the advantages of splicing applications over each other are given as a table.

Table 7. Belt splicing methods strength and standard deviation values

Splicing Method	Specimen 1	Specimen 2	Specimen 3	Strength Values [N/mm²]
Unspliced	46.219	46.456	46.260	46.312 ±0.127
Vulcanized	33.361	33.203	33.241	33.268 ±0.082
Mechanical	23.161	23.087	23.476	23.241 ±0.206

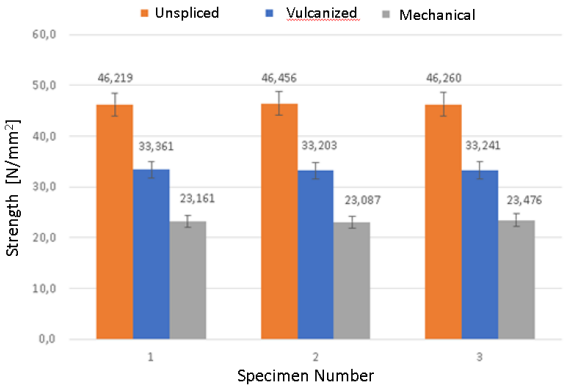

Figure 17. Comparison of strength of belt splicing methods

Table 8. Splicing methods comparison chart

	Mechanical Splicing	Vulcanized Splicing
Strength	Low	High
Being affected by humidity and humidity	Yes	No
Loss of Transported Material (Spill from Joint)	Yes	No
Potential to Damage Other System Equipment	Yes	No
Application time	Short	Long
Applicability	Easy	Difficult
Control and Inspection Status	Easy	Difficult
Experience Requirement	Less	More
The Need for Special and Expensive Equipment	No	Yes

4. CONCLUSIONS AND RECOMMENDATIONS

In this study. a belt with a tensile strength of 630 N/mm and a 4-layer polyester polyamide blend cord fabric. which is used as a conveyor belt in industrial facilities. was used. Splices were formed on the band in question by using mechanical splicing and vulcanization methods. and the strengths of the joints were investigated experimentally. The results obtained from this study are summarized below.

• Specimens extracted from conveyor belts with spliced joints were subjected to the tensile test. and according to the tensile test results. the tensile strength of the unspliced belt was found to be 46.312 N/mm² (648.36 N/mm). The fact that this result was above the minimum tensile strength value of 45 N/mm² (630 N/mm) confirmed the suitability of the result.

• The tensile strength of the belt spliced by using the vulcanization method was found to be 33.268 N/mm² (465.76 N/mm). According to this value. it was concluded that there was a 28.2% decrease in tensile strength compared to an unspliced belt.

• The tensile strength of the mechanically spliced belt was found to be 23.24 N/mm² (325.38 N/mm). According to this value. it was concluded that there was a 49.8% decrease in tensile strength compared to a unsanlicedriods belt. In the light of these results. it has been observed that the belts spliced by using the vulcanization method are 21.6% more durable than the mechanical splicing method. although there is a decrease in strength of approximately 28.2%.

• In addition to these results. considering the duration of the belt splicing applications. it is concluded that the mechanical splicing application. which can be performed in the range of 1 to 2 hours. significantly reduces the downtime of the plant compared to the hot vulcanization application. which can be performed in the range of 6 to 8 hours.

In addition to the above-mentioned results. the findings that emerged as a result of the studies and site observations are given below.

• It has been observed that mechanical fasteners provide a splice that is easy to control and inspect. and can be easily applied by existing plant maintenance personnel.

• The low cost of mechanical attachments and the ability to be stored for long pe make the mechanical splicing method advantageous.

• The vulcanization method is a more comprehensive and costly process and can be performed by professionally trained personnel.

• Belts move through scrapers. relays and drums for continuous transmission. The fasteners used in the mechanical joining method move by rubbing and hitting the conveyor belt elements. As a result. it has been observed that the same situation. which can cause damage to mechanical splicing elements and conveyor equipment over time. is not encountered in the vulcanization method because it does not require any mechanical element.

If a general evaluation is made. as a result of the obtained strength values and other observations. it has been understood that the vulcanization method is more advantageous than the mechanical splicing method.

In the continuation of this study. studies can be carried out to determine the effects of the application parameters used in the hot vulcanization method. which turned out to be more advantageous than the mechanical splicing method. on the strength of the spliced belt. and to optimize the parameters.

REFERENCES

[1] X. Li, X. Long, H. Jiang and H. Long, “Influence of different cord pitch on the pullout force of steel cord conveyor belt splice.” Journal of Adhesion Science and Technology. vol. 32, pp.2268-2281, no. 20. 2018.

[2] X. Long, X. Li and H. Long, “Analysis of influence of multiple steel cords on splice strength.” Journal of Adhesion Science and Technology. vol. 32, pp.2753-2763, no. 24. 2018.

[3] W. Song, W. Shang and X. Li, “Finite element analysis of steel cord conveyor belt splice.” International Technology and Innovation Conference. 2009.

[4] X. Li, X. Long, Z. Shen and C. Miao, “Analysis of Strength Factors of Steel Cord Conveyor Belt Splices Based on the FEM.” Advances in Materials Science and Engineering. vol. 2, pp. 1-9.2019.

[5] L. Nordell, X. Qiu and V. Sethi“Belt conveyor steel cord splice analysis using finite element methods.” Bulk Solids Handling. vol. 11, pp. 863-868, no. 4. 1991.

[6] M.. Hardygora. M.. Bajda and R.. Blazej. “Laboratory Testing of Conveyor Textile Belt Joints Used in Underground Mines.” Mining Science. vol. 22. pp.161-169. 2015.

[7] C. Chuen-Shii. L.. Ching-Liang and C.. Wei-Chung. “Optimum conditions for vulcanizing a fabric conveyor belt with better adhesive strength and less abrasion.” Materials & Design. vol. 44. pp.172-178. 2013.

[8] D. A.. Şahbaz. Soğuk vulkanize yapıştırıcı üretimi ve uygulama koşullarının değerlendirilmesi. Doktara Tezi. Bilecik Şeyh Edebali Üniversitesi Fen Bilimleri Enstitüsü. Bilecik. 2017.

[9] K.. Çankır. Lastik konveyör bantlarının ekleme yöntemleri ve teknik ayrıntıları. Yüksek Lisans Tezi. Mustafa Kemal Üniversitesi Fen Bilimleri Enstitüsü. Antakya. 2006.

[10] B.. Soyubel. Elastomerlerin statik ve dinamik özelliklerinin incelenmesi. Yüksek Lisans Tezi. Uludağ Üniversitesi Fen Bilimleri Enstitüsü. Bursa. 2006.

[11] E. Öztürk. Farklı kauçuk karışımlarının vulkanizasyonuna hızlandırıcıların etkisi. Yüksek Lisans Tezi. Sakarya Üniversitesi Fen Bilimleri Enstitüsü. Sakarya. 2008.

[12] Vahapoğlu. V. Kauçuk türü malzemeler 1. doğal kauçuk. Celal Bayar Üniversitesi Fen Bilimleri Dergisi. vol. 3.1 pp. 57-70. 2007.

[13] TS ISO 37. Lastikler ve Termoplastikler – Çekme gerilmesi-uzama özelliklerinin tayini. T.S.E.. Ankara. 2017.

[14] TS EN ISO 1120. Konveyör bantları-Mekanik bağlantıların dayanımının belirlenmesi-Statik deney metodu. T.S.E.. Ankara. 2013.

[15] ISO 18573. Konveyör bantları - Test atmosferleri ve koşullandırma süreleri. 2012.

[16] MEGEP. Konveyör Bakımı. Metalurji Teknolojisi. Ankara. 2011.

[17] İ.. Uğur. Transport Tekniği Ders Notları. İstanbul Teknik Üniversitesi Maden Mühendisliği Bölümü. İstanbul. 2010.

[18] Labris Maden ve Makina Sanayi A.Ş. Ürün kataloğu. 2021. http://www.labris.com.tr/images/urunler/f4bccc422b85ef42.pdf

[19] R.. Kessentini. O.. Klinkova. I.. Tawfiq and M.. Haddar. “Modeling the moisture diffusion and hygroscopic swelling of a textile reinforced conveyor belt.” Polymer Testing. vol. 75. pp. 159-166. 2019.

[20] TS EN ISO 283. Tekstil konveyör bantları-Tam kalınlıkta çekme mukavemeti. kopma uzaması ve referans yükte uzama- Deney metodu. T.S.E.. Ankara. 2016.

BIOGRAPHIES

Savaş Kirenli completed his primary. secondary and high school education in Karabük. He graduated from Sakarya University. Faculty of Engineering. Mechanical Engineering Department in 2014. He received her master's degree from Karabuk University. Graduate Education Institute in 2021. In his work. he carried out studies on conveyor belts. which are frequently used in industrial facilities and are indispensable for transportation systems. He worked as a Mechanical Maintenance Engineer in Düzce Cam A.Ş. in 2015. Kardemir A.Ş. He started to work as an Installation Pipe Engineer at the Central Maintenance and Construction Directorate In 2016. and continues to work in the same position.

Recep Demirsöz obtained his BSc degree in Mechanical Engineering from Yıldız Technical University (YTU) in 2000. He received the MSc. diploma in Mechanical Engineering from the Istanbul Technical University (ITU) in 2004. He received PhD. diploma in Mechanical Engineering from the Karabuk University (UNIKA) in 2018. His research interests are abrasive and erosive wear. In 2020 he joined the Faculty of Engineering. Karabuk University as an assistant professor.

European Journal of Technique

journal homepage: https://dergipark.org.tr/en/pub/ejt

Vol.12, No.1, 2022

Investigation of Mechanical Properties of Composite Al6061/Ni-Al_2O_3 Produced by Stir Casting Process

Oktay Adıyaman[1*]

[1*]Batman University, Faculty of Technology, Mechanical and Manufacturing Engineering, Batman, Turkey. (e-mail: adiyamanoktay@gmail.com).

ARTICLE INFO

Received: Dec., 28. 2021
Revised: Apr., 18. 2022
Accepted: May, 01. 2022

Keywords:
Composite
Al_2O_3
Microhardness
Al6061
Mechanical Properties
Stir Casting

Corresponding author: *Oktay Adıyaman*

ISSN: *2536-5010* | e-ISSN: *2536-5134*

DOI: https://doi.org/10.36222/ejt.1049835

ABSTRACT

Composites are widely used material types today, and it is known that matrices and additives in composites improve the mechanical properties of the material. In this study, Al6061 matrix and Ni-Al_2O_3 reinforced composite material was produced by stir casting method and the effect of Ni- Al_2O_3 mixture reinforcement on the hardness and tensile properties of the produced composite material was investigated. The determination of the mechanical properties of the samples obtained after the casting process was determined by the results of microhardness analysis and tensile test, and the internal structure of the material was examined by XRD analysis. According to the results of XRD analysis, it was determined that Ni and Al_2O_3 phases were formed together with the matrix element Al. The results of the tensile analyzes showed that the amount of strain in the composite material changed depending on the ratio of the reinforcement element, and the highest strain value occurred in the Ni-Al_2O_3 reinforced sample with Al matrix. However, it was observed that the brittle fracture mechanism was effective in all samples. While the highest microhardness value was obtained in sample 4 (Al6061+ (wt. 15%) Ni+ Al_2O_3) with 89.6 $HV_{0.5}$ value, the lowest microhardness value was obtained from pure Al sample with 66.7 $HV_{0.5}$ value. As a result, it was determined that the Ni-Al_2O_3 reinforcement element increased the microhardness value in the Al matrix composite material.

1. INTRODUCTION

With today's developing technology, it is demanded that the materials should possess more than one properties in themselves at the same time. It is possible that a material is expected to be not only resistant to high wear and corrosion but also light and aesthetic at the same time. For this aim, the composite materials developed in recent years have come forefront. The main material composite materials defined as materials fulfilling more than one function at the same time using the advantageous properties of two or more materials brought together [1-3] is defined as matrix and the materials added into this are called additives. Composite materials are sorted out as metal matrix composites (MMC), ceramics matrix composites (CMC) and polymer matrix composites (PMC) [3]. The interest in MMC has increased due to properties such as high thermal resistance, hardness, resistance to corrosion and wear, ability to resist to tensions steadily in high temperatures together with lightness in industrial applications. Thanks to these advantages, MMCs have been started to be used widely in many sectors such as automotive, aviation and defence industry [3-7]. While the engineering materials, Al, Mg, Zn, Cu, Ti, Ni, Fe, and Co elements and alloys are used as matrix materials in MMC materials, ceramics such as SiC, Al_2O_3 (Alumina), WC, TiC and B_4C are added to MMC as reinforcement materials [2, 8-9].

After steel; Aluminium, one of the materials possessing a wide usage in industry, comes into prominence because of the properties such as high resistance to corrosion, high electric conductivity, low density and recyclability; and owing to these advantages, it is highly preferred in MMCs [10,11].

In this study, Al 6061 serial materials used as matrix are highly preferred materials in especially automotive sector due to their properties such as being casted easily, appropriateness for serial production, easy machinability and low density [12,13].

In addition, aluminium based aluminium metal matrix composites (AMMC), taking place among MMC material types, are materials having the potential to be used in aviation, marine, defence and automotive sectors thanks to their advantages such as low weight, high flexibility, low toughness and excellent resistance in especially low wear and low heat working conditions, though they have low wear resistance and heat performance [14-16].

The resistance of AMMC materials to wear and corrosion is reinforced by adding ceramics as reinforcement elements such as SiC, Al_2O_3 and B_4C in the matrix [17, 18].

Since Al_2O_3 ceramics, which take place among reinforcement elements and relatively have high melting point, offer advantageous properties such as high hardness, resistance to corrosion and wear besides providing

compressive strength; therefore, AMMC composites reinforced with Al_2O_3 are widely used in the sectors mentioned above [9, 19, 21].

Raghavendra et al. coated the surface of Al 6061 with Ni-Al_2O_3 material by means of electrodepositing method; and they investigated the effect of this coat material. At the end of the study, they found that the nano-Al_2O_3 particles in Ni matrix gained higher micro hardness and wear resistance [22]. In the study they conducted, Cooke et al. coated the surface of Al 6061 with Ni- Al_2O_3 at 600 ℃ by means of temporary liquid phase diffusion bond (TLP). They stated that in their study results, using TLP diffusion in Al_2O_3 of Ni coatings containing nano-dispersion, they showed successfully the binding property of the composite. [23]. As a result of literature research, it was established that the studies related to Ni- Al_2O_3 reinforced Al 6061 were mainly based on coating of these materials and the performance of the coating materials; however, it was found out that there were not adequate studies on obtaining Al_2O_3 reinforced Al 6061 material through stir casting process.

In this study, adding the reinforcement materials such as Ni, Al_2O_3 and Ni-Al_2O_3 into Al6061 aluminum serial material, the composites were produced through stir casting method. After manufacturing, the effects of Ni-Al_2O_3 reinforcement material on mechanical (hardness and tensile strength) and microstructure properties of metal matrix composite were studied.

2. MATERIALS and METHOD

Al6061 used as AMMC matrix material in casting process was obtained from Sekoç Aluminum Company. The chemical composition of Al6061is presented in Table 1.

TABLE I
CHEMICAL COMPOSITION OF AL6061

Fe	Si	Cu	Mg	Mn
0,7	0,40-0,8	0,15-0,40	0,8-1,2	0,15
Cr	Ti	Zn	Other	Al
0,04-0,35	0,15	0,25	0,15	Remaining

Reinforcement materials Ni powder (-325 mesh dimension) and Al_2O_3 powder (approximately 1.5 µm) were obtained from the importer company Alfa Easer via Elista Company. General properties of AMMC reinforcement powders are given in Table 2.

TABLE II
PROPERTIES OF THE POWDERS USED IN EXPERIMENTS

Material	Degree of Purity by weight (%)	Powder Dimension (mesh)	Melting Point (°C)	Specific Weight (gr/cm^3)	Atomic mass (gr/mol)
Nickel	99,5	-325	1453	8.908	58.71
Al_2O_3	96.21	1.5 µm	2.072	3,95	101,96

Before melting process, Al6061 matrices material cut in 15 mm x 15 mm dimensions so that the pieces could go into melting pot, then these pieces were cleaned from oil and impurities on them by submerging them into alcohol. Before casting process, the matrix material, Al6061, weighed in a precise balance and put into the melting pot. The powders used as reinforcement materials added into the matrix material were added in matrix being prepared at a rate of wt. 15% of matrix weight (Table 3)

TABLE III
CASTING PARAMETERS

Sample	Casting Sample
N1	Al6061
N2	Al6061+ (wt. 15%)Al_2O_3
N3	Al6061+(wt. 15%)Ni
N4	Al6061+(wt. 15%)Ni+Al_2O_3

Ni-Al_2O_3, the mixture powder, was mixed with the help of a mixer at 300 rpm/min for 3 hours to obtain a homogenous mixture. After the powders were mixed, Al6061 matrix material and reinforcement material were put in a 10 kg melting pot, and they were melted in this pot (Figure 1).

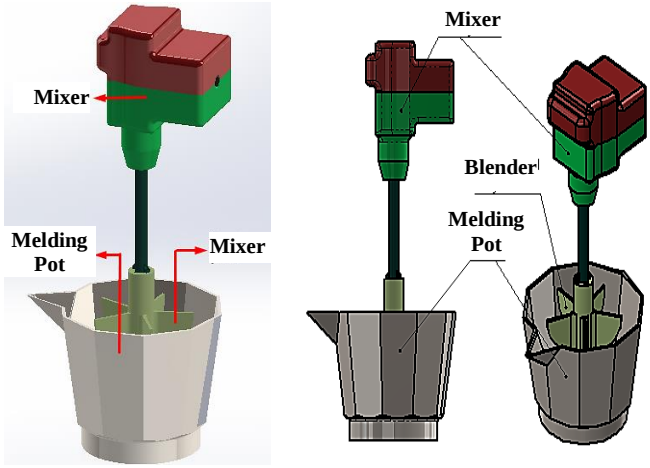

Figure 1. Mixture Preparation Figure for Composite Mixture

In order to melt the matrix material in the melting pot, a heat source was formed out of propane. After waiting about 90 min., the slag layer forming on the melted and liquefied matrix material was taken then mixing process was carried out; and then the reinforcement materials were added in the molten material. After mixing process was completed, the casting of melted mixture into the sample space prepared in dimensions of 15*25*200 mm in a sand mould with a system of sprue at room temperature as presented in the schematic picture in Figure 2.

The molten composite poured down into the sample cavity through sprue was let to solidify at room temperature for 15 min. then the sand moulds were broken and the cast samples were taken out of the mould. The excesses formed in the samples obtained after the casting process were cleaned and the samples were made ready for metallographic and mechanical examinations (Figure 3).

The casted samples were cut sensitively at the sensitive sample taking machine in vertical direction in accordance with the length of the sample for micro-structure and microhardness analyses. The cut samples were exposed to surface polishing process by means of SiC sandpaper within the mesh clearance ranging from 120 to 1200. After polishing process, the surfaces were applied final polishing process and for this, broadcloth was utilized, then the samples were polished with diamond solution with the dimensions of 1 µm and 3 µm. The samples whose polishing process were completed were submerged into Keller solution for cauterization before microstructure examinations. Tensile tests were carried (according to ASTM E8) out at SCHMADZU brand with 1 mm/min. constant feed rate and

250 kN load capacity by preparing the samples whose dimensions are given in Figure 4.

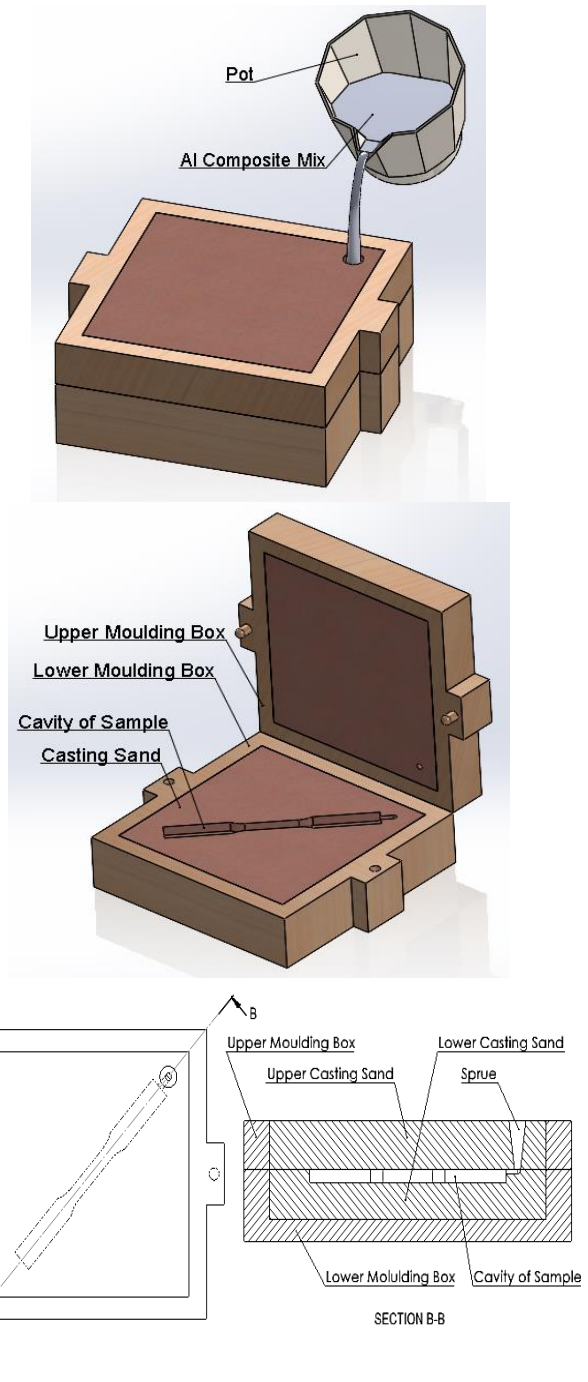

Figure 2. Shematic Picture and section of Sprue Gate

The microhardness analyses were performed by using Future Tech FM700 model digital hardness measurement device from seven different areas. After the cauterization process, the microstructure analyses of the samples were conducted with the help of Nicon optical microscope. In determination of phase components of the samples, X radiation diffraction (XRD) technique was utilized. The XRD analyses were conducted with the help of Rigaku RadB-DMax II diffractometer using cobalt target (λ=1.79026 A^0) and considering a 10° scanning speed per minute at 0.02° foot dimension and 20°-90° scanning intervals.

Figure 3. Separating the excesses and sprues of produced cast samples

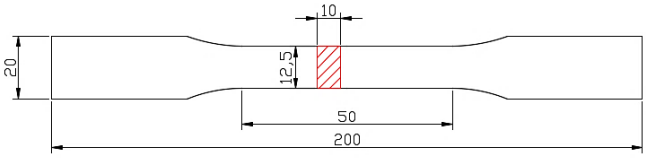

Figure 4. Technical drawing of tensile sample

3. DISCUSSION

The macro-photographs belonging to samples produced after casting process are given place in Figure 5a-d. The samples were produced as mass and tensile samples. Tensile samples were produced considering chip processing shares. It was observed that the amount of pores and spaces were in great number (Figure 5d); after some preventive measures, the samples could be produced properly in a nonporous structure (Figure 5a-c). To produce the samples in nonporous form, it was determined that performing pressured casting of the melted mixture in the mould cavity and adjustment of binding ratios added into the sand prepared for the mould in appropriate portions and improvement of mould design were effective.

In Figure 6, XRD graphic of Al matrix Ni-Al_2O_3 reinforced sample is given place. As can be seen in peak values in the graphic, it was determined that Al element was dense, yet Ni and Al_2O_3 elements were formed low peaks. That Al_2O_3 and Ni were not dense is considered that the reinforcement elements do not provide a proper dispersion in the molten liquid during mixture.

The images of the samples and rupture areas after the tensile test are shown in Figure 7 and the physical properties of the cast samples are given in Table 4. When the surfaces in the rupture regions are examined, it is observed that the samples exhibited a brittle fracture mechanism. It is seen that this result is compatible with previous studies. Karabulut et al. stated that the composite material produced with ceramic reinforcement elements used as reinforcement in aluminium

matrix composites is harder and more brittle than pure aluminium material [24]. At this point, it is possible to explain the two reasons why necking region is not formed in the middle of the test samples. The first one was the selection of the tips of test samples as the melt entry point in the casting (Figure 3, 5a-d). This causes different cooling rates to occur in different parts of the material. As a result, it is inevitable that very small amount of irregularities in the lattice structure and grain density will occur. When the fracture regions are examined (Figure 7), it is seen that all test samples fracture from the same region. This situation supports our opinion. The second reason is thought that the irregularities that may occur in the material mixture may cause the fracture zone not to occur in the middle of the sample.

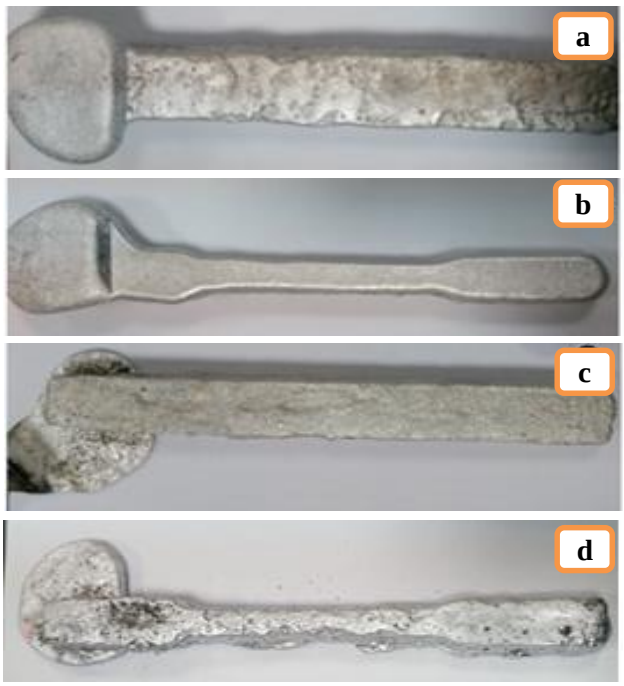

Figure 5. Samples produced after casting process

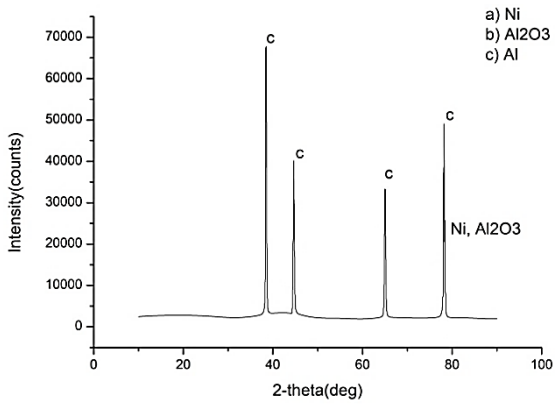

Figure 6. XRD analysis results of Al/Ni-Al_2O_3 sample

When Figure 7 is examined, it is seen that the other test samples (samples 1, 2, 3, excluding sample 4) broke off from the radius region, whereas in sample no. 4, the rupture region was in the region farther from the radius region. The tensile graph of the tensile test of the composite samples obtained is shown in Figure 9. According to this graph, it was observed that the lowest elongation value was in sample 2 and the highest elongation was in sample 4. When all the data obtained in Figure 7 and Figure 8 are examined, it is concluded that Ni-Al_2O_3 reinforcement material in the cast composite material has an effect on increasing the tensile strength of the composite material. Similarly, it is understood from the graph in Figure 8 that the tensile strength of sample 3 is better than samples 1 and 2. It is seen in most studies that the addition of Ni into aluminium alloys increases the density; and this increases the strength and hardness of the material. The high-density value of nickel, 8.9 g/cm^3, led to an increase in the density of aluminium alloys with the increase of nickel content [25-29].

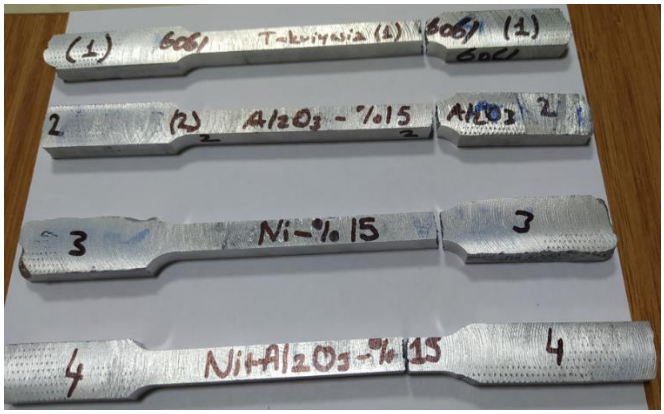

Figure 7. Test samples and rupture regions obtained after tensile test

TABLE IV
PHYSICAL PROPERTIES OF THE CAST SAMPLES

Material	Modulus of Elasticity (Gpa)	Density (MJ/m^3)
Al 6061	3,24	1,55
Al6061 (%15 Al_2O_3)	2,29	0,78
Al6061 (%15 Ni)	2,92	2,31
Al6061(%15 Ni+ Al_2O_3)	2,70	2,41

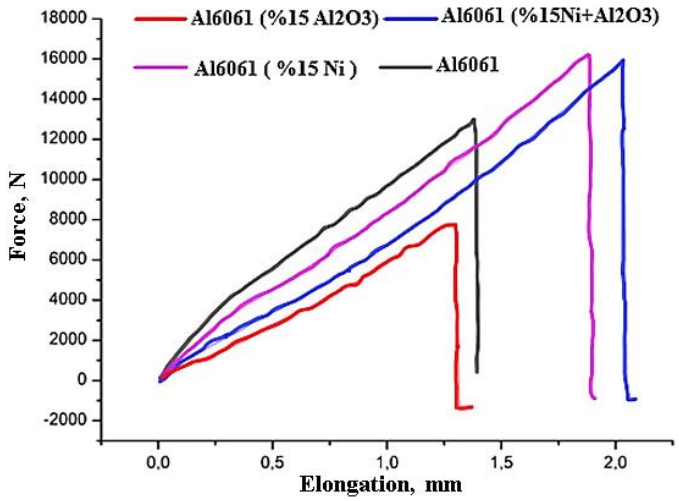

Figure 8. Result graph of tensile test

Microhardness measurements of the samples produced by stir casting method with Al6061 matrix and reinforced with wt.15% Al_2O_3, wt.15% Ni and wt.15% Al_2O_3+Ni by weight, respectively, were made. The average hardness values of these measurements are shown in Figure 9.

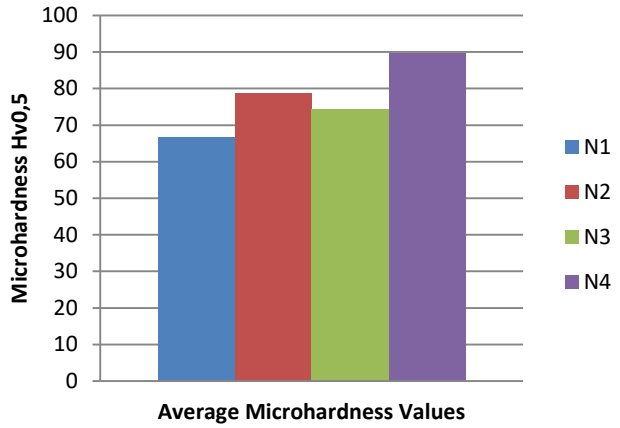

Figure 9. Microhardness values of samples

As a result of the hardness measurements, the highest average hardness value was obtained as 89.6 $HV_{0.5}$ in the sample reinforced with wt.15% Ni-Al_2O_3. The lowest hardness value was obtained as 66.7 $HV_{0.5}$ from the test sample no. 1 (Al) without reinforcement. The microhardness values obtained in other samples were measured as 78.6 $HV_{0.5}$ in Al_2O_3 reinforced test sample no. 2 and as 74.3 $HV_{0.5}$ in Ni added test sample no. 3, respectively.

Sivananthan et al. added Al_2O_3 at different rates as a reinforcement element into Al6061 by stir casting method. In their hardness measurements after the tests, they stated that they obtained 81 HV hardness values in the 4% by weight Al_2O_3 reinforced sample and an average of 75 HV hardness values in the 2% weight samples. In the light of these results, both in this study and in previous studies [29], it was observed that the microhardness of the Al6061 alloy increased with the increase in the amount of Al_2O_3 particles in the composite material.

It is known that the hard and brittle Al_2O_3 particles used as reinforcements cause dispersion hardening in the matrix. It was seen in previous studies that these particles act as the second phase in the matrix and contribute to the hardening of the composites by resisting the movement of the dislocations. [31,32]. In another study, Ni and Al_2O_3 were added as reinforcing elements into the Al matrix, and as a result, higher hardness obtained with the increase of nickel amount in the samples with 10% Ni-40% Al_2O_3-50% Al mixture ratios. It was stated that the decrease in the amount of Al used as a matrix element contributed to the high hardness value [25]. In another study, it was observed that the hardness value increased as B_4C grain reinforcement ratio increased. While the highest hardness value was obtained as 68.1 $HV_{0.5}$ from 16% reinforced B_4C and Al matrix composite, the lowest hardness value was obtained as 48.5 $HV_{0.5}$ from pure Al [33]. Kılıç stated that in the B_4C reinforced coating study, the hardness value of the coating layer was 2-2.5 times higher than the substrate [34]. Considering the previous studies, it is seen that the hardness of Al matrix composites varies depending on the added reinforcement element and its amount. In this study, it was determined from the results obtained that the results obtained increased due to the increase of the reinforcement element in parallel with the literature

4. CONCLUSION

In this study, Ni-Al_2O_3 composite material with Al6061 matrix was produced using the stir casting method. After production, the effect of the reinforcing element Ni-Al_2O_3 matrix on the hardness and tensile properties was investigated. After the analysis and evaluation of the data obtained after the evaluation, the following conclusions were reached;

- It was determined that the highest elongation value at which the tensile analyses changed depending on the reinforcement element occurred in Ni- Al_2O_3 reinforced sample with Al matrix.
- However, it was observed that the brittle fracture mechanism was effective in all samples.
- While the highest microhardness value was obtained in sample 4 with 89.6 $HV_{0.5}$ value, the lowest value was obtained from pure Al sample with 66.7 $HV_{0.5}$.
- In the light of the results obtained, it was determined that Ni-Al_2O_3 reinforcement element increased the Al matrices microhardness.
- As a result of XRD analysis, it was determined that Al element is dense, while Ni and Al_2O_3 elements also occur at low peaks.

REFERENCES

[1] Senel M.C. et al., "The investigation on mechanical properties and microstucture of SiC reinforced aluminum matrix composites," Technological Applied Sciences (NWSATAS), to be published. DOI:10.12739/NWSA.2018.13.2.2A0142.

[2] Oztop B, Gurbuz M, "Investigation of properties of composites produced by reinforcement graphene matrix obtained from waste aluminium," International Journal of Multidisciplinary Studies and Innovative Technologies, vol. 1, no 2, pp 4 – 8, 2017.

[3] Rangrej S. et al., "Effects of reinforcement additions on properties of aluminum matrix composites – A review," Materials Today: Proceedings, to be published. DOI: 10.1016/j.matpr.2020.10.604.

[4] O'Connor M.J., Wawner F.E., Jones C.C., "An investigation of the microstructure and mechanical properties of the macro-interface in selectively reinforced aluminium castings," Journal of Materials Science, vol. 31, pp. 164-171, 1996.

[5] Shunmugasundaram M., Kumar A.P., Sankar L.P., Sivasankar S., "Experimental investigation and process parameters optimization of stir cast aluminium metal matrix composites to improve material removal rate," Materials Today: Proceedings, vol. 27, pp. 883–888, 2020.

[6] Rao E.S., Ramanaiah N., "Influence of heat treatment on mechanical and corrosion properties of aluminium metal matrix composites (AA 6061 reinforced with MoS2)," Materials Today: Proceedings, vol. 4, pp. 11270–11278, 2017.

[7] Schneider Y., Soppa E., Kohler C., Mokso R., Roos E., "Numerical and experimental investigations of the global and local behaviour of an Al(6061)/Al2O3 metal matrix composite under low cycle fatigue," Procedia Engineering, vol. 10, pp. 1515–1520, 2011.

[8] Karakoc H., Cıtak R., "Study on weldability of B_4C reinforced aluminium composite materials with TIG welding," El-Cezerî Journal of Science and Engineering, vol. 4, no. 3, pp. 584-592, 2017.

[9] Senthil S. et al., "Manufacturing processes and recent applications of aluminium metal matrix composite materials: A review," DOI: 10.1016/j.matpr.2020.08.792.

[10] Gokce A., Findik F., Kurt A.O., "Powder metallurgy processing of aluminum alloys," Engineer and Machinery, vol. 58, no. 686, pp. 21-47, 2017.

[11] Venkata S. et al., "Investigation of SiC and AL_2O_3 – Reinforced with aluminium composites- A review," DOI: 10.1016/j.matpr.2020.10.276.

[12] Prajulraj P. et al., "Experimental investigation on mechanical and morphological properties of AA 6061 reinforced with silicon carbide," DOI: 10.1016/j.matpr.2020.07.501.

[13] Ramesh C.S., Keshavamurthy R., Channabasappa B.H., "Abrar Ahmed, Microstructure and mechanical properties of Ni–P coated Si3N4 reinforced Al6061 composites," Materials Science and Engineering A, vol. 502, pp. 99–106, 2009.

[14] Su H., Gao W., Feng Z., Lu Z., "Processing, microstructure and tensile properties of nano-sized Al_2O_3 particle reinforced aluminum matrix composites," Materials and Design, vol. 36, pp. 590–596, 2012.

[15] Okumuş M., Bülbül B,. "Investigation of Thermal and Microstructural Properties of Al-4.5Cu/SiC Composite Produced by Mechanical Alloying Method," GU J Sci, Part C, vol. 8, no. 2, pp. 405-417, 2020.

[16] Panwar N., Chauhan A., "Fabrication methods of particulate reinforced Aluminium metal matrix composite-A review," Materials Today: Proceedings, vol. 5, pp. 5933–5939, 2018.

[17] Bayar H., Subasi M., Karatas C., "SiC takviyeli alüminyum alaşim matrisli kompozit malzemenin yüksek basinçli kalip dökümü ve mekanik özellikleri," Gazi University Journal of Science GU J Sci Part C, vol. 3, no. 4, pp. 603-612, 2015.

[18] Kalaiselvan K., Murugan N., Parameswaran S., "Production and characterization of AA6061–B4C stir cast compo," Materials and Design, vol. 32, pp. 4004–4009, 2011.

[19] Shang F., Cao Z., Zhang P., Qiao B., Li H., "Microstructure and properties of Ni/ Al_2O_3 composites prepared by powder injection molding," IOP Conf. Series: Materials Science and Engineering, vol. 389, pp. 012-022, 2018.

[20] Sajjadi S.A., Ezatpour H.R., Beygi H., "Microstructure and mechanical properties of Al– Al_2O_3 micro and nano composites fabricated by stir casting," Materials Science and Engineering A, vol. 528, pp. 8765–8771, 2011.

[21] Yang G., Song W., Lu J, Hao Y, Li Y, Ma Y,. "Microstructure of surface composite Al_2O_3/Ni on copper substrate produced by vacuum infiltration casting," Materials Science and Engineering A, vol. 418, pp. 223–228, 2006.

[22] Raghavendra C. R., Basavarajappa S., Sogalad I, "Influence of pin temperature on dry sliding wear behaviour of Ni– Al_2O_3 composite coating on Al6061 substrate," J. Inst. Eng. India Ser. C, vol. 101, no. 4, pp. 671–681, 2020.

[23] Cooke K O, Khan T I, Oliver G D,. "Effect of Ni– Al_2O_3 nanocomposite coating thickness on transient liquid phase bonding of Al 6061 MMC," Science and Technology of Welding and Joining, vol. 17, no. 1, pp. 22-31, 2012.

[24] Karabulut H., Citak R., Cinici H., "Effect of mechanical alloying duration on transverserupture stregth of Al+10% Al_2O_3 composites," Journal of the Faculty of Engineering and Architecture of Gazi University, vol. 28, no. 3, pp.635-643, 2013.

[25] Sak N., Zeren M., Yamanoglu R., "Characterization of properties in alumina doped and nickel alloyed aluminum based composites," Koc. Üni. Fen Bil. Der., vol. 1, no. 1, pp. 1-7, 2018.

[26] Bhattacharyya M., Kumar A. N., Kapuria S. "Synthesis and characterization of Al/SiC and Ni/Al_2O_3 functionally graded materials," Materials Science and Engineering: A, vol. 487, no. 1-2, pp. 524-535, 2008

[27] Fahrenholtz W. G., Ellerby D. T., Loehman R. E. "Al2O3–Ni composites with high strength and fracture toughness," Journal of the American Ceramic Society, vol. 83, no. 5, pp.1279-1280, 2000.

[28] Kilic M., "The Investigation of microstructures and fabrication of functionally graded intermetallic materials by self-propagating high-temperature synthesis," Batman University Journal of Life Sciences, vol. 5, no.2, pp. 87-98, 2015.

[29] Imak A., Kirik I., Kilic M., "Comparison of microstructure and wear behaviors of PTA coated AISI 304 with alumina, boron and ekaboron III powder," Materials Testing, vol. 64, no. 4, pp. 541-549, 2022.

[30] Sivananthan S., Reddy V.R., Samuel C.S.J., "Preparation and evaluation of mechanical properties of 6061Al- Al_2O_3 metal matrix composites by stir casting process," Materials Today: Proceedings, vol. 21, pp. 713–716, 2020.

[31] Baradeswaran A., Perumal A.E., "Study on mechanical and wear properties of Al 7075/ Al_2O_3/graphite hybrid composites," Composites: Part B, vol. 56, pp. 464–471, 2014.

[32] Pathak J.P., Singh J.K., Mohan S., "Synthesis and characterisation of aluminium– silicon–silicon carbide composites," Indian J Eng Mater., vol. 13, pp. 238–46, 2006.

[33] Celik Y.H., Secilmis K., "Investigation of wear behaviours of Al matrix composites reinforced with different B_4C rate produced by powder metallurgy method," Advanced Powder Technology, vol. 28, no. 9, pp. 2218-2224, 2017.

[34] Kilic M., "Microstructural Characterization of Ni-Based B_4C Reinforced Composite Coating Produced by Tungsten Inert Gas Method," Arch. Metall. Mater. Vol. 66, no. 3, pp. 917-924, DOI: 10.24425/amm.2021.136398.

BIOGRAPHIES

Oktay ADIYAMAN obtained his BSc degree in Mechanical Education from Gazi University in 1994. He received the BSc., and MSc. diploma in Mechanical Engineering from the Gazi University in 1998 and 2003 respectively, and PhD degrees in Graduate School of Science, Engineering and Technology of the Firat University in 2015. His research interests are machinebility, manufacturing and tribology. In 2016 he joined the Faculty of Technology, Batman University as a Assist Prof. where he is presently a professor.

European Journal of Technique

journal homepage: https://dergipark.org.tr/en/pub/ejt

Vol.12, No.1, 2022

Effects of Biodiesel Fuels Produced from Vegetable Oil and Waste Animal Fat on the Characteristics of a TDI Diesel Engine

Ertan Alptekin[1,4], **Huseyin Sanli**[2,4], **Mustafa Canakci**[3,4*]

[1] Department of Automotive Engineering, Kocaeli University, 41001, Izmit, Turkey. (e-mail: ertanalptekin@kocaeli.edu.tr).
[2] Department of Automotive Technology, Tekirdag Namik Kemal University, 59860, Corlu, Turkey. (e-mail: hsanli@nku.edu.tr).
[3*] Department of Automotive Engineering, Kocaeli University, 41001, Izmit, Turkey. (e-mail: canakci@kocaeli.edu.tr).
[4] Alternative Fuels R&D Center, Kocaeli University, 41275 Izmit, Turkey

ARTICLE INFO

Received: Oct., 23. 2021
Revised: Jan., 04. 2022
Accepted: Jan., 05. 2022

Keywords:
Vegetable Oil
Waste Animal Fat
Biodiesel
Engine Test
Diesel Engine

Corresponding author: *Mustafa Canakci*

ISSN: *2536-5010* | e-ISSN: *2536-5134*

DOI: https://doi.org/10.36222/ejt.123456

ABSTRACT

In this study, four different biodiesel fuels obtained from corn oil, safflower-rapeseed oil mixture (50%-50% v/v), waste chicken fat, and waste fleshing oil were tested in a six-cylinder, water-cooled, TDI diesel engine. Vegetable oil and waste animal fat origin biodiesel fuels' effects on the performance, injection, combustion and emission characteristics of test engine were compared with each other and petroleum-based diesel fuel as reference fuel. Biodiesel fuels (regardless of their feedstock) increased in-cylinder gas pressure, brake specific fuel consumption, and NO_x emissions while decreased THC and CO emissions compared to pure diesel fuel. In comparison to petro-diesel, the start of fuel injection timing advanced but the end of fuel injection timing retarded with biodiesels. In addition, comparatively higher fuel injection pressure values were attained with all biodiesel fuels. Waste animal fat and vegetable oil origin biodiesel fuels showed similar in-cylinder gas pressures, fuel injection characteristics and brake specific fuel consumption values. However, vegetable oil-based biodiesel fuels' CO emissions were lower than those of waste animal fat-based biodiesels, but NO_x emissions were higher.

1. INTRODUCTION

The share of pollutants from the transportation sector in the total environmental pollution has been increasing. In order to decrease tailpipe emissions, very strict emission regulations are being come into force and the upper limits are reduced step by step towards the ultimate target of near-zero emissions. In every new emission standard, meeting the permitted exhaust emission limits (especially in diesel engines) becomes more challenging for the automotive industry. One of the methods that can be considered to reduce exhaust emissions released from vehicles (together with the improvements in fuel injection systems and strategies, combustion chamber design, and exhaust gas after-treatment technologies) is the usage of environmentally friendly alternative energy sources in internal combustion engines.

Biodiesel is a renewable, biodegradable, domestically producible, and environmentally friendly alternative diesel fuel. It can be produced from various feedstocks such as vegetable oils, animal fats and their wastes [1]. Diesel engines can be powered with neat biodiesel fuel. According to the European Union diesel fuel standard (EN-590), diesel fuel can contain up to 7% (on volume basis, v/v) biodiesel which meets the specifications in the European biodiesel fuel standard (EN-14214), regardless of its feedstock. Although there are many feedstocks that can be used in biodiesel production, the vast majority of industrial-scale biodiesel comes from high-quality edible vegetable oils. The use of high-quality but unacceptably expensive edible oils in the biodiesel industry inevitably increases its unit price as well as negatively affects the food chain by increasing the prices of those vegetable oils. Low-cost feedstocks such as waste frying oils and waste animal fats should be preferred in biodiesel production in order to make it an economically viable fuel and to prevent the rise in edible oil prices [2]. In addition to its positive impact on biodiesel fuel's break-even price, the usage of waste feedstocks will prevent the environmental contamination caused by their disposal.

It should be strongly highlighted that various triglycerides as the biodiesel feedstock (vegetable oils, animal fats or their wastes) will have different fatty acid compositions, leading to different physico-chemical properties [3]. Biodiesel fuels having different fuel properties inevitably influence the engine characteristics. Because of this, the effects of biodiesel

fuels of different origin on the diesel engine characteristics should be investigated in detail. However, when the studies in the literature about the effects of biodiesel fuels on engine characteristics are examined, it is seen that these studies are generally carried out with vegetable oil-based biodiesels. In particular, the number of experimental articles comparing the influences of biodiesel fuels of vegetable oil and animal fat origin under the same engine operating conditions is quite limited.

Barrios et al. [4] produced biodiesel fuels from soybean oil and animal fat. Animal fat feedstock was a blend of pork, poultry and beef fat. They prepared six different biodiesel-diesel fuel blends (10-20-25-30-40-50 %, v/v). Biodiesel fuels were not used in the engine tests as neat fuel. The authors have detected higher brake specific fuel consumption (BSFC) values and brake thermal efficiencies (BTE) with all biodiesel fuels compared to petro-diesel fuel (PDF). All biodiesel blends decreased particulate matter (PM) emission but caused to higher oxides of nitrogen (NO_x) emissions than diesel fuel. Although there were no significant differences between NO_x emissions of biodiesel fuels of different origin, PM emissions of animal-fat based biodiesel blends were less than those of vegetable oil-based biodiesel blends. Animal fat-based biodiesel fuel blends had better engine characteristics than soybean oil-based biodiesel blends especially at 40% and 50% biodiesel-diesel fuel concentrations. In order to minimize harmful emissions, BSFC and maximize BTE, the authors have concluded that 30% animal fat based biodiesel-diesel fuel was the ideal blend ratio.

Ahmed et al. [5] investigated the effects of beef tallow-based biodiesel fuel and its blends with PDF in the ratios of 20-40-60% (v/v). Engine tests were conducted in a single cylinder, four-stroke, water-cooled diesel engine. BSFC values of all test fuels decreased with increasing engine load. Biodiesel fuels' BSFC values were higher than that of PDF at all loads and this difference increased as biodiesel percentage of the blend increased. BTE of all test fuels increased as the engine load was increased. Biodiesel fuels had relatively higher BTE at all operating conditions. The authors detected that biodiesel fuel and its blends started to burn earlier than PDF. Although the max in-cylinder pressures were very close to each other, the crank angles at which the max in-cylinder pressures were attained advanced with biodiesel fuels. Biodiesel fuel and its blends reduced carbon monoxide (CO), total hydrocarbon (THC) and smoke emissions but increased NO_x emissions. In order to decrease NO_x emissions of biodiesel fuels, the authors used exhaust gas recirculation (EGR) in the ratios of 10-20-30%. At the EGR ratio of 10%, lower bsfc, higher BTE, lower CO and THC emissions were observed. In addition, the decrease in NO_x and smoke emission was 16.5% and 17.5%, respectively. The authors reported that animal fat origin biodiesel-diesel fuel blend ratio of 20% could be used in a diesel engine with 10% EGR application without causing higher NO_x emissions and bsfc values.

Sathiyagnanam et al. [6] produced biodiesel fuel from waste pork lard. They blended biodiesel fuel with PDF in the ratios of 25-50-75% (v/v). Engine test were carried out in a one-cylinder, four-stroke, water-cooled, DI diesel engine. Throughout the engine tests, engine speed was not changed (1500 rpm) while engine load was increased from 0% to full load with the steps of 25%. Biodiesel fuel and its blends had higher bsfc and lower BTE values than diesel fuel at all engine loads tested. The combustion started comparatively earlier for biodiesel fuels than diesel fuel. Peak in-cylinder pressure values declined with increasing biodiesel content in the blend. The relatively shorter ignition delay periods for biodiesel fuel and its blends were reported. Because of the longer ignition delay and better volatility, the premixed combustion phase of PDF was more intense than biodiesel and its blends. Biodiesel fuels significantly decreased CO, HC and smoke emissions. Nevertheless, their NO_x emissions were higher. To reduce NO_x emissions and to determine the optimum ratio, the various percentages of urea were injected to the engine exhaust. The authors expressed that 30% urea and 70% water gave the max NO_x reduction without deteriorating CO emissions.

In this experimental study, in order to partially fill the gap in the literature about the impacts of biodiesel fuels of different origin on the engine characteristics, the influences of biodiesel fuels obtained from two different waste animal fats and two different vegetable oils on the performance, injection, combustion and emission characteristics of a TDI diesel engine were investigated and compared with petroleum-based diesel as reference fuel.

2. MATERIALS AND METHODS

Corn oil biodiesel (COB) and safflower-rapeseed oil biodiesel (SRB) fuels as the vegetable oil-based biodiesels, waste fleshing oil biodiesel (WFB) and waste chicken fat biodiesel (WCB) fuels as the animal fat-based biodiesels were used in the engine tests. Waste fleshing oil was obtained from the solid waste processing plant in Istanbul Leather Organized Industrial Zone while waste chicken fat was obtained from the rendering facility at Beypilic Bolu Factory. Corn oil and PDF were purchased from local store and gas station. Biodiesel productions from corn oil, waste chicken fat and waste fleshing oil were performed in the pilot-scale biodiesel plant at Kocaeli University. SRB fuel was obtained from DB Agricultural Energy Co. Inc. in Izmir. Physico-chemical fuel properties of test fuels were given in Table 1.

Engine tests were carried out in a four-stroke, six cylinders, direct-injection, turbocharged diesel engine. Technical specifications of the test engine were shown in Table 2. A schematically view of the test system was depicted in Fig. 1. The engine was tested at the condition of 1400 rpm and 600 Nm engine load. No modifications were made to the engine prior to the engine tests. The test engine was equipped with an in-line type fuel injection pump. In-cylinder pressure was measured via Kistler (6061B) pressure sensor while Kistler (6005) sensor was used for fuel-line pressure. AVL SESAM FITR exhaust emission analyzer measured the exhaust emissions. Specifications of the exhaust emission device were given in Table 3.

TABLE I
TEST FUELS' PHYSICO-CHEMICAL FUEL PROPERTIES

Property	Unit	PDF	SRB	COB	WCB	WFB
Density (15 ºC)	$kg.m^{-3}$	829	883.6	886.0	889.7	876.7
Viscosity (40 ºC)	$mm^2.s^{-1}$	2.96	4.3	4.6	5.3	4.7
Flash Point	ºC	63	186	169	169	168
Water Content	ppm	20	240	440	440	410
Acid Value	$mgKOH.g^{-1}$	-	0.28	0.21	0.43	0.28
Monoglyceride	% (w/w)	-	0.49	0.06	0.02	0.06
Diglyceride	% (w/w)	-	0.15	0.17	0.05	0.02
Triglyceride	% (w/w)	-	0.01	0.06	0.06	0.20
Free Glycerol	% (w/w)	-	0.001	0.01	0.008	0.01
Total Glycerol	% (w/w)	-	0.15	0.06	0.03	0.05
Copper Strip Corrosion (3 h, 50 ºC)	Degree of corrosivity	No 1	No 1	No 1	No 1	No 1
Heating Value	$MJ.kg^{-1}$	45.96	40.05	39.88	39.69	39.89
Cetane Number	-	56.8	53.0	54.2	52.3	58.8
Methanol Content	% (w/w)	-	0.00	0.03	0.05	0.01
CFPP	ºC	-15	-9	-5	3	10

TABLE II
TECHNICAL SPECIFICATIONS OF THE TEST ENGINE

Engine	6 liter, Ford Cargo
Type	Direct Injection, turbocharged-intercooled, four-stroke, water cooled
Number of cylinder	6
Bore - stroke	104.00 – 114.9
Compression ratio	16.4:1
Injection pump	In-line type
Injector opening pressure	197 bar
Maximum power	136 kW (2400 rpm)
Maximum brake torque	650 Nm (1400 rpm)

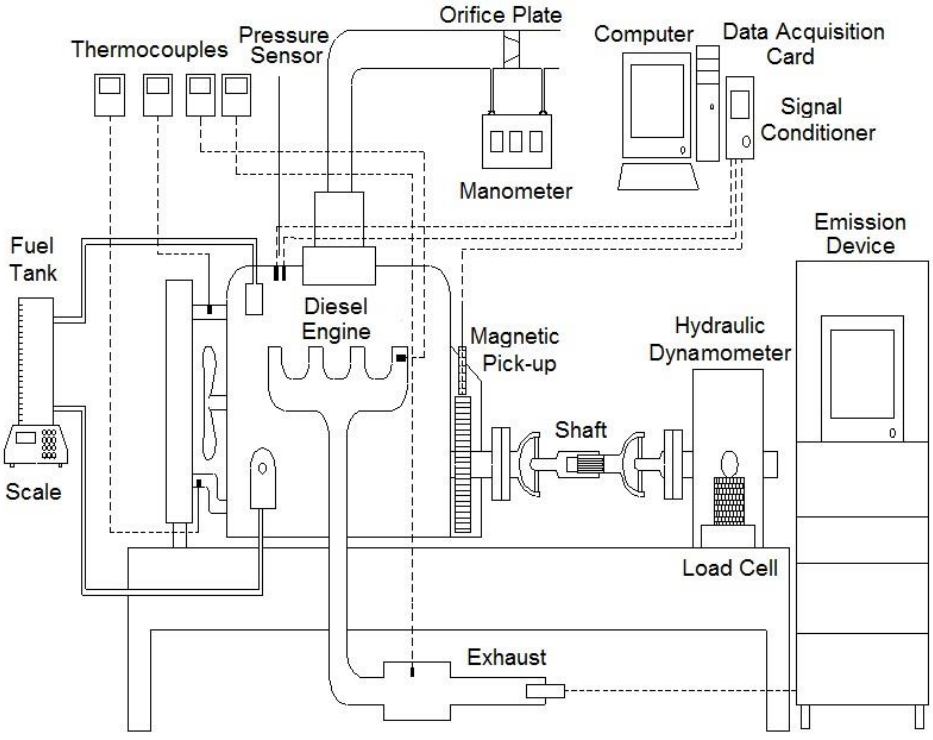

Figure 1. The experimental setup.

TABLE III
SPECIFICATIONS OF EXHAUST EMISSION DEVICE

Parameter	Unit	Measuring Range	Accuracy
HC	ppm	0-20,000	Better than 2% ± of measured value
CO	ppm	0-8,000 (low) 8,000-100,000 (high)	Better than 2% ± of measured value
NO_x	ppm	0-10,000	Better than 2% ± of measured value

3. RESULTS AND DISCUSSION

3.1. Brake Specific Fuel Consumption

Brake specific fuel consumption (BSFC) is one of the most critical parameters used for comparing the effects of different fuels on engine performance. Fig. 2 shows the BSFC values of the test fuels. As can be understood from the figure, all biodiesel fuels led to increment in BSFC values. Comparative to BSFC value of PDF, the rise in BSFC values was 11.8%, 13.7%, 11.8% and 10.8% for WFB, WCB, COB and SRB, respectively. The high BSFC values of biodiesel fuels can be explained with their comparatively low calorific values than that of PDF. As given in Table 1, the calorific values of biodiesel fuels used in engine tests were about 13% lower than that of PDF. Buyukkaya [7] found similar results in their studies.

Among the biodiesel fuels, WCB had the highest BSFC value. The relatively high viscosity and density values of WCB may have negatively affected the atomization quality and inevitably the combustion efficiency, resulting in higher BSFC value. SRB had lower BSFC value than the other biodiesel fuels. This may be resulted from its low viscosity and high calorific value. WFB and COB fuels had were very close BSFC values. It is quite remarkable that viscosity and calorific values of these biodiesel fuels were also almost the same (Table 1).

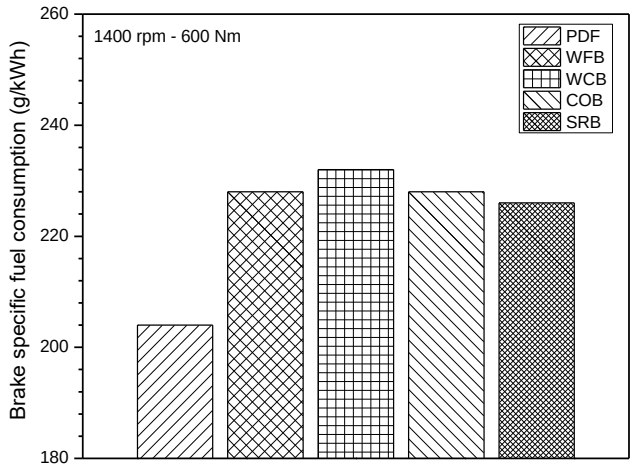

Figure 2. Brake specific fuel consumption of test fuels.

3.2. Fuel Injection and Combustion Characteristics

Injection characteristics such as start and end of injection, injection duration and injection pressure directly affect the combustion phenomenon and inevitably exhaust emission profile of the engine [8]. Therefore, it is very important to analyze the injection characteristics of different fuels. Test engine is equipped with mechanically controlled in-line type fuel injection system. Before presenting and interpreting the data on the fuel injection characteristics of test fuels, it will be helpful to remember some critical issues on this type of fuel injection system. In mechanic fuel injection systems, fuel injection is performed with the fuel pressure. Namely, high-pressure transfer pump compress the fuel and this rise in pressure progresses in fuel line and reaches injector. When the injector pressure exceeds the spring pressure that presses the injector needle down, the injector needle lifts and fuel injection begins. In-line type fuel injection system controls the end of injection process. In order to increase the fuel quantity to the engine, it regulates the injector closing timing. In other words, if it is necessary to inject more fuel, the end of injection is delayed [9].

Since the injector needle-lifting sensor was not used in this study, the injector opening pressure (197 bar) was accepted as the start of injection. Fuel line pressure values obtained with test fuels were given in Fig. 3. As can be seen in the figure, start of injection advanced with all biodiesel fuels compared to PDF. SRB and WCB fuels had almost the same start of injection timing while WFB and COB fuels were in the second and the third order, respectively. The earlier start of injection with biodiesel fuels relative to PDF can be explained with their compressibility. If a fuel is less compressible, fuel line pressure will increase faster and thus injection will start sooner [10]. Because of this, the fuel type that is used in a diesel engine with mechanical fuel injection system directly influences the start of injection and the other injection characteristics. Two critical properties affecting the injection timing are the propagation speed of the pressure waves in fuel line (speed of sound) and the capacity of the fuel to dampen this pressure (bulk modulus) [11]. Related studies have revealed that when biodiesel fuels are used, in comparison to PDF, pressure waves proceed faster and the fuel dampens the pressure less [12]. As a combined result of these two factors, fuel line pressure increases faster with biodiesel fuel and so the start of injection advances.

The end of fuel injection retarded for all biodiesel fuels. Since more fuel needs to be injected into the engine in case of biodiesel usage (see Fig.2), the in-line type fuel injection pump retarded the injector closing by regulating the end of injection, as mentioned above. With all biodiesels (regardless of the feedstock), the injection duration was prolonged because of the advanced start and the delayed end of fuel injection. Another important point is the injection pressures of all biodiesel fuels, which were higher than those of PDF.

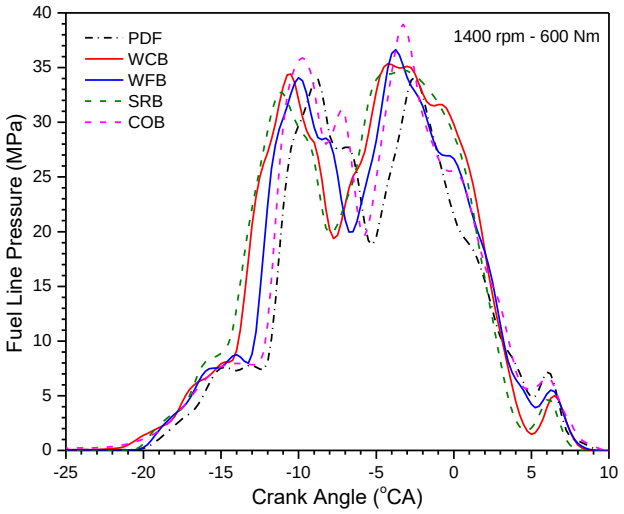

Figure 3. Fuel line pressures of test fuels.

In-cylinder pressure and heat release rate (HRR) values and their alterations with crank angle give critical information about the start, the propagation, and the end of combustion phenomenon. These data have critical importance in order to compare the combustion characteristics of alternative fuels with different physico-chemical fuel properties. In-cylinder pressures and HRRs of

test fuels were depicted in Fig. 4. As seen, slightly higher in-cylinder pressures were attained with biodiesel fuels both vegetable oil and animal fat origin compared to PDF. Two main reasons for the higher in-cylinder pressures are biodiesels' the earlier start of injection timings and their oxygen contents. The extra oxygen in the combustion media coming from the biodiesel chemical structure increases the flame speed, resulting in higher in-cylinder pressures [13].

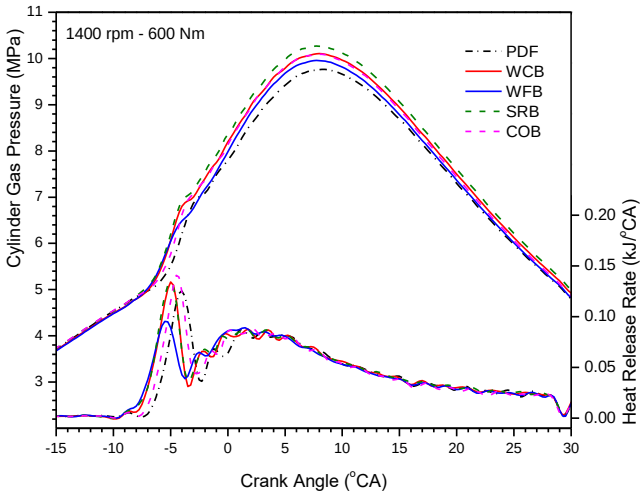

Figure 4. Cylinder gas pressure and heat release rates of test fuels

As given in Fig. 5, the maximum in-cylinder gas pressure (P_{max}) values of vegetable oil and animal fat-based biodiesel fuels were close to each other. Among the test fuels, the highest in-cylinder pressure of 10.27 MPa was attained with SRB fuel. The maximum gas pressures obtained with WCB and COB were almost the same. Similar results can be found in the literature [14]. When the HRR graphs were viewed it is seen that start of combustion timings of all biodiesel fuels were earlier compared with PDF and also relatively higher HRR values were attained with biodiesels.

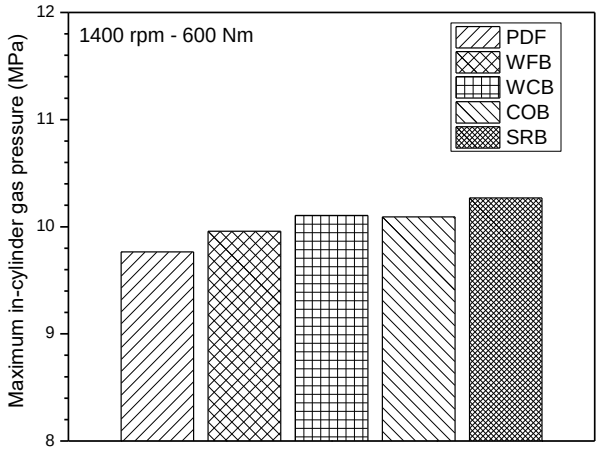

Figure 5. P_{max} values of test fuels

Test fuels' some critical fuel injection and combustion data that were obtained by analyzing the fuel-line pressures and HRR graphs can be seen in Table 4. When the results are examined, it is seen that the start of fuel injection timing of the test fuels was different from each other. The difference in the fuel properties of the test fuels caused the different fuel injection characteristics. The start of fuel injection of PDF retarded as compared to biodiesel fuels and the biggest difference of 2 crank angle (ºCA) was detected with SRB fuel. In the experimental study that was performed at full load, Monyem et al. [15] reported approximately 2 ºCA advanced start of fuel injection with biodiesel fuels relative to PDF. As can be understood from the Table, all biodiesel fuels started to burn at earlier crank angles than PDF. Cetane number is a critical indicator of self-ignitability of a fuel. According to the European diesel fuel standard (EN-590), the minimum cetane number has to be 51. Nevertheless, cetane number of LSD and ULSD fuel (euro-diesel) is higher than 55. Cetane number of PDF used in engine tests was 56.8. Except for WFB, PDF's cetane number was higher than those of biodiesel fuels (see Table 1). The comparatively higher saturated fatty acid content of WFO than the other biodiesels is the most important parameter increasing cetane number of this biodiesel fuels. The highest cold filter plugging point value (10 ºC) of WFB among the test fuels is another indicator of its high saturation level. Although cetane number of WFB was higher, its start of combustion was relatively later than SRB fuel. Despite SRB's less cetane number, it's the earlier start of injection and better volatility resulted in the earlier start of combustion.

Ignition delay (ID) can be defined as the time interval between the start of injection and the start of combustion [16]. The maximum difference among ID periods of the test fuels was measured between PDF and WCB. Although the start of combustion of WCB was earlier, its start of injection was about 2 ºCA earlier than PDF, leading to a longer ID period. The minimum ID value was detected for WFB, which had the maximum cetane number.

TABLE IV
FUEL INJECTION and COMBUSTION RESULTS

Parameter (ºCA)	PDF	SRB	COB	WCB	WFB
Start of Combustion (b TDC)	7.75	9.75	8.00	8.50	9.25
Start of Injection (b TDC)	11.25	13.25	11.50	13.00	12.25
Ignition Delay	3.50	3.50	3.50	4.50	3.00

3.3. Exhaust Emission Characteristics

Carbon monoxide (CO) is a colorless, odorless and highly toxic gas. When there is not enough oxygen in the combustion reaction in order to convert the carbon atoms into carbon dioxide, CO emission forms [17]. The most important parameter influencing CO emission is the fuel/air equivalence ratio. The importance of the other parameters that should be considered in terms of CO emission such as injection advance, the shape of the combustion chamber, etc. is less than that of the fuel/air equivalence ratio. Especially fuel-rich mixtures cause to increment in CO emission [18]. CO emission profiles of test fuels were given in Fig. 6. As can be seen, CO emission of PDF was higher than those of biodiesel fuels. The most critical parameter on the less CO emissions of biodiesel fuels is their oxygen contents. Biodiesel fuels have about 10% oxygen in their chemical structures. This extra oxygen coming from the fuel in the combustion media improves the combustion reaction, resulting in less CO emission. In addition, the advanced start of fuel injection timing and the higher fuel injection pressure that are attained with biodiesel fuels (see Fig. 3) are also

effective on their better CO emissions. Canakci and Gerpen [19] reported similar results with biodiesel fuels. When biodiesels are compared to each other, it is seen that CO emissions of vegetable oil-based biodiesel fuels were significantly less than those of animal fat-based biodiesels. WFB and WCB fuels' relatively higher viscosity and density values worsening the atomization quality may be influential on their high CO emissions.

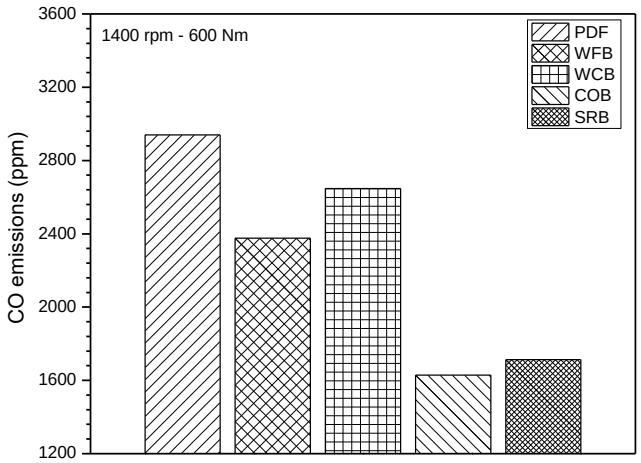

Figure 6. CO emission values of test fuels

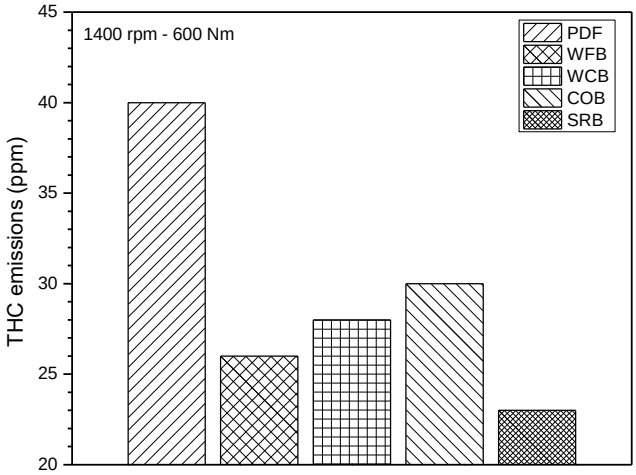

Figure 7. THC emission values of test fuels

Hydrocarbon emissions (HC) are the result of incomplete combustion and indicate unburned or partially burned fuel in the exhaust emission. Although HC emissions are incomplete combustion products like CO emissions, the parameters such as the chemical structure of the fuel, combustion chamber geometry (length of flame paths) and engine operating conditions are more critical for this emission type compared to air excess ratio. HC emissions from engines are generally divided into two different groups: Total Hydrocarbon (THC) emissions and non-methane Hydrocarbon emissions (NMHC) [20]. THC emissions of all test fuels were depicted in Fig. 7. THC emissions of biodiesel fuels were significantly lower than that of PDF. Despite biodiesel fuels' higher kinematic viscosity and density values deteriorating the fuel atomization quality and causing higher and heavier fuel droplets, their relatively lower THC emissions might be explained by the earlier fuel injection timing and the higher fuel injection pressures. In addition, biodiesel fuels' molecular oxygen content can also be considered for their lower THC emissions. Biodiesel fuels' THC emissions were close to each other. Among the biodiesel fuels, COB and SRB had the highest and the lowest THC emissions, respectively. Sanli [21] also detected lower THC emissions with biodiesel fuels compared to PDF.

Nitrogen Oxide (NO_x) emissions can be considered as the most critical one among diesel engine exhaust emissions. NO_x emissions occur with the reaction of oxygen and nitrogen at high temperatures (approximately 1800 K and higher degrees). A large part of NO_x emissions is composed of NO emissions, a small part is NO_2 emissions, and the remaining trace amount is other oxygen-nitrogen combinations. In-cylinder temperatures and pressures, air/fuel ratio, fuel's cetane number, combustion duration, the oxygen concentration in combustion media, fuel injection timing, and fuel injection pressure are the critical parameters in terms of NO_x emissions [22]. As can be seen in Fig. 8, all biodiesel fuels (regardless of its feedstock) caused higher NO_x emissions. As compared to PDF, the increase in NO_x emission was 4.7%, 7.7%, 9.9% and 11.2% for WFB, WCB, SRB and COB, respectively. The higher NO_x emissions of biodiesel fuels may be caused by their higher fuel injection pressures, the advanced start of fuel injection (see Fig.3), the higher in-cylinder pressures and heat release rates (see Fig. 4). In addition, the molecular oxygen contents of biodiesel fuels could also be effective on this result. Chen et al. [23] reported higher NO_x emissions with biodiesel fuels. Another issue that should be underlined in terms of NO_x emissions is that the NO_x emissions of animal fat-based biodiesels were lower than those of vegetable oil-based biodiesels. Both of WFB and WCB had better NO_x emissions than SRB and COB (on average 4% lower). Relatively higher in-cylinder pressure and HRR values of COB and SRB could be reasons for the higher NO_x emissions of these biodiesel fuels (see Fig. 4). Moreover, the higher cetane number of animal-fat based biodiesels could also be effective on their better NO_x emissions results. Wyatt et al. [24] also detected lower NO_x emissions with animal-fat based biodiesel fuels than vegetable oil-based biodiesels.

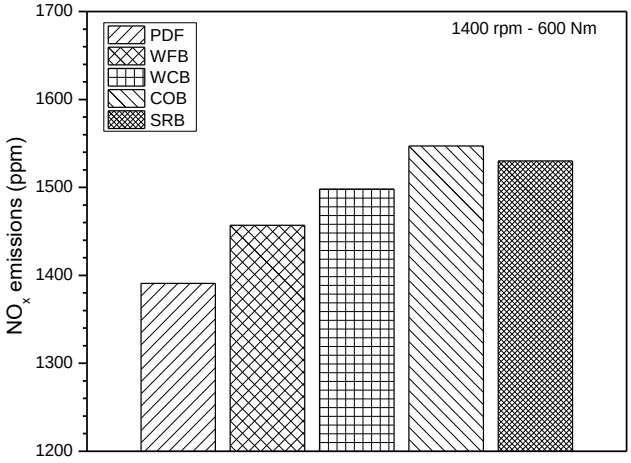

Figure 8. NOx emission values of test fuels

4. CONCLUSIONS

The use of alternative fuels in diesel vehicles is a critical issue in order to reduce harmful emissions released from these vehicles. Biodiesel is one of the important, environmentally friendly and sustainable alternative fuels. Although biodiesel can be produced from many different feedstocks, a very portion of industrial biodiesel production is obtained from vegetable oils. If biodiesel fuel is produced from different feedstocks, the unit price of biodiesel will be affected as well as the engine characteristics will be affected since the fuel properties will change. In this study, it was aimed to compare the effects of vegetable oil-based biodiesels and animal fat-based biodiesels on the performance, combustion, injection and exhaust emission characteristics of a TDI diesel engine. Petroleum-based diesel fuel was used as the reference fuel. Engine tests were conducted at the engine operating conditions of 1400 rpm and 600 Nm. BSFC values of all biodiesel fuels were higher than that of PDF. Animal fat-based and vegetable oil-based biodiesels had close BSFC values. Relatively higher in-cylinder pressures were attained with biodiesel fuels. Although there was no significant difference between them, the highest in-cylinder pressure was measured with SRB biodiesel. Fuel injection pressure was lower with PDF compared to all biodiesel fuels. Compared to PDF, the advanced start of fuel injection and the start of combustion timings were detected with all biodiesel fuels. When the biodiesels were compared each other, it was seen that the start of fuel injection timing of SRB and WCB fuels were almost the same and they was injected approximately 2 ºCA earlier than PDF. Regardless of the feedstock from which it is produced, CO and THC emissions of all biodiesel fuels were lower than PDF, but NO_x emissions were higher. The most significant difference between vegetable oil-based and animal fat- based biodiesels was seen in CO and NO_x emissions. SRB and COB fuels had lower CO emissions

REFERENCES

[1] F. Yasar, "Evaluation of renewable energy source algae as biodiesel feedstock," European Journal of Technique, vol. 9, no. 2, pp. 298-311, 2019.

[2] S. Aydin, "Thorough analysis of combustion and emissions of power generator diesel engine at high idling operations fueled with low percentage of biodiesel blends," European Journal of Technique, vol. 10, no. 1, pp. 184-195, 2020.

[3] S. B. Gok et al., "Fatty acid composition of Silybum Marianum L. seeds and antimicrobial activity of seed oil and silymarin extract," The Journal of Food, vol. 46, no. 1, pp. 110-118, 2021.

[4] C. C. Barrios et al. "Effects of animal fat based biodiesel on a TDI diesel engine performance, combustion characteristics and particulate number and size distribution," Fuel, vol. 117, pp. 618-623, 2014.

[5] S. A. Ahmed, et al., "Evaluation of animal fat based biodiesel blends and effects of exhaust gas recirculation on the suitable blend in single cylinder four stroke diesel engine," Energy Sources Part A: Recovery, Utilization, and Environmental Effects, to be published. DOI: 10.1080/15567036.2020.1862368.

[6] A. P. Sathiyagnanam, et al. "Biodiesel production from waste pork lard and experimental investigation of its use as an alternate fuel in a DI diesel engine," International Journal of Mechanical Engineering and Robotic Research, vol. 1, no. 3, pp. 176-191, 2012.

[7] E. Buyukkaya, "Effects of biodiesel on a DI diesel engine performance, emission and combustion characteristics," Fuel, vol. 89, no. 10, pp. 3099-3105, 2010.

[8] W. W. Pulkrabek, "Engineering fundamentals of the internal combustion engine," 1st ed, Pearson Publishing House, USA, 1997.

[9] J. B. Heywood, "Internal combustion engine fundamentals," 1st ed, McGraw Hill, USA, 1989.

[10] P. Richards, "Alternative Fuel Reference Book," 3rd ed, SAE International, USA, 2014.

[11] O. Armas, "Alternative method for bulk modulus estimation of diesel fuels," Fuel, vol. 167, pp. 199-207, 2016.

[12] M. Lapuerta et al., "Bulk modulus of compressibility of diesel/biodiesel/HVO blends," Energy Fuels, vol. 26, no. 2, pp. 1336-1343, 2012.

[13] H. Sanli, "An experimental investigation on the usage of waste frying oil-diesel fuel blends with low viscosity in a common rail DI-diesel engine, Fuel, vol. 222, pp. 434-443, 2018.

[14] E. Alptekin et al., "Combustion and performance evaluation of a common rail DI diesel engine fueled with ethyl and methyl esters," Applied Thermal Engineering, vol. 149, pp. 180-191, 2019.

[15] A. Monyem et al., "The effect of timing and oxidation on emissions from biodiesel-fueled engines," Transactions of the American Society of Agricultural Engineers, vol. 44, no. 1, pp. 35-42, 2001.

[16] P. A. Lakshminarayanan et al., "Ignition delay in a diesel engine, in: Modeling Diesel Combustion," Springer, USA, 2010.

[17] A. A. Abdel-Rahman, "On the emissions from internal combustion engines: a review," International Journal of Energy Research, vol. 22, no. 6, pp. 483-513, 1998.

[18] H. Sanli et al., "Effects of waste frying oil based methyl and ethyl ester biodiesel fuels on the performance, combustion and emission characteristics of a DI diesel engine," Fuel, vol. 159, pp. 179-187, 2015.

[19] M. Canakci, J. Van Gerpen, "Comparison of engine performance and emissions foe petroleum diesel fuel, yellow grease biodiesel, and soybean oil biodiesel," Transactions of the American Society of Agricultural Engineer, vol. 46, no. 4, pp. 937-944, 2003.

[20] M. Wang et al. "Ambient non-methane hydrocarbons (NMHCs) measurement in Boading, China: sources and roles in ozone formation," Atmosphere, vol. 11, no. 11, pp. 1-17, 2020.

[21] H. Sanli, "Influences of biodiesel fuels produced from highly degraded waste animal fats on the injection and emission characteristics of a CRDI diesel engine," International Journal of Automotive Engineering and Technologies, vol. 8, pp. 11-21, 2019.

[22] C. Sayin et al., "Influence of injection timing on the exhaust emissions of a dual-fuel CI engine," Renewable Energy, vol. 33, no. 6, pp. 1314-1323, 2008.

[23] H. Chen et al., "NOx emission of biodiesel compared to diesel: higher or lower?," Applied Thermal Engineering, vol. 137, pp. 584-593, 2018.

[24] W. T. Wyatt et al., "Fuel properties and nitrogen oxide emission levels of biodiesel produced from animal fats," Journal the American Oil Chemists' Society, vol. 82, pp. 585-591, 2005.

BIOGRAPHIES

Ertan Alptekin obtained his B.Sc. degree from Automotive Engineering Technology - Kocaeli University in 2004. He received his M.Sc. and Ph.D. degrees from the same university. In 2014, Dr. Alptekin started to work as an Assistant Professor in Kocaeli University. Currently, he has been working as an associate professor in the Department of Automotive Engineering in the same university. His research interests are biofuels, IC engines, combustion and engine tests.

Huseyin Sanli obtained his B.Sc. degree from Automotive Engineering Technology - Kocaeli University in 2001. He received his M.Sc. and Ph.D. degrees from the same university. In 2001, he worked as a lecturer in Golcuk Vocational School, Kocaeli University. Dr. Sanli had served as an assistant professor in Ford Otosan Ihsaniye Automotive Vocational School, Kocaeli University between 2015-2020. He currently works as an associate professor in Department of Automotive Technologies, Corlu Vocational School, Tekirdag Namik Kemal University. Dr Sanli's interest areas are biofuels, IC engines, combustion and engine tests.

Mustafa Canakci received his B.Sc. degree from Automotive Engineering Technology - Gazi University in 1989. He earned his M.Sc. and Ph.D. degrees from Vanderbilt University and Iowa State University in 1996 and 2001, respectively. After working as a Research Fellow in Engine Research Center (University of Wisconsin - Madison), he started to work as an Assistant Professor in Kocaeli University. Currently, Dr. Canakci has been working as a Professor in the Department of Automotive Engineering in the same university. His research areas are combustion, performance and emissions of IC engines, biodiesel production, alternative fuels and HCCI engines.

European Journal of Technique

journal homepage: https://dergipark.org.tr/en/pub/ejt

Vol.12, No.1, 2022

Investigation of Power Consumption in the Machining of S960QL Steel by Finite Elements Method

Rüstem Binali[1*], Süleyman Yaldız[2] and Süleyman Neşeli[3]

[1*]Selçuk University, Mechanical Engineering Department, Konya, Turkey. (e-mail: rustem.binali@selcuk.edu.tr).
[2] Selçuk University, Mechanical Engineering Department, Konya, Turkey. (e-mail: syaldiz@selcuk.edu.tr).
[3] Selçuk University, Mechanical Engineering Department, Konya, Turkey. (e-mail: sneseli@selcuk.edu.tr).

ARTICLE INFO

Received: Feb., 01. 2022
Revised: Mar., 22. 2022
Accepted: Mar., 28. 2022

Keywords:
Machinability
Structural steel
Power consumption
S960QL
Finite elements

Corresponding author: *Rüstem Binali*

ISSN: *2536-5010* | e-ISSN: *2536-5134*

DOI: https://doi.org/10.36222/ejt.1066472

ABSTRACT

Armor steels have good strength and corrosion resistance; however, due to their difficult machinability, high power consumption occurs. High power consumption increases the cost in machinability studies. Therefore, minimizing power consumption is important for sustainable and cleaner production. For the purpose of minimize power consumption in the course of machining, factors such as workpiece material, cutting tool material and geometry, machining conditions and cutting parameters must be compatible with each other. For this reason, power consumption modeling was carried out in the milling of S960QL structural steel material according to the finite elements method, depending on the cutting parameters. In this context, simulation processes were carried out at three levels for each factor: cutting speed, lateral depth, axial depth and feed rate. The most effective parameter in power consumption was the axial deep of cut. There was a 476% change between the highest and lowest power consumption. It is concluded that finite element modeling is feasible for the purpose of determine the effect of processing parameters on power consumption.

1. INTRODUCTION

The industry accounts for almost half of the energy consumption worldwide, and energy consumption is increasing day by day [1]. In addition, rapid growth in the manufacturing sector, global warming and local wastes pose many economic and social problems [2]. Therefore, besides product quality, energy efficiency has become important criteria in the manufacturing industry. Because machine tools in the manufacturing industry have less than 30% efficiency [3]. The environmental impacts that affect the efficiency of these machines are more than 99% [1]. Machine tools need power during stock removal, from production to machining, to sustain cutting tool and slide systems after machining. In the manufacturing industry, it usually includes machining operations such as milling, turning, drilling and grinding [4].

Milling is widely used to bring materials into desired shapes and sizes. It is necessary to reduce power consumption in metal removal processes in order for the processes to be sustainable [5]. Thus, environmental impacts due to energy consumption are reduced and product efficiency can be increased. Armor and structural steels are materials that are difficult to process due to their high ductility and strength. It is significant to determine the machinability parameters and to minimum the power consumption in machining operations. By improving the machining parameters such as an axial depth, lateral depth feed rate per tooth and cutting speed reducing the power consumption by reducing the cutting force can be directly regulated [4,6]. Most of the previous studies on milling seem to be on process outputs such as machining parameters such as surface roughness, tool wear and cutting force [7-10].

Recently, researchers have been carrying out studies on the power consumption of cutting parameters during machining [4,11,5,1]. The studies have been carried out with both physical and finite element methods and it has been stated that they are compatible with each other [12-15]. In his study, Bhushan used Response Surface Methodology analysis to define optimal machinability parameters when machining AA7075 SIC using tungsten carbide cutting tool to acquire max. tool life and min. power consumption. In his study, he stated that cutting speed is the most important parameter for tool life and consumption for power, followed by feed rate, nose radius and cutting depth [16]. Camposeco-Negrete (2013) tried to achieve optimization of machining parameters for energy consumption and surface roughness in the course of machining of AISI 6061T6 under roughing conditions using the Taguchi method. As a result of the research, he stated that the most important factor is the feed rate with an impact rate of 87.79% in order to minimum energy consumption [5]. Yan and Li (2013) submitted an optimization method based on RSM to optimize machinability parameters in

the milling process in the course of carbide tool dry machining of medium carbon steel to acquire min cutting energy and surface roughness. As a result of their studies, they reported that the most effective parameter is the lateral cutting depth [17]. Campatelli et al (2014) used the response surface methodology to analyze the effect of machining parameters on energy consumption in the course of milling of carbon steel. They reported that the ideal radial cutting depth and feed rate should be 1 mm and 0.12 mm/tooth, respectively, for the purpose of minimize the energy consumed for cutting efficiency [18]. El-Tamimi and El-Hossainy (2008), investigated the efficiency of machining parameters by turning AISI 420 steels. Mutual effect graphs were created to determine the most effective parameters. They stated that the most significant parameter on the major cutting force is the feed rate, and the more significant parameter on the consumption of power is the cutting speed [19]. Valiorgue et al. (2012) evaluated the estimation of residual stress variation in hard machining of AISI 304-L stainless steel. They created a mixed technique combining numerical and experiments work. They stated that the numerical model appeared to provide trustworthy results in proportion to the empirical results for a wide range of feed rates and cutting speeds [20]. Galanis et al. (2014) studied finite element (FE) modeling to predict cutting forces when machining AISI 316-L stainless steel. The empirical cutting force worths were compared with the numeral results and they concluded that they can be estimated with good correctness when machining with FE modeling [21]. Li et al. investigated the processing-induced surface plastic deformation and microstructural texture development of Ti-6Al-4V alloy by FEM simulation [22]. Budak and Ozlu stated that the developed FEM model can be used in industrial applications by applying the Johnson-Cook material model together with the slip and adhesion models in order to use the thermomechanical dual zone model in cutting processes [23].

As a result of the literature research, it has been determined that there is no study on the energy consumption of the S960QL material. In this study, the effects of machinability parameters on power consumption in the course of machining of S960QL structural steel material were analyzed using finite element modeling.

2. MATERIAL AND METHOD

In this research study carried out with the FE method, the effects of cutting parameters on power consumption were examined in finite element up milling of S960QL structural and armor steel material with TiAlN coated carbide cutting tools. The study was carried out with three-dimensional milling process. Three different cutting speeds, three different lateral depths, three different axial depths and three different feed per tooth were selected as machining parameters. These parameters have been established by considering the studies made for structural steels and the values recommended by KENNAMETAL. Cutting parameters are given in Table 1.

TABLE 1
CUTTING PARAMETERS.

Radial Deep of Cut	Axial Deep of Cut	Cutting Speed	Feed Rate
0.8-1.2-1.6 mm	4-6-8 mm	180-200-220 m/min	0.08-0.12-0.16 mm/tooth

2.1. Workpiece Material

The mechanical properties and percent chemical compositions of the S960QL material used in the study are given in Table 2.

TABLE 2
MECHANICAL PROPERTIES AND CHEMICAL COMPOSITION [24].

Chemical Composition (%)				
C	Mn	Si	S	P
0.20	1.60	0.50	0.010	0.020
Cr	Cu	Ni	Mo	B
0.80	0.3	2.0	0.70	0.005
Mechanical Properties				
Minimum yield strength $R_{p0.2}$ (MPa)				960
Minimum tensile strength R_m (MPa)				980-1150
Elongation A_5(min %)				12

The Johnson Cook (JC) material model which is required and widely used for simulations of machining processes, is given in Equation 1 [25].

$$\sigma^0=(A+B(\varepsilon^p)^n(1+C\ln\left(\frac{\dot{\varepsilon}^p}{\dot{\varepsilon}_0}\right))(1-(\frac{T-T_r}{T_m-T_r})^m) \quad (1)$$

Parameters in Equation 1;
A: yield stress at temperature of room
B: strain hardening
C: constant of the strain rate
n: exponent of deformation hardening
m: exponent of sensitivity of deformation rate

Other parameters in the equation are εp, $\dot{\varepsilon} p$, $\dot{\varepsilon}0$, Tm, Tr and T, respectively, equivalent plastic strain, rate of plastic strain, rate of reference strain, melting temperature of the material, temperature of room and reference temperature. The specified $\dot{\varepsilon}0$ and C are values generally measured at and/or beneath the reference temperature. JC model parameters of S960QL structural steel are given in Table 3.

TABLE 3
JC MODEL PARAMETERS FOR S960QL [26].

A (MPa)	1034
B (MPa)	828
n	0.6539
c	0.015045
m (400 °C)	1.028
m (550 °C)	1.277
m (average)	1.154

The Finite Element Modeling design used is given in Table 4.

2.2. Cutting Tool

Kennametal EDCT 10T308PDERLD grade KC725M and TiAlN coated inserts were used as cutting tools in 3D milling simulations. The cutting tool has a corner radius of 0.8, a thickness of 3.75 mm, a cutting-edge length of 12.05 mm and

an approach angle of 15^0. In order for the cutting tool to be used in the finite element program, its three-dimensional scan was made and modeled in the CATIA program, and its positioning on the material is given in Figure 1.

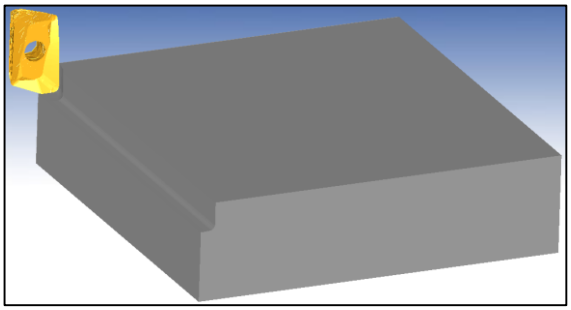

Figure 1. 3D model of Finite element.

TABLE 4
MACHINING PARAMETERS LEVELS.

Radial Deep of Cut	Axial Deep of Cut	Cutting speed	Feed Rate
1	1	1	1
1	2	2	2
1	3	3	3
2	1	2	3
2	2	3	1
2	3	1	2
3	1	3	2
3	2	1	3
3	3	2	1

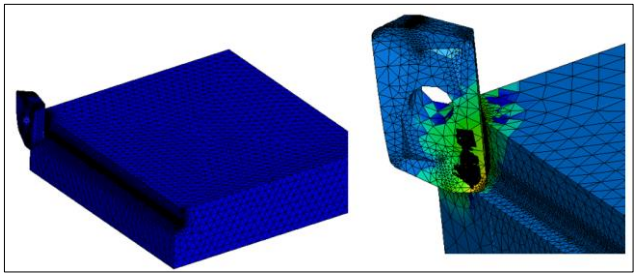

Figure 2. Cutting scheme and mesh structure for simulations.

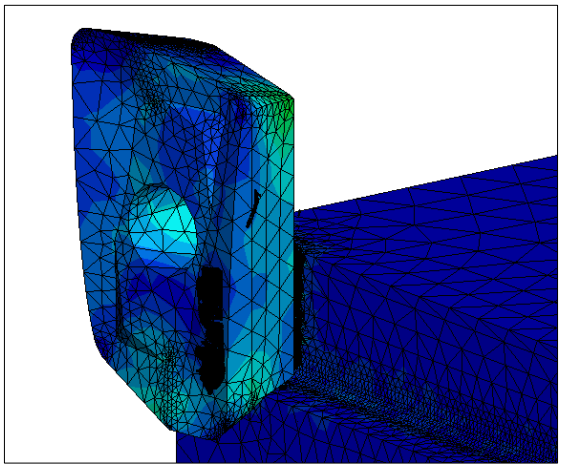

Figure 3. The stresses occurring at the tooltip.

2.3. Finite Element Simulations

The effects of processing parameters on power consumption were investigated with finite element modeling. The finite element program for machinability experiments uses an discretionary Lagrangian solver and has adaptable remeshing functionality to acquire more precise results though it takes more time. The length, width and height of the workpiece model used in the first stage of the simulations are 50, 50 and 10 mm respectively, and all simulations were carried out with these dimensions. The second step is to define the geometry of tool and tool material parameters. In the last step, after the meshing parameters and friction coefficient are set, necessary machining simulation parameters like cutting speed, lateral and axial depth and feed rate are entered into the software.

For 3D simulations, the interface friction coefficient between the workpiece and the cutting tool is modeled with a standard Coulomb friction of 0.5. Corner milling (cutting edge) and same-directional milling were selected in the simulation processes. A tetrahedral mesh type was used by choosing 0.01 mm as the element size.

For the effects of machinability parameters on power consumption, the workpiece material was cut 90^0 with a 16 mm tool diameter in the FE simulations. After the machining process, numerical results were obtained on the finite element model. Simulation model, mesh structure and cutting diagram for 3D simulations are given in Figure 2. In addition, images of stresses occurring at the tool tip are given in Figure 3.

3. RESULT AND EVALUATION

In this research study, simulations of 3D milling with FE method were made based on machining parameters. The results were obtained by defining the friction coefficient as 0.5 and the mesh dimensions as 0.1 mm. In the 3D milling simulations, the power consumption (P) was calculated by considering the resultant values of the forces F_x, F_y, F_z. The power consumption values calculated by multiplying the resultant cutting force and cutting speed were made with the formula in equation 2. This formula is generally used in machining processes [6,4,27].

$$P = Fx\frac{V}{60} \tag{2}$$

Parameters in Equation 1;
P: Power (w)
V: Cutting speed (m/min.)
F: Force (N)

The resultant V in Equation 2 ($\sqrt{F_x^2 + F_y^2 + F_z^2}$) is the cutting speed and F is the cutting force. We can express the cutting speed equations in detail as follows.

$$V = \frac{\pi xDxN}{1000} \tag{3}$$

Parameters in Equation 3;
V: Cutting speed (m/min.)
N: Spindle speed (rpm)
D: Tool diameter (mm)

The power values measured in physical experiments are based on measuring the magnetic field and voltage around the transmission cable [28]. However, it is measured with the package program used in the finite element method. A graphical example of the simulation result obtained from the finite element software is given in Figure 3. The simulated results for P and F are acquired from Figure 3 taking on the average value of a given interval. In general, it is known that with increasing feed rate and lateral and axial cutting depth, all

the cutting force components and power consumption increase [4,29].

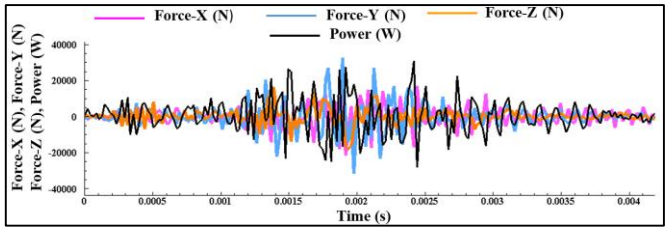

Figure 3. Graphical view of the simulation result.

3.1. Power Consumption

The changes in power consumption accordingly the processing parameters are given in Figure 4. It has been concluded that the increase in feed rate, lateral and axial cutting depth and cutting speed increase the power consumption in general.

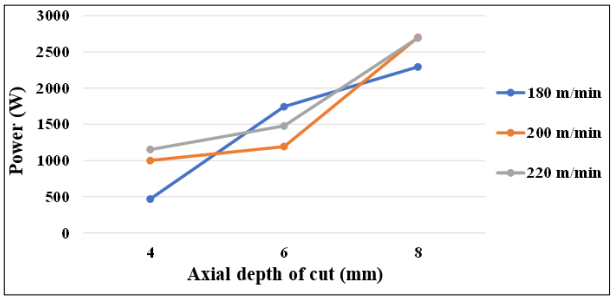

Figure 4. Power consumption variation graph based on axial depth and cutting speed.

By examining the graph based on axial depth and cutting speed, an increase in power consumption occurs with an increase in axial force and cutting speed in general. However, with each increase in cutting speeds, a fluctuating change has occurred in power consumption, not a parallel increase. In this case, fluctuating results may occur because the milling cutting mechanics process is different [30]. According to Figure 4, the highest power consumption (2700.299 W) occurred at a cutting speed of 200 m/min and an axial depth of 8 mm. The lowest power consumption (468.893 W) occurred at 180 m/min cutting speed and 4 mm axial depth. There was a 476% change between the highest and lowest power consumption.

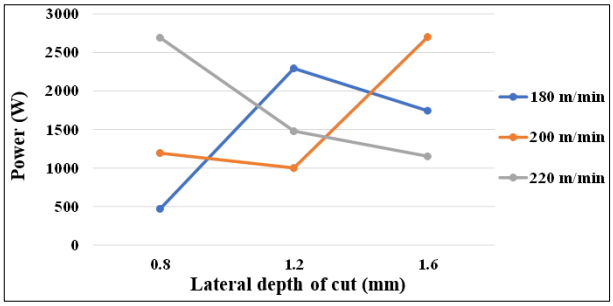

Figure 5. Power consumption variation graph based on lateral depth and cutting speed.

As a result of examining the effect of lateral depth and cutting speed in Figure 5, the highest power consumption occurred at a cutting speed of 1.6 mm lateral depth and 200 m/min. The lowest value was 0.8 mm lateral depth and 180 m/min cutting speed. The highest change occurred with the increase of lateral depth from 0.8 mm to 1.2 mm at 180 m/min cutting speed with 389%. The lowest power consumption change occurred with an increase of lateral depth from 0.8 mm to 1.2 mm at 200 m/min cutting speed with a 19% change.

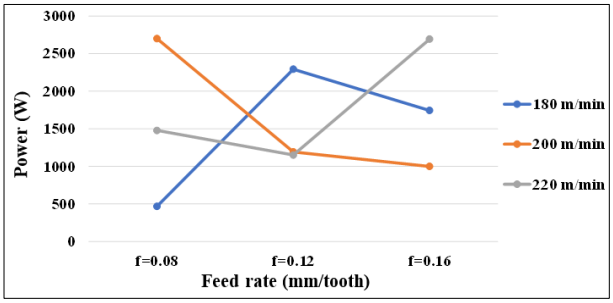

Figure 6. Power consumption variation graph based on feed rate and cutting speed.

By examining the graph in Figure 6, depending on the cutting speed and feed rate the highest power consumption value occurred at 0.08 mm/tooth feed rate and 200m/min cutting speed. The lowest power consumption value was observed at a cutting speed of 180 m/min and a feed rate of 0.08 mm/tooth. The highest rate of change between the parameters occurred in the increase from 0.08 mm/tooth advance to 0.12 mm/tooth advance amount. The lowest rate of change occurred in the increase from 0.12 mm/tooth advance to 0.16 mm/tooth advance amount. Generally speaking, an increase in power consumption is expected with an increase in the amount of feed [4]. However, in milling mechanics, it is acceptable to result in such a result, since the multi-toothed tools and the cutting edge are different from the single-edged tools.

Taguchi analysis was performed to determine the parameters that significantly affect the power consumption in the simulation results. In order to find the optimum points of the processing parameters used in the study, the S/N ratios were determined by taking into account the smaller-the-better quality characteristic objective function (Table 5) [31,32].

TABLE 5
AVERAGE S/N RESPONSE FOR THE POWER CONSUMPTION.

Level	Radial Deep of Cut (mm)	Axial Deep of Cut	Cutting Speed (m/min.)	Feed Rate (mm/tooth)
1	-61.19	-58.22	-61.82	-61.82
2	-63.54	-63.26	-63.39	-63.33
3	-64.90	-68.15	-64.41	-64.48
Delta	3.71	9.93	2.59	2.66
Rank	2	1	4	3

According to the average smallest best S/N values found in Table 4, the values with the highest Delta levels specified for each level have the greatest effect on power consumption. Impact rankings in the tables are expressed with "rank". Thus, it has been determined that the most effective parameter in power consumption is axial depth. In addition, it was concluded that the lateral depth of cut 1, the axial depth of cut 1, the cutting speed 1 and the feed per tooth 1 level for the optimum power consumption value. Finally, it was concluded that

minimum cutting speed, lateral and axial cutting depth and feed rate should be used for less power consumption and therefore an environmentally friendly environment.

The graph of the S/N ratio responses for power consumption is given in Figure 7. The maximum points of the slopes in the figure give information about the efficiency levels of the processing parameters.

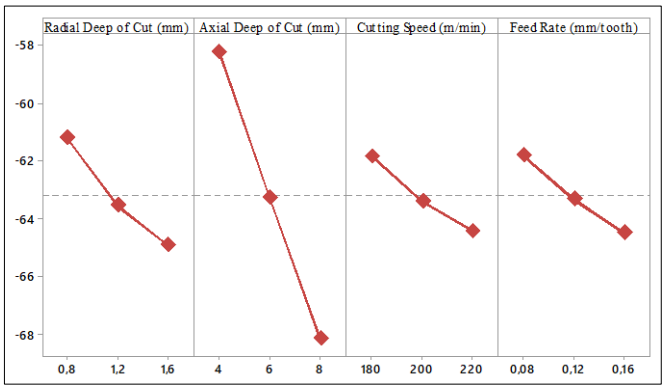

Figure 7. S/N chart for power consumption.

4. CONCLUSION AND SUGGESTIONS

In this study, the finite element method was used to increase the machinability of S960QL structural steel. Similar studies were previously an investigated by Bouzid et al. [29] and Korkmaz et al. [4] with finite element modeling and mathematical modeling to estimate the power consumption of processing parameters. In addition, a similar study was conducted by Günay et al. [33]. The summary of the work done is given below.

The power consumption increased with increasing cutting depth.

The highest power consumption (2700.299 W) occurred at an axial depth of 8 mm and a cutting speed of 200 m/min.

The lowest power consumption (468.893 W) occurred at an axial depth of 4 mm and a cutting speed of 180 m/min.

According to Taguchi analysis, it was concluded that the most effective parameter in power consumption is axial depth, and the parameter with the lowest effect is cutting speed.

It is concluded that lower power consumption can be achieved by optimizing the processing parameters.

It has been concluded that the processing parameters can be used for the estimation of power consumption with the finite element method.

The finite element method can be used to determine the machinability parameters of structural steels and materials with difficult machinability at the optimum level and to make the machining industry sustainable.

Comparisons can be made with experimental studies.

This study will contribute to the studies to be carried out with the finite element method.

ACKNOWLEDGEMENT

This study was supported by Selcuk University Scientific Research Projects Unit as a PhD thesis project. Project Number: 20111014.

REFERENCES

[1] Kant, G. and Sangwan, K. S., Prediction and optimization of machining parameters for minimizing power consumption and surface roughness in machining, *Journal of Cleaner Production*, (2014), 83 pp. 151-164.

[2] Sangwan, K. S., Development of a multi criteria decision model for justification of green manufacturing systems, *Int. J. Green. Econ.*, (2011), no. 5, pp. 285-305.

[3] He, Y., Liu, B., Zhang, X., Gao, H. and Liu, H., A modeling method of task-oriented energy consumption for machining manufacturing system, *J. Clean. Prod.*, 23, (2012), pp. 167-174.

[4] Korkmaz, M. E. and Günay, M., Finite Element Modelling of Cutting Forces and Power Consumption, *Arabian Journal for Science and Engineering*, 43, (2018), pp. 4863-4870.

[5] Composeco-Negrete, C., Optimization of cutting parameters for minimizing energy consumption in turning of AISI 6061 T6 using Taguchi methodology and ANOVA, *J. Clean. Prod.*, 53, (2013), pp. 195-203.

[6] Black, J. T. and Kohser, R. A., DeGarmo's Materials and Processes in Manufacturing, 11th edition, *John Wiley&Sons*, Hoboken, 2013.

[7] Coşkun, M., Çiftçi, İ. and Demir, H., AISI P20S Kalıp Çeliğinin İşlenebilirliğinin İncelenmesi, *İmalat Teknolojileri ve Uygulamaları*, 2, (2021), 2, pp. 1-9.

[8] Uzun, M., Usca, Ü. A., Kuntoğlu, M. and Gupta, M. K., Influence of tool path strategies on machining time, tool wear, and surface roughness during milling of AISI X210Cr12 steel, *The International Journal of Advanced Manufacturing Technology*, (2022), pp. 1-12.

[9] Usca, Ü. A., Uzun, M., Sap, S., Kuntoğlu, M., Giasin, K., Pimenov, D. Y. and Wjciechwski, S., Tool wear, surface roughness, cutting temperature and chips morphology evaluation of Al/TiN coated carbide cutting tools in milling of Cu-B-CrC based ceramic matrix composites, *Journal of Materials Research and Technology*, 16, (2022), pp. 1243-1259.

[10] Haddag, B., Atlati, S., Nouari, M. and Moufki, A., Dry machining aeronautical aluminum alloy AA2024-T351: Analysis of cutting forces, chip segmentation and built-up edge formation, *Metals*, 6, (2016), 9, p. 197.

[11] Aggarwal, A., Singh, H., Kumar, P. and Singh, M., Optimizing power consumption for CNC turned parts using response surface methodology and Taguchi's techniqueda comparative analysis, *J. Mater. Process. Technol.*, 200, (2008), pp. 373-384.

[12] Daoud, M., Chatelain, J. F. and Bouzid, A., Effect of rake angle-based Johnson-Cook material constants on the prediction of residual stresses and temperatures induced in Al2024-T3 machining. *International Journal of Mechanical Sciences*, 122, (2017), pp. 392-404.

[13] Umbrello, D., M'saoubi, R. and Outeiro, J. C., The influence of Johnson–Cook material constants on finite element simulation of machining of AISI 316L steel. International Journal of Machine Tools and Manufacture, 47(3-4), (2017), pp. 462-470.

[14] Jain, A., Khanna, N. and Bajpai, V., FE simulation of machining of Ti-54M titanium alloy for industry relevant outcomes. Measurement, 129, (2016), pp. 268-276.

[15] Bouderbala, K. and Nouira, H., FEM and experimental investigation of the thermal drift in ultra-high precision measuring machines for dimensional metrology. Measurement, 90, (2016), pp. 250-264.

[16] Bhushan, R. H., Optimization of cutting parameters for minimizing power consumption and maximizing tool life during machining of Al alloy SiC particle composites, *J. Clean. Prod.*, 39, (2013), pp. 242-254.

[17] Yan, J. and Li, L., Multi-objective optimization of milling parameters e the trade tradeoffs between energy, production rate and cutting quality, *J. Clean. Prod.*, 52, (2013), pp. 462-471.

[18] Campatelli, G., Lorenzini, L. and Scippa, A., Optimization of process parameters using a Response Surface Method for minimizing power consumption in the milling of carbon steel, *Journal of Cleaner Production*, 66, (2014), pp. 309-316.

[19] El-Tamimi, A. M. and El-Hossainy, T. M., Investigating the machinability of AISI 420 stainless steel using factorial design, *Mater. Manuf. Process.*, 23, (2008), 4, pp. 419-426.

[20] Valiorgue, F., Rech, J., Hamdi, H., Gilles, P. and Bergheau, J. M., 3D modeling of residual stresses induced in finish turning of an AISI304L stainless steel, *Int. J. Mach. Tool. Manuf.*, 53, (2012), 1, pp. 77-90.

[21] Galanis, N. I. and Manolakos, D. E., Finite element analysis of the cutting forces in turning of femoral heads from AISI 316L stainless steel, *In: Proceedings of theWorld Congress on Engineering 2014*, London, 2014.

[22] Li, A., Pang, J., Zhao, J., Zang, J. and Wang, F., FEM-simulation of machining induced surface plastic deformation and microstructural

texture evolution of Ti-6Al-4V alloy. International Journal of Mechanical Sciences, 123, (2017), pp. 214-223.

[23] Budak, E. and Ozlu, E., Development of a thermomechanical cutting process model for machining process simulations. CIRP annals, 57(1), (2008), pp. 97-100.

[24] https://www.ssab.com.tr/products/brands/strenx/products/str enx-960-e-f

[25] Johnson, G. J. and Cook, W. H., A constitutive model and data for metals subjected to large strains, high strain rates and high temperatures, *In: Proceedings of the Seventh International Symposium on Ballistics*, The Hague, 1983.

[26] Cadoni, E. and Forni, D., Mechanical behaviour of a very-high strength steel (S960QL) under extreme conditions of high strain rates and elevated temperatures, *Fire Safety Journal*, (2019), pp. 1-14.

[27] Eren, N., Hayat, F. and Günay, M., Sertleştirilmiş 1.2367 Takım Çeliğinin İşlenmesinde Enerji Tüketiminin Analizi ve Modellenmesi, *İmalat Teknolojileri ve Uygulamaları,* 1, (2020), 3, pp. 41-49.

[28] Aslan, A., Tornalamada Akustik Emisyon ve Motor Akımı Optimizasyonu ve Analizi. Avrupa Bilim ve Teknoloji Dergisi, (25), (2021), pp. 50-57.

[29] Bouzid, L., Yallase, M. A., Chaoui, K., Mabrouki, T. and Boulanouar, L., "Mathematical modeling for turning on AISI 420 stainless steel using surface response methodology," *Proc. IMechE Part B J. Eng. Manuf.*, 229, (2015), 1, pp. 45-61.

[30] Binali, R., Sıcak iş takkım çeliğinin (TOOLOX 44) işlenebilirliğinin incelenmesi, MSc. Thesis, *Karabük Üniversitesi Fen Bilimleri Enstitüsü,* Karabük, 2017.

[31] Neşeli, S., Tırlama titreşimleri üzerine süreç sönümleme etkisinin analitik olarak araştırılması ve tornalamada kararlı kesme derinliği ile süreç sönümleme değerlerine bağlı parametre optimizasyonu, PhD. Thesis, *Selçuk Üniversitesi Fen Bilimleri Enstitüsü,* Konya, 2013.

[32] Vidal, C., Infante, V. and Vilaca, P., "Assessment of Improvement Techniques Effect on Fatigue Behaviour of Friction Stir Welded Aerospace Aluminium Alloys," *Procedia Engineering*, 2, (2010), pp. 1605-1616.

[33] Günay, M., Korkmaz, M. E. and Yaşar, N., Finite element modeling of tool stresses on ceramic tools in hard turning. Mechanics, 23(3), (2017), pp. 432-440.

BIOGRAPHIES

Rüstem Binali obtained his undergraduate degree from Karabuk University (KBÜ) Manufacturing Engineering Department in 2014. He received his master's degree from the same university, Department of Manufacturing Engineering, Institute of Science and Technology, Department of Manufacturing Engineering in 2017. He is continuing his doctorate education at Selçuk University Mechanical Engineering Department. He works in the fields of machining, machine tools, finite element method, CAD/CAM/CAE. Recently, he focused on machinability studies with the finite element method. In 2018, he was appointed as a Research Assistant to the Department of Mechanical Engineering, Faculty of Technology, Selcuk University.And he is still working at Selcuk University.

Süleyman Yaldız obtained his undergraduate education from Gazi University (GU) Machine Education Department in 1979. He received his master's degree from Selçuk University, Department of Agricultural Machinery in 1990. He received his Ph.D. from Selçuk University Mechanical Engineering Department in 1996. He works in the fields of Production Technologies, Computer Aided Design, Machine Design and Machine Elements. He started his academic life at Selçuk University in 1986 and retired in 2021.

Süleyman Neşeli obtained his undergraduate degree from Gazi University (GU) Mechanical Education Department in 2002. He received his master's degree from Selcuk University, Department of Mechanical Education in 2006. He received his Ph.D. from Selçuk University Mechanical Engineering Department in 2013. He works in Manufacturing Technologies, Computer Aided Design, Machine Design and Machine Elements, CAD/CAM/CAE, experimental design and optimization. He started his academic life at Selcuk University in 2002 and is still working as Prof. Dr. continues his academic career.

European Journal of Technique

journal homepage: https://dergipark.org.tr/en/pub/ejt

Vol.12, No.1, 2022

Variations in the Concentration of Air Pollutants due to the COVID-19 Lockdown in Istanbul, Turkey

Aytac Perihan AKAN

Hacettepe University, Environmental Engineering Department, 06800, Çankaya, Ankara, Turkey. (e-mail: apakan@hacettepe.edu.tr).

ARTICLE INFO

Received: Feb., 15. 2022
Revised: Mar., 04. 2022
Accepted: May, 04. 2022

Keywords:
Air Pollution
COVID-19
Lockdown
Air Pollutants
Greenhouse Gas Emissions

Corresponding author: *A.P. Akan*

ISSN: *2536-5010* | e-ISSN: *2536-5134*

DOI: https://doi.org/10.36222/ejt.1073950

ABSTRACT

Countries have implemented partial or full quarantine practices to reduce the effects of the COVID-19 pandemic, which severely affects the whole world and controls the increase in cases and deaths. Studies have observed improvements in air pollution due to reducing emissions from traffic and industrial processes during lockdown periods. In this study, the effects of quarantine activities on air quality in the pre-COVID-19 period and during the COVID-19 pandemic, both in 2020 and 2021, were examined through the data obtained from the air quality monitoring stations located in the three districts with the highest traffic density in Istanbul, the most populated city of Turkey.

Based on the findings obtained from the study, it can be concluded that lockdown applications contributed to the reduction of air pollution in the examined regions. In addition, another finding is that there is a positive correlation between air quality parameters. It is expected that the results of the study will lead the decision-makers in the areas of dissemination of renewable energy systems instead of energy generation from coal-fired power plants and the widespread use of electric vehicles instead of diesel-fueled vehicles for many countries that have committed to net-zero carbon emissions within the scope of the Paris Agreement and the European Green Deal.

1. INTRODUCTION

It is well known that the SARS-CoV-2 virus, which was first recorded in Wuhan, China, in December 2019, quickly spread to other countries and was declared a pandemic by the World Health Organization (WHO) on March 11, 2020 [1-2].
Due to the rapidly peaking number of cases, many countries have started implementing restrictive measures such as curfew at certain time intervals to prevent the increase in the number of cases [1]. Globally, as of February 01, 2022, there have been 376.478.335 confirmed cases of COVID-19, including 5.666.064 deaths, reported to WHO. As of January 30, 2022, a total of 9.901.135.980 vaccine doses have been administered [3]. The first case in Turkey was recorded on March 11, 2020, and the first death occurred on March 17, 2020. By February 01, 2022, the total number of cases and deaths reached 10,808,770 and 85,600 [4]. Turkey began to take many measures to prevent the increase in confirmed cases. The first measure started with the suspension of all flights from China on February 05, 2020. After that, on March 16, 2020, face-to-face education was suspended in primary and secondary schools and universities, and online education was started. The first curfew was imposed on citizens over 65 years of age and those with chronic diseases on March 22, 2020. Between April 11 and April 19, 2020, a curfew was imposed in Zonguldak and 30 major cities on weekends. In addition, a wider curfew was introduced during the official holidays of April 23 and May 01, and 23-26 April and 01-03 May 2020 were declared as quarantine periods. In addition, a curfew was implemented in 15 provinces between 8-10 May and 15-19 May 2020, while a curfew was implemented in all provinces of Turkey on 22-26 May 2020. The lockdowns imposed in 2021 were as follows: A 2-week partial lockdown was implemented starting from 19.00 on April 14, 2021. A curfew was imposed between 19.00 and 05.00 on weekdays and covered the entire weekend. A full lockdown had been announced until 05:00 on May 17, effective from 19:00 on April 29, 2021 [5]. With the implementation of the curfew, it is possible to reduce emissions from traffic and industrial facilities.

Air pollution, which occurs depending on natural (i.e., volcanic eruptions) and anthropogenic drivers (i.e., greenhouse gases caused by traffic emissions, industrial activities, such as the burning of fossil fuels in power plants and during the production of cement), is of severe significance on public health as one of the most important environmental issues, regionally or globally. Air pollutants are classified as sulfur dioxide (SO_2), carbon monoxide (CO), nitrogen dioxide

(NO_2), ozone (O_3), lead (Pb), and particulate matter (PM) by Environmental Protection Agency [6].

Studies in the literature focus on the effects of quarantine practices on air pollution. Most studies have revealed that lockdown applied partially or fully positively impacts declining air pollution [7-9]. Some studies examining the effects of quarantine measures on air quality are presented below.

Ali Sahraei et al. (2021) [1] investigated the improvements in air quality in Turkey's Istanbul and Ankara provinces based on the limitation in public transportation usage. Due to lockdown measures from January to May 2020, the improvements were estimated at 9% and 47% for Ankara and Istanbul. Gao et al. (2021) [10] investigated the impact of changes in human activities on air quality during the COVID-19 pandemic by determining the relationships between air quality, traffic volume, and meteorological conditions based on lockdown activities, considering megacities of China, such as Wuhan, Beijing, Shanghai, and Guangzhou for the period January–May between 2016 and 2020. Following the results obtained from the present work, the change rates of $PM_{2.5}$, NO_2, and SO_2 before and during the lockdown in the four megacities showed diversities from −55.4% to 78.2% because of meteorological conditions of provinces. Gautam et al. (2021) [11] investigated the air quality index (AQI) of Delhi (DTU, Okhla and Patparganj), Haryana (Jind, Palwal and Hisar), and Uttar Pradesh (Agra, Kanpur and Greater Noida) from February 17, 2020, to May 4, 2020, including lockdown period started from April 25, 2020, by the Government of India. Results suggested that AQI has improved by up to 30–46.67% after lockdown. Goren et al. (2021) [12] investigated the impacts of lockdown on the air quality of 11 cities, looking at concentrations of air quality parameters containing $PM_{2.5}$, PM_{10}, SO_2, NO_2, NO, NO_x, O_3 and CO obtained from 51 air quality measurement stations (AQMS) from March – April period of 2020 compared with that of the previous year. While $PM_{2.5}$ and PM_{10} concentrations were not significantly affected, NO, NO_2 and NO_X concentrations were decreased, SO_2 did not show a significant change. Hu et al. (2021) [13] assessed air quality by looking at the variations in the concentration of air pollutants and air quality index in China (Wuhan), Japan (Tokyo), the Republic of Korea (Daegu), and India (Mumbai) during and after lockdowns. The results indicated that air pollution levels were positively correlated with reducing pollutant levels during and after lockdowns in these cities. Moreover, the lockdown policy generally reduced air pollution, which is more significant for regions with high air pollution levels. Sahoo et al. (2021) [14] investigated the changes in air quality, comparing the COVID-19 pandemic periods, including the lockdown and unlock period (post-lockdown) with pre-lockdown in the state of Maharashtra, the worst-hit state in India. Results demonstrated that atmospheric pollutants such as $PM_{2.5}$, PM_{10}, NO_x, and CO were substantially reduced during the lockdown and unlock phases, with the greatest reduction in cities having larger traffic volumes. Compared with the immediate pre-lockdown period, the average $PM_{2.5}$ and PM_{10} were reduced by 51% and 47%, respectively, during the lockdown periods, resulting in a 'satisfactory' air quality index level (AQI) a result of reduced vehicular traffic and industrial closing. Shakoor et al. (2020) [15] investigated the impacts of lockdown on the environmental pollutants (CO, NO_2, SO_2, $PM_{2.5}$ and PM_{10}) with (the year 2020) and without (the year 2019) the lockdown period in the majorly hit states and provinces of the USA and China, respectively. The results showed that the overall concentrations of CO, NO_2 and $PM_{2.5}$ were decreased by 19.28%, 36.7% and 1.10%, respectively, while PM_{10} and SO_2 were increased by 27.81% and 3.81%, respectively, in five selected states of the USA during the lockdown period. However, in the case of chosen provinces of China, overall, the concentrations of all selected pollutants, i.e., CO, NO_2, SO_2, $PM_{2.5}$ and PM_{10}, were reduced by 26.53%, 38.98%, 18.36%, 17.78% and 37.85%, respectively. Shehzad et al. (2020) [16] investigated the variation in the air pollution in India to demonstrate the impacts of COVID-19 lockdown from January 2020 to April 2020 using data from European Space Agency (ESA) and Central Pollution Control Board (CPCB) online portal. Results illustrated that the air quality of Indian territory improved significantly during COVID-19. NO_2 concentration showed a substantial decrease in Mumbai and Delhi, which are among the most populated cities in India.

Within the scope of this study, the changes in air quality parameters containing PM_{10}, SO_2, CO, NO_2 and O_3 based on full and partial lockdowns implemented in Istanbul in 2020 and 2021 were examined using data obtained from Air Quality Monitoring (AQM) stations installed in Aksaray, Beşiktaş and Kadıköy districts, where the traffic density is high almost every hour of the day in Istanbul, the most crowded city of Turkey, for April and July of 2019, 2020 and 2021. The difference of the present study from the previous works conducted for the province of Istanbul in the literature is that it covers the lockdown period imposed in 2021 and compares the quarantine process applied in two different periods (years 2020 and 2021).

2. METHODS

2.1. Description of the regions

The present work examined variations in the air quality of the Istanbul province of Turkey using data from AQM stations located in three different zones with different population densities. Locations of AQM stations examined in the present work are presented in Figure 1. Stations in Aksaray and Beşiktaş are located on the European side of Istanbul, and Kadıköy is located on the Asia continent. The general information about locations is presented in Table 1.

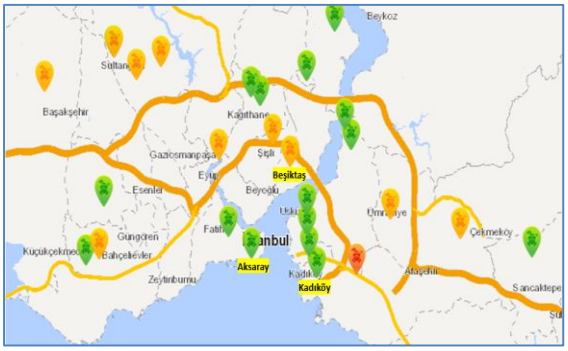

Figure 1. Locations of Air Quality Monitoring Stations (Adopted from National Air Quality Monitoring Network, Republic of Turkey, Ministry of Environment, Urbanization and Climate Change, NAQMN, 2022) [17].

TABLE I
THE PROPERTIES OF AQM STATIONS

AQM Stations	Latitude	Longitude	Population
Aksaray	28.9547	41.0147	382.990
Beşiktaş	29.0100	41.0538	178.938
Kadıköy	29.0336	40.9919	485.233

2.2. Data collection

The present work examined variations in the air quality of Istanbul province of Turkey for pre-and during the COVID-19 pandemic period using data obtained from Air Quality Monitoring Stations under the Ministry of Environment, Urbanization and Climate Change [17].

2.3. Statistical Analysis

To evaluate the interactions of air quality parameters statistically, Pearson's rank correlation tests were used as empirical methodologies by the Statistics Software IBM SPSS® version 23. The value of 0.05 was considered the significance level.

3. RESULTS AND DISCUSSION

3.1. Variations in the concentration of air pollutants

Sources of air pollutants, such as sulfur dioxide (SO_2), nitrogen oxides (NO_x), carbon monoxide (CO), volatile organic compounds (VOCs), and particulate matter (PM), vary widely. In this context, burning fuels for road transport and electricity generation is particularly important. Pollutants directly released into the atmosphere are called primary pollutants, while some pollutants that are chemically reacted with other pollutants in the air are known as secondary pollutants. The major sources of SO_2 and CO are the combustion of fossil fuels containing sulfur and carbon, particularly from power stations burning coal and vehicles. The pathways for NOx formation are lightning, forest fires and microbial activities in the soil [18]. Vehicle emissions and gas stoves are the major sources of most outdoor and indoor NO_2. Moreover, the precursors of ozone are produced by vehicle emissions, industrial processes, chemical solvents, and natural sources [19]. Studies in the literature have depicted improvements in air pollution due to the reductions in the activities of sectors that contribute significantly to greenhouse gas emissions, such as roads and airlines, due to the restrictions during the pandemic. The results obtained differ according to countries, cities and even districts [20-21]. Ekici et al. (2021) [20] investigated the concentration values of air pollutants caused by commercial air transport in Turkey regarding quarantine applications of the COVID-19 pandemic period accepted from March to August 2020 compared with starting from January 2017. The monthly pollutant amount showed remarkable declines during the pandemic due to reducing domestic flights and international traffics. Ghahremanloo et al. (2021) [21] investigated the air pollution levels comparing pre-lockdown and lockdown periods (between February 2019 and February 2020) based on the COVID-19 outbreak in East Asia, including Beijing-Tianjin-Hebei (BTH), Wuhan, Seoul, and Tokyo regions using data from the Sentinel-5P and the Himawari-8 satellites to examine concentrations of NO_2, HCHO, SO_2, and CO, and the aerosol optical depth (AOD). Results showed that the greatest reductions in pollutants occurred in Wuhan, with a decrease of almost 83%, 11%, 71%, and 4% in the column densities of NO_2, HCHO, SO_2, and CO, respectively, and a decrease of about 62% in the AOD. With large reductions in the concentrations of NO_2 during lockdown situations, they suggested that significant increases in surface ozone in East China from February 2019 to February 2020 are likely the result of less reaction of NO and O_3 caused by significantly reduced NO_X concentrations and less NO_X saturation in East China during the daytime. Within the scope of this study, how the decrease in the use of public transportation, the reduction in the working load of industrial facilities and the decline in traffic density affect the air pollution due to partial and full-time lockdowns based on the COVID-19 outbreak were determined considering the year 2019 before the pandemic. Statistical values, including minimum, maximum and average concentration values of air pollutants, including PM_{10}, SO_2, CO, NO_2 and O_3 obtained from three AQM stations located in Istanbul for years between 2019 and 2021, including only three months (April 01 – July 01) showing the lockdown periods in 2020 and 2021 were presented in Table 2.

TABLE II
STATISTICAL VALUES OF AIR POLLUTANTS BETWEEN APRIL 01 AND JULY 01, 2019-2021 IN AQM STATIONS

Period		Air Quality Monitoring Stations								
		Aksaray			Beşiktaş			Kadıköy		
April – July 2019		Min	Max	Mean	Min	Max	Mean	Min	Max	Mean
Air Quality Parameters (μgm^{-3})	PM_{10}	22.6	101	46.7±16.2	14.1	82.7	36.3±13.1	11.9	81.6	33.7±14.1
	SO_2	0.89	14.3	3.68±2.67	1.09	16.5	4.12±3.18	1.07	12.6	3.41±2.35
	CO	2.74	947	440±142	145	905	433±118	119	954	470±130
	NO_2	71.0	158	112±18.8	41.9	127	74.5±21.9	26.2	87.5	49.5±13.8
	O_3	7.04	65.7	25.8±15.1	8.90	63.9	30.4±13.5	8.20	52.7	29.3±10.8
April – July 2020										
Air Quality Parameters (μgm^{-3})	PM_{10}	16.5	83.9	36.4±12.9	11.7	55.9	27.0±9.81	6.19	86.3	29.2±17.8
	SO_2	0.83	5.25	2.42±0.93	0.93	12.3	3.77±2.27	2.04	9.14	4.52±1.45
	CO	133	876	409±160	78.5	1066	297±168	187	983	564±191
	NO_2	24.0	150	88.2±30.9	8.96	105	53.2±24.1	42.0	199	83.9±23.1
	O_3	9.73	66.9	35.9±15.0	7.22	53	24.7±12.1	6.40	40.6	18.4±7.46
April – July 2021										
Air Quality Parameters (μgm^{-3})	PM_{10}	14.1	100	36.6±15.8	10.1	70.5	27.5±11.6	7.87	80.1	26.7±13.9
	SO_2	1.39	12.1	4.67±1.89	0.67	15.2	4.94±2.84	0.82	8.62	2.99±1.28
	CO	58.4	1016	454±160	235	899	517±109	37.9	659	219±181
	NO_2	31.7	299	186±61.6	10.1	62.3	32.0±11.0	24.5	97.3	56.5±17.8
	O_3	2.28	40.6	16.6±9.19	1.23	46.8	11.4±10.1	6.54	32.4	23.1±5.18

Although Istanbul's Aksaray, Beşiktaş, and Kadıköy districts differ in terms of air quality, it can be expressed by looking at the decrease in the average concentrations of CO, NO_2 and O_3 pollutants that the quarantine practices covering the year 2020 contributed to the improvement of the air quality, especially in Beşiktaş. According to Table 1, it can be concluded that the district with a more effective improvement in air quality in 2021 is Kadıköy. Normalized concentrations of air pollutants

based on pre-COVID-19 and COVID-19 periods for AQM stations examined in the present work are demonstrated in Figure 2.

To better understand the impact of lockdown applications on air quality improvements, variations in the concentration of air pollutants were also presented in Table 3. When Figure 2 and Table 3 are evaluated together, a decrease was observed in the concentrations of all pollutants except for the O_3 parameter for the Aksaray district with the lockdown effect applied in 2020, while there was a decrease in only the O_3 concentration in 2021. For the Beşiktaş district, it is seen that the quarantine implemented in 2020 improved the air quality in all parameters, and there was a decrease in NO_2 and O_3 concentrations in 2021. As for the district of Kadıköy, it is noticed that quarantine practices in 2020 caused a decline in PM_{10} and O_3 concentration, and in 2021, lockdown had a better influence on air pollution.

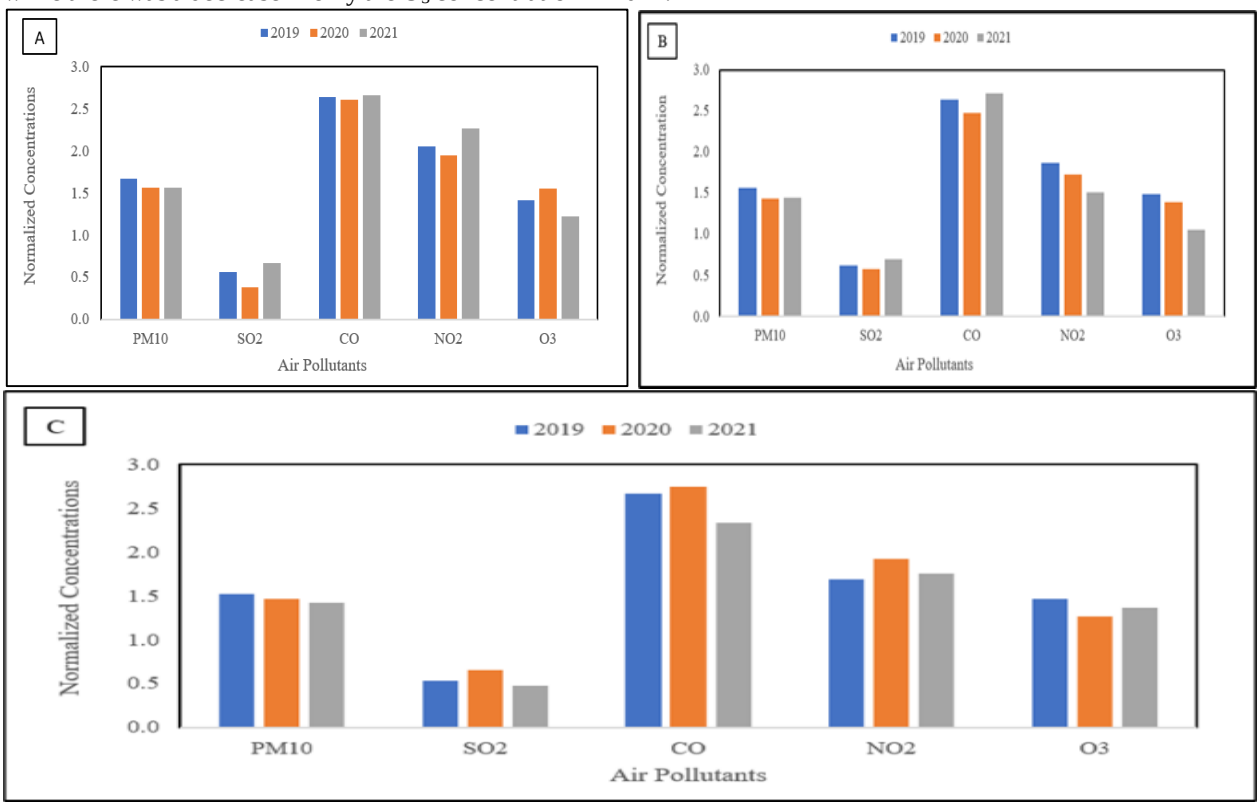

Figure 2. Normalized Concentrations of Air Pollutants based on pre-COVID-19 and COVID-19 Period for Three AQM Stations, in which A stands for Aksaray, B is Beşiktaş and C represents Kadıköy. The pre-COVID-19 period stands for 2019, and the COVID-19 period represents 2020 and 2021.

TABLE III
VARIATIONS IN THE CONCENTRATION OF AIR POLLUTANTS BETWEEN PRE-COVID-19 AND COVID-19 PERIOD

Pollutants	Variations (µg/m^3)								
	Aksaray			Beşiktaş			Kadıköy		
	2019-2020	2020-2021	2019-2021	2019-2020	2020-2021	2019-2021	2019-2020	2020-2021	2019-2021
PM_{10}	-10.3	0.20	-10.1	-9.30	0.50	-8.80	-4.50	-2.50	-7.00
SO_2	-1.26	2.25	0.99	-0.35	1.17	0.82	1.10	-1.53	-0.42
CO	-31.0	45.0	14.0	-136	220	84.0	94.0	-345	-251
NO_2	-23.8	97.8	74.0	-21.3	-21.2	-42.5	34.4	-27.4	7.00
O_3	10.1	-19.3	-9.20	-5.70	-13.3	-19.0	-10.9	13.2	-24.1

It can be said that the results of the present study are consistent with those of previous studies. Baysan et al. (2021) [5] compared average values of air quality parameters, including particulate matter (PM_{10}), sulfur dioxide (SO_2), carbon monoxide (CO), nitrogen dioxide (NO_2), and ozone (O_3) values in March, April, and May between 2017 and 2020 and their activity data in the same months of 2020 when Turkey applied the strict measures to prevent the fast increase in the confirmed cases of 31 cities consisting of 30 metropolitan cities and Zonguldak. Results showed that during the lockdown period, the PM_{10} and NO_2 levels decreased from 47.6 µg/m^3 to 38.1 µg/m^3 and from 54.8 µg/m^3 to 25.7 µg/m^3, respectively, compared with the 3-month average parameters of the previous 3 years. Celik- Gul (2021) [22] investigated how the concentration values of the air quality parameters consisting of particulate matter (PM_{10}), sulfur dioxide (SO_2), carbon monoxide (CO), nitrogen dioxide (NO_2), nitrogen oxide (NO), nitrogen oxides (NO_x), and ozone (O_3) concentrations obtained from 19 air monitoring stations (AMSs) in Istanbul, the most affected city with more than half of Turkey's cases change with lockdown applications. Results indicated a clear decline in

PM_{10}, NO_2, NO, and NOx concentration levels during the pandemic compared to the normal times in Istanbul.

Ozbay and Koc (2021) [23] investigated the variations in air pollution during the COVID-19 pandemic lockdown period (March–June 2020) for an industrialized city of Turkey, Izmit using data from four different air quality monitoring stations. Results showed that the lockdown period reduced pollution levels in urban, industrialized, and rural areas.

The current study presents the variations as percentages in the air pollutants between 2019 and 2021 in Figure 3. When compared to the 3-month average values of the previous year, in 2020 in the Aksaray district, the pollutant SO_2 showed a maximum decrease with a decrease from 3.68 µg/m^3 to 2.42 µg/m^3. According to the quarantine process implemented in 2021, when the concentration values are compared with the previous two years, the maximum decrease was observed in O_3, which decreased from 25.8 µg/m^3 to 16.6 µg/m^3 in a ratio of 55.4%.

In Beşiktaş, when the concentration of pollutants during the first lockdown applications of the COVID-19 was compared to the 3-month average values of the previous year, it was observed that the concentrations of CO, NO_2, PM_{10}, O_3 and SO_2 pollutants decreased by 46, 40, 34, 23 and 9 %, respectively. In 2021, the highest reduction in the concentration of pollutants was observed in O_3 (62.5 %), followed by NO_2 (57%) and PM_{10} (32%). As for the Kadıköy district, only O_3(59 %) and PM_{10} (15%) showed a decrease in their concentration in 2020 compared to the previous year.

Considering the comparison of values between 2019 and 2021, the maximum decline was observed in O_3 (82 %), similar to Beşiktaş province, followed by CO (53 %), PM_{10} (26 %) and SO_2 (14 %). As a result, the pollutant, which was observed with the highest reduction in its concentration during the first lockdown implementation compared to the pre-COVID-19 period, was determined as O_3 with a ratio of 59 %; similarly, in 2021, O_3 showed the maximum reduction in its concentration compared with others. Moreover, results obtained from the current study pointed out that Aksaray, Beşiktaş and Kadıköy demonstrated the highest decline in SO_2, CO and O_3, respectively, during the first period of lockdown applications.

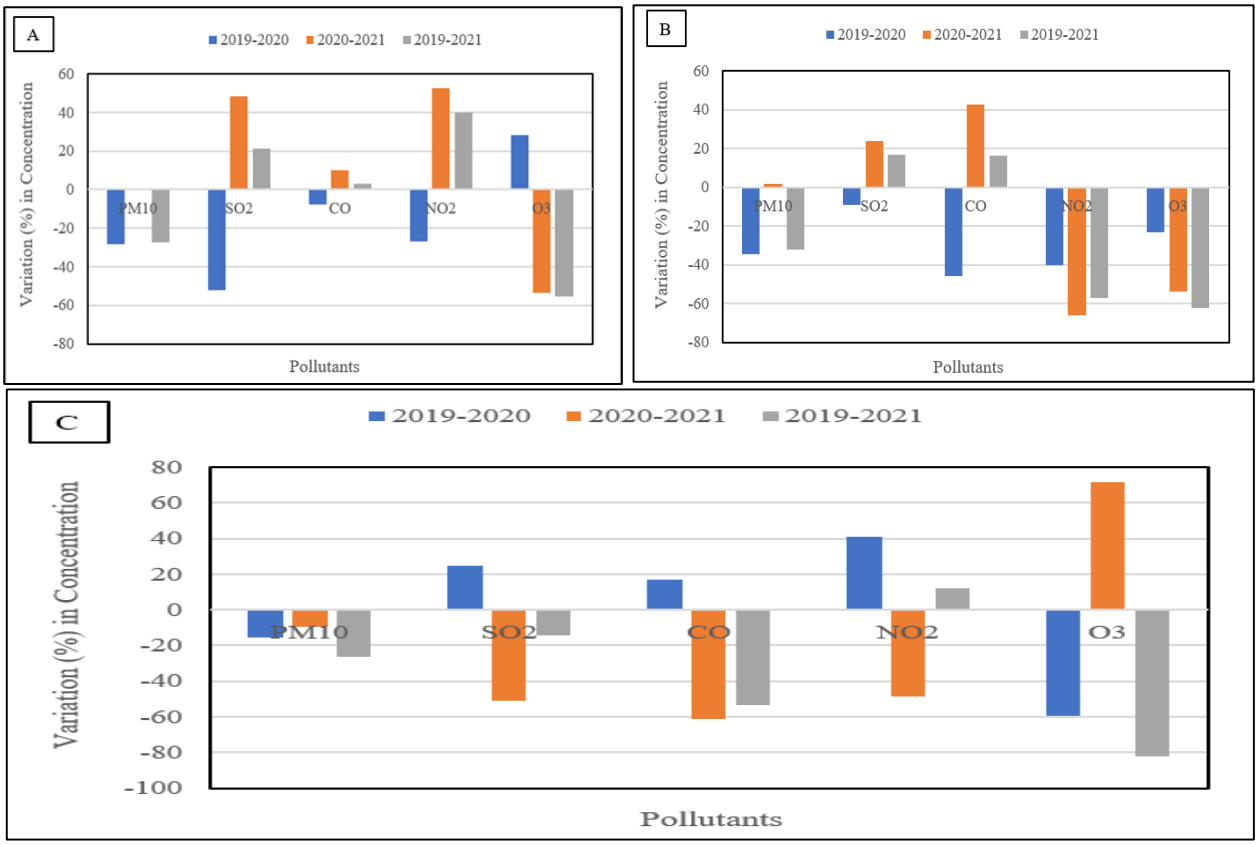

Figure 3. Variations of Air Pollutants as Percentage based on pre-COVID-19 and COVID-19 Period for Three AQM Stations, in which A stands for Aksaray, B is Beşiktaş, and C represents Kadıköy.

Similar results showing the decline in the concentration of air pollutants depending on lockdown measures were also reported in the previous works [7,24-25]. Dabbour et al. (2021) [7] compared concentration levels of air pollutants containing PM_{10}, CO, NO_2 and SO_2 pollution in the three largest cities of Jordan, including Amman, Irbid and Zarqa, over the period from March 15 to June 30 during the years from 2016 to 2020 using a paired sample t-test to determine the impacts of the reduced traffic due to mandated business closures during the pandemic period. Results indicated that Zarqa had the highest decline in SO_2 and NO_2 concentration during the lockdown period. The maximum reductions in Irbid city were in CO and PM_{10} concentrations. Kumari et al. (2020) [24] investigated the impact of lockdown on air pollutants levels in 39 different cities of India (including 10 Indian cities considered among the world's 20 most polluted cities), comparing the pollutants levels from 24th March-31st May in 2020 with the same period in 2019. After implementing lockdown measures, air pollution decreased. The most significant reduction was observed for nitrogen dioxide (NO_2) (3– 79%) and carbon monoxide (CO) (2–61%). The maximum reduction observed in PM_{10} and $PM_{2.5}$ was 58 and 57%, respectively, during the lockdown period in 2020 compared to the previous year. Orak and Ozdemir (2021)

[25] investigated the impact of lockdown measures on air quality parameters, including PM_{10} and SO_2, in 81 cities in Turkey. They found that PM_{10} and SO_2 concentrations were lower in 67% and 59% of the cities, respectively, in April 2020 compared to the previous five years (2015–2019).

3.2. Correlations between air pollutants

When Table 4 is examined, it can be said that there is a positive relationship between parameters in all districts. Therefore, it can be thought that an increase in the concentration of one of the parameters increases the concentration of the other parameter, or vice versa, that a decrease in the concentration of one parameter causes a reduction in the concentration of the other parameter.

TABLE IIII
CORRELATIONS BETWEEN AIR POLLUTANTS FROM DIFFERENT AQM STATIONS

AQM Stations	Correlated Parameters	Pearson's Correlation Coefficient	P-value
Aksaray	PM_{10}-SO_2	0.086	0.94
	PM_{10}-CO	0.23	0.85
	PM_{10}-NO_2	0.27	0.83
	PM_{10}-O_3	0.04	0.97
	SO_2-CO	0.98	0.09
	SO_2-NO_2	0.94	0.23
	SO_2-O_3	0.99	0.02
	CO-NO_2	0.88	0.32
	CO-O_3	0.98	0.12
	NO_2-O_3	0.95	0.20
Beşiktaş	PM_{10}-SO_2	0.18	0.89
	PM_{10}-CO	0.18	0.88
	PM_{10}-NO_2	0.84	0.36
	PM_{10}-O_3	0.70	0.51
	SO_2-CO	0.93	0.23
	SO_2-NO_2	0.68	0.52
	SO_2-O_3	0.83	0.38
	CO-NO_2	0.38	0.75
	CO-O_3	0.58	0.61
	NO_2-O_3	0.97	0.15
Kadıköy	PM_{10}-SO_2	0.11	0.93
	PM_{10}-CO	0.58	0.61
	PM_{10}-NO_2	0.35	0.77
	PM_{10}-O_3	0.69	0.51
	SO_2-CO	0.87	0.33
	SO_2-NO_2	0.89	0.29
	SO_2-O_3	0.64	0.55
	CO-NO_2	0.56	0.62
	CO-O_3	0.19	0.88
	NO_2-O_3	0.92	0.26

In the Aksaray district, the degree of the strongest relations between the parameters can be listed as follows: SO_2-O_3 > SO_2-CO = CO-NO_2 > NO_2-O_3 > SO_2-NO_2. In Beşiktaş, this order is as follows: NO_2-O_3 > SO_2-CO > PM_{10}-NO_2 > SO_2-O_3. In Kadıköy, the strongest correlation between parameters was observed between NO_2-O_3, followed by SO_2-NO_2 and SO_2-CO parameters. When the statistical significance of the relations between the parameters for these three districts is evaluated, it can be said that there is a statistically significant positive and very strong association between only SO_2-O_3 in the Aksaray district.

As a result, it can be expressed that the restrictions during the quarantine period made a positive contribution to the fight against air pollution in Istanbul, similar to the previous studies for different countries and regions. El Kenawy et al. (2021) [9] investigated the percentage changes in the concentration of air pollutants during the COVID-19 lockdown period in 21 metropolitan areas in the Middle East. The results indicated considerable reductions in the levels of atmospheric pollutants, particularly NO_2, SO_2, and CO. Air quality improved significantly during the middle phases of the lockdown (April and May), especially in small metropolitan cities like Amman, Beirut, and Jeddah, while it was less significant in megacities like Cairo, Tehran, and Istanbul. Fu et al. (2020) [26] investigated the effects of the COVID-19 pandemic lockdown on the air quality of 20 major cities on six continents, evaluating Air Quality Index (AQI) to estimate the change in air quality. The results showed that AQI in NO_2, SO_2, CO, $PM_{2.5}$ and PM_{10} in most cities was significantly reduced because of decreasing transportation, industry and commercial activities during the lockdown.

The associations between the parameters resulting from the decrease or increase in air pollution are vital to evaluate variations in the concentration of pollutants. In this regard, the Pearson correlation test was used to determine how the interaction of air pollutants affects air pollution. The results from correlations between the concentration of air pollutants taken from AQM stations located in three different districts of Istanbul are presented in Table 4.

By contrast, the changes of AQI in ground-level O_3 were not significant in most cities, as meteorological variability and ratio of VOC/NO_x are key factors in ground-level O_3 formation. Dursun et al. (2021) [8] investigated the impacts of COVID-19 measures on the improvements of air quality in Turkey, evaluating daily means of air pollutants including PM_{10}, $PM_{2.5}$, NO_2, CO, O_3, and SO_2 in 29 metropolitan cities and the province of Zonguldak for two periods: a period before the COVID-19 measures between January 1 and March 15, 2020, and the period in which the measures were in force between March 16 and April 15. Results suggested that the measures taken during the pandemic period significantly improved the air quality of provinces.

Alharbi et al. (2022) [27] investigated the changes in the concentrations of air pollutants (NO, NO_2, NO_x, SO_2, CO, O_3, PM_{10}, and $PM_{2.5}$) at three sites with different traffic loads (work, residential, and traffic sites) before, during, and after the COVID-19 lockdown applied in Riyadh City which is the capital of Saudi Arabia. Results indicated that the average concentrations of NO, NO_2, NO_x and CO decreased during the lockdown period by 73%, 44%, 53%, and 32% at the work site; 222%, 85%, 100%, and 60% at the residential site; and 133%, 60%, 101%, and 103% at the traffic site relative to the pre-lockdown period, respectively. The average concentration of O_3 increased by 6% at the worksite, whereas the concentration of SO2 increased by 27% at the residential site and decreased by 6.5% at the worksite.

Bhatti et al. (2022) [28] investigated the change in air pollution by analyzing AQI, six ambient air pollutants, including NO_2, O_3, SO_2, CO, PM_{10} and $PM_{2.5}$ for three periods: pre-COVID (from January 1 to May 30, 2019), active COVID (from January 1 to May 30, 2020) and post-COVID (from January 1 to May 30, 2021) in the Jiangsu province of China. Results exhibited that the mean change $PM_{2.5}$ from pre-COVID to active COVID decreased by 18%; post-COVID, it has only decreased by 2%. PM_{10} decreased by 19% from pre-COVID to active COVID, but post-COVID pollutant concentration has seen a 23% increase.

4. CONCLUSION

It is a well-known fact that vehicle emissions and industrial processes are the major sources of air pollutants. During the lockdown period of COVID-19, greenhouse gas emissions caused by traffic and industrial plants demonstrated a declining trend as expected. In this respect, the values of air pollutant concentrations obtained from the air quality monitoring stations in the regions with the highest workload and traffic density in Istanbul, the most populated city in Turkey, were compared with the values of the previous year in the quarantine periods, and the statistical changes in the concentrations were tried to be explained within the scope of this study.

According to the study results, the pollutant that showed the highest decrease in its concentration in 2020 compared to the previous year was observed in Ozone concentration in Kadıköy. According to the evaluations based on districts, the pollutants showing the maximum decrease in 2020 compared to 2019 were SO_2 in Aksaray district, CO in Beşiktaş district and O_3, as stated before in Kadıköy. When this comparison is made for the period between April 01 and July 01 in 2020 and 2021, when quarantine applications are made, O_3 was the pollutant with the maximum decrease in both Aksaray and Beşiktaş districts, while CO showed the maximum reduction in Kadıköy. Finally, when 2019, which was the pre-pandemic period, as compared with 2021, which did not exist in previous studies and which revealed the novelty of this study, and between April 01 and July 01, which includes quarantine practices, the pollutant showing the maximum decrease did not change in all districts and became O_3. Another result obtained from the study is that the interaction of the parameters directly affects their concentrations. According to the correlation results, it was determined that there was a statistically positive relationship between only SO_2 and O_3 parameters in the Aksaray district.

As can be understood from the results of this study, the reduction of traffic-related emissions and the reduction of greenhouse gases originating from industrial facilities are of great importance in air pollution control. In particular, supporting users by governments with initiatives such as tax reductions in the usage of electric vehicles instead of diesel-fueled those, expanding the use of renewable energy instead of electricity generation from coal-fired thermal power plants, giving importance to energy efficiency in buildings and workplaces, and providing thermal insulation in buildings should be considered and implemented by decision-makers as measures to cope with increasing air pollution in the cities.

REFERENCES

[1] M. A. Sahraei, E. Kuşkapan, and M. Y. Çodur, "Impact of COVID-19 on public transportation usage and ambient air quality in Turkey," Traffic and Environment (Ecology), vol. 33, no. 2, pp. 171-191, Dec. 2020

[2] Y. Yao, J. Pan, W. Wang, Z. Liu, H. Kan, Y. Qui, X, Meng, W. Wang, "Association of particular matter pollution and case fatality rate of COVID-19 in 49 Chinese cities," Science of The Total Environment, vol. 741 no. 140396, Nov. 2020.

[3] WHO, 2022, World Health Organization, https://covid19.who.int/.

[4] COVID-19, 2022, Information about COVID-19 cases from the Republic of Turkey Ministry of Health. https://covid19.saglik.gov.tr/,

[5] C. Baysan, S. Palanbek Yavaş, M. Çöl, "Change in air pollutants and human mobility trends during COVID-19 lockdown measures in Turkey," The Anatolian Journal of Family Medicine, vol. 4 no. 2, pp. 170-177, Aug. 2021.

[6] M. F. Sari, Y. Tasdemir, F. Esen, "Major air pollutants in Bursa, Turkey: their levels, temporal changes, interactions, and sources," Environmental Forensics, vol. 20, no. 2, pp. 182-195, Apr. 2019.

[7] L. Dabbour, E. Abdelhafez, M. Hamdan, "Effect of climatology parameters on air pollution during COVID-19 pandemic in Jordan," Environmental Research, vol. 202, no. 111742, July 2021.

[8] S. Dursun, M. Sagdic, H. Toros, "The impact of COVID-19 measures on air quality in Turkey," Environmental Forensics, to be published. DOI: 10.1080/15275922.2021.1892876.

[9] A. M. El Kenawy, J. I. Lopez-Moreno, M. F. McCabe, F. Domínguez-Castro, D. Peña-Angulo, I. M. Gaber, A. S. Alqasemi, K. M. Al Kindi, T. Al-Awadhi, M. E. Hereher, S. M. Robaa, N. Al Nasiri, S. M. Vicente-Serrano, "The impact of COVID-19 lockdowns on surface urban heat island changes and air-quality improvements across 21 major cities in the Middle East," Environmental Pollution, vol. 288, no. 117802, July 2021.

[10] C. Gao, S. Li, M. Liu, F. Zhang, V. Achal, Y. Tu, S. Zhang, C. Cai, "Impact of the COVID-19 pandemic on air pollution in Chinese megacities from the perspective of traffic volume and meteorological factors," Science of The Total Environment, vol. 773, no. 145545, Feb2021.

[11] A. S. Gautam, N. K. Dilwaliya, A. Srivastava, S. Kumar, K. Bauddh, D. Siingh, M. A. Shah, K. Singh, S. Gautam, "Temporary reduction in air pollution due to anthropogenic activity switch-of during COVID-19 lockdown in northern parts of India," Environment, Development and Sustainability, vol. 23, pp. 8774-8797, 2021.

[12] A. Y. Goren, M. Genisoglu, H. E. Okten, S. C. Sofuoglu, "Effect of COVID-19 pandemic on ambient air quality and excess risk of particulate matter in Turkey," Environmental Challenges, vol. 5, no. 100239, Aug 2021.

[13] M. Hu, Z. Chen, H. Cui, T. Wang, C. Zhang, K. Yun, "Air pollution and critical air pollutant assessment during and after COVID-19 lockdowns: Evidence from pandemic hotspots in China, the Republic of Korea, Japan, and India," Atmospheric Pollution Research, vol. 12, pp. 316-329, 2021.

[14] P. K. Sahoo, S. Mangla, A. K. Pathak, G. N. Salãmao, D. Sarkar, "Pre-to-post lockdown impact on air quality and the role of environmental factors in spreading the COVID-19 cases - a study from a worst-hit state of India," International Journal of Biometeorology, vol. 65, pp. 205-222, 2021.

[15] A. Shakoor, X. Chen, T. H. Farooq, U. Shahzad, Ashraf, F., Rehman, A., N. E. Sahar, W. Yan, "Fluctuations in environmental pollutants and air quality during the lockdown in the USA and China: two sides of COVID-19 pandemic", vol. 13, pp. 1335-1342, Aug 2020.

[16] K. Shehzad, M. Sarfraz, S. G. M. Shah, "The impact of COVID-19 as a necessary evil on air pollution in India during the lockdown," Environmental Pollution, vol. 266, no. 115080, June 2020.

[17] NAQMN, 2022, National Air Quality Monitoring Network, Republic of Turkey, Ministry of Environment, Urbanization and Climate Change), https://www.havaizleme.gov.tr/.

[18] C. Holman, "Sources of Air Pollution," in Air Pollution and Health, S. T. Holgate, H. S. Koren, J. M. Samet, R. L. Maynard, Ed. Academic Press, 1999, pp. 115-148.

[19] J. Ciencewicki, I. Jaspers, "Air pollution and respiratory viral infection," Inhalation Toxicology, vol.19, pp. 1135–1146, 2007.

[20] S. Ekici, Y. Şöhret, H. Gürbüz, "Influence of COVID-19 on air pollution caused by commercial flights in Turkey," Energy Sources, Part A: Recovery, Utilization, and Environmental Effects, to be published. DOI: 10.1080/15567036.2021.1906358.

[21] M. Ghahremanloo, Y. Lops, Y. Choi, S. Mousavinezhad, "Impact of the COVID-19 outbreak on air pollution levels in East Asia," Science of The Total Environment, vol. 754, no. 142226, 2021.

[22] E. Celik, M. Gul, "How Covid-19 pandemic and partial lockdown decisions affect air quality of a city? The case of Istanbul, Turkey," Environment, Development and Sustainability, to be published. DOI: 10.1007/s10668-021-01328-w.

[23] B. Ozbay, Y. Koc, "Impact of Covid-19 lockdown period on variations of air pollutants around an industrialized city of Turkey, Izmit," Environmental Forensics, to be published. DOI: 10.1080/15275922.2021.1892882.

[24] S. Kumari, A. Lakhani, K. M. Kumari, "COVID-19 and Air Pollution in Indian Cities: World's Most Polluted Cities," Aerosol and Air Quality Research, vol. 20, pp. 2592-2603, 2020.

[25] N. H. Orak, O. Ozdemir, "The impacts of COVID-19 lockdown on PM_{10} and SO_2 concentrations and association with human mobility across Turkey," vol. 197, no. 111018, March 2021.

[26] F. Fu, K. L. Purvis-Roberts, B. Williams, "Impact of the COVID-19 Pandemic Lockdown on Air Pollution in 20 Major Cities around the World," Atmosphere, vol. 11, no. 1189, pp. 1-18, 2020.

[27] B. H. Alharbi, H. A. Alhazmi, Z. M. Aldhafeeri, "Air Quality of Work, Residential, and Traffic Areas during the COVID-19 Lockdown with Insights to Improve Air Quality", International Journal of Environmental Research and Public Health, vol. 19(2), pp. 727, 2022. https://doi.org/10.3390/ijerph19020727

[28] U. A. Bhatti, Z. Zeeshan, M. M. Nizamani, S. Bazai, Z. Yu, L. Yuan, (2022). "Assessing the change of ambient air quality patterns in Jiangsu Province of China pre-to post-COVID-19 ", Chemosphere, vol 288, 132569, 2022. https://doi.org/10.1016/j.chemosphere.2021.132569

BIOGRAPHIES

Aytac Perihan Akan obtained her BSc degree in Environmental Engineering from Trakya University, Turkey, in 2008. She received her MSc. degrees from Bogazici University, Turkey, Environmental Technology in 2014 and Hacettepe University, Turkey, Industrial Engineering - Quality Engineering Department in 2016, respectively. She got her Ph.D. degree from Hacettepe University, Environmental Engineering Department, in 2019. She implemented her Ph.D. thesis at the New Jersey Institute of Technology, USA, Chemical and Materials Engineering Department between 2018 and 2019. She also worked as a visiting researcher at Universite Catholique de Louvain, Belgium, Materials and Process Engineering in 2018. She was a postdoctoral research fellow at Middle East Technical University, Turkey, Chemical Engineering Department between February 2020 and September 2021. She has been a research and teaching assistant at Hacettepe University Environmental Engineering Department since October 2013. Her research areas cover air pollution control, membrane technologies, life cycle assessment, advanced oxidation technologies, renewable energy systems, energy efficiency, and energy storage.

European Journal of Technique

journal homepage: https://dergipark.org.tr/en/pub/ejt

Vol.12, No.1, 2022

Examining the Carsharing System in Terms of Urban Transportation

Emre Kuşkapan[1*], Muhammed Yasin Çodur[2]

[1*] Erzurum Technical University, Civil Engineering Department, 25010, Erzurum, Turkey. (e-mail: emre.kuskapan@erzurum.edu.tr).
[2] Erzurum Technical University, Civil Engineering Department, 25010, Erzurum, Turkey. (e-mail: mycodur@erzurum.edu.tr).

ARTICLE INFO

Received: Sep., 10. 2020
Revised: May, 25. 2022
Accepted: Jun, 06. 2022

Keywords:
Carsharing
Fuel saving
Sustainable transportation

Corresponding author: *Emre Kuşkapan*

ISSN: *2536-5010* | e-ISSN: *2536-5134*

DOI: https://doi.org/10.36222/ejt.793458

ABSTRACT

With the increasing population in the world, individual vehicle ownership is increasing day by day. The increase in individual vehicle ownership causes heavy traffic jams in the city centers. In addition to traffic congestion, noise pollution, harmful gas emission, parking lot problems also increase. Besides, the fact that most of the vehicles use petroleum derivatives, which are a depleted energy source, pose big problems for the economy. In this context, various studies are carried out to reduce the use of individual vehicles and to prevent the mentioned problems. One of these studies is the carsharing system. In this study, the applicability of the vehicle sharing system was investigated by surveys of Erzurum Metropolitan Municipality personnel. The city is divided into certain regions, taking into account the locations of individuals' homes. Later, the carsharing model was created with the mobile application designed for individuals living in the region. Monthly total economic gain and savings per individual were calculated in the analysis made as a result of the model. Thanks to the study, it has been revealed that the carsharing system within the institutions provides feasibility and many advantages.

1. INTRODUCTION

Various policies are implemented across the world to reduce the use of individual vehicles by people. The most important of these is the development of public transportation systems. But often the capacity of public transport systems may be insufficient. In addition to this, the increase in the number of transfers may be among the reasons that direct people to the use of individual vehicles. For this reason, methods that will be an alternative to public transportation systems are being developed. Thanks to the alternative methods applied, problems in traffic can be minimized. Also, performance situations can be determined by observing the applied changes [1-3].

The carsharing system (CSS) is encouraged to reduce the use of individual vehicles and to increase the occupancy of these vehicles in developed and developing countries [4]. There are different types of systems. In the first model, the individual is applied by sharing his car with other people going in the same direction or accompanying the person with the individual's car. In this model, it is enough for only one of the individuals sharing cars to have a car. In the case of cars in more than one individual, carsharing can be made with a single vehicle, provided that a certain cycle is achieved [5]. In the developing version of this model in recent years, it is provided with the help of mobile applications or websites, and to make travel companions on long distances. In this structure, the individual can find his companion by sharing his/her location, destination, and date information. Thus, it saves money by sharing travel expenses with others [6-8]. Again, for this situation, at least one of the individuals traveling together has a car.

In the second model, there is a car rental process similar to the normal car rental system. Thanks to the car rental process with other individuals, the costs are greatly reduced. The most important advantage is that you don't have to bring the car back to where you bought it [7-9]. Companies applying this system give a membership card to the user who is a member. With this card, the vehicle to be rented can be opened and closed. The person can find the vehicle closest to the region where the car rental process will begin and travel by the people who will share the car [10,11]. They can leave the vehicle in the region where the journey ends. Since car rental companies can see from which location the vehicles are picked up and left, they are charged accordingly. On the other hand, renting individuals pay the expenses along the way together. While this model is actively used in many developed countries in the world, it is limited to only big cities such as Istanbul in our country [12-14].

In the third model, as in the second model, there is a rental car for transportation. However, instead of the company car, individuals' personal cars are rented and traveled. In this system, the person who hires his car earns money. But, since the system has various security weaknesses, its use is less

frequent. Thanks to the CSS models, increasing in-vehicle occupancy rates, reducing the number of vehicles in traffic, transporting the same number of people with less fuel and vehicles, contributing to both the economy of the individual and the country, reducing the exhaust emission, creating a culture of travel together, developing feelings of co-existence and social responsibility, and occupancy in parking areas reduction of the rate is provided [15-17]. It is aimed to speed up the working process of the building by producing web sites and mobile applications in many developed and developing countries that take into account these benefits of the CSS. Thanks to these applications, the reliability, and usability of the system are increased. Besides, the end-of-journey evaluation can be made about the people traveling together. With this situation, the possibility of choosing the companion may also arise in individuals using the CSS [18,19].

In this study, a CSS has modeled as a result of the surveys conducted by the Erzurum Metropolitan Municipality (EMM) personnel. In this model, the areas where the surveyed individuals have their homes are divided into certain regions. With the mobile application design, the status of participation in the CSS has examined. According to the status of participation in the CSS, monthly total economic gain and savings per individual have calculated.

2. MATERYAL AND METHOD

2.1. Survey data

EMM, which is determined as the study area, is located in the most central location of the city. A survey was conducted on 100 staff working in various departments in the main building of the municipality. With the questions asked in the questionnaires, the usability of the CSS was investigated. In the questions asked, the locations of the individuals' homes, what is the transportation to the workplace, the status of joining the CSS, the fuel characteristics of their vehicles, and the most disturbing issues in transportation were determined. The percentage of answers given as a result of the surveys conducted are shown in Fig. 1.

When the responses are examined, a great majority of the municipal employees provide their transportation with the help of motor vehicles. 16% of the centrally located people provide transportation to the workplace on foot or by bicycle. The remaining 84% prefer cars or public transport. Also, more than half of these individuals provide their transportation with their vehicles. This can cause serious traffic jams and parking problems. As a matter of fact, these issues and fuel costs are included in subjects that individuals find most disturbing in transportation. The attitudes of these individuals towards the CSS were also determined to reduce the problems stated by the individuals. A large number of individuals approach the car-sharing system positively. Individuals who prefer motor vehicles in accessing their workplaces and homes, find the car-sharing system useful and who can participate in this system contain a 76% segment. 8% of people think that the CSS is not suitable for them and prefer to provide transportation with their personal vehicles. In this regard, the applicability of the CSS appears to be quite high.

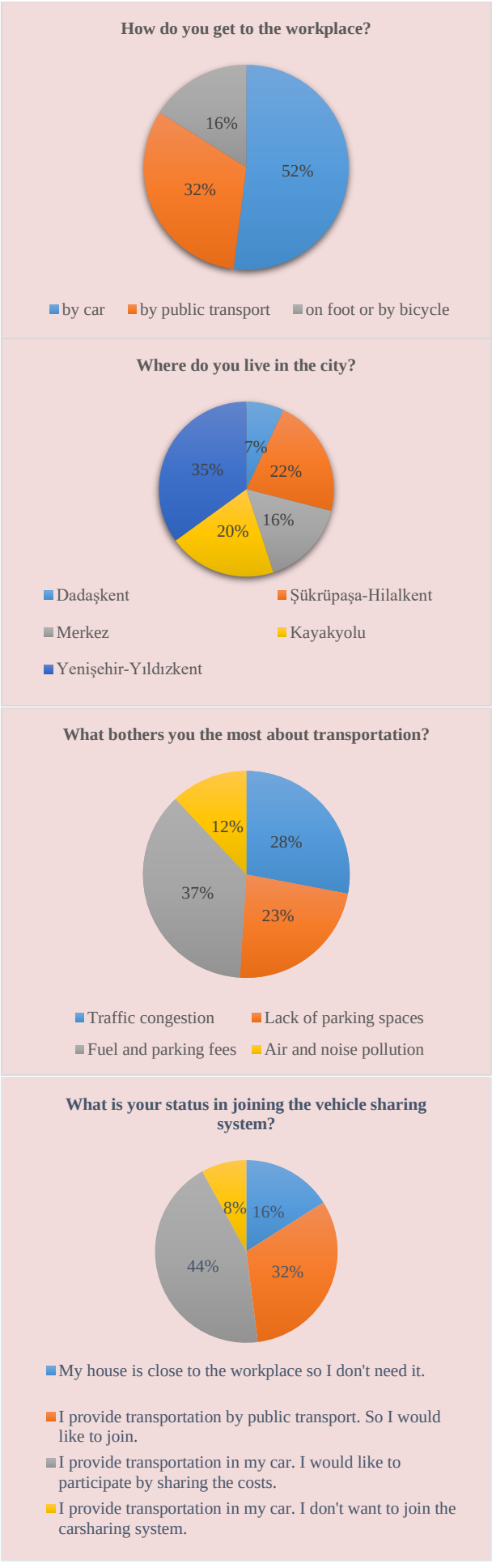

Figure 1. Percentage of EMM employees' responses to the survey questions

2.2. Study area

EMM, which is determined as the study area, is located in the most central location of the city. As a result of the surveys, the locations of these individuals' homes are located in five regions. These regions are named as Dadaşkent, Kayakyolu, Merkez, Yenişehir-Yıldızkent, Şükrüpaşa-Hilalkent due to their locations. The average distances of these regions to EMM and their areas are shown in Figure 2. 7% of individuals are located in the Dadaşkent region, which is approximately 6.4 km from the workplaces [20,21]. The other 3 regions, which are accessible by motor vehicles, are at an average distance of 3 kilometers from the workplace (Fig. 2).

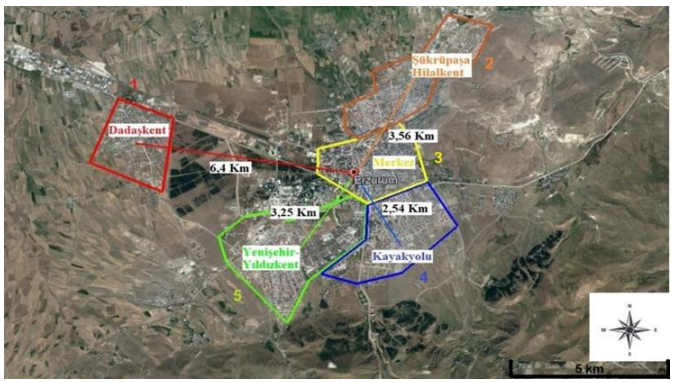

Figure 2. Average distances of the regions to EMM (The average distances shown are highway distances)

In the region where EMM is located, there are important public buildings such as the Provincial Directorate of Environment and Urbanization, Palandöken District Governorate, Land Registry, and Cadastral Regional Directorate, Erzurum Courthouse. It is known that many citizens, as well as individuals working in these buildings, have visited these public buildings. In this case, an important vehicle density emerges. Although there are parking areas around the region, it is insufficient and due to this density, contrary parking is frequently encountered at the roadside.

2.3. Carsharing system

A mobile application interface has been created for individuals to make travel companions via CSS. Individuals who register to this interface with their personal information indicate whether they have a vehicle and in which location they reside. Then, if they own the car, they specify how many passengers they can get in their car, the meeting time and address they have set to go to work, and finally their phone number and the unit they work for. If the individual does not own the vehicle, he/she can see the phone number of the individuals who own the vehicle in this region and request to use the CSS in the tab after stating in which region he/she is living and can communicate with them. In this way, individuals who intend to use CSS will be able to choose the people to use this system. The interface designed for this system is shown in Fig. 3.

Figure 3. Mobile application interface designed for CSS

3. RESULTS AND DISCUSSION

With the grouping created for the CSS structure, it was decided to take 2 or 3 passengers for each car, excluding the driver. Because the individuals demanding to join the system requested this direction to have a comfortable journey and to minimize delays. There are 44 cars in total for individuals who want to join the carsharing system. Rotating the cars in the same region on a weekly basis is important to ensure equality. If the vehicle is shared as a result of the examination and where the locations of the individuals are taken into account, the sharing status is given in Tab. I was obtained.

TABLE I
DATA OBTAINED IN CASE OF APPLICATION OF CSS BY REGIONS

Region No	Number of Individuals	Number of individuals who want to join CSS	Number of individuals who do not want to participate in CSS	Number of vehicles in people who want to join CSS	Number of vehicles used with CSS
1	7	7	0	4	2
2	22	19	3	12	5
3	16	0	16	-	-
4	20	18	2	11	5
5	35	32	3	17	8
Total	100	76	24	44	20

Before the CSS system, 44 of 76 individuals requesting to join this system provide their transportation, while 32 provide their transportation by public transportation. With the CSS application, taking into account the locations of these individuals, the number of vehicles required was 20. In this case, the number of vehicles in use decreased by approximately 55%. This provides significant gains in the name of fuel and parking fees. In addition to this situation, the total amount of 32 people pay daily for public transportation is 122 TL. The fuel consumption and the resulting charges for the vehicles are shown in Tab. 2.

TABLE II
CALCULATION OF THE EARNINGS OBTAINED BY THE IMPLEMENTATION OF CSS

Region No	Daily fuel fee (TL) before CSS	Daily fuel fee (TL) after CSS	Daily parking fee (TL) before CSS	Daily parking fee (TL) after CSS	Daily-earnings (TL)	Monthly earnings (TL)
1	28,16	14,08	8	4	18,08	415,84
2	46,99	19,58	24	10	41,41	952,43
3	-	-	-	-	-	-
4	30,73	13,97	22	10	28,76	661,48
5	60,78	28,6	34	16	50,18	1154,14
Total	166,66	76,23	88	40	138,43	3183,89

* Parking fees are calculated on a monthly subscription.
* Fuel charges have calculated separately for diesel, gasoline, and LPG vehicles.
* Calculation has made considering that there is an average of 23 working days in 1 month.

When the table is examined, if the CSS system is applied, a saving of 138,43 TL per day is provided for automobile fuel and parking fees. Besides, 122 TL is saved for individuals who provide their transportation by public transportation. When both cases are calculated monthly, Tl 5989.89 is saved. An average of 78.81 TL of monthly income is earned per individual participating in the system. The implementation of CSS is quite easy, but the gains are also high. Especially in the long term, it can provide serious financial gains for individuals. On the other hand, situations such as air pollution, traffic congestion, insufficient parking areas, and noise pollution, which increase due to the increase in the number of vehicles in daily life, can be significantly reduced with the CSS method.

4. CONCLUSION

In this study, in addition to the existing methods, the applicability of CSS within the institutions was investigated. A mobile application interface is designed based on the locations of individuals' homes and whether they own a vehicle or not. Accordingly, as a result of the survey conducted for 100 individuals working in the EMM, it was determined that 76 individuals wanted to participate in CSS. For these individuals, daily and monthly expenses were calculated by determining the usage of public transportation, fuel prices of individual vehicles, and parking fees. Then, the expenditures that will occur by calculating CSS are calculated. When both cases are compared, a saving of nearly 6 thousand TL per month is achieved. In addition to this financial gain, since the number of vehicles in traffic will decrease, delays can be reduced, parking areas can be found, harmful gas emissions and noise pollution can be reduced. Since the system has such a beneficial aspect, the CSS system should be widely used, especially in areas where government agencies and business centers are located. Also, individuals can be encouraged by government agencies to increase the usability of the system. Accordingly, it is possible to design more livable cities.

ACKNOWLEDGEMENT

This research was supported by Erzurum Metropolitan Municipality as data. We would like to thank all Erzurum Metropolitan staff who support the study.

REFERENCES

[1] N. Morelli, “Developing new product service systems (PSS): methodologies and operational tools,” J. Cle. Pro., vol. 14, no. 17, pp. 1495-1501, 2006.
[2] M. H. Coll, M. H. Vandersmissen, and M. Thériault, “Modeling spatio-temporal diffusion of carsharing membership in Québec City,” J. Trans. Geo., vol. 38, pp. 22-37, 2014.
[3] S. A. Shaheen, and A. P. Cohen, “Growth in worldwide carsharing: An international comparison,” Trans. Res. Rec., vol. 1992, no. 1, pp. 81-89, 2007.
[4] F. Güneş, S. Bayraklı, and A. Zaim, “Study of Performance Measures of Traffic Flow at Signalized Intersection with Queueing Theory,” European J. Sci. Tech., vol. 19, pp. 56-65, 2020.
[5] M. Namazu, D. MacKenzie, H. Zerriffi, and H. Dowlatabadi, “Is carsharing for everyone? Understanding the diffusion of carsharing services,” Trans. Pol., vol. 63, pp. 189-199, 2018.
[6] J. Hamari, M. Sjöklint and A. Ukkonen, “The sharing economy: Why people participate in collaborative consumption,” J. Assoc. Inf. Sci. Tech., vol. 67, no. 9, pp. 2047-2059, 2016.
[7] J. Müller, and K. Bogenberger, “Time series analysis of booking data of a free-floating carsharing system in Berlin,” Trans. Res. Pro., vol.10, pp. 345-354, 2015.
[8] S. De Luca and R. Di Pace, “Modeling the propensity in adhering to a carsharing system: a behavioral approach” Trans. Res. Pro., vol. 3, pp. 866-875, 2014.
[9] T. Yoon, C. R. Cherry and L. R. Jones, “One-way and round-trip carsharing: A stated preference experiment in Beijing,” Trans. Res. Part D, vol. 53, pp. 102-114, 2017.
[10] M. M. Lopes, L. M. Martinez, G. H. de Almeida Correia, Simulating carsharing operations through agent-based modeling: an application to the city of Lisbon, Portugal. Transportation Research Procedia, vol. 3, pp. 828-837, 2014.
[11] C. Costain, C. Ardron, K. N. Habib, “Synopsis of users’ behaviour of a carsharing program: A case study in Toronto,” Trans. Res. Part A, vol. 46, no. 3, pp. 421-434, 2012.
[12] F. Giesel, and C. Nobis, “The impact of carsharing on car ownership in German cities,” Trans. Res. Pro., vol. 19, pp. 215-224, 2016.
[13] M. Duncan, “The cost saving potential of carsharing in a US context,” Trans., vol. 38, no. 2, pp. 363-382, 2011.
[14] Bruglieri, M., Colorni, A., & Lue, A. (2014). The vehicle relocation problem for the one-way electric vehicle sharing: an application to the Milan case. Procedia-Social and Behavioral Sciences, 111, 18-27.
[15] B. Boyacı, and K. G. Zografos, “Investigating the effect of temporal and spatial flexibility on the performance of one-way electric carsharing systems,” Trans. Res. Part B, vol.129, pp. 244-272, 2019.
[16] J. Firnkorn, “Triangulation of two methods measuring the impacts of a free-floating carsharing system in Germany,” Trans. Res. Part A, vol. 46, no. 10, pp. 1654-1672, 2012.
[17] A, Avcı, and H. Karakay, “Calculating energy-induced carbon footprint: Batman University case,” Euro. J. Tech., vol. 9, no. 1, pp. 114-120, 2019.
[18] D. Jorge, C. Barnhart, and G. H. de Almeida Correia, “Assessing the viability of enabling a round-trip carsharing system to accept one-way trips: Application to Logan Airport in Boston,” Trans. Res. Part C, vol. 56, pp. 359-372, 2015.
[19] M. Repoux, M. Kaspi, B. Boyacı and N. Geroliminis, “Dynamic prediction-based relocation policies in one-way station-based carsharing systems with complete journey reservations,” Trans. Res. Part B, vol. 130, pp. 82-104, 2019.

[20] Erzurum Metropolitan Municipality, https://www.erzurum.bel.tr/
[21] E. Kuşkapan, M. A. Sahraei, M. K. Çodur, and M. Y. Çodur, "Pedestrian safety at signalized intersections: Spatial and machine learning approaches," J. Trans. & Health, vol 24, no. 101322, 2022.

BIOGRAPHIES

Emre Kuşkapan obtained his BSc degree in civil engineering from Yıldız Technical University in 2015. He received M.S. degree in civil engineering from the Erzurum Technical University in 2019. He is currently Ph.D. student at Erzurum Technical University, Erzurum, since 2018 where he works as a research assistant. He is active research in the artificial intelligence, machine learning, data mining, transportation planning, traffic accidents modeling.

Muhammed Yasin Çodur obtained his BSc MSc and Ph. D. degree in civil engineering from Atatürk University, Erzurum. Currently he is working as an Associate Professor in Erzurum Technical University, Erzurum. His research interests are transportation systems, traffic safety, transportation planning, traffic accidents, artificial neural networks, highway systems, transportation networks, railway transportation, public transportation, multi-criteria decision-making.

European Journal of Technique

journal homepage: https://dergipark.org.tr/en/pub/ejt

Vol.12, No.1, 2022

Structural Controls of High-Temperature and Deep Geothermal Systems Associated with Detachment Fault

Adil Ozdemir[1*], Yildiray Palabiyik[2], and Fahri Arabaci[3]

[1*] Ataturk University, Institute of Science and Technology, Division of Geological Engineering, Erzurum, Turkey. (adilozdemir2000@yahoo.com).
[2] Istanbul Technical University, Department of Petroleum and Natural Gas Engineering, İstanbul, Turkey. (palabiyiky@itu.edu.tr).
[3] Iskenderun Technical University, Department of Petroleum and Natural Gas Engineering, Hatay, Turkey. (fahri.arabaci@gmail.com).

ARTICLE INFO

Received: Jun., 21. 2021
Revised: Apr., 19. 2022
Accepted: May, 25. 2022

Keywords:
High-temperature geothermal field
Detachment fault
Transfer fault
Listric faulting
Western Anatolia

Corresponding author: *Adil Ozdemir*

ISSN: *2536-5010* | e-ISSN: *2536-5134*

DOI: https://doi.org/10.36222/ejt.955186

ABSTRACT

In this study, the structural controls of a high-temperature system (188 to 287 ºC) associated with the detachment fault in Gediz Graben generating approximately half of this electricity generation in Turkey which is in the top five of the world in the generation of electricity from geothermal resources are examined. The high-temperature geothermal reservoirs associated with detachment fault in the study area have formed along the normal faults nearly in E-W orientation and in intensely fractured rocks in a structurally complex manner associated with transfer faults approximately in N-S orientation. Generally, it has been determined that the reservoirs are closely located to strike-slip faults intersecting, overlapping, and/or terminated with Quaternary transfer faults. The same results as this study have also presented in the studies performed in western Anatolia and some regions of the world. Since the detachment fault and the high-angle normal faults cutting the detachment fault form the paths, this mechanism ensures that the geothermal fluids are drained from the surface to the reservoir rock environment. High-angle normal faults cutting the detachment fault and the transfer faults cutting the detachment-high-angle normal faults constitute the carrier systems. This causes that the fluids heated in the reservoir rock environment at the depths are carried to the surface. Therefore, transfer faults control the position of high-temperature geothermal systems and should be used as the primary guide for geothermal exploration.

1. INTRODUCTION

The first geothermal activities in Gediz Graben in Western Anatolia started in the 1960s due to high-temperature hot springs (Figure 1). In recent years, geothermal fluids have been produced up to 287 ºC. Geothermal resources are used in regional and greenhouse heating, chemical production, tourism, health facilities, and mainly in electricity production [1-8]. The installed geothermal power capacity of Turkey reached 1668 MWe in 2020. There are more than 200 deep geothermal wells in the Gediz Graben. Numerous geothermal power plants are currently operating, and approximately 500 MW of electricity is generated from these power plants [9-17].

The high-temperature Kavaklıdere Geothermal Field (Alaşehir) is located along the active southern margin of the Gediz Graben (Figure 1). It is noteworthy that high-temperature geothermal fields in Western Anatolia are lined up along detachment faults on the edges of Büyük Menderes and Gediz grabens (Figure 1). This situation creates a need to investigate the role of a detachment fault in the occurrence of high-temperature geothermal systems (is detachment fault a channel for geothermal fluids or a physical mechanism that increases the geothermal gradient by generating frictional heat?). Therefore, in this study, structural controls in the Kavaklıdere field, a high-temperature field associated with the Gediz detachment fault, are investigated. The temperatures of geothermal reservoirs in the field range from 188 to 287 ºC. The field contains numerous geothermal reservoirs in intersection areas with N-NNE trending transfer faults and the Gediz Detachment Fault [2-4, 8]. The main research focus of this study is to survey the structural controls of a high-temperature geothermal field related to the detachment fault.

2. GEOLOGICAL SETTING

Aegean extensional province occurs above the north-dipping Hellenic subduction zone in Africa-Eurasia convergent boundary in the Eastern Mediterranean region. There are two sets of Cenozoic extensional grabens and sedimentary basins in and around the Menderes Massif: those with NNE-SSW-trending and filled with lower Miocene and younger siliciclastic, volcaniclastic, and volcanic rocks, and those ~E-

W-trending and filled mainly with siliciclastic rocks [18-21]. Most of these grabens are bounded by high-angle normal faults with strike-slip components [18, 21, 22]. These E-W-trending grabens and basins are bounded by normal faults dipping with high to moderate-angles, some of which are seismically active [23-26], and destroying and crosscutting NNE-SSW-trending grabens and basins.

[18] reported that NNE-trending grabens locally occur as 'hanging grabens' in the E-W trending ones' footwalls and that the trapped structures and sedimentary units of these older NNE-trending grabens are distinguishable in the seismic profiles. 2D gravity and magnetotelluric (MT) modeling of the Gediz Graben's structure has revealed the existence of a series of these NE- trending grabens are distinguishable in the seismic profiles. 2D gravity and magnetotelluric (MT) modeling of the Gediz Graben's structure has revealed the existence of a series of these NE-SW-trending grabens and sub-basins at deeper depths [3, 4, 26, 27]. It also indicates that the regional structural fabric seen at the surface continues beneath the Quaternary sedimentary fill of the E-W-trending modern graben system.

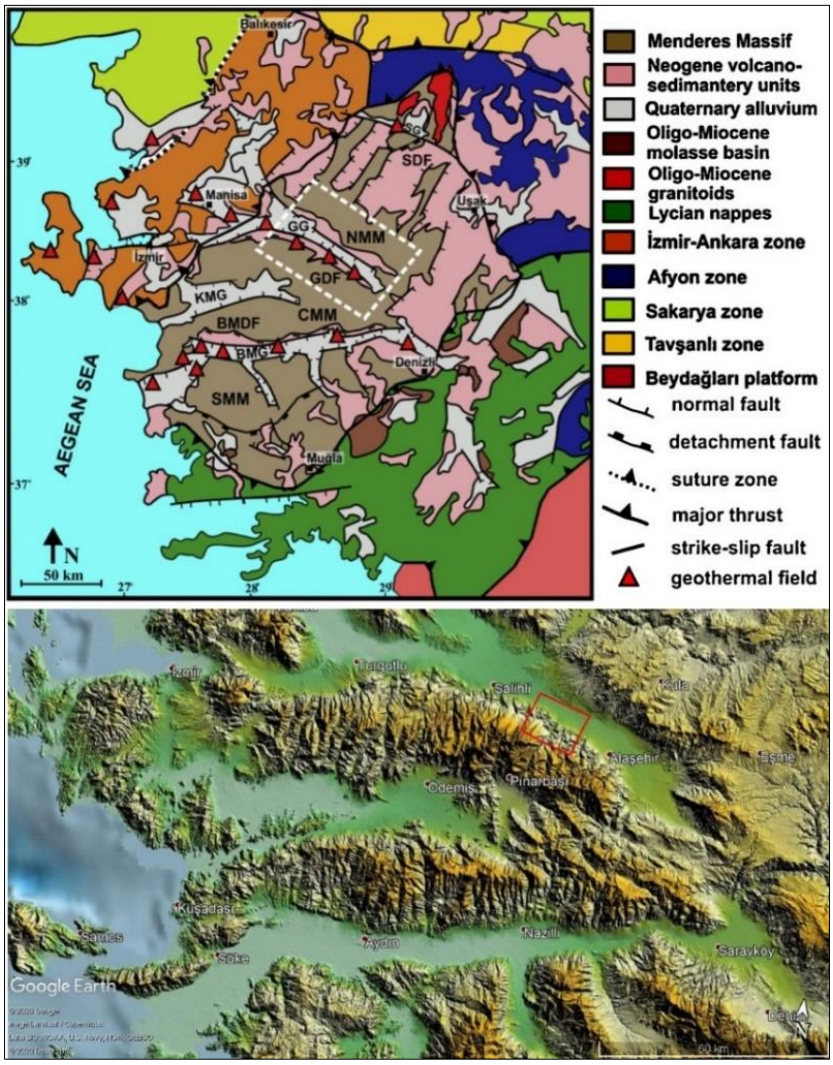

Figure 1. Location map of the study area. Main structures and grabens: NMM: Northern Menderes Massif, CMM: Central Menderes Massif, SMM: Southern Menderes Massif, BMG: Büyük Menderes Graben, GG: Gediz Graben, KMG: Küçük Menderes Graben, GDF: Gediz Detachment Fault, BMDF: Büyük Menderes Detachment Fault (the map is modified from [5]). The investigation area is marked on the map (red polygon).

Six different units have been determined in the investigation area. These units from bottom to top are as follows: (1) Metamorphic rocks (gneiss, calc-schist, quartz-schist, phyllite, mica-schist) of the Precambrian-Middle Triassic Menderes Massif (2) Paleozoic marbles (3) Granitic rocks (4) Upper Miocene-Lower Pliocene Gediz formation (5) Upper Pliocene-Quaternary sediments and Kaletepe formation (6) Quaternary alluviums, respectively (Figure 2) [2].

3. STRUCTURAL GEOLOGY

The study area is located within the Gediz Graben, extensional basin of 140 km in length, roughly E-W oriented and concaved southward, extending bein the north of Menderes massif. Normal faults border the graben from both margins (Figure 1). However, in this basin, that narrows in the eastern border, the western portion's morphologic boundaries are difficult to distinguish.

Dip-slip normal faults located in the south of the graben are intersected by NE-SW and NW-SE trending oblique and strike-slip faults in many places. The dip-slip normal faults prominently identified as detachment faults in the south have a listric faulting character. The detachment fault exhibits geometric features in the form of jumps. Transfer faults have developed in those stepping areas. The faults in the southern section of the graben are generally younger from the south to the north.

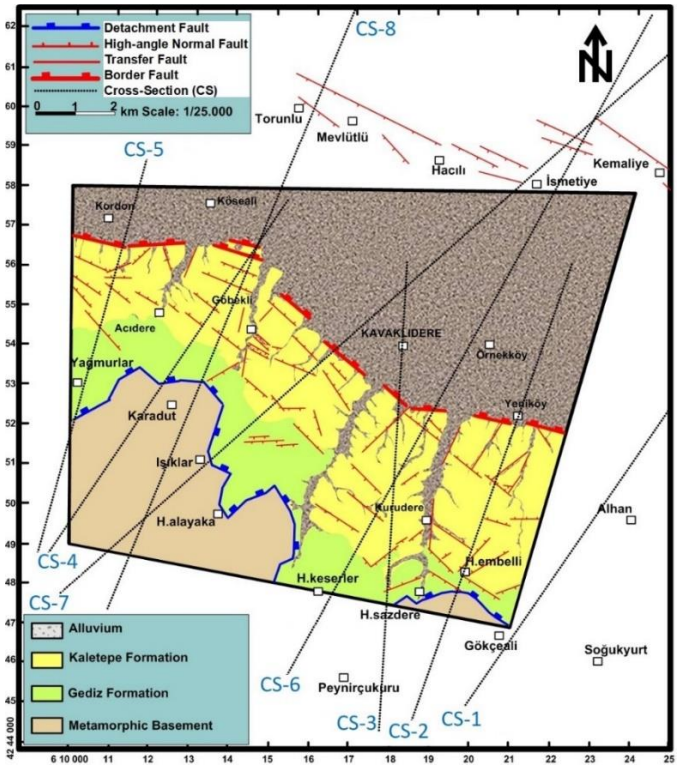

Figure 2. Simplified geological map and cross-section lines the study area (see Section 3.2 for cross-sections) (modified from [2]).

Metamorphics that constitute the highlands surrounding the graben from the south and north consist of gneiss, marbles, quartzites, and schists. Some of the faults bordering the graben formed contacts between the metamorphic basement rocks and Miocene, Pliocene, and Quaternary sediments. The Upper Miocene units are formed from conglomerates and sandstones outcropping at the margins of the graben. Pliocene units consist of dendritic sandstones and claystones, and the graben faults cut quaternary sediments.

Dips of fault planes of the normal faults in the investigation area located in the Gediz graben vary between 30° and 60°. To a certain degree, lower dips are measured. These faults are usually characterized by listric faulting. The layers are generally horizontal, and no folding has developed at the sediments between the fault blocks. On the other hand, the topographic surfaces of the footwall blocks sloped towards the hanging-wall blocks. It is known that the basement of the graben was downthrown by a minimum displacement of 1500 m after Pliocene [2].

The observations have been performed at 66 different stop points to explain the structural features of the region in which the study area is located and to reveal its faulting type, geometric properties, and faulting mechanism in detail. Faults with four different mechanisms are identified in the study area (Figure 2) [2]. These are;

- Detachment fault,
- Low-angle normal faults,
- High-angle normal faults,
- Transfer faults.

In light of the information obtained from the stop points (the stations), structural geological cross-sections of the study area have been prepared.

3.1. The Gediz Detachment Fault

The Gediz Detachment Fault bordering the study area from the south is remarkable, and the related detachment faults are generally NW-SE trending, nevertheless, they partially show different orientations. The detachment faults make the step to the right and left, and are dipped into the basin along with 20-30 degrees. Precambrian-Middle Triassic metamorphic rocks are juxtaposed with Upper Miocene-Lower Pliocene Gediz formation along the detachment fault. The detachment fault with mylonitic and breccia characteristics formed a large zone of 100-150 m in width (Figure 3). The upper parts of the metamorphic units were completely altered along the detachment fault zone and gained breccia characteristics. The eastern half of the study area contains breccia-mylonitic mica-schists/phyllites and marbles above the detachment fault zone, and the western part includes quartz-schists and calc-schists.

The detachment fault has a 100-150 m thick mylonitic-brecciated zone (the reservoir in the geothermal field). Completely disintegrated brecciated marbles are located at the upper levels of this zone (Figure 3). There is an elevation difference of approximately 3000 m between the detachment fault and the basin plane.

The juxtaposition of the Gediz formation to the metamorphic units along the detachment fault zone indicates that the detachment fault may have been formed during or after the occurrence of the Gediz formation. This opinion is supported by the fact that the base levels of the Gediz formation are highly deformed. The strata are tilted towards the detachment fault, and the Gediz formation contains low-angle normal faults.

A great number of NW-SE trending high-angle normal faults intersecting the Gediz and Kaletepe formations are developed on the hanging wall of the detachment fault. Partly, NE-SW trending dip-slip normal faults exist as well. It is foreseen that the high-angle normal faults intersect and displace the detachment faults at the depths. It is also observed that the high-angle normal faults in the areas close to the detachment fault dip towards SW while the faults in the areas close to the basin do towards NE. The differences in the dip directions have caused the formation of mini-grabens on the downthrown block of the detachment fault and the formation of a horst-shaped area between the aforementioned grabens. By the way, the listric character of the detachment fault has

contributed to the shape of an asymmetric graben currently observed in the basin.

Figure 3. Views from the detachment fault and breccia zone (the reservoir formation observed in the study area).

3.2. Geological cross-sections

Based on the findings from the geological and tectonic field studies carried out and the estimated total fault displacements in the area, eight geological cross-sections have been taken in NW-SW (3 of them) and NE-SW (3 of them) directions in the study area (Figure 2). It is estimated that the total displacement of the normal faults, which bounds the study area from the south, is about 1500-2000 m. This total displacement is considered in each geological cross-section.

To find an answer to questions:

(1) how the detachment fault in the study area extends geometrically from south to north to the basin,

(2) how the high-angle normal faults affect the detachment fault at the depths,

(3) how the thickness of the sediments in the basin reached up to 2000 meters.

The detailed interpretations of the geological cross-sections taken for the study area are performed below.

15 km long-cross-section 1 (CS-1) in NE-SW direction extends along Alhan creek between Gökçealan in the SW and Piyadeler in the NE, from a part close to the SW corner of the study area (Figures 2 and 4). As it is clearly seen in Cross-section 1, the detachment fault exposes in the SW. However, it reaches the deeper areas being cutting and making offset by the high-angle normal faults towards into the basin to the NE. The detachment fault has a listric character.

The metamorphic units juxtapose with Gediz formation along the detachment fault in the SW. Displacements of the high-angle normal faults increase towards the NE from the SW. As a result of vertical displacements, the thicknesses of Gediz and Kaletepe formations increase to continue towards the NE from the SW and reach the maximum values in the basin. These phenomena point out that the high-angle normal faults have been active in the area until today since the occurrence of the detachment fault. There is an elevation difference of approximately 850 m between the detachment fault and the basin plain.

15 km long-cross-section 2 (CS-2) in NE-SW direction, close to the eastern border of the study area, extends between Gökçealan in NE and Yeniköy in GB, and is parallel to the east edge of the Hacıahmet creek (Figures 2 and 5).

As seen in cross-section 2, the detachment fault deepens towards the NE from the SW. However, in the northern of Yeniköy, it is displaced downwards up to 1500-2000 m at the hanging-wall block. Unlike this cross-section, several antithetic stepping faults dipped towards the detachment fault are located. In other words, the faults dipped towards the SW and the area between the detachment fault and the basin are uplifted.

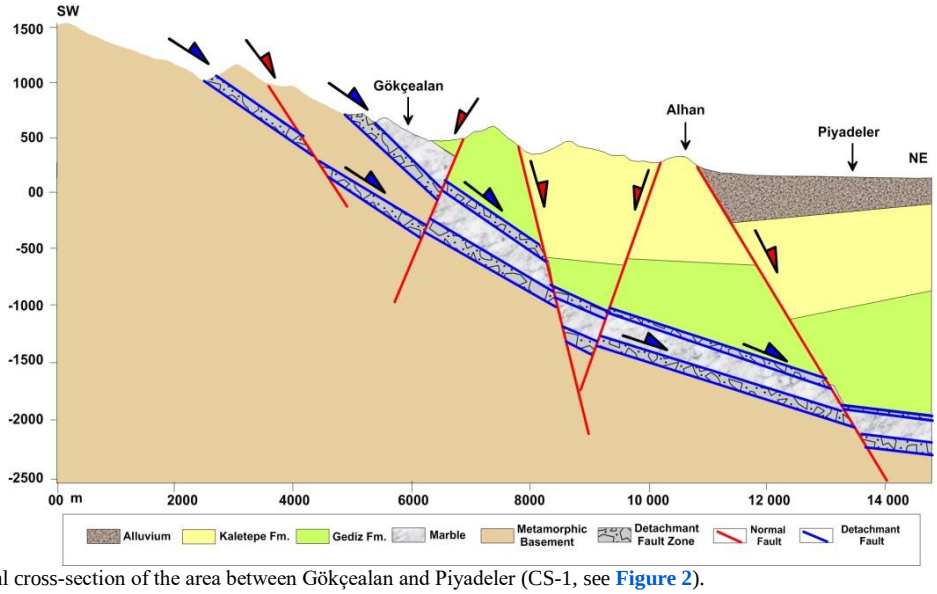

Figure 4. Geological cross-section of the area between Gökçealan and Piyadeler (CS-1, see **Figure 2**).

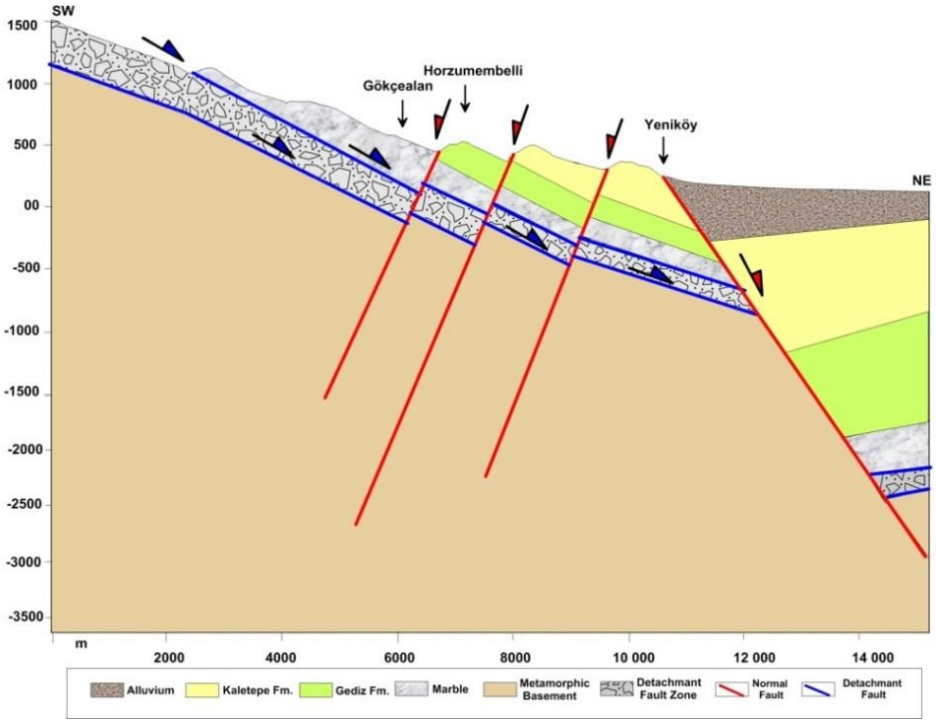

Figure 5. Geological cross-section of the area between Gökçealan and Yeniköy (CS-2, see **Figure 2**).

15 km long-cross-section 3 (CS-3) in N-S direction extends between Peynirçukuru village in the SW and Kavaklıdere in the NE, close to the center of the study area (Figures 2 and 6).

Cross-section 3 has a structure similar to Cross-sections 1 and 2. The detachment fault continues by deepening and uplifting towards the north, so it is downthrown up to 1500-2000 m by the main fault.

There is a thick and brecciated marble zone above the detachment fault. The high-angle normal faults dip towards the detachment fault in the south and towards the basin side in the north. As a result of the dipping towards the SW and NE, a subsidence is occurred towards the detachment fault's side. An elevation difference of approximately 800 m is present between the detachment fault and the basin plain.

15 km long-cross-section 4 (CS-4) in N-S direction extends between Karadut village in the SW and Köseali in the NE. It is parallel to the western edge of the Göbekli stream, close to the west side of the study area (Figures 2 and 7). While the detachment fault continues into the deep and is vertically displaced towards the northeast, it is displaced up to 1500-2000 m downward by the border (main) fault. Brecciated quartz schists overlie the detachment fault.

On the hanging wall of detachment fault, continuous depression is occurred towards the basin as a result of a series of stepping faults dipped to the NE towards the north apart from the antithetic faulting dipping towards the SW. However, the most extensive subsidence and deposition area has been occurred. There is an elevation difference of approximately 400 m between the detachment fault and the basin plain in the vicinity of Karadut and 1300 m with the part behind it.

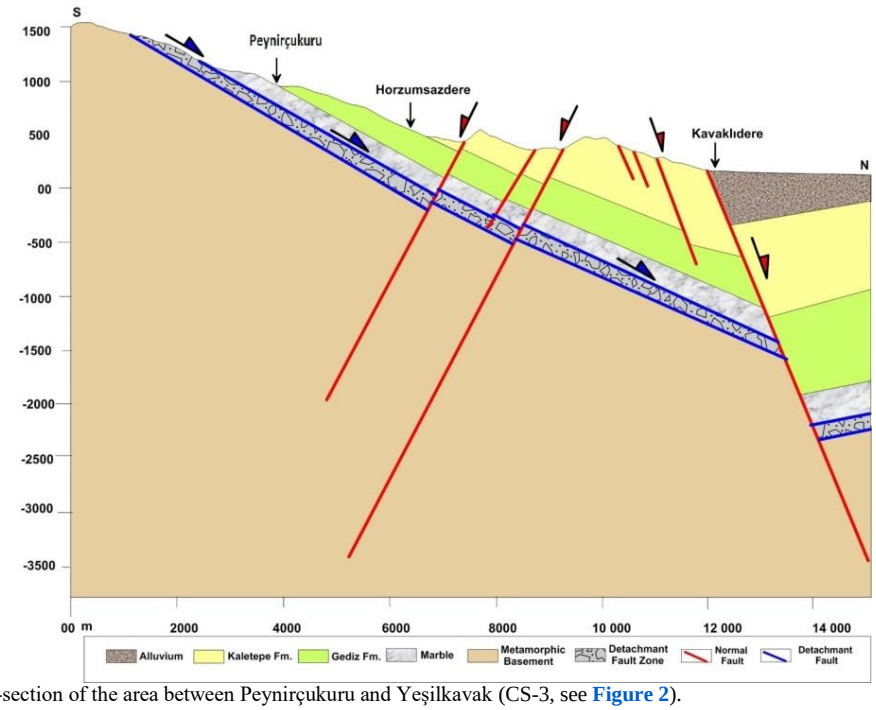

Figure 6. Geological cross-section of the area between Peynirçukuru and Yeşilkavak (CS-3, see **Figure 2**).

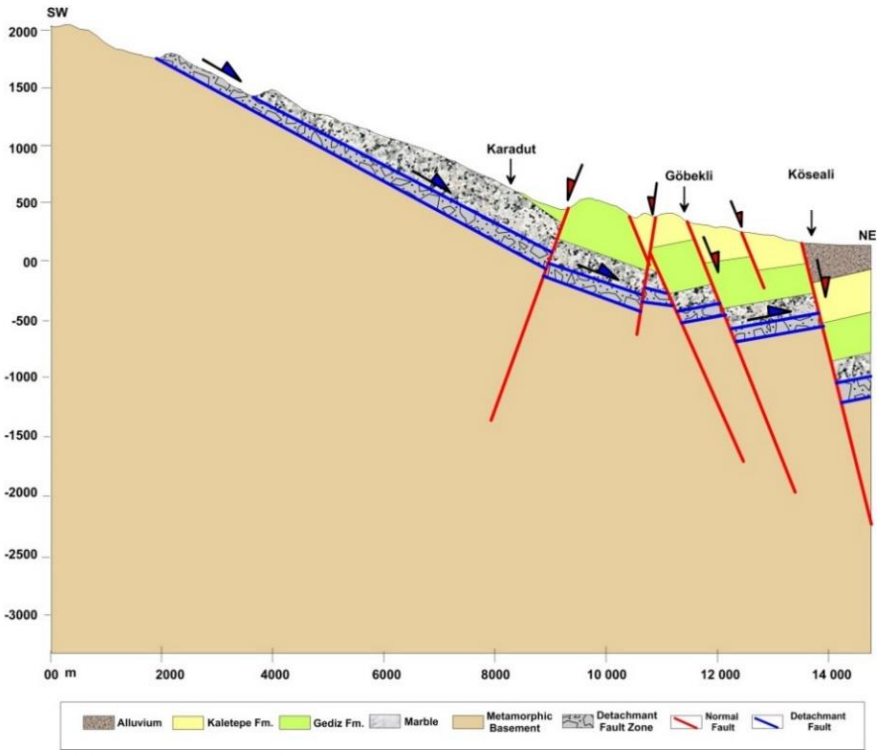

Figure 7. Geological cross-section of the area between Karadut and Köseali (CS-4, see **Figure 2**).

13 km long-cross-section 5 (CS-5) in NNE-SSW direction extends between Yağmurlar village in the SW and Kordon in the NE (Figures 2 and 8). It has a structure that is very similar to the cross-section 4. Brecciated calc-schists are exposed above the detachment fault.

As a consequence of the antithetic faulting dipped towards the SW in front of the detachment fault, a depression occurs between the detachment fault and antithetic faults and an uplifting area in the north of the detachment fault. Continuous subsided areas develop towards the basin. There is an elevation difference of approximately 450 m between the detachment fault and the basin plain in the vicinity of Yağmurlar and 1000 m behind it.

35 km long-cross-section 6 (CS-6) in NE-SW direction extends between Karadağ village in the SW and İsmetiye in the NE, on the eastern side of the study area (Figures 2 and 9).

The detachment fault becomes listric faulting towards the basin depths from the SW to the NE and deepens by vertical displacement of the high-angle faults. It is downthrown approximately 1500-2000 m by the main fault bordering the basin from the south. It is anticipated that the antithetic faults border the basin from the north and dipped towards the SW.

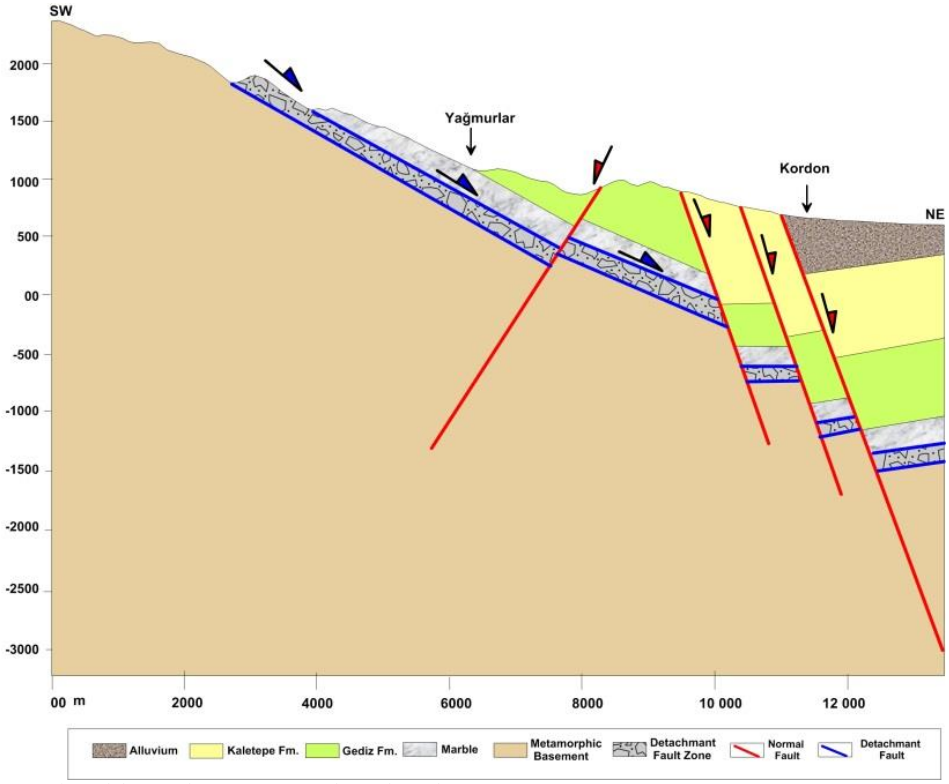

Figure 8. Geological cross-section of the area between Yağmurlar and Kordon (CS-5, see **Figure 2**).

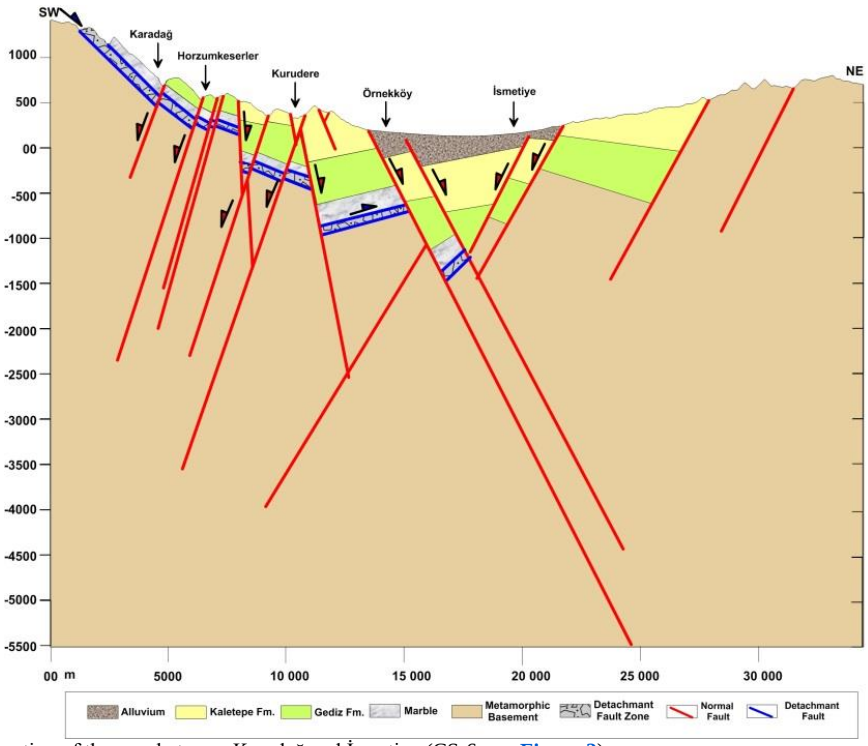

Figure 9. Geological cross-section of the area between Karadağ and İsmetiye (CS-6, see **Figure 2**).

The high-angle normal faults between the detachment fault and Kurudere dip towards the SW. However, this bordering from the south of the basin in Kurudere has a dip towards the NE. Because of the high-angle normal faults dipping towards the SW and NE, mini horst and graben areas are developed between the detachment fault and the basin. In this section, there is an elevation difference of 800 m between the SW and NE of the basin and 650 m between the detachment fault and the basin plain. Depending on the total displacement of the high-angle normal faults, the thicknesses of alluvium at the bottom of the basin, Kaletepe formation, and Gediz formation reach the maximum level. As the detachment fault progresses towards from the basin, the thickness relatively decreases.

32 km long-cross-section 7 (CS-7) in NE-SW direction, which is towards the NE corner from the SW corner of the study area, extends between Işıklar village in the SW and İsmetiye in the NE (Figures 2 and 10).

The detachment fault becomes listric towards the basin from the SW to the NE in depth similar to the structure in the Cross-section 6 and deepens by being displaced by the high-angle faults. It is predicted that the total displacement of the main fault bordering from the south of the basin is about 1500-2000 m.

Unlike Cross-section 6, the detachment fault continues towards the NE of the basin. It is cut and displaced by the antithetic faults which border the basin from the north and dip towards the SW. Furthermore, the high-angle normal faults have a stepping faulting character and dip to the basin towards the NE. It is assumed that the detachment fault is located in the metamorphic basement at the depths. In other words, the basin margin has been continuously downthrown towards the NE from the SW. In this section, there is an elevation difference of 1200 m between the SW and NE of the basin and 450 m between the detachment fault and the basin plain.

27 km long-cross-section 8 (CS-8) in NE-SW direction extends between Karadut village in the SW and Mevlütlü in the NE, on the western side of the study area (Figures 2 and 11). Although the cross-section 8 is very similar to the faulting structure in the cross-section 7, the only difference is that the bottom of the detachment fault forms a mylonitic-breccia zone at the thickness of 100-150 meters, which consists of calcschists, under Gediz formation. In this section, there is an elevation difference of 600 m between the SW and NE of the basin and 200 m between the detachment fault and the basin plane.

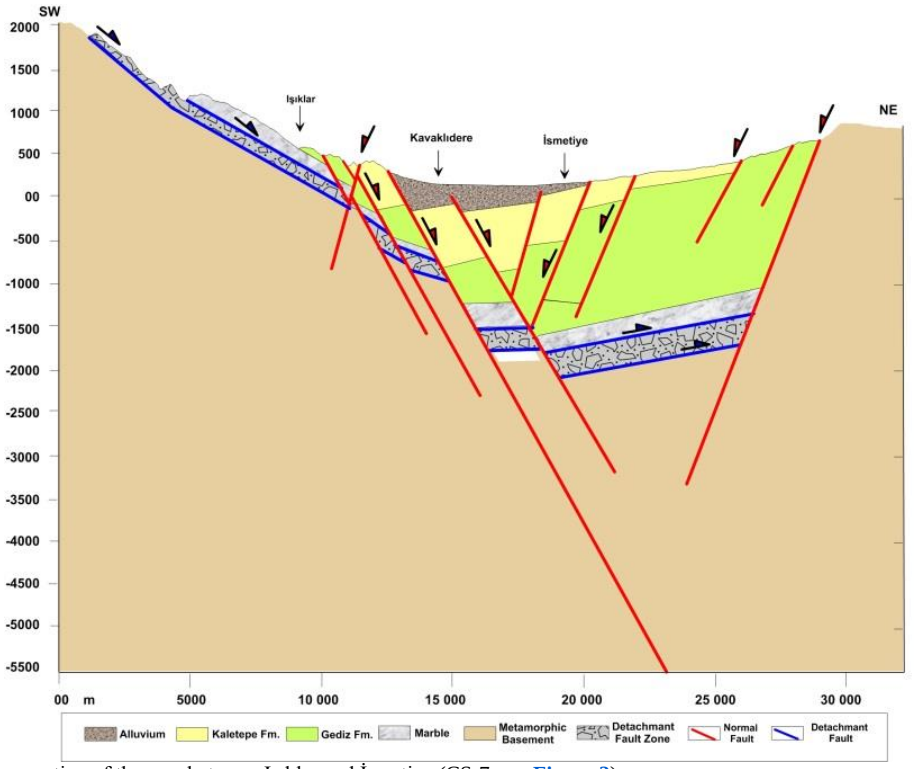

Figure 10. Geological cross-section of the area between Işıklar and İsmetiye (CS-7, see **Figure 2**).

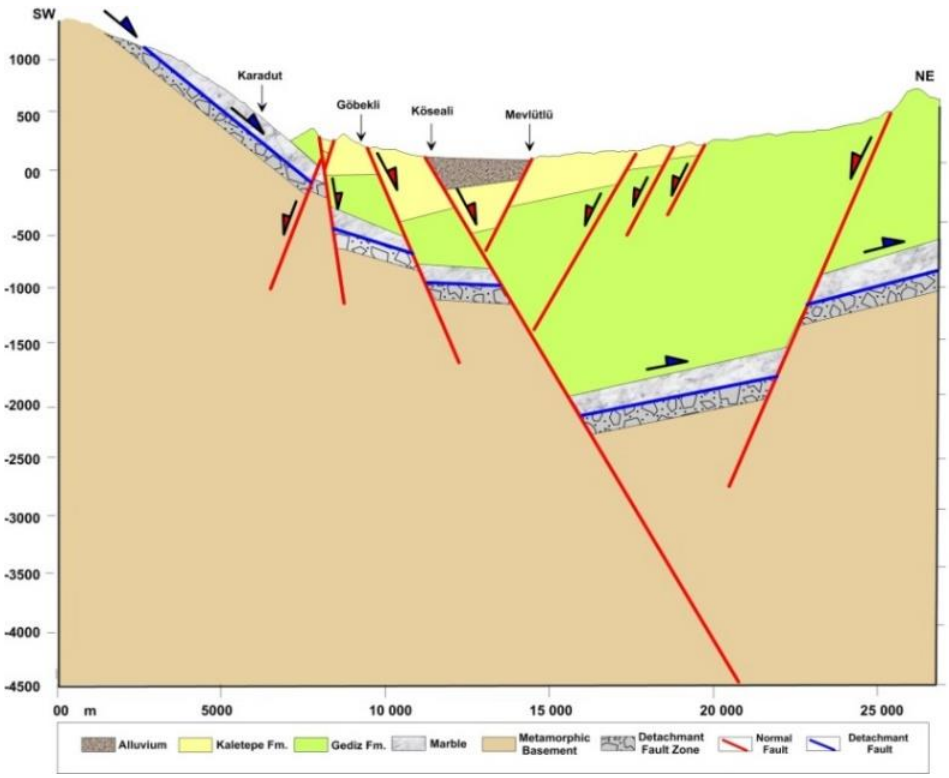

Figure 11. Geological cross-section of the area between Karadut and Mevlütlü (CS-8, see **Figure 2**).

3.3. Relationship between structural controls and high-temperature geothermal systems

Back-arc basins are known to be controlled by deep subduction dynamics. In the Aegean domain, the slab retreat led to the formation of crustal-scale low-angle normal faults (detachment faults) that were involved in the exhumation of Metamorphic Core-Complexes in this region. The detachment system in western Anatolia can be given as an example of these kinds of crustal-scale low-angle normal faults. These large-scale structures are associated with heat exchange and fluid circulations representing a major interest in understanding hydrothermal systems. The Menderes massif of western Anatolia is the location of active exploitation of high-temperature geothermal resources related to extension and the activity of the main detachments. However, the rock-fluid interactions in the deep part of the geothermal reservoir are not accessible to observation. The detachments are coeval with the emplacement of granitoids and associated with the formation of a supra-detachment sedimentary basin during the Late Miocene [28]. Young tectonism (Gediz detachment fault) and young volcanism (Salihli granitoid and/or Kula volcanism) in the study area have caused the occurrence of a high-temperature geothermal system [2, 8].

High-temperature geothermal resources aligned on both the northern and southern edges of detachment faults in western Anatolia demonstrate that the heating source is related to active tectonism (shear heating) rather than a magmatic origin [2, 29]. The highest heat flow values in western Anatolia have a remarkable perfect harmony with detachment faults. This indicates that detachment faults provide a channel in the fluid circulation and can be regarded as a possible source of heat [29]. The Menderes Province represents a favorable setting for amagmatic high-enthalpy geothermal resources. The origin of these systems' heat may be also related to a deeper source induced by subduction dynamics (i.e., magmatic underplating under the overriding plate) [5, 30-32].

The geothermal reservoir in the study area appears to lie on the intersections of northerly striking sinistral normal transfer faults and the Gediz detachment fault. Left steps in the transfer faults at the intersection with the detachment fault are represented dilational jogs that provide channel ways for geothermal fluids. The left steps may result from refraction across the detachment surface that asides from the mechanical contrast between hanging-wall sedimentary rocks and basement gneisses, marbles, and schists in the footwall. Brecciated marble zone (Figure 3) at these intersections provides suitable reservoirs for the accumulation of geothermal fluids. The geothermal reservoirs are plunged gently northward along the intersection of the detachment fault with the transfer faults. Although this model can account for the shallow reservoir and surface springs, it may not be appropriate to predict the location of the main upwelling that feeds these geothermal systems. Significant steps in the Alaşehir border (main) fault or complex fault intersections between the transverse faults and WNW-striking normal faults may accommodate upwelling in the study area (Figure 12).

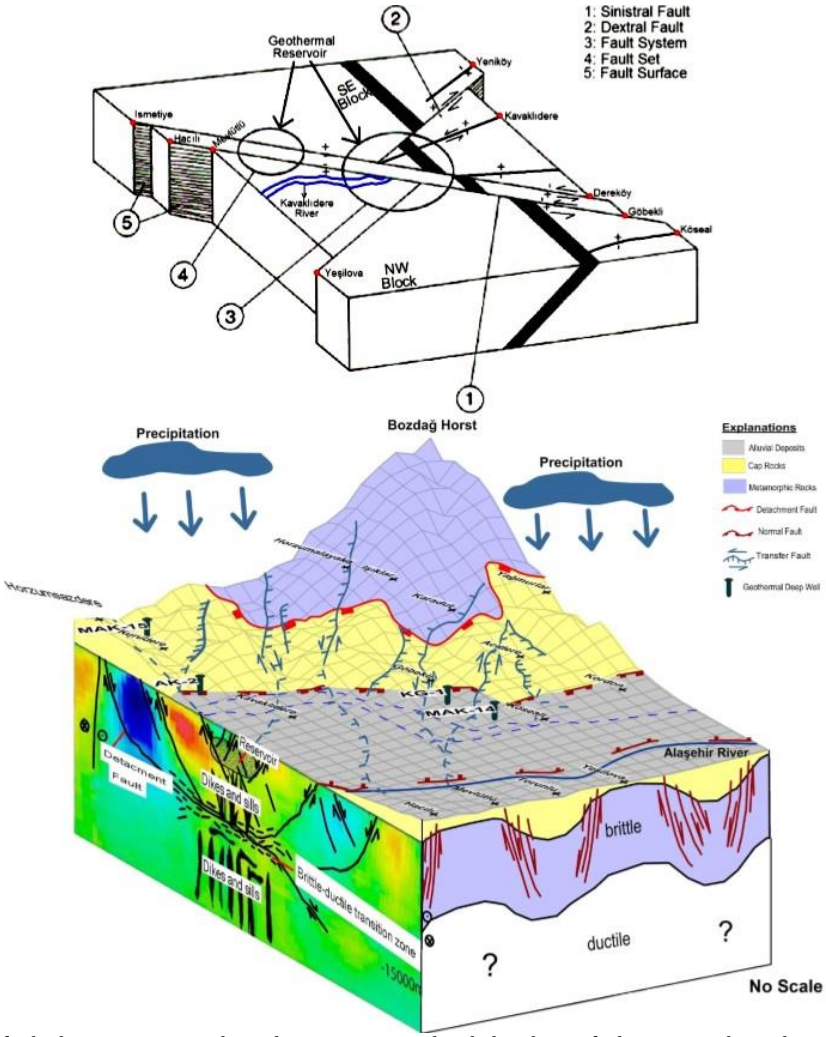

Figure 12. Conceptual models for high-temperature geothermal system associated with detachment fault system in the study area (modified from [2]).

The high-temperature geothermal reservoirs associated with detachment fault in the study area have formed along the normal faults nearly in E-W orientation and in intensely fractured rocks in a structurally complex manner associated with transfer faults approximately in N-S orientation. Generally, the high-temperature reservoirs are closely located to strike-slip faults intersecting, overlapping, and/or terminated with Quaternary transfer faults (oblique-slip hinge fault) (Figures 12 and 13). [33] emphasized the similar structural controls in the Kızıldere field, which is a high-temperature geothermal field associated with the Büyük Menderes Detachment Fault in western Anatolia. The same results as this study have also presented in the studies performed in western Anatolia and some regions of the world [31, 34-36].

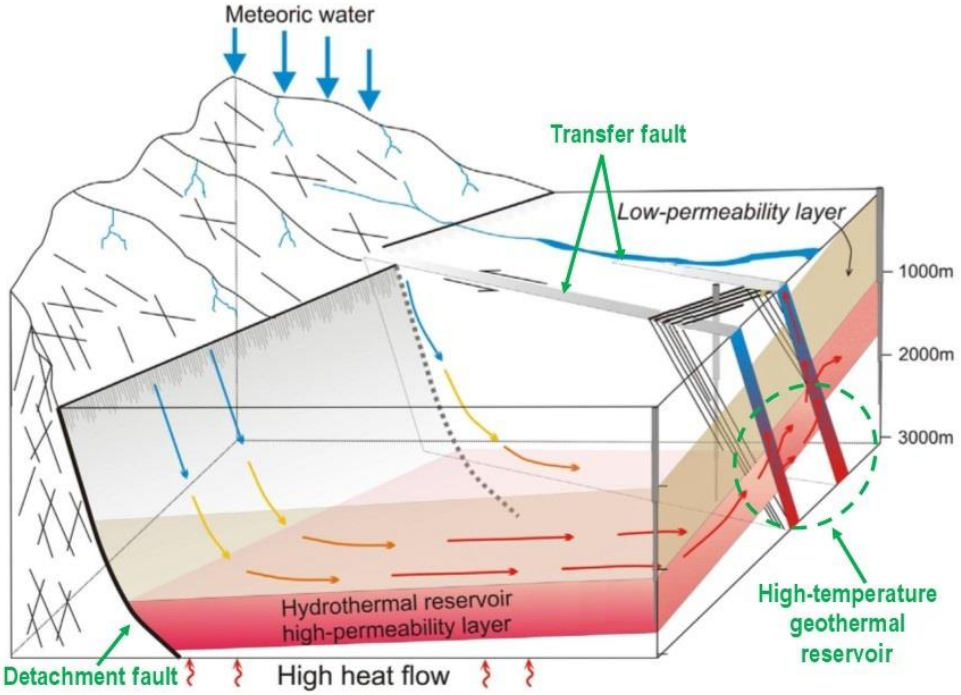

Figure 13. Schematic representation of a high-temperature geothermal reservoir formed at the intersection of the detachment fault and transfer fault (oblique-slip hinge fault) (modified from [35, 37].

4. CONCLUSIONS

High-temperature geothermal fields on Büyük Menderes and Gediz grabens' detachment faults show that these faults can be considered as one of the most potential areas in terms of research and exploration of high-temperature geothermal systems. Thus, in this study, to characterize the structural control of detachment, transfer, and dip-slip normal faults' association in the occurrence of high-temperature geothermal reservoirs, the main concentration has been on the determination of transfer faults and investigation of their relationships with detachment and dip-slip faults in high-temperature geothermal reservoir exploration activities associated with detachment fault in a detailed fashion. Since the detachment fault and the high-angle normal faults cutting the detachment fault form the paths, this mechanism ensures that the geothermal fluids are drained from the surface to the reservoir rock environment. High-angle normal faults cutting the detachment fault and the transfer faults cutting the detachment-high-angle normal faults constitute the carrier systems. This causes that the fluids heated in the reservoir rock environment at the depths are carried to the surface. Transfer faults control the position of high-temperature geothermal systems and should be used as the primary guide for geothermal exploration.

REFERENCES

[1] Ozdemir, A. "Geothermal Energy in Turkey: Potential, exploration methods, and features of known geothermal fields". Elma Publishing 354 p., 2012 (in Turkish).

[2] Ozdemir, A., Yaşar, E., Çevik, G. "An importance of the geological investigations in Kavaklıdere geothermal field (Turkey)". Geomechanics and Geophysics for Geo-Energy and Geo-Resources 3, 29-49, 2017.

[3] Ozdemir, A. Palabiyik, Y. "A new method for geological interpretation of 3D MT (Magnetotelluric) depth maps of high-temperature and deep geothermal fields: A case study from Western Turkey". Paper Presented at the 2nd Congress on Applied Sciences, Ankara, Turkey, 28-30 October, 2019.

[4] Ozdemir, A., Palabiyik, Y. Geological interpretation methods of resistivity measurements of high-temperature and deep geothermal fields: A study from Western Anatolia. European Journal of Science and Technology, 17, 1075-1091. 2019 (in Turkish).

[5] Hacıoğlu, Ö., Başokur, A.T., Diner, Ç., et al. "The effect of active extensional tectonics on the structural controls and heat transport mechanism in the Menderes Massif geothermal province: Inferred from three-dimensional electrical resistivity structure of the Kurşunlu geothermal field (Gediz Graben, western Anatolia)". Geothermics, 85, 101708, 2020

[6] Üner, S., Dogan, D.D. "An integrated geophysical, hydrological, thermal approach to finite volume modelling of fault-controlled geothermal fluid circulation in Gediz Graben". Geothermics, 90, 102004, 2021.

[7] Ozdemir, A., Arabaci, F., Palabiyik Y. "Reevaluation of geothermal potential of Çubukludağ Graben (Western Anatolia, Turkey)". International Journal of Earth Sciences Knowledge and Applications 3(2), 70-88, Y., 2021.

[8] Ozdemir, A., Palabiyik, Y., Arabaci, F. "Geological structure and geothermal potential of the southeastern Alaşehir, Gediz Graben (western Anatolia, Turkey)". International Journal of Earth Sciences Knowledge and Applications 3(3), 190-207, 2021.

[9] Ülgen, B.U., Damcı, E., Rose, F. "A new insight of the geothermal systems in Turkey: First geothermal power plant in mountainous area, "ÖZMEN-1 GEPP". Presented at the 7th Geological Congress of Turkey, Ankara, Turkey, 23-27 April, 2018.

[10] Aydin, H., Akin, S., Şentürk, E. "Evaluation of Production Capacity of Geothermal Power Plants in Turkey". GRC Transactions, 40, 163-174, 2020.

[11] Aydin, H., Akin, S., Tüzen, M.K., et al. "Artificial lifting in liquid dominated high-temperature geothermal fields in Turkey: Lessons learned". Paper Presented at the 46th Workshop on Geothermal Reservoir Engineering, Stanford University, Stanford, California, USA, 15-17 February, 2021.

[12] Aydin, H., Merey, Ş. "Changing casing-design of new geothermal wells in western Anatolia for adapting to the changes in reservoir conditions". Paper Presented at the 46th Workshop on Geothermal Reservoir Engineering, Stanford University, Stanford, California, USA, 15-17 February, 2021.

[13] Mertoğlu, O., Şimşek, Ş., and Başarır, N., "Geothermal energy use: Projections and country update for Turkey". Proceedings World Geothermal Congress 2020, Reykjavik, Iceland, April 26 - May 2, 2020.

[14] Mertoğlu, O., Şimşek, Ş., Başarır, N., Paksoy, H., "Geothermal energy use, country update for Turkey". European Geothermal Congress 2019, Den Haag, The Netherlands, 11-14 June, 2019.

[15] Canbaz, C.H., Temizel, C., Palabıyık, Y., Balıkçıoğlu, A., Yılmaz, İ.Ö., Aytuna, S., Aminzadehd, F., and Pamir, N., "Evaluation of geothermal potential of Turkey as an alternative source of energy under demand and supply dynamics of other energy resources". Turkey IV. Scientific and Technical Petroleum Congress, Ankara, Türkiye, 18 - 20 Kasım, pp. 37-48, 2020.

[16] Haklidir, F.S.T., and Nyokabi, J., "The comparison of reservoir characterizations and operational challenges at high temperature geothermal reservoirs in western Anatolia (Turkey) and Kenya". Proceedings, 8th African Rift Geothermal Conference, Nairobi, Kenya, 2 - 8 November, 2020.

[17] European Geothermal Energy Council (EGEC), "Geothermal Market Report; Key Findings", 23 p., 2021.

[18] Yılmaz, Y., Genç, S.C., Gürer, Ö.F., et al. "When did western Anatolian grabens begin to develop?" In: Bozkurt, E., Winchester, J.A., and Piper, J.D.A. (Eds.), Tectonics and Magmatism in Turkey and the Surrounding Area. Geological Society London Special Publications, 173, 353-384, 2000.

[19] Purvis, M., Robertson, A.H.F. "Sedimentation of the Neogene-Recent Alasehir (Gediz) continental graben system used to test alternative tectonic models from western (Aegean) Turkey". Sedimentary Geology 173, 373-408, 2005.

[20] Ersoy, Y.E., Helvaci, C. Stratigraphy and geochemical features of the Early Miocene bimodal (ultrapotassic and calc-alkaline) volcanic activity within the NE trending Selendi Basin, Western Anatolia, Turkey. Turkish Journal of Earth Sciences 2007, 16: 117-139.

[21] Ersoy, Y.E., Helvaci, C., Sözbilir, H. "Tectono-stratigraphic evolution of the NE-SW-trending superimposed Selendi basin: Implications for late Cenozoic crustal extension in Western Anatolia, Turkey". Tectonophysics, 488, 210-232, 2010.

[22] Bozkurt, E. "Origin of NE-trending basins in western Turkey". Geodinamica Acta, 16: 61-81, 2003.

[23] Arpat, E., Bingol, E. The rift system of western Turkey: Thoughts on its development. Bulletin of the Mineral Research and Exploration Institute of Turkey, 1969, 75: 1-9.

[24] Eyidogan, H., Jackson, J. "A seismological study of normal faulting in the Demirci, Alasehir, and Gediz earthquakes of 1969-70 in western Turkey: Implication for the nature and geometry of deformation in the continental crust". Geophysical Journal of the Royal Astronomical Society, 81, 569-607, 1985.

[25] Çiftçi, N.B., Bozkurt, E. "Pattern of normal faulting in the Gediz Graben, SW Turkey". Tectonophysics, 473, 234-260, 2009.

[26] Çiftçi, N.B., Bozkurt, E. Structural evolution of the Gediz Graben, SW Turkey: Temporal and spatial variation of the graben basin. Basin Research 22: 846-873, 2010.

[27] Gürer, A., Gürer, Ö.F., Pinçe, A., et al. "Conductivity structure along the Gediz graben, West Anatolia, Turkey: Tectonic implications". International Geology Review, 43, 1129-1144, 2001.

[28] Faure, A., Jolivet, L., Verlaguet, A., et al. "Fluid circulations in detachment faults: insights from Mykonos Metamorphic Core Complex". EGU General Assembly, 4-8 May, 2020.

[29] Kaya, A., Aydın, A., Taşdelen, S., et al. "An assessment on heat source of geothermal fields in Büyük Menderes and Gediz grabens, SW Turkey". International Journal of Advances in Science Engineering and Technology, 5(3), 36-42, 2017.

[30] Roche, V., Sternaid, P., Guillou-Frottier, L. et al. "Emplacement of metamorphic core complexes and associated geothermal systems controlled by slab dynamics". Earth and Planetary Science Letters, 498, 322-333, 2018.

[31] Roche, V., Bouchot, V., Beccaletto, L., Jolivet, L. et al. "Structural, lithological, and geodynamic controls on geothermal activity in the Menderes geothermal Province (Western Anatolia, Turkey)". International Journal of Earth Sciences, 108, 301-328, 2019.

[32] Hermant, B., Colas, E., Patriarche, D., Auxiètre, J., and Bellanger, M. "New Classification of High Temperature Geothermal Systems Based on 110 Geothermal Fields Worldwide". European Geothermal Congress, Den Haag, The Netherlands, 11-14 June, 2019.

[33] Aksu, B. "Structural Controls on Kızıldere Geothermal Field, Denizli-Turkey". Middle East Technical University, MSc Thesis, Ankara, 2019.

[34] Faulds, J.E. and Hinz, N.E. "Favorable tectonic and structural settings of geothermal systems in the Great Basin region, Western USA: Proxies for discovering blind geothermal systems". Proceedings Presented at World Geothermal Congress, Melbourne, Australia, 19-25 April, 2015.

[35] Ozdemir, A. and Palabiyik, Y. "Role of scissor faults in geothermal reservoir occurrence". Presented at Congress of UMUH-BILMES, Ankara, Turkey, 07-10 November, 2019.

[36] Palabiyik, Y. and Ozdemir, A. "Potential of detachment folds to become a geothermal reservoir in a horst". Presented at Congress of UMUH-BILMES, Ankara, Turkey, 07-10 November, 2019.

[37] Moeck, I. "Catalog of geothermal play types based on geologic controls". Renewable and Sustainable Energy Reviews, 37, 867-882, 2014.

BIOGRAPHIES

Adil Ozdemir started his career as a drilling worker/driller. He graduated from the Drilling Technology Division of Cumhuriyet University as a Technician, from the Geological Engineering Department of Ankara University as an Engineer, from the Civil Engineering Department (Geotechnical Division) of Gazi University with a Master of Science degree. He continues his doctoral courses at the Geological Engineering Department of Ataturk University. Researcher in Scientific Research Projects of İstanbul Technical University, Marmara University, İstanbul Gedik University and İstanbul Esenyurt University, Adjunct Professor at Petroleum and Natural Gas Engineering Department of İskenderun Technical University, and General Manager Consultant at Turkish Petroleum International Company (TPIC) has worked. He has 11 professional books published and more than 100 articles and full-text conference papers in professional national and international journals/congresses. He is an editorial board member (Earth Sciences, International Journal of Earth Sciences Knowledge and Applications, Journal of Petroleum Engineering & Technology, etc.) and reviewer (Petroleum Science and Technology, International Review of Applied Sciences and Engineering, Journal of Petroleum Engineering & Technology, etc.) in many international scientific journals. He has scientific studies as a chapter author in professional books published by leading publishing houses of the World and Turkey (Elsevier, Springer, etc.). He has worked in subsurface resources (geothermal, mineral, coal, groundwater, and oil & gas) research and exploration projects for more than 20 years. Currently, He works as an engineer and consultant in the energy and mining sectors.

Yildiray Palabiyik is an assistant professor of the Petroleum and Natural Gas Engineering Department (PNGED) at Istanbul Technical University (ITU) in Turkey. He holds BSc degree from the Geological Engineering Department at the Dokuz Eylul University of Turkey. He has also MSc and PhD degrees from PNGED at ITU. He has over 15 years of experience related to research, teaching, and supervising at ITU and 1-year postdoctoral research associate associated with Unconventional Reservoir Engineering Project (UREP) Consortium at Petroleum Engineering Department of Colorado School of Mines in USA. He has over 80 publications available in the literature.

Fahri Arabaci received his BSc degree in geological engineering from Kocaeli University in 2017. Currently, he is an MSc student in Petroleum and Natural Gas Engineering at The Graduate School of Natural and Applied Science, Iskenderun Technical University. His main research interest is drilling engineering, geothermal research, oil & gas exploration. He is currently a engineer in the energy and mining sectors.

European Journal of Technique

journal homepage: https://dergipark.org.tr/en/pub/ejt

Vol.12, No.1, 2022

Contagious Effect of COVID-19 Pandemic by High Speed Train Transportation in Turkey

Hümeyra BOLAKAR TOSUN

Aksaray University, Civil Engineering Department, Aksaray, Turkey. (bolakarhumeyra@gmail.com)

ARTICLE INFO

Received: Apr., 06. 2022
Revised: May., 16. 2022
Accepted: May, 20. 2022

Keywords:
Transportation
Covid 19
Risk of covid transmission
High speed train
Regression

Corresponding author:
Hümeyra Bolakar Tosun

ISSN: *2536-5010* | e-ISSN: *2536-5134*

DOI: https://doi.org/10.36222/ejt.1099728

ABSTRACT

The transportation sector was affected by the Covid-19 pandemic all over the world. In this study, the relationship between the passenger density at high-speed train points and the spread of the Covid-19 epidemic was examined. In addition, the temporal situation of the pandemic was examined by evaluating based on a year and month. In this context, high-speed train passenger movement is mathematically modelled using regression analysis. Strong relation between number of patient and number of passenger. As a result, it was observed that the number of patients increased as the number of passengers increased. In order to limit the epidemic, it may be recommended to increase measures especially in transportation centres.

1. INTRODUCTION

Towards the end of December, the Chinese government reported an outbreak of a novel coronavirus disease (COVID-19) in Wuhan city, Hubei Province, China [1]. The outbreak rapidly spread from Wuhan into all provinces of China and then at least 24 countries, which led the WHO (World Health Organization) to declare the coronavirus disease 2019 (COVID-19) outbreak a pandemic on March 11, 2020, when the disease was confirmed to have reached Turkey. Since then, COVID-19 had spread all over [2-4]. Transportation developments in the industry can reach many parts of the World. But when it comes to a disaster such as a pandemic, global transportation networks can contain significant threats [5]. Especially in long-distance travel, because of limited space in transportation the risk of disease transmission was increasing [6]. Pandemics are often seeing where places in mobile population, and transportation systems due to high population density [7]. Global transportation points such as airports, ports, and stations, can become easily the center of disease distribution. The reason for the rapidly spread of the Spanish Flu around the world is that the transportation systems are developed at the global level [8]. In a pandemic disease such as SARS, air and sea travels have a great effect on the spread of the disease [9]. Shen et. al., studied the experience of the prevention and control measures for public transportation in China to promote the global response to COVID-19 [10]. Setiawan et.al. studied constructs and visualizes bibliometric networks research in Covid19, Sustainable Mobility And Transportation Research [11]. Ballard in his study obtained that roadway and rail transportation further spread the infection across cities and countries [12].

Chechulin et al. in their study showed that the highest rate of spread of disease was seen in intercity public transportation and private transportation [13]. Public transport systems, cause it to be seen rapidly and intensely in megacities the spread of the virus by creating serious risks in the spread of diseases and the formation of pandemics [14,15]. Transportation developments in the industry can reach many parts of the World. But when it comes to a disaster such as a pandemic, global transportation networks can contain significant threats.

Considering the past experiences, epidemic diseases are primarily spread from global transportation networks, then from central transportation points to cities and rural areas. Domestic transportation systems are an indispensable part of human activities. High-speed trains bring convenience to people's life and are generally considered one of the most sustainable developments for public transportation. In Turkey, the Ankara-Eskişehir section, the first phase of the Ankara-İstanbul High-Speed Railway Project, was put into service in 2009, and the Eskişehir-İstanbul section in 2014 in order to reduce the travel time between Ankara and İstanbul, which are the biggest cities of Turkey. The high-speed train operation is being successfully performed over a corridor of 1,213 km, covering 13 cities and 42 percent of the population in Turkey, with combined transportation between Ankara, Istanbul,

Eskişehir, and Konya. More than 52 million people have travelled on these lines (see Fig. 1) [16].

Figure 1. Destinations of high-speed trains in Turkey.

Ankara is the capital city of Turkey and the country's second-largest city after Istanbul and most important the high-speed train operation hub in Turkey. High-speed train destinations constitute approximately 90% of the total population of Turkey.

The aim of this study examined the relationship between the passenger density at high-speed train points and the spread of the COVID 19 pandemic. In this context, high-speed train passenger movement is mathematically modeled using regression analysis. The number of trips and the number of patients was examined by months and by 2020 and 2021. In order to evaluate the effect of public transportation in the spatial transmission of COVID 19, it was examined that daily High-speed trains from Ankara to these cities.

2. MATERIAL AND METHODS

2.1. Regression Analysis

There are two separate purposes of multiple linear regression analysis:

- By means of indicators that are determined to affect the dependent indicator
- To determine the rate at which the independent indicators are thought to affect the dependent indicator [17].

According to multiple linear regression analysis, there should be at least two independent indicators. Y relationship model between the dependent indicator and p number of independent indicators. This is shown in equation (1).

$$Y = b_0 + (b_1\ x\ i_1) + (b_2\ x\ i_2) + \ldots + (b_p\ x\ b_p) + e_i \quad (1)$$

In there b0, b1,...,bp unknowns part are regression coefficients.

2.2. Estimation of Coefficients İn Multiple Linear Regression Analysis

The simple linear regression model may be suitable for many situations, but in real life, explanatory variables are needed to explain many models. More than one Model with explanatory variables is called a multiple regression model. Multiple In the regression model, there is a single dependent variable and two or more independent variables. The relationship between the variables is investigated. A dependent indicator showing normal distribution is a random variable [18]. The relationship between dependent and independent variables in multiple linear regression analysis shows the strength of the multi-correlation coefficient and has an unlimited number of explanations for the dependent variable [19].

2.3. Statistical Analysis Methods

In the analysis of data; descriptive statistics are presented with mean and standard deviation values. Mann Whitney U test and Kruskall Wallis test were applied to examine the measurements according to the study groups. The All-pairwise method was used to evaluate the measurements that differed from the Kruskall Wallis test. Correlation analyzes were applied to determine the relationship between the measurements. Regression analysis was performed to examine the relationship between the number of patients and the number of passengers at multiple levels. Analyzes were made with SPSS (Statistical Package for the Social Sciences) 25.00 package program.

3. FINDINGS AND DISCUSSION

The purpose of multiple regression analysis is to explain and predict the effect of change in independent variables on the dependent variable. In the study, the analysis results of the relationship between the number of passengers and the number of patients are expressed with tables and figures.

TABLE I
EVALUATION OF THE NUMBER OF PASSANGER and PATIENTS by MONTH AND YEAR

		Total number of passenger		Total number of patients	
		X+s.s (arithmetic mean)	p	X+s.s. (arithmetic mean)	p
Month	1	4704.82+1333.67	0.34	5699.18+2594.34	0.08
	11	4876.17+377.51		6991.50+460.59	
	12	4222.26+1661.94		5096.45+2141.60	
Year	2020	4328.30+1543.11	0.11	5403.76+2086.38	0.19
	2021	4704.82+1333.67		5699.18+2594.34	

In the study, it was determined that the total number of passengers was not at different levels according to the months, and the total number of passengers in the 1st, 11th, and 12th months was found to be at similar levels (p=0.34). Similarly, it was determined that the total number of patient was not at different levels according to the months, and the total number of the patients in the 1st, 11th, and 12th months were found to be at similar levels (p=0.08).

According to the study, it was determined that the total number of passengers was not at different levels according to the years, and the total number of passengers in 2020 and 2021 was at similar levels in the study (p=0.11). And, it was determined that the total number of cases was not at different levels according to the years, and the total number of cases in 2020 and 2021 were found to be at similar levels (p=0.19).

TABLE II
RELATIONSHIP BETWEEN PATIENT and PASSANGER NUMBER in 2020 and 2021

Year			Total number of patients
2020	Total number of passenger	r	0.89*
		p	0.01
2021	Total number of patients	r	0.95*
		p	0.01
Total	Total number of passenger	r	0.90*
		p	0.01

*Correlation analysis was performed.

It has been observed that there is a very strong and positive relationship between the total number of passengers and the number of patients for the period of 2020 and 2021. It can be stated that increase number of passengers will increase the number of patients. (r=0.90, p=0.01). (correlation coefficient takes a value between -1<r<1.

TABLE III
MODELING THE PATIENT and PASSANGER NUMBER RELATIONSHIP in 2020 and 2021

Year	Dependent Variable	Independent Variables: Total number of passenger (β)	F_{Model}	R^2
2020	Total number of patients (Y)	0.89 t=11.48 p=0.01	F=131.68 (p=0.01)	0.78
2021	Total number of patients (Y)	0.95 t=13.52 p=0.01	F=175.1 (p=0.01)	0.89
2020	Total number of patients (Y)	0.90 t=9.29 p=0.01	F=233.19 (p=0.01)	0.80

** Regression analysis was performed.

In the study, regression analysis was performed in order to determine whether there is a multiple relationship between the number of cases and the number of passengers in all three models made at the 2020-2021.

All three models obtained in the study were found to be significant (p=0.01). The coefficients (β) of the variable of the number of passengers in the model were found to be significant for 2020, 2021 and the total period (p=0.01). The explanatory ability of the model for 2020 was 78% (R2 =0.78), the explanatory ability for 2021 was 89% (R2 =0.89), and the explanatory ability for the total model was 80% (R2 =0.80).

In general, it was observed that there was a very strong and positively relationship between the number of patients and the number of patients in both of the 2020 and 2021 periods (p=0.01). But the relationship in 2021 is stronger than in 2020.

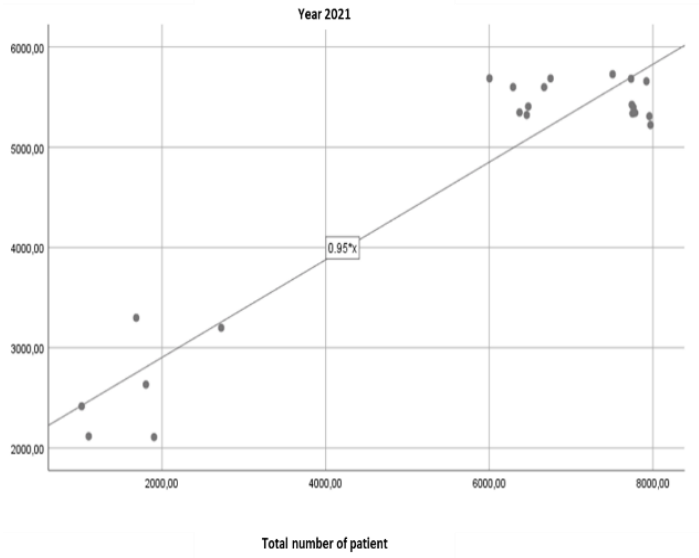

Figure 2. Modeling the Patient and Passenger Number relationship for 2020.

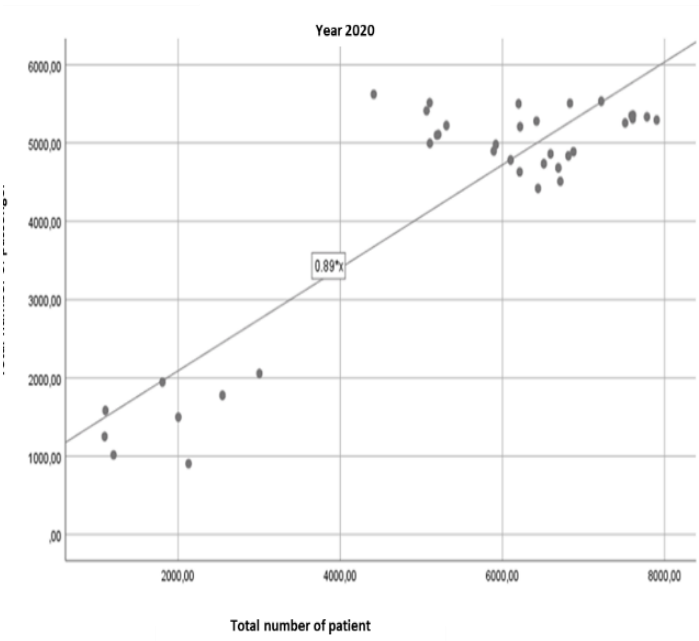

Figure 3. Modeling the Patient and Passenger Number relationship for 2021.

The model was obtained according to these results:

2020 Total number of patients (Y)= (0,89)* Total number of passenger

2021 Total number of patients (Y)= (0.95)* Total number of passenger

Total number of patients (Y)= (0.90)* Total number of passenger

The increase in the number of passengers for all three models caused an increase in the number of patients However, the most increasing effect occurred in 2021. It has been observed that the effect of the number of passengers has a high effect on the number of patients.

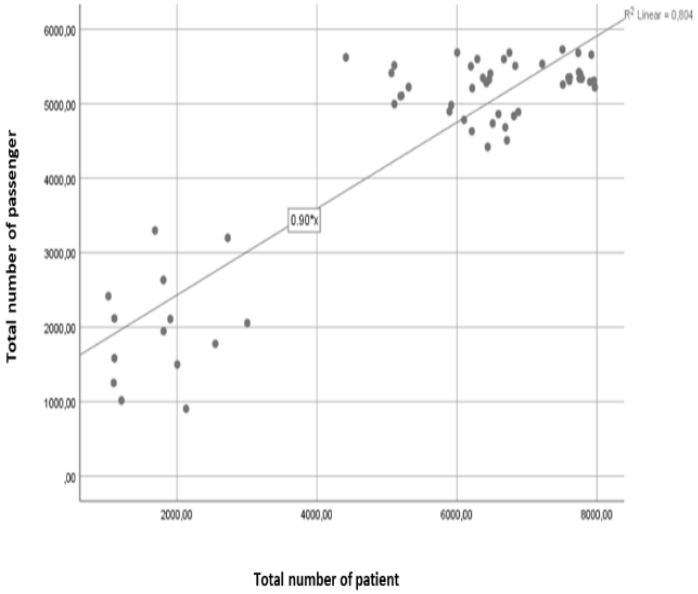

Figure 4. Modeling the Patient and Passenger Number Relationship for Total Period.

4. CONCLUSION

It has been determined that there is an increase in the number of covid 19 cases in the settlement provinces where the number of high-speed train passengers is dense. When we look at the types of transportation in general, they are vehicles such as buses, taxis, minibuses, trains and planes. Depending on the nature of the microorganism that causes the disease in public transportation vehicles, the ways of transmission are differentiated as direct contact, indirect contact, droplet contact or airborne transmission. Direct transmission is the transmission of the microorganism responsible for the disease by physical contact. Increasing contact in increasingly crowded public transport environments also increases the possibility of transmission of the disease. Indirect transmission, on the other hand, refers to the transmission of the disease when it comes into contact with a contaminated surface, although it depends on the type of microorganism, the material of the surface, and the frequency of cleaning and spraying the surface.

In order to limit the pandemic, it may be recommended to increase measures especially in transportation centers. After the pandemic, the developments enabled us to experience urban mobility in extraordinary conditions such as epidemics, reminding once again that it is inevitable to make urban transportation durable and sustainable. Considerable efforts to reduce transmission will be required to control outbreaks. Measures to prevent or reduce transmission should be implemented in travel populations at risk. As a result of this, applications to open more space for pedestrian and bicycle transportation, which are the main components of sustainable transportation, started to increase all over the world

ACKNOWLEDGEMENT

I want to thank State Railways of the Republic of Turkey for giving the data.

REFERENCES

[1] Li, Q., Guan, X., Wu, P. “Early transmission dynamics in Wuhan, China, of novel coronavirus-infected pneumonia” N Engl J Med., 29, 2020. doi: 10.1056/NEJMoa2001316.

[2] Zhu, N., Zhang, D.,Wang, W., Li, X., Yang, B., Song, J., Zhao, X., et al. “A Novel Coronavirus from Patients with Pneumonia in China” The New England Journal of Medicine, 382, 727-733, 2019. DOI: 10.1056 / NEJMoa2001017.

[3] Kang, D., Choia, H., Kimb, C.H., Choic, J. “Spatial epidemic dynamics of the COVID-19 outbreak in China” International Journal of Infectious Diseases, 2020. doi.org/10.1016/j.ijid.2020.03.076.

[4] Satici, B.G., Tekin, E, Deniz, M.E, Satici, S.A. “Adaptation of the Fear of COVID-19 Scale: Its Association with Psychological Distress and Life Satisfaction in Turkey” International Journal of Mental Health and Addiction, 2020.

[5] Erkek, E. E. and Çabuk, S. N. COVID-19 “Pandemi Sürecinde Toplu Ulaşım Sistemlerinin Değerlendirilmesi” GSI Journals Serie B: Advancements in Business and Economics, 3(2), 17-31, 2021.

[6] Litman, T. “Pandemic - Resilient Community Planning” The National Academies of Sciences, Engineering, and Medicine, 27p., 2020. https://www.vtpi.org/PRCP.pdf.

[7] Lak, A., Shakouri Asl, S. and Maher, A. Resilient Urban Form to Pandemics: Lessons From COVID-19. Medical Journal of The Islamic Republic of Iran (MJIRI), 34(1), 502–509, 2020. https://doi.org/10.34171/MJIRI.34.71

[8] Rodrigue, J.-P., Comtois, C. and Slack, B. “The Geography of Transport Systems” In The Geography of Transport Systems, 2013. https://doi.org/10.4324/9781315618159-8

[9] Meyer, M. and Elrahman, O. “Transportation and Public Health” In Transportation and Public Health, 201–253, 2019. https://doi.org/10.1016/B978-0-12-816774-8.00008-6

[10] Shen, J., Duan, H., Zhang, B., Wang, J., Ji, J. S., Wang, J., & Shi, X. (2020). “Prevention and control of COVID-19 in public transportation: Experience from China” *Environmental pollution*, *266*, 115291. Chechulin, D., Melnikov, L. and Pokotilo, V. Reopening Cities After COVID-19. McKinsey & Company, July, 2020.

[11] Setiawan, M. I., Nasihien, R. D., Razi, M. A. M., Sukoco, A., & Rosyid, A. (2021). Covid19, “Sustainable Mobility and Transportation Research” IJEBD International Journal Of Entrepreneurship And Business Development eISSN 2597-4785 pISSN 2597-4750, 4(1), 123-130.

[12] Ballard, M. “ How big of a factor were commuters in spreadingcoronavirus in Louisiana?” p.13, 2020.

[13] Betkier, I. “Safety of Urban Transport Users During The Covıd-19 Pandemic” July, 2020.

[14] Qian, X., Sun, L., & Ukkusuri, S. V. “Scaling of Contact Networks for Epidemic Spreading in Urban Transit Systems” 24–26, 2020. http://arxiv.org/abs/2002.03564.

[15] Yılmaz, V., Arı, E. “The effects of service quality, image, and customer satisfaction on customer complaints and loyalty in high-speed rail service in Turkey: a proposal of the structural equation model” Transportmetrica A: Transport Science, 2324-9943, 2016.

[16] Ai, B., Cheng, X., Kürner, T., Zhong, Z.D., Guan, K., He, R.S. “Challenges toward wireless communications for high-speed railway” Iee Transactıons on İntellegent Transportation Systems, 15, 5, 2014.

[17] Alpar, R. “Uygulamalı Çok Değişkenli İstatistiksel Yöntemlere Giriş I” Nobel Yayın Dağıtım, 408, 2013.

[18] Atalay, A, “Türkiye’deki Trafik Kazalarının Mekansal ve Zamansal Analiz”. Ph.D. Thesis, Atatürk University, Erzurum, 2010.

[19] Ünver, Ö., Gamgam, H. “Uygulamalı Temel İstatistik Yöntemler” Seçkin Kitapevi, 424, 2008.

BIOGRAPHIES

Hümeyra Bolakar Tosun was born in Aksaray, Turkey. She has a PhD dgree from Ataturk University, the Department of Transportation Discipline in Civil Engineering. She has been working Assist Professor in the Department of Civil Engineering, Aksaray University.

European Journal of Technique

journal homepage: https://dergipark.org.tr/en/pub/ejt

Vol.12, No.1, 2022

The Effects of Reinforcement with TaC on the Microstructure and Wear Properties of Lamellar Graphite Cast Irons

Rifat Yakut[1*], **Ömer Çiftçi**[2]

[1*]Batman University, Department of Energy Systems Engineering, Batman, Turkey. (e-mail: rifat.yakut@batman.edu.tr).
[2] Batman University, Department of Mechanical Engineering, Batman, Turkey. (e-mail: 93ciftciomer@gmail.com).

ARTICLE INFO

Received: Mar., 16. 2021
Revised: Jun., 22. 2022
Accepted: Jun, 30. 2022

Keywords:
Wear
Lamellar Graphite Cast Iron
Tantalum Carbide (TaC)

Corresponding author: *Rifat Yakut*

ISSN: *2536-5010* | e-ISSN: *2536-5134*

DOI: https://doi.org/10.36222/ejt.1088994

ABSTRACT

In this study, changes in the wear volumes, wear rates, wear track profiles, and friction coefficients of lamellar graphite cast irons in which Tantalum Carbide (TaC) was added at different reinforcement ratios (A (0.025 wt.%), B (0.155 wt.%), C (0.285 wt.%), and K (unreinforced, 0 wt.%)) were investigated. Additionally, by examining the wear surfaces of the samples using a scanning electron microscope (SEM), their wear mechanisms were determined. As a result of the analyses, it was determined that different reinforcement ratios did not have a noticeable effect on wear track profiles under a load of 1 N. On the other hand, different reinforcement ratios showed an effect on wear track profiles under loads of 3 N and 5 N. The most perceptible wear track profile was formed in Sample C under 5 N. It was observed that increased load values resulted in increased wear volumes, but the increases in the wear rates of the samples were not significant, and the numerical values were close to each other. The highest wear volumes were determined in the reinforced C sample and the unreinforced K sample under 5 N load. As the magnitude of the load that was applied increased, the friction coefficients of Samples B and C decreased, but the friction coefficients of Samples K and A increased.

1. INTRODUCTION

The first development in the production of cast iron materials has been the production of lamellar graphite cast irons (gray cast irons) by applying the inoculation method [1, 2]. Lamellar graphite cast irons are the most frequently used material in machine manufacturing [3-7]. They are inexpensive and easily accessible materials in the manufacturing of piston rings and cylinder jackets in the automotive industry. The unique properties of cast iron consist of a combination of good mechanical and physical properties and economical manufacturing processes [8-14]. As a disadvantage, they have weak weldability [15].

One of the significant problems that are frequently encountered in today's industry is wear. In the technical sense, wear is the phenomenon where an unwanted change occurs in the material as a result of the separation of microparticles from the surface of the material caused by a mechanical factor or mechanical energy [16]. In a wear system, the main material (wearing material), the counter material (abrasive), the spacing material, load and motion constitute the primary elements of wear. The system created by all these elements is called a "Tribological System". In a wear system, environmental conditions are also important factors. The exposure of system elements to humidity or corrosive effects also speeds up wear [2, 17]. The properties of the main material (e.g., microstructure, surface hardness, heat treatment), the properties of the counter material, and atmospheric conditions such as temperature and humidity are factors that affect wear in a tribological system. In addition to these, some properties of materials depending on their service conditions (e.g., form of loading) have a substantial effect on their wear mechanism [18].

TaC is a highly popular material due to its resistance to high temperatures and good mechanical properties at high temperatures. In this study, materials were produced by adding TaC as reinforcement at varying ratios (A, B, C, and unreinforced K) to materials that are used in the production of lamellar graphite cast irons. Experimental samples were prepared from the materials produced at different reinforcement ratios, and mechanical and wear tests were carried out. In these tests, the effects of the TaC reinforcement ratios on lamellar graphite cast irons were investigated.

2. MATERIAL AND METHOD

2.1. Material manufacturing

The chemical compositions of the A, B, C and K (unreinforced) alloys are shown in Table 1. These alloys were melted in a casting furnace and poured separately into sand molds at a final pouring temperature of 1375°C. TaC had a purity of 99.9%, and its particle size was 3 µm. During the casting process, inoculation material was added at a ratio of 0.3% by weight. The chemical composition of the inoculation material is given in Table 2.

TABLE I.
CHEMICAL COMPOSITIONS OF SAMPLES (WT.%)

No	C	Si	Mn	P	S	Cr	Cu	Al	Ti	TaC
A	3.36	2.68	0.68	0.006	0.067	0.28	0.08	0.001	0.033	0.025
B	3.38	2.70	0.64	0.017	0.083	0.28	0.12	0.001	0.033	0.155
C	3.23	2.71	0.63	0.016	0.086	0.28	0.12	0.001	0.025	0.285
K	3.30	2.70	0.63	0.016	0,080	0.28	0.12	0.001	0.025	-

TABLE II.
CHEMICAL COMPOSITION OF INOCULATION MATERIAL

	% Si	% Al	% Ca	% Sr
Min-Max	73.0-78.0	0.50 max	0.100 max	0.80-1.40
Sample Castings	75.0	0.32	0.020	1.06

2.2. Sample preparation for wear tests

After the casting process, the samples were taken out of their sand molds when they reached room temperature. Samples for the wear tests were prepared at dimensions of 50 mm × 30 mm × 5 mm, and the wear test surfaces were polished. The wear tests were carried out in 3 repetitions for each reinforcement ratio.

2.3. Wear tests

The wear tests were conducted using a reciprocating Tribotech tribotester device (Figure 1) under normal atmospheric conditions (22±1°C and 30±2% humidity) in a dry setting. Alumina balls with a diameter of 6 mm were used as the abrasive material. The tests were performed under load values of 1 N, 3 N and 5 N, with a sliding speed of 10 mm/s, a sliding length of 5 mm, and a total sliding distance of 50 m. Coefficients of friction were recorded during the tests. After the wear tests, the wear tracks were examined using a surface profilometer (Veeco Dektak 6M) and SEM [19, 20].

Figure 1. Wear test device

3. RESULTS AND DISCUSSION

3. 1. Wear tests

Coefficients of friction, wear track profiles, wear volumes and wear rates were determined in the wear tests for the samples that were prepared at different TaC reinforcement ratios (0.025, 0.155, and 0.285 wt.%), and the values were compared to those of the unreinforced sample (0 wt.%). Table 3 presents the wear volume, wear rate and mean coefficient of friction values of the samples.

TABLE III.
WEAR VOLUME, WEAR RATE AND MEAN COEFFICIENT OF FRICTION VALUES OF THE SAMPLES

Sample	Load (N)	Wear Volume ($\times 10^{-3}$ mm^3)	Wear Rate ($\times 10^{-5}$ mm^3/Nm)	Mean Coefficient of Friction
K (0 wt.% TaC)	5	4.2	1.7	0.508
A (0.025 wt.% TaC)	5	3.8	1.5	0.475
B (0.155 wt.% TaC)	5	4.0	1.6	0.548
C (0.285 wt.% TaC)	5	4.3	1.7	0.555
K (0 wt.% TaC)	3	2.1	1.4	0.530
A (0.025 wt.% TaC)	3	2.4	1.6	0.516
B (0.155 wt.% TaC)	3	2.2	1.5	0.561
C (0.285 wt.% TaC)	3	2.9	1.9	0.608
K (0 wt.% TaC)	1	0.9	1.7	0.507
A (0.025 wt.% TaC)	1	1.2	2.3	0.453
B (0.155 wt.% TaC)	1	0.8	1.5	0.572
C (0.285 wt.% TaC)	1	0.9	1.9	0.575

As seen in Table 3, in the comparison of the results of each load value, with the increasing reinforcement ratios, there were no increases in the wear volume and wear rate values of the samples, and the values stayed more or less constant. With increased load values, there were increases in the wear volume results, while the wear rate results were similar to each other at different loads. The highest wear volume values were found under the 5 N load in Sample C as 4.3×10^{-3} mm^3 and the unreinforced K sample as 4.2×10^{-3} mm^3. The highest wear rate was found under the 1 N load in Sample A as 2.3×10^{-5} mm^3/Nm. Şimşek et al. added SiCp reinforcement into the A356 matrix at ratios of 5%, 10%, 15%, and 20% and subjected the samples to wear tests at 0.2 m/s, under a load of 15 N, and at a total distance of 1500 m. As a result of the tests, they determined that as the reinforcement ratio increased at constant load values, the number of particles breaking off the sample decreased, and thus, at increased reinforcement ratios, weight loss decreased [21]. In this study, when each load among the 1 N, 3 N and 5 N load values was analyzed independently of the other loads, it was seen that wear rates had an increasing trend along with increased reinforcement ratios, but there was no substantial change in the wear volumes.

To determine the wear profiles of the samples, the depths and widths of the wear tracks that formed on the surface during the experiments were measured using a Veeco Dektak 6M model surface profilometer. Figure 2 shows the schematic representation of the depth and width of a wear track. Using these depth and width values and assuming that the wear track was semielliptical, wear volume was first calculated using equation (1), and then, wear rate was calculated using equation (2). The wear track profiles of the samples that were subjected to wear experiments are given comparatively in Figure 3.

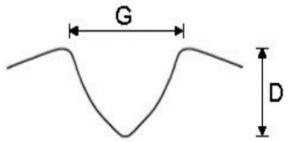

Figure 2. Schematic display of the depth and width of the wear track [20, 22, 23].

$$V = \frac{\pi}{4} \cdot G \cdot D \cdot \mathrm{L} \quad (1)$$

$$W = \frac{V}{F \cdot S} \quad (2)$$

V: Wear volume (mm^3), G: Wear track width (mm), D: Wear track depth (mm), L: Reciprocal motion amplitude (5 mm), W: Wear rate (mm^3 / Nm), F: Experimental load (N), S: Total sliding distance (50 m)

In the examinations of the wear track profiles of the samples, it was observed that changes in reinforcement ratios under 1 N of load did not have a noticeable effect on these profiles. On the other hand, under the 3 N load, changes in reinforcement ratios affected the wear track profiles of the samples. The most prominent wear track profile under the 3 N load was formed in Sample C. Under the 5 N load, the varying reinforcement ratios had the highest effects on the wear track profiles of the samples, where the most prominent wear track profile was found in Sample C.

The changes that occurred in the friction coefficients of the samples that were subjected to wear experiments depending on sliding distance can be seen in Figure 4. In the wear experiments, the coefficients of friction reached steady-state values following a sliding distance of 10 m, no significant change was observed in these values until the end of the experiments.

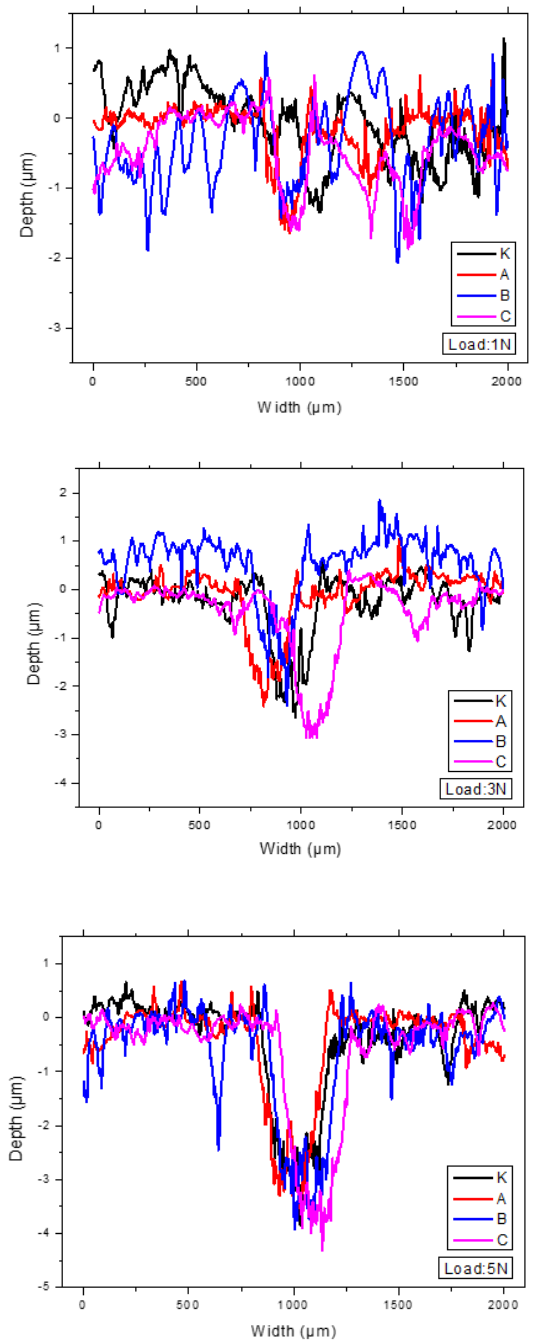

Figure 3. Comparison of the wear track profiles under 1 N, 3 N, and 5N

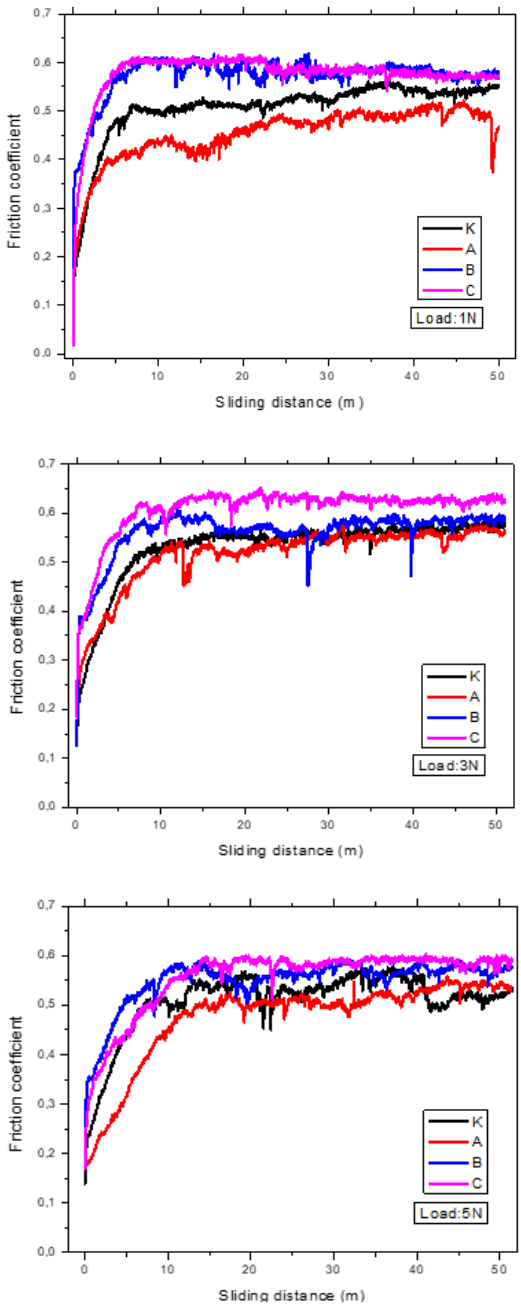

Figure 4. Comparison of the coefficients of friction under 1 N, 3 N, and 5 N

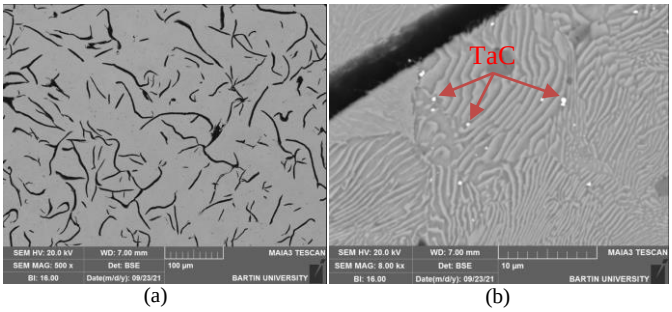

(a) (b)

Figure 5. SEM Microstructure image of sample no. B, a,b

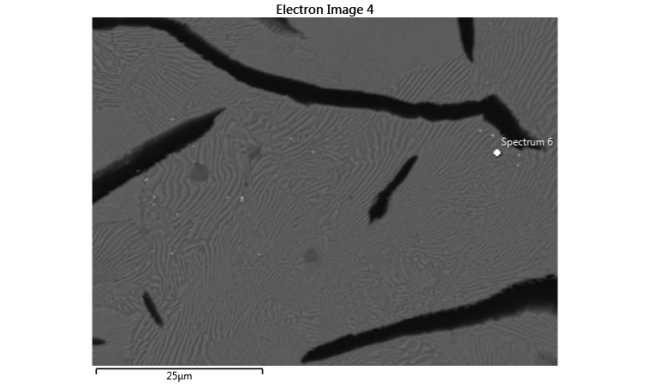

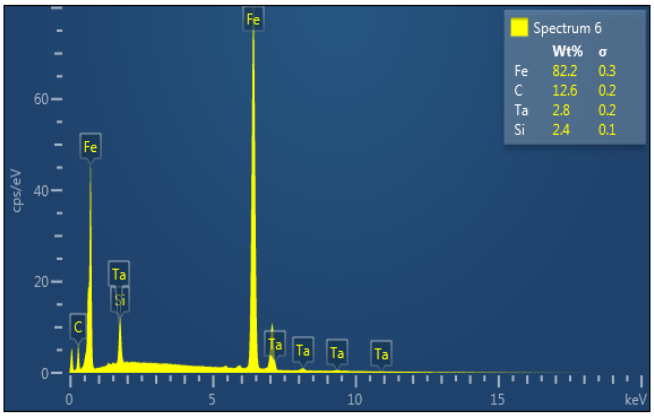

Figure 6. EDS Analysis of sample no. B

As demonstrated in Figure 4, as the load values applied to the samples increased, the friction coefficients of Samples B and C decreased, but the friction coefficients of Samples K and A increased. The reason for this was that the contact surface between the sample and Alumina ball created high frictional heat and force values during its constant reciprocal motion under high loads. When each of the 1 N, 3 N and 5 N load values was analyzed separately from the others, it was found that under a constant load, as the reinforcement ratio increased, there was also an increase in the coefficient of friction. The highest coefficient of friction was found in Sample C under all three load values. In the study conducted by Arslan, the AZ91 magnesium alloy that was produced with the cold chamber high-pressure die casting method was subjected to dry sliding wear tests under three different loads as 2 N, 5 N and 10 N, with an amplitude of 10 mm, a sliding speed of 5 mm/s, and a total sliding distance of 12 m. The author observed that increased hardness values resulted in lower coefficients of friction on the wear surfaces of the samples. They identified a relationship between coefficients of friction and hardness. The amount of wear that was inversely proportional to hardness was, on the other hand, directly proportional to the coefficient of friction. That is, as the amount of wear decreased, the coefficient of friction was observed to increase [24].

3. 2. Microstructure analyses

SEM (Scanning Electron Microscope) images (Figure 5) and EDS (Energy Dispersive X-Ray Spectrometer) images (Figure 6) of the samples before the wear test are shown.

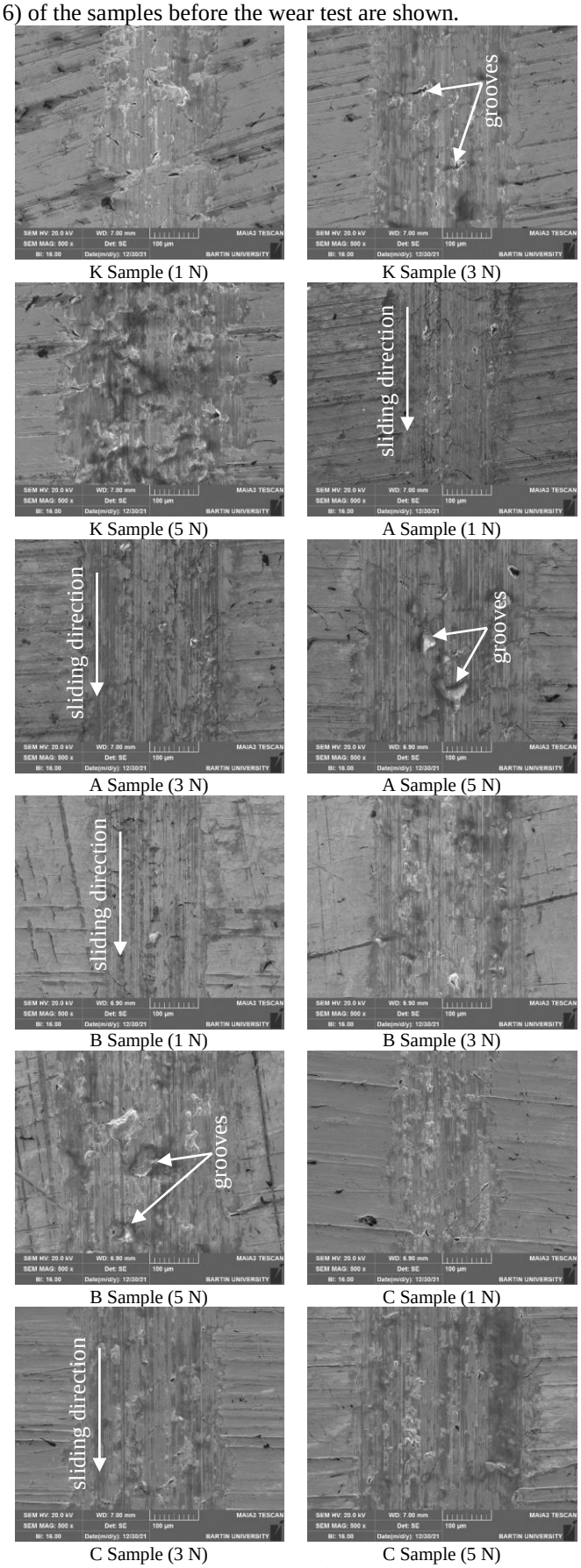

K Sample (1 N) K Sample (3 N)
K Sample (5 N) A Sample (1 N)
A Sample (3 N) A Sample (5 N)
B Sample (1 N) B Sample (3 N)
B Sample (5 N) C Sample (1 N)
C Sample (3 N) C Sample (5 N)

Figure 7. SEM images after the wear tests

The SEM images of the microstructures of the sample surfaces after the wear tests are shown in Figure 7.

As demonstrated in the SEM images in Figure 7, in Sample K that did not include TaC reinforcement, increased load values resulted in increased wear volumes. The highest wear occurred under the 5 N load in the form of abrasion. There were also abrasions on the wear surfaces for the load values of 1 N and 3 N, but these abrasions were not as severe as those that formed under the 5 N load. According to the SEM images of Sample A, abrasive wear occurred on the surface under the 5 N load. Under the load values of 1 N and 3 N, wear was observed without abrasion. The SEM images of Sample B revealed abrasive wear under the 5 N load. The wear surfaces of Sample B did not show abrasion under the 1 N and 3 N loads, and these results were similar to those of Sample A. Based on the SEM images of Sample C, because the highest reinforcement ratio was in this sample, no abrasion was observed under the 1 N, 3 N and 5 N loads. The appearance of the wear surface was similar for all load values.

4. CONCLUSION

a) Varying reinforcement ratios did not have a noteworthy effect on the resulting wear track profiles under the 1 N load. On the other hand, different reinforcement ratios resulted in changes in the wear track profiles under 3 N and 5 N. The most noticeable wear track profile was found in Sample C under the 5 N load.

b) Increased load values resulted in increased wear volumes, but they did not result in significant wear rate value changes, and the wear rate values were similar to each other. The highest wear volume was found under the 5 N load as 4.3×10^{-3} mm^3 in Sample C and 4.2×10^{-3} mm^3 in Sample K.

c) When each of the load values of 1N, 3N, and 5N was analyzed independently of the others, it was observed that as the reinforcement ratio increased, there was a tendency for the wear amounts to increase.

d) The friction coefficient values decreased while the load values which is applied to the B and C samples was increased. On the other hand, for K and A samples, the friction coefficient values increased while load values were increased.

e) At constant load values, as the reinforcement ratio increased, the coefficients of friction also increased. The highest coefficient of friction was found in Sample C for all three load values.

REFERENCES

[1] E. Tan, “The effect of adding ratio of copper to the wear behavior of rolls manufactured by cast iron”, M.S. thesis, Institute of Sciences, Pamukkale University, Denizli, Turkey, 2005.

[2] D. Sağlam, “Wear properties of cast iron”, M.S. thesis, Institute of Sciences, Marmara University, İstanbul, Turkey, 2009.

[3] D. Mu and B. Shen, “The kinetics and dry-sliding wear properties of boronized gray cast iron”, Advances in Materials Science and Engineering, vol. 2013, pp. 1-7, 2013.

[4] H. Berns, “Comparison of wear resistant MMC and white cast iron”, Wear, vol. 254, no. 1-2, pp. 47-54, 2003.

[5] C. Kowandy, C. Richard, Y. M. Chen, and J. J. Tessier, “Correlation between the tribological behaviour and wear particle morphology-case of grey cast iron 250 versus Graphite and PTFE”, Wear, vol. 262, no. 7-8, pp. 996–1006, 2007.

[6] E. Albertin and A. Sinatora, “Effect of carbide fraction and matrix microstructure on the wear of cast iron balls tested in a laboratory ball mill”, Wear, vol. 250-251, no. 1, pp. 492-501, 2001.

[7] J. Asensio, J. A. Pero-Sanz, and J. I. Verdeja, “Microstructure selection criteria for cast irons with more than 10 wt.% chromium for wear applications”, Materials Characterization, vol. 49, no. 2, pp. 83-93, 2002.

[8] A. R. Riahi and A. T. Alpas, “Wear map for grey cast ıron”, Wear, vol. 255, no. 1-6, pp. 401–409, 2003.

[9] M. K. Bilici, “Wear Properties Of An Alloy Cast Iron”, M.S. thesis, Institute of Sciences, Marmara University, İstanbul, Turkey, 2004.

[10] R. Ghasemi and L. Elmquist, “A study on graphite extrusion phenomenon under the sliding wear response of cast iron using microindentation and microscratch techniques”, Wear, vol. 320, pp.120-126, 2014.

[11] Z. Chen, T. Zhou, R. Zhao, H. Zhang, S. Lu, W. Yang and H. Zhou, “Improved fatigue wear resistance of gray cast iron by localized laser carburizing”, Materials Science & Engineering A, vol. 644, pp. 1-9, 2015.

[12] T. Willidal, W. Bauer and P. Schumacher, “Stress/strain behaviour and fatigue limit of grey cast iron”, Materials Science and Engineering A, vol. 413-414, pp. 578-582, 2005.

[13] G. Bertolino and J. E. Perez-Ipina, “Geometrical effects on lamellar grey cast iron fracture toughness”, Journal of Materials Processing Technology, vol. 179, pp. 202-206, 2006.

[14] M. Ramadan, M. Takita and H. Nomura, “Effect of semi-solid processing on solidification microstructure and mechanical properties of gray cast iron”, Materials Science and Engineering A, vol. 417, pp. 166-173, 2006.

[15] A. Sadeghi, A. Moloodi, M. Golestanipour and M. M. Shahri, “An investigation of abrasive wear and corrosion behavior of surface repair of gray cast iron by SMAW”, Journal of Materials Research and Technology, vol. 6, no. 1, pp. 90-95, 2017.

[16] F. Münker, “Wear properties of hardened cast irons”, M.S. thesis, Institute of Sciences, Marmara University, İstanbul, Turkey, 2010.

[17] F. Okay, “An investigation of adhesive wear behavior of TiN coated austempered ductile iron with PVD”, M.S. thesis, Institute of Sciences, Gazi University, Ankara, Turkey, 2006.

[18] H. İ. Filiz, “The effect of microstructure on impact sliding wear behavior of aisi D2 cold work tool steels, M.S. thesis, Graduate Education Institute, Istanbul Technical University, Istanbul, Turkey, 2021.

[19] O. Tazegul, F. Muhaffel, O. Meydanoglu, M. Baydogan, E. S. Kayali and H. Cimenoglu, “Wear and corrosion characteristics of novel alumina coatings produced by micro arc oxidation on AZ91D magnesium alloy”, Surface & Coatings Technology, vol. 258, pp. 168-173, 2014.

[20] B. Bilim, “Investigation of wear behaviour of hot dip aluminized tool steels produced by powder metallurgy”, M.S. thesis, Graduate Education Institute, Istanbul Technical University, Istanbul, Turkey, 2021.

[21] I. Şimşek, D. Şimşek and D. Özyürek, “Investigation of Wear Behaviors of Al-SiC Composite Materials Produced by Semi-Solid Process Method”, SETSCI Conference Proceedings, vol. 4, no. 1, pp. 545-548, 2019.

[22] S. İ. Akray, “The effect of coatings on wear characteristics of spherodial graphite cast iron”, M.S. thesis, Institute of Sciences, Istanbul Technical University, Istanbul, Turkey, 2007.

[23] A. Ayday, “Surface Properties Improvement of Nodular Cast Iron Modified by Electrolytic Plasma Technology”, PhD Thesis, Institute of Sciences, Sakarya University, Sakarya, Turkey, 2013.

[24] R. Arslan, “Döküm presi ile elde edilen magnezyum alaşımlarının mekanik özelliklerinin belirlenmesi”, M.S. thesis, Institute of Sciences, Kırşehir Ahi Evran University, Kırşehir, Turkey, 2019.

BIOGRAPHIES

Rifat Yakut received the B.S. degree from the Machine education Department, Fırat University, Elazığ, Turkey, in 2005, and B.S. degree from the Mechanical Engineering Department, Sivas Cumhuriyet University, Sivas, Turkey, in 2017, and the M.S. degrees from the Selcuk University in 2008 and Ph.D. degrees from the Trakya University in 2015. He was appointed as an Assistant Professor to the Department of Energy Systems Engineering at Batman University in 2016. His research interests include Composite materials, Cast irons, Manufacturing technologies, Tribology, Material design and behavior.

Ömer Çiftçi received the B.S. degree from the Mechanical Engineering Department, Fırat University, Elazığ, Turkey, in 2018. He started his master's degree in Batman University's mechanical engineering department in 2019. His research interests include Cast irons, Tribology, Material design and behavior.

European Journal of Technique

journal homepage: https://dergipark.org.tr/en/pub/ejt

Vol.12, No.1, 2022

Comparative Modelling and Experimental Verification of a PMSM Drive System

Gullu Boztas[1*]

[1*]Firat University, Electrical and Electronics Engineering, Elazig, Turkey. (e-mail: gboztas@firat.edu.tr).

ARTICLE INFO

Received: Apr., 11. 2022
Revised: Jun., 13. 2022
Accepted: Jun, 30. 2022

Keywords:
Permanent magnet synchronous motor
Modelling
Simulation
Experimental verification

Corresponding author: *Gullu Boztas*

ISSN: *2536-5010* | e-ISSN: *2536-5134*

DOI: https://doi.org/10.36222/ejt.1101838

ABSTRACT

This paper presents a comparative study on three simulation models and an experimental model for a Permanent Magnet Synchronous Motor (PMSM) drive system. A realistic modelling and simulation of a PMSM drive system are very useful before developing an experimental study. In particular, analyzing the performance of the motor drive and control algorithm in a simulation environment provides many advantages. The motor and drive system can be tested by using a simulation environment with various realistic scenarios in order to reduce testing costs and time span. Therefore, a comparative simulation study was performed in this paper to show the simulation results similarity with real application results. Three PMSM drive systems were modelled by using MATLAB environment based on SimPowerSystems, Simscape Electrical, and based C-language. All models and experimental system were operated under the same conditions. These models were compared with each other and verified with an experimental system. The waveforms were analyzed comparatively such as current, speed, mechanical position of the motor.

1. INTRODUCTION

PMSM is a rotating electric machine having a conventional three-phase stator like that of an induction motor (IM) and permanent magnets mounted on its rotor surface. PMSM is equivalent to an IM in which the air gap magnetic field is generated by a permanent magnet. The stator current of IM contains both magnetizing and torque generating components. It is unnecessary in order to obtain magnetizing current through the PMSM stator for constant air gap flux because the rotor of the PMSM has permanent magnet. The stator current only needs to produce torque. Therefore, the PMSM operates at a higher power factor and PMSM is more efficient due to the absence of magnetizing current according to IM for the same output [1,2]. DC motors used in many applications requiring high performance began to be replaced by PMSMs with the using of magnet materials such as samarium-cobalt (SmCo) and neodymium-ironboron (NdFeB) in the 1970s and 1980s [3]. PMSM has such as high power factor, high power density, robustness, small size, lightness, low noise and high torque compared to other electric motors [4–10]. Permanent magnets are used instead of the field windings in the rotor of the PMSM. Permanent magnets can produce magnetic flux in an air gap without field excitation windings and electrical power losses. PMSM has higher efficiency than other AC motors because the rotor of PMSM produces magnetic flux with permanent magnets. Therefore, PMSM is widely used in electric vehicle, military and aviation industries [11]. Additionally, PMSMs have become the key and core components of complex electromechanical systems such as robotic application, urban rail vehicles, ship propulsion systems, high-speed elevators and wind power generation because the motors have high efficiency, large torque-inertia ratio, fast dynamic torque response, high overload capacity, wide speed range advantages [12–18]. The phase voltages and currents of the PMSM stator are ideally sinusoidal. The flux of the motor provides an ideal sinusoidal flux distribution by the installation of rotor magnets in the air gap. The installation of the rotor magnets can be in different shapes called as surface mounted, inset radial, interior, and spoke [19]. The location and the shape of the magnets change dynamic features of the motor. DC motor was widely used in position and speed control applications for many years because the motor control is easy. The motor stator currents must be controlled directly in order to obtain the desired performance from PMSMs such as the behavior of DC motors. Accurate speed control of PMSM driver is a complex issue due to the nonlinear relationship between winding current and the rotor speed of the PMSM. Electromagnetically produced torque of the motor is non-linearity due to the magnetic saturation of the rotor core. Therefore, it is difficult in order to control of the motor [20]. AC motor drive systems and motor control schemes have been studied in many literature [21–23]. Field oriented control (FOC) and direct torque control (DTC) are

two control strategies commonly used for industrial motor drives [24]. A comparative study of DTC controlled PMSM is performed using Matlab/Simulink and DSPACE-1104 [25, 26]. A novel method for magnetization fault detection in PMSM is presented by using finite element analysis with simulation environment [27]. FOC is generally the most effective and reliable control method for PMSM drives [28]. Synchronous and asynchronous motors could be controlled just like a DC motor with the introduction of vector control theory in the 1970s. FOC method was first proposed by F. Blaschke in order to control IMs in the early 1970s. The vector control technology has been widely used in high performance AC drives over the past two decades due to the rapid development in power electronics, computing, and microelectronics [29]. The FOC technique provides decoupling of flux and torque similar to that of a DC motor. FOC method includes current control loops in order to control the direct axis current and the quadrature axis current [30, 31]. FOC method commonly used in the control system of the PMSM consists of an internal current loop and an external speed loop. Proportional integral (PI) control is used in speed and current loops in FOC [32].

In this study, 3 different simulation models and experimental results for a PMSM drive system were comparatively analyzed. All simulations were developed in MATLAB environment. Control algorithms and sampling times were the same for all simulations. The first two simulation models were performed using available tools and the other was developed by using the C-language. The details of the blocks used in the simulations were analyzed in detail in the paper. The parameters used in the simulations were taken by measuring from the real system. The simulations and real results were performed under the same conditions. Results were analyzed in terms of motor speed, stator currents and harmonic spectra of the currents. Additionally, the execution times of the simulations were compared for same conditions. This paper is organized as follows: The mathematical model of the PMSM is described in Section 2. The simulation results and experimental verification are presented in Section 3 and Section 4, respectively. Finally, conclusions are discussed in Section 5.

2. MATHEMATICAL MODELLING OF PMSM

The d and q- axis currents converted from 3 to 2 phases in an AC motor represent the field and armature current, respectively. The control of AC machine can be achieved with different algorithms by using static and rotating reference frames. The coordinate system is generally obtained by the Clarke Transform of the $\alpha\beta$-fixed reference frame and the Park Transform of the dq-rotating reference frame. The equivalent circuit of the PMSM is illustrated in Fig. 1. In this study, rotating frame was aligned with the phase A axis. Therefore, the voltage equations can be derived as given in the Eq. (1). c refers to cosine and s refers to sinus function in the equation.

$$\begin{bmatrix} u_d \\ u_q \\ u_0 \end{bmatrix} = \frac{2}{3}\begin{bmatrix} c(\omega t) & c(\omega t - 2\pi/3) & c(\omega t + 2\pi/3) \\ s(\omega t) & s(\omega t - 2\pi/3) & s(\omega t + 2\pi/3) \\ 1/2 & 1/2 & 1/2 \end{bmatrix}\begin{bmatrix} u_a \\ u_b \\ u_c \end{bmatrix} \quad (1)$$

where u_a, u_b and u_c are the three phase voltages of the stator windings fed by inverter output. The voltage equations of the PMSM can be derived as shown in Eq. (2) and Eq. (3). Additionally, linkage fluxes of the dq-axis are given in Eq. (4) and Eq. (5).

$$u_d(\mathrm{t}) = R_s i_d(\mathrm{t}) + \frac{d}{dt}\left(L_d i_d(\mathrm{t})\right) - \omega_e L_q i_q(\mathrm{t}) \quad (2)$$

$$u_q(\mathrm{t}) = R_s i_q(\mathrm{t}) + \frac{d}{dt}\left(L_q i_q(\mathrm{t})\right) + \omega_e L_d i_d(\mathrm{t}) + \omega_e \psi_m \quad (3)$$

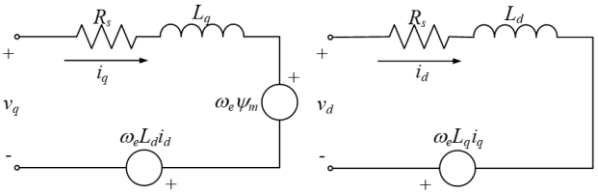

Figure 1. Equivalent circuit of the PMSM

$$\psi_d = \psi_m + L_d i_d \quad (4)$$

$$\psi_q = L_q i_q \quad (5)$$

where, i_d and i_q are dq-axis current. ωe is the electrical velocity of the PMSM. Additionally, ψ_d and ψ_q are dq- axis linkage fluxes while ψm is the magnet flux of the rotor. R_s, L_d and L_q are stator winding resistance, dq-axis stator inductance, respectively. These inductances represent the relation between phase inductance and the position of rotor due to the rotor saliency. The measured inductance between the a and b phases is given in Eq. (6).

$$L_{ab} = L_d + L_q + \left(L_d - L_q\right)\cos(2\theta_e + \pi/3) \quad (6)$$

where θ_e is electrical angle of the PMSM rotor. The mechanical equations of the PMSM are given as shown in Eq. (7) and Eq. (8).

$$T_e = T_L + \mathrm{j}\frac{d\omega_m}{dt} + \mathrm{B}\omega_m \quad (7)$$

$$T_e = \frac{3}{2}\mathrm{p}(\psi_m \mathrm{i}_q + (\mathrm{L}_d - \mathrm{L}_q)\mathrm{i}_d \mathrm{i}_q) \quad (8)$$

where T_e and T_L represent the electromagnetic torque and load torque, respectively. J and B are the moment of inertia and the friction. ω_m is the mechanic velocity of the PMSM and p is pole pair of the motor.

Vector control algorithm and PMSM's model require Park and Inverse-Park transformation. The transformation equations can be derived by using vector diagram of the abc-frame which is give in Fig. 2. Park transformation uses the three phase vectors to transform dq rotating frame. The equations of Park transformations are given in Eq. (9) - Eq. (11). The inverse Park transformation is used to derive abc-frame vectors which are given in Eq. (12) - Eq. (14). The rotating frame alignment to 90 degrees when ωt is zero.

$$V_d = \frac{2}{3}\left(V_a \sin(\omega t) + V_b \sin\left(\omega t - \frac{2\pi}{3}\right) + V_c \sin\left(\omega t + \frac{2\pi}{3}\right)\right) \quad (9)$$

$$V_q = \frac{2}{3}\left(V_a \cos(\omega t) + V_b \cos\left(\omega t - \frac{2\pi}{3}\right) + V_c \cos\left(\omega t + \frac{2\pi}{3}\right)\right) \quad (10)$$

$$V_0 = \frac{1}{3}\left(V_a + V_b + V_c\right) \quad (11)$$

$$V_a = V_d \sin(\omega t) + V_q \cos(\omega t) + V_0 \quad (12)$$

$$V_b = V_d \sin\left(\omega t - \frac{2\pi}{3}\right) + V_q \cos\left(\omega t - \frac{2\pi}{3}\right) + V_0 \quad (13)$$

$$V_c = V_d \sin\left(\omega t + \frac{2\pi}{3}\right) + V_q \cos\left(\omega t + \frac{2\pi}{3}\right) + V_0 \quad (14)$$

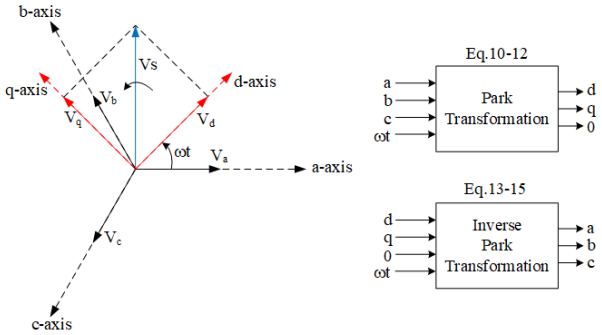

Figure 2. abc-frame and dq-frame for Park transformation

3. SIMULATION OF PMSM DRIVE SYSTEM

In this study, PMSM models were obtained by using MATLAB environment. Three different models were created separately and tested under the same conditions. All simulation models were operated with 1.6 μs sample time. The same control blocks, labeled as Field Oriented Control (FOC) and switching technique Space Vector Pulse Width Modulation (SVPWM) shown in Fig. 3, were used in all simulations. The internal block diagrams of control and SVPWM with dead-time (3.2 μs) are given in Fig. 3(b). The parameters of the PI controllers are determined using Internal Model Control technique [33]. The PI parameters of speed controller were determined as $kp\ (speed)$ = 0.156 and $ki\ (speed)$ = 13.431. The PI controller parameters of the dq-axis were determined as $kp\ (dq)$ = 21.671 and $ki(dq)$ = 29, 759.12. A switching frequency of 16 kHz, which is also used in the experimental system, was selected in the simulation. Three simulation environments are named as SimPowerSystems, Simscape Electrical, and C-language model.

MATLAB has some tools for modelling/simulating electrical power systems included power electronics and electric machines. One of these is SimPowerSystems which is named as Specialized Power Systems for new version of MATLAB. It can be easily connected commonly used Simulink blocks as shown in Fig. 4(a). Many applications of power systems, electrical machines and power electronics can be carried out easily by using this tol. Especially, it helps to develop control algorithms for motor drive applications of any kind of motor type. In this study, the PMSM model and its driver system were used as shown in the Fig. 4(a). A single-phase voltage source was used 220 V, 50 Hz and the source rectifiers by using a full-wave rectifier based on diode. The diode parameters have the same values as the diode KBPC3510 in the experimental system. The inverter block is used with parameters that same values as a PM20CSJ-060 coded IGBT inverter module. The back electromotive force waveform was selected as sinusoidal in the PMSM block configuration because the motor type is a surface mounted PMSM in the experimental study. The DC-link capacitor value was taken as 3x470 µF which has been selected in the real application. Simscape Electrical toolbox is a new generation simulation environment for modelling and simulating electronic, electrical power systems, and electric machines like

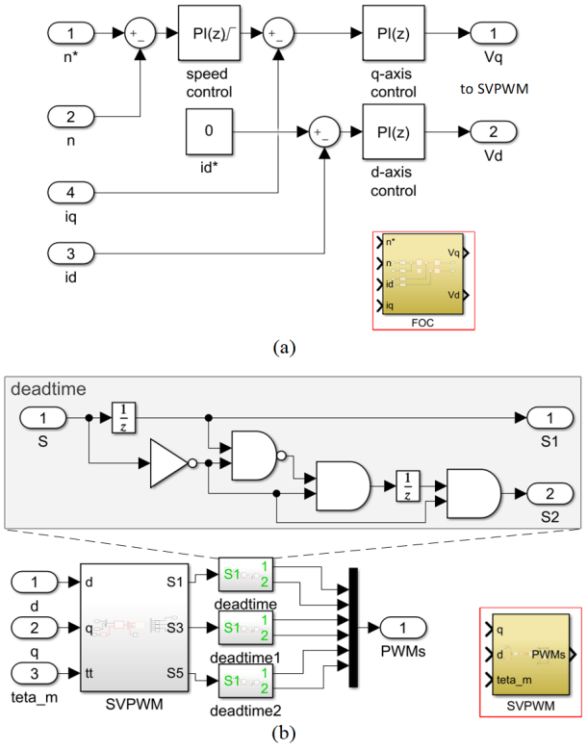

Figure 3. a) Block diagram of control, and b) SVPWM and dead-time blocks

SimPowerSystems. Additionally, Simscape Electrical toolbox is also integrated mechanical, hydraulic, thermal, and other physical systems. SPICE models are also supported by this tool. In this study, existent power electronics devices are used in the simulation environment as shown in Fig. 4(b). The diodes can be configured differently, such as exponential or piecewise linear. In this simulation, the diode and IGBT parameters, all electrical and mechanical values are used the same as in the previous mentioned simulation. Additionally, all mechanical variables can be connected externally as shown in the Fig. 4(b) without the need to use a mechanical variable in the motor model. Thus, a desired mechanical model can be connected to the motor by using Simscape Driveline blocks as a load. A local solver configuration was used in the simulation with backward Euler solver type. MATLAB supports free and open source software development environment Mingw-w64 C-language. In this study, simplified PMSM was developed by using Mingw-w64 C with mathematical equations mentioned first section of this paper. The model masked with a subsystem as shown in Fig. 4(c). The motor winding ports fed from inverter voltage outputs are labeled as "U, V, W". The "T_m" port is the input mechanical torque of the load. Signal routing labeled "$Load$" is used for load output in all simulations.

The inverter block only converts PWM signals to the voltage signal using by multiplying half of the dc-link voltage value with the difference between the upper and lower switches' states. The losses of the semiconductor switches were ignored in the inverter block. The interior block diagram of PMSM model based on script is shown in Fig. 5a. The detailed script is given in Fig. 5b. The variables in red are pointers that represent input and output of the PMSM block. The electrical and mechanical equations were defined in the second section of the paper. The coulomb and viscous friction model was added as labeled "cvf" in the script. The motor was not operated at negative speed region. In this study, a simplified model was compared with other models and a real system. Therefore, many system losses were neglected except for the simplified equations. The model presented in Fig. 5 can

be obtained easily in any simulation environment. The simulation models were compared with each other as shown in Fig. 6. The motor was operated at a nominal constant speed of 3000 rpm at half-load and full-load transition. The PMSM was started under the half-load condition and the motor was operated for full-load after 1.5 seconds. The full-load transition is given in detailed Fig. 6b and Fig. 6d for speeds and stator currents, respectively. Subsequently, load was reduced in half of rated load. The transition details are shown in Fig. 6c and Fig. 6e. It is possible to say that all the simulation models give results very close to each other. The harmonic contents of the currents were different although the results were similar. The Total Harmonic Spectrum (THD) at the full-load condition was calculated as 2.3%, 3.89%, 2.04% for Simpower model, Simscape model and C-model, respectively. Additionally, the execution times of the simulations were different from each other. The simulations were performed on a computer with a clock frequency of 4.2 GHz. For 1 second simulation time with 1.6 μs sampling time, execution times are required 20 seconds, 83 seconds, 13 seconds for Simpower model, Simscape model and C-model, respectively. A large amount of execution time was required for Simscape model.

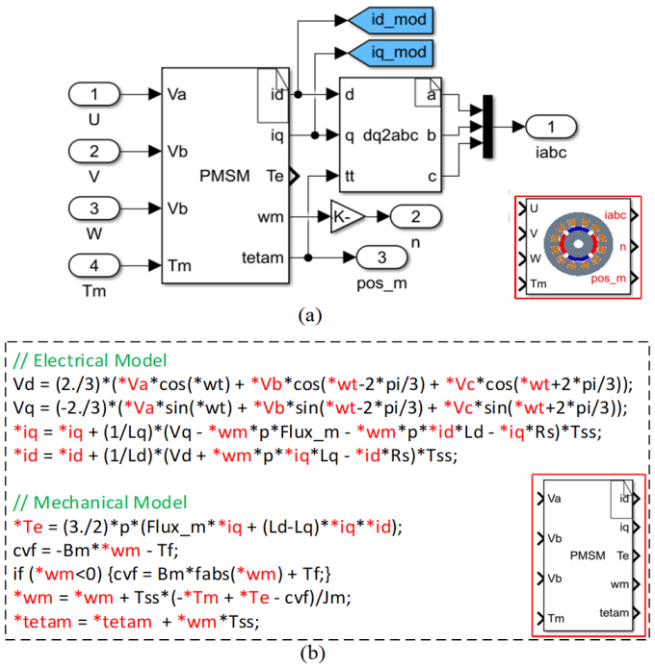

Figure 5. a) Interior block diagram of script based PMSM model, b) Script based model

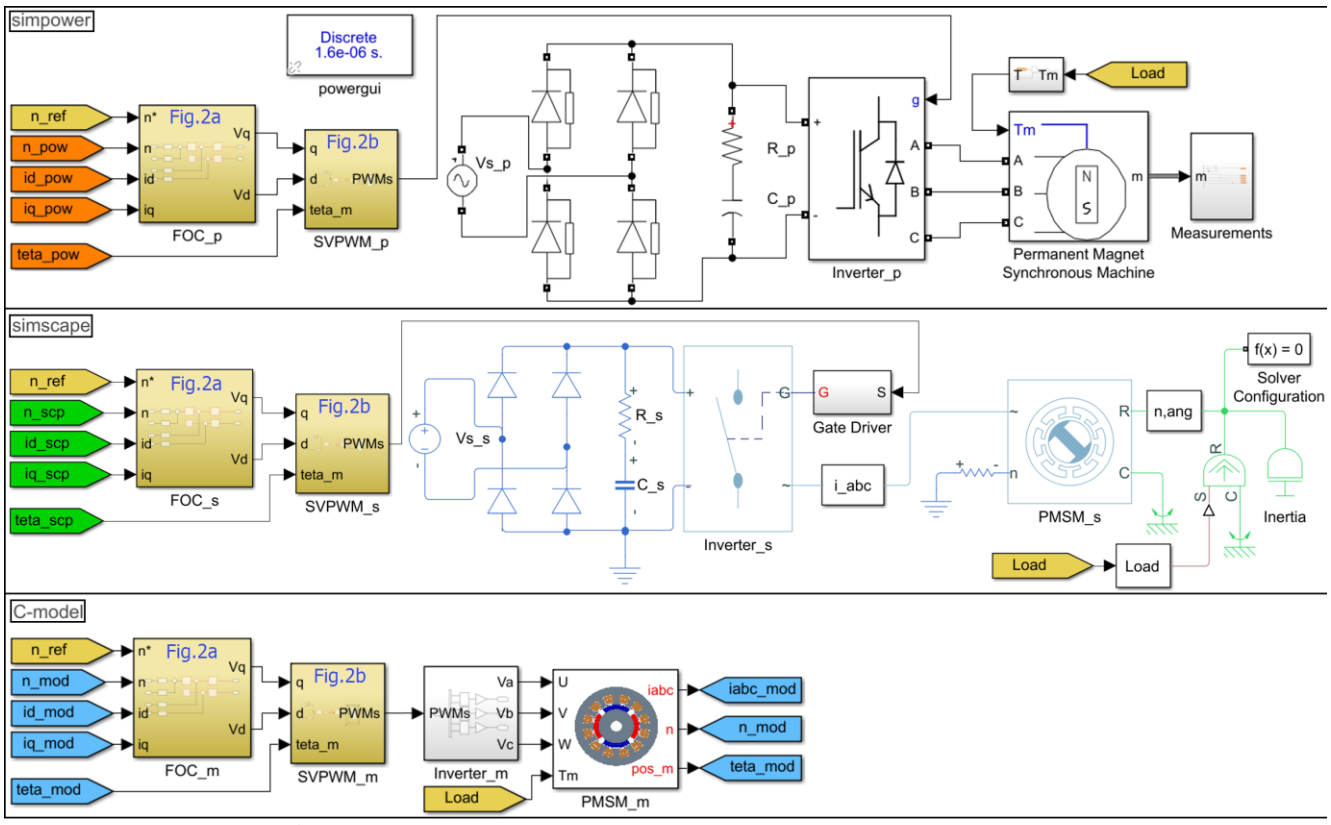

Figure 4. Simulation diagram of PMSM control based on; a) SimPowerSystems, b) Simscape Electrical, c) C-language model

4. EXPERIMENTAL VERIFICATION

The models were compared with a real system shown in Fig. 7 after the mentioned models were compared among themselves. All parameters used in the simulation environment are the values measured from the real system. A surface-mount PMSM was used for this application. The motor parameters are given in Table I. The motor has a 10,000 pulse/rev resolution encoder which is connected to the inverter and 12-bit Digital Analog Converter (DAC). The speed and mechanical position were measured by a scope connected to the DAC. The stator current was measured via a clamp sensor connected to scope. A magnetic-powder brake was used as a load as shown in the Fig. 7. The PMSM was operated for 12 seconds as shown in Fig. 8. The B-channel in the scope shows motor speed in 1,000 rpm/V scale. The D-channel of the scope measures the U-phase stator winding current of the PMSM. The motor was operated at half-load condition for about 5 seconds as shown in the current waveform. The PMSM was then operated at full-load for about 4 seconds. The time-base was set as 1 sec/div in the scope. The channel of current probe was set to 2 A/div as shown in the Fig. 8a. The effective current of half-load and full-load are measured about 0.84 A and 1.63 A, respectively. Similar results were performed in

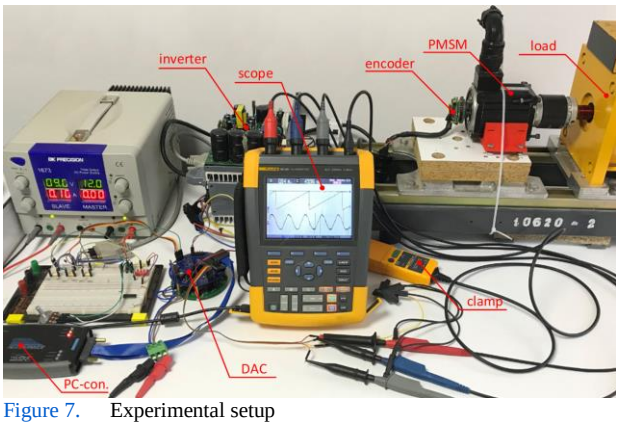

Figure 7. Experimental setup

TABLE I
PARAMETERS OF THE MOTOR

Motor parameter	Value
Armature resistance (R_s)	7.514 Ω
d-axis inductance (L_d)	15.78 mH
q-axis inductance (L_q)	15.78 mH
Pole number (P)	4
Rotor Moment of Inertia (J_m)	1.0314*10^{-3} kg*m^2
Friction factor (B_m)	8.2*10^{-6} N*m*s

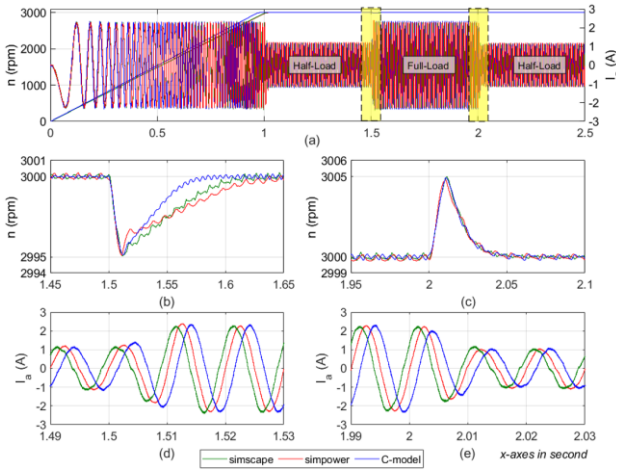

Figure 6. a) Speed and stator current, b,d) Full-Load transition, c,e) Half-Load transition.

the simulation environment as shown in the Fig. 8b. Current response at load transitions is not similar to that in the simulation environment due to the magnetic powder brake dynamics coupled to the motor as a load. The load used in the experimental study cannot performed an instantaneous output torque transition. The load can reach the set value after a short latency as shown in the experimental results. This nonlinear behavior is entirely due to the dynamics of magnetic powders in the load system. For this reason, there was no need to model the load dynamics in the simulation environment.

The signals given in Fig. 8 were analyzed in detailed for both simulation and experiment environment as shown in Fig. 9 for under full-load and half-load conditions. Fig. 9a and Fig. 9b present the experimental results. The B-channel in blue is the PMSM speed, C-channel in black is mechanical position and D-channel in green is the stator current of the motor in the Fig. 9a and Fig. 9b. Similarly, the simulation results are presented in Fig. 9c and Fig. 9d for different load conditions. Due to the 4 poles of motor, two periods of a current waveform are seen versus one period of a mechanical position of the motor. The electrical frequency is twice the mechanical frequency. For this reason, the mechanical frequency is 50 Hz while the motor is rotating at 3000 rpm as shown in the Fig. 10a and Fig. 10b. The reason why the simulation results do not appear in the same time axis is that the PMSM models cannot reach the speed set at the same time.

Fast Fourier transform (FFT) analysis was performed for the obtained results at the full-load condition as given in Fig. 10. Percentage values are used according to the magnitude value of the fundamental signals which are labeled as yellow in the figure. The bars in spectra at the same frequencies are shown in similar colors to make it easier to understand. Simscape result was obtained as 3.85% as the closest value to the experimental result while the real system current THD simulation environment. was calculated as 4.17%. The current THD of the Simpower and script based models are obtained as 1.8% and 2.02%, respectively. As a result of the FFT analysis, it is possible to say that the simulation performed with Simscape gives a more realistic result. It is possible to say that the THD values and spectrum amplitudes obtained in the experimental and Simscape simulation results are similar to each other. Brief comparisons of the models are given in Table II.

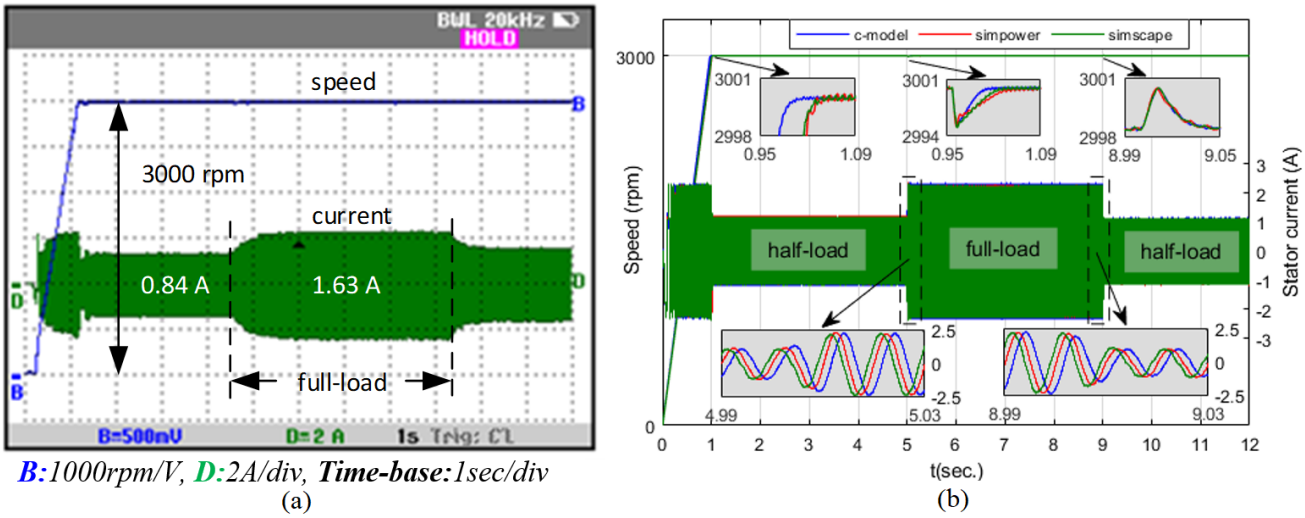

Figure 8. Speed and stator current; a) Experimental results b) Simulation results

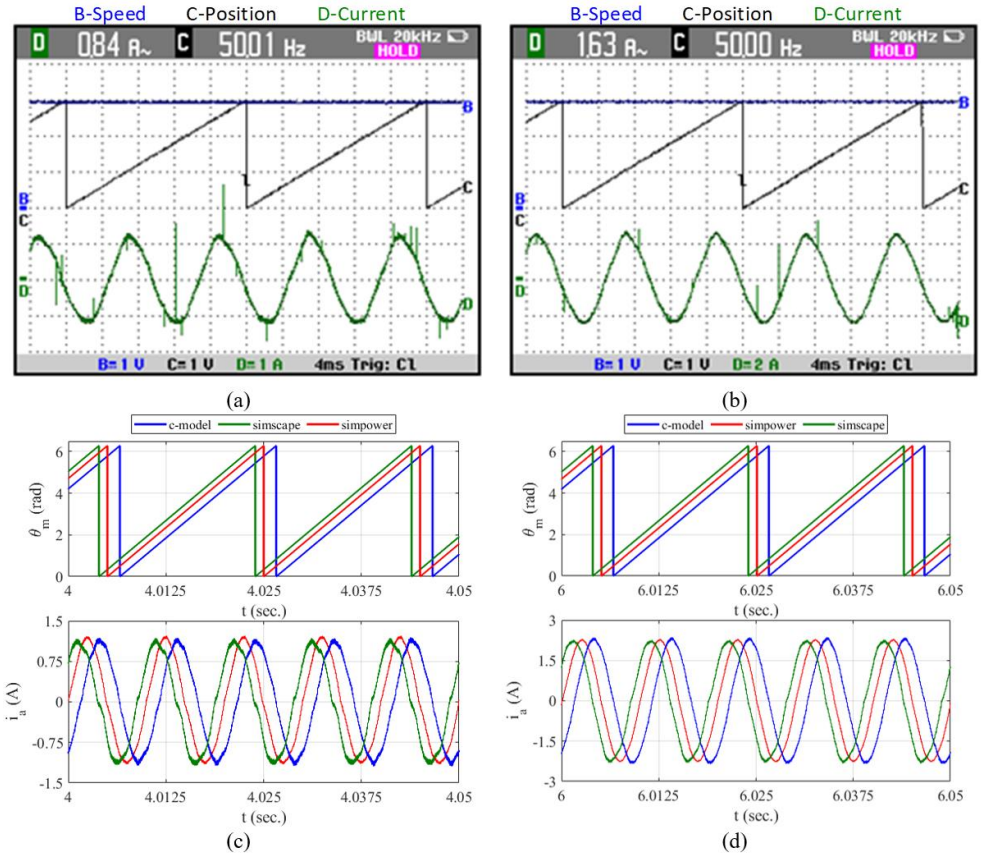

Figure 9. Experimental; a) half-load, b) full-load, Simulation; c) half-load, d) full-load

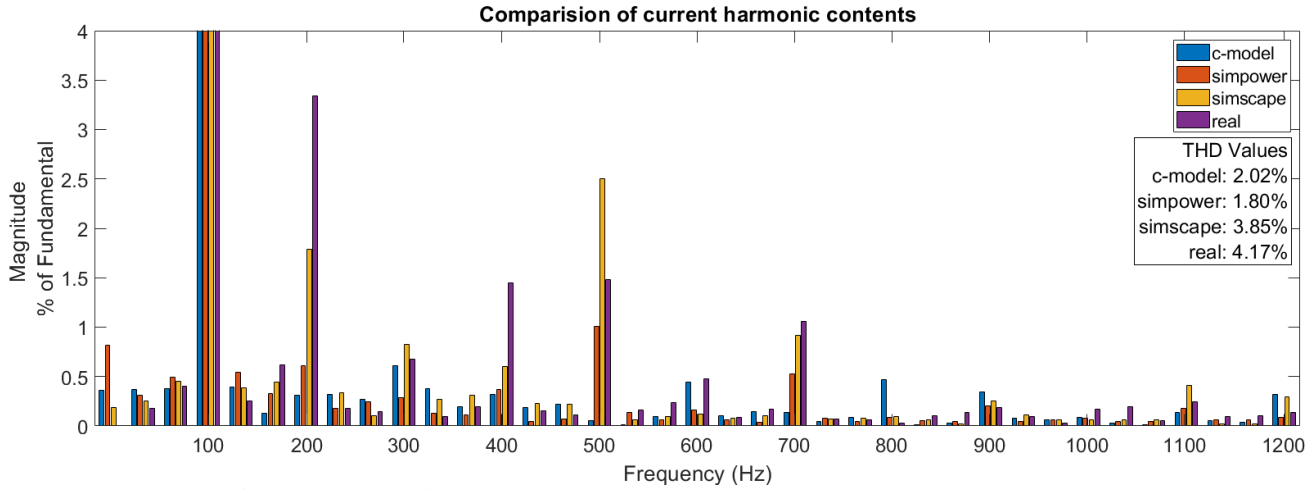

Figure 10. FFT spectra of the stator current at full-load

TABLE II
BRIEF OF COMPARISON OF MODELS

	Simpower	Simscape	C-language	Real system
Execution time	20 sec.	83 sec.	13 sec.	1 sec.
Current Ia THD	1.80 %	3.85 %	2.02 %	4.17 %
Spend time	Medium	Medium	Low	High
Platform support	MATLAB	MATLAB	Many	Real

5. CONCLUSION

The interest in PMSM is increasing in many application areas, especially in robotics, automation, and military. Therefore, working with a simulation environment is much easier and cost-effective than working on a real system environment. For this reason, obtaining a realistic simulation result is an important issue. The simulation environment offers various conditions for developing a real system before it can be experimentally performed. Simulation work is particularly advantageous for developing algorithms and software in motor drive applications. Nowadays, there are many simulation platforms which offer user friendly tool. Among these platforms, MATLAB software, which is widely preferred from the academic community and some commercial companies, was used in this paper. The PMSM drive systems obtained by using Simpower, Simscape, and C-language were compared with each other. However, comparing the simulations among themselves does not give an idea of which one is more realistic. Therefore, all these simulation results were compared with a real system. It is possible to say that all simulations give similar results when all the results are compared to the experimental results. The C-language based PMSM model was obtained with a very low execution time. More accurate results were achieved by using

Simscape model. It can be said that the sample time and real system parameters affected the results. In addition, it was presented that the addition of inverter switching dead-time is a critical issue in a motor drive circuit to obtain more realistic results from the simulation environment. However, it should be said that the simulation results need a longer execution time to obtain a more realistic result.

REFERENCES

[1] P. Pillay, and R. Krishnan, "Modeling, Simulation, and Analysis of Permanent-Magnet Motor Drives. Part I: The Permanent Magnet Synchronous Motor Drive," IEEE Transactions on Industry Applications, vol.25, no.2, pp.265–273, 1989.

[2] O. Aydogmus, and S. Sunter, "Implementation of ekf based sensorless drive system using vector controlled pmsm fed by a matrix converte,". International Journal of Electrical Power & Energy Systems, vol. 43, no. 1, pp. 736–743, 2012.

[3] A. Kumar, S. Marwaha, A. Singh, and A. Marwaha, "Performance investigation of a permanent magnet generator. Simulation Modelling Practice and Theory," vol. 17, no. 10, pp. 1548–1554, Nov 2009.

[4] W. Wang, Y. Feng, Y. Shi, M. Cheng, W. Hua, and Z. Wang, "Direct Thrust Force Control of Primary Permanent-Magnet Linear Motors with Single DC-Link Current Sensor for Subway Applications," IEEE Transactions on Power Electronics, vol. 35, no. 2, pp. 1365– 1376, Feb. 2020.

[5] M. Cheng, W. Hua, J. Zhang, and W. Zhao, "Overview of stator-permanent magnet brushless machines," IEEE Transactions on Electronics, vol. 58, no. 11, pp. 5087-5101, Nov 2011.

[6] G. Huang, E. F. Fukushima, J. She, C. Zhang, and J. He, "Estimation of sensor faults and unknown disturbance in current measurement circuits for pmsm drive system," Measurement, vol. 137, pp. 580–587, 2019.

[7] W. Wang, Z. Lu, W. Hua, Z. Wang, and M. Cheng, "A Hybrid Dual-Mode Control for Permanent-Magnet Synchronous Motor Drives," IEEE Access, vol. 8, pp. 105864–105873, 2020.

[8] W. Tong, S. Dai, S. Wu, and R. Tang, "Performance comparison between an amorphous metal pmsm and a silicon steel pmsm," IEEE Transactions on Magnetics, vol. 55, no. 6, Jun 2019.

[9] X. Yuan, Sh. Zhang, and C. Zhang, "Enhanced robust deadbeat predictive current control for PMSM drives," IEEE Access, vol. 7, pp. 148218–148230, 2019.

[10] F. Grouz, L. Sbita, M. Boussak, and A. Khlaief, "FDI based on an adaptive observer for current and speed sensors of PMSM drives," Simulation Modelling Practice and Theory, vol. 35, pp. 34–49, Jun 2013.

[11] D. W. Seo, Y. Bak, S. Cho, K. Bae, and K. B. Lee, "An improved flying restart method of sensorless PMSM drive systems fed by an ANPC inverter using repetitive zero voltage vectors," 2019 IEEE Applied Power Electronics Conference and Exposition (APEC), 17-21 March, 2019.

[12] S. Morimoto, Y. Tong, and T. Hirasa, "Loss Minimization Control of Permanent Magnet Synchronous Motor Drives," IEEE Transactions on Industrial Electronics, vol. 41, no. 5, pp. 511–517, 1994.

[13] T.M. Jahns, G. B. Kliman, and T. W. Neumann, "Interior Permanent-Magnet Synchronous Motors for Adjustable-Speed Drives," IEEE Transactions on Industry Applications, vol. IA-22, no. 4, pp. 738– 47, 1986.

[14] Z. Chen, M. Tomita, S. Doki, and S. Okuma, "An extended electromotive force model for sensorless control of interior permanent-magnet synchronous motors," IEEE Transactions on Industrial Electronics, vol. 50, no. 2, pp.288–295, Apr. 2003.

[15] S. Morimoto, Y. Takeda, and T. Hirasa, "Current Phase Control Methods for Permanent Magnet Synchronous Motors," IEEE Transactions on Power Electronics, vol. 5, no. 2, pp. 133–139, 1990.

[16] X. Chen, J. Hu, K. Chen, and Z. Peng, "Modeling of electromagnetic torque considering saturation and magnetic field harmonics in permanent magnet synchronous motor for HEV," Simulation Modelling Practice and Theory, vol. 66, pp. 212–225, Aug. 2016.

[17] W. Liu, L. Liu, Il Yop Chung, D. A. Cartes, and W. Zhang, "Modeling and detecting the stator winding fault of permanent magnet synchronous motors," Simulation Modelling Practice and Theory, vol. 27, pp. 1–16, Sep. 2012.

[18] S. Maiti, C. Chakraborty, and S. Sengupta, "Simulation studies on model reference adaptive controller based speed estimation technique for the vector controlled permanent magnet synchronous motor drive," Simulation Modelling Practice and Theory, vol. 17, no. 4, pp. 585–596, Apr. 2009.

[19] G. Boztas, and O. Aydogmus, "Comparison of Permanent-Magnet Assisted Synchronous Reluctance Motors with Different Rotor Structures," 11th International Conference on Electrical and Electronics Engineering (ELECO), 28-30 November, 2019.

[20] F. Dalvand, M. Mardaneh, and J. Milimonfared, "Development of genetic-pi based controller for interior permanent magnet synchronous motor drive over wide speed range," 3rd IET International Conference on Power Electronics, Machines and Drives - PEMD 2006, 4-6 April, 2006.

[21] T. M. Jahns, "Flux-weakening regime operation of an interior permanent-magnet synchronous motor drive," IEEE Transactions on Industry Applications, vol. IA-23, no. 4, pp. 681–689, 1987.

[22] M. Miyamasu and K. Akatsu, "An approach to generate high reluctance torque in an inset-type PMSM by square current excitation," 2012 IEEE International Conference on Power and Energy (PECon), 2-5 December, 2012.

[23] T. Ameid, A. Menacer, H. Talhaoui, and I. Harzelli, "Rotor resistance estimation using extended kalman filter and spectral analysis for rotor bar fault diagnosis of sensorless vector control induction motor," Measurement, vol. 111, pp. 243–259, 2017.

[24] A. Gundogdu, R. Celikel, B. Dandil, and F. Ata, "Fpga in-the-loop implementation of direct torque control for induction motor," Automatika, vol. 62, no. 2, pp. 275–283, 2021.

[25] A. Ghamri, R. Boumaaraf, M.T. Benchouia, H. Mesloub, A. Goléa, and N. Goléa, "Comparative study of ann dtc and conventional dtc controlled pmsm motor," Mathematics and Computers in Simulation, vol. 167, pp. 219–230, 2020.

[26] H. Mesloub, R. Boumaaraf, M.T. Benchouia, A. Goléa, N. Goléa, and K. Srairi. Comparative study of conventional dtc and dtc svm based control of pmsm motor — simulation and experimental results. Mathematics and Computers in Simulation, vol. 167, pp. 296–307, 2020.

[27] J. Zhang, A. Tounzi, A. Benabou, and Y. L. Menach, "Detection of magnetization loss in a pmsm with hilbert huang transform applied to non-invasive search coil voltage," Mathematics and Computers in Simulation, vol. 184, pp. 184–195, 2021.

[28] K. Gulez, A. A. Adam, I. E. Buzcu, and H. Pastaci, "Using passive filters to minimize torque pulsations and noises in surface PMSM derived field oriented control," Simulation Modelling Practice and Theory, vol. 15, no. 8, pp. 989–1001, Sep. 2007.

[29] M. Marufuzzaman, M. B. I. Reaz, and M. A. M. Ali, "FPGA implementation of an intelligent current dq PI controller for FOC PMSM drive," 2010 International Conference on Computer Applications and Industrial Electronics, 5-8 December, 2010.

[30] W. Wang, Y. Feng, Y. Shi, M. Cheng, W. Hua, and Z. Wang, "Fault-Tolerant Control of Primary Permanent-Magnet Linear Motors with Single Phase Current Sensor for Subway Applications," IEEE Transactions on Power Electronics, vol. 34, no. 11, pp. 10546–10556, Nov. 2019.

[31] S. G. Petkar and T. V. Kumar, "Computationally efficient model predictive control of three-level open-end winding permanent-magnet synchronous motor drive," IET Electric Power Applications, vol. 14, no. 7, pp. 1210–1220, Jul. 2020.

[32] X. Liu, H. Yu, J. Yu, and L. Zhao, "Combined Speed and Current Terminal Sliding Mode Control with Nonlinear Disturbance Observer for PMSM Drive," IEEE Access, vol. 6, pp. 29594–29601, May 2018.

[33] O. Wallmark, "Control of a Permanent Magnet Synchronous Motor with Non-Sinusoidal Flux Density Distribution," PhD thesis, Chalmers University of Technology, Goteborg, Sweden, 2001.

BIOGRAPHIES

Gullu Boztas received the B.S. (2011), M.S. (2015), and Ph.D. (2019) degree in electric-electronics engineering from the University of Firat Since 2013, she has been a Research Assistant in Department of Electrical & Electronics Engineering, Faculty of Technology, Firat University, Elazig, Turkey. Her interests include power electronics and electric machines..

European Journal of Technique

journal homepage: https://dergipark.org.tr/en/pub/ejt

Vol.12, No.1, 2022

Finite Element Analysis of Safety Pin in Snowplow Equipment

Mehmet Şükrü Adin[1*], Hamit Adin[2], and Raşit Koray Ergün[3]

[1] Batman University, Mechanical Engineering Department, Batman, Turkey. (e-mail: mehmetsukru.adin@batman.edu.tr).
[2] Batman University, Mechanical Engineering Department, Batman, Turkey. (e-mail: hamit.adin@batman.edu.tr).
[3] Batman University, Mechanical Engineering Department, Batman, Turkey. (e-mail: rasitkoray.ergun@batman.edu.tr).

ARTICLE INFO

Received: Mar., 11. 2022
Revised: May., 20. 2022
Accepted: Jun, 26. 2022

Keywords:
Safety pin
Finite element analysis,
Stress
Snow plow equipment

Corresponding author: *Raşit Koray Ergün*

ISSN: *2536-5010* | e-ISSN: *2536-5134*

DOI: https://doi.org/10.36222/ejt.1086422

ABSTRACT

Snow plow equipment is produced with chassis connections suitable for trucks, pickup trucks, tractors, construction machines and pick-ups and mounted in front of the vehicles. In this study, the stress and deflection values of the safety pin used in snow plow equipment will be examined by testing with finite element analysis. In this study, a damaged safety pin was analyzed numerically. The damaged safety pin was modeled with Solidworks package program and stress analysis was performed by ANSYS Workbench package program. In this analysis, the properties of the safety pin made of St37 steel were used. As a result , it was observed that the safety pin was damaged due to the stress distribution.

1. INTRODUCTION

Snow plows are vehicles that clear the roads and open them to transportation in cases where there is heavy snowfall that prevents transportation. It is mounted on dump trucks as front and side snow blades for snow removal. Salt spreader and front snow blade can be installed on the dump truck with a capacity suitable for the needs of the institution. Side snow blades can also be fitted on high-capacity trucks [1]. Shafts; bearing rotating elements such as gear wheels, pulleys, clutches; providing force/moment transmission; are machine elements supported by bearings. The shaft carries the elements attached to it. In addition, the clutch transmits the torque it receives from the gear wheel or pulley to other elements [2]. Shafts are forced by torsional moment during power transmission with rotational speed. As a result, torsional stress occurs in the shaft. In addition, the power transmission elements on the shafts apply force to the shafts. With the effect of these forces, the shafts are also forced to bend. Since normal stresses occur simultaneously in any section of a power-transmitting shaft due to torsional stress and bending, the equivalent stress is taken into account when dimensioning the shaft [3]. Shaft design is the accurate determination of the shaft diameter to provide sufficient strength and rigidity under various operating and loading conditions [4]. Only the bending condition applies to Axles. If it is in torsion then its name will be shaft. Therefore, the axles do not transmit the torque from the engine. They carry the loads on them just like a beam. If the axle is rotating or there is a vibrating load on it, they must be calculated according to the continuous strength, as with the shafts. For this reason, the safety stresses to be used should also be the safety stresses taken according to the continuous strength [5]. Due to the power transmission elements on the shafts, they are forced by shear force, bending moment, torsion moment and axial force. The shaft diameter is calculated by including the physical properties of the shaft material, the positions of the supporting and power transmission elements on the shaft and their effects on the shaft [6-8]. In the light of this information, the designer can determine the diameters required for different regions of the shaft. Adin et al. introduced the mechanical properties of the damaged helical gear to the system and performed the mesh operation by selecting the mesh structure. As a result, they realized that it would be possible to prevent the wrong material selection, which is the biggest damage cause, with the help of numerical analysis [9]. Yavuz et al. in their study; analyzed the damage analysis of a car's disc brake system. In addition, the damaged brake disc was analyzed by the finite element method. As a result, they determined that lamellar graphite cast iron was used as disc material in experimental

studies [10]. Yavuz et al. in their study; investigated the fractured surfaces of a machine gear with a spur gear profile that was damaged by fracture. As a result, according to the literature review, they observed that the hardness value was high in the material and ductile fractures were observed due to the ferrite phase formed at the grain boundaries. [11]. Erdogan et al. in their study; performed damage analysis of the gearbox of BMC 935 trucks. As a result, they found that gearbox damage was caused by fatigue [12]. Considering the stress concentrations caused by the cross-sectional differences, the variability of the forces acting on the shaft, the control of the stiffness of the shafts, and the fact that the shaft can be made hollow in the calculation of the diameters, the necessity of using a computer automatically emerges. Snowplow equipment is positioned suspended in the air with the help of pistons when the vehicle is not in use while in motion. A safety system is used to prevent the weight of the snowplow equipment suspended in the air from damaging the pistons. In this study, the damaged safety pin was redesigned and improved by the authors. The values of both safety pins were compared.

2. MATERIAL AND METHOD

The carbon ratio of St 37 steels is around 0.20 maximum. It is the softest of the hot rolled steels. St 37 quality steels are known for their features such as being easy to process, welding and cutting without problems. It is one of the most preferred types of steel construction structures. St 37 (s235) quality class steels come first among the commercial grades of structural steel construction profiles and sheets [13]. The 3D redesign was made for the safety pin by reverse engineering with the help of Solidworks design program as shown in Figure 1. Dimensions were detailed in the technical drawing section.

The physical and chemical properties of the safety pin material were given in Table 1. and Table 2.

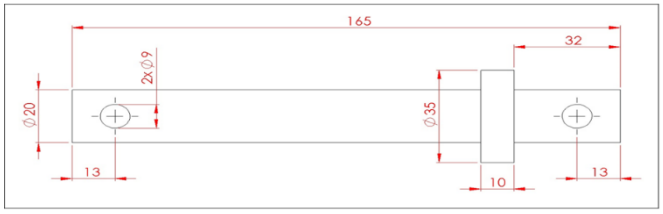

Figure 1. Technical drawing of safety pin

TABLE I.
CHEMICAL PROPERTIES OF SAFETY PIN MATERIAL

Chemical Properties - 1.0037 (S235JR)						
C	Mn	P	S	N	Cu	CEV
0,18-0,2 %	1,4-1,6 %	0,04-0,045 %	0,04-0,045 %	0,009-0,012 %	0,45-0,55 %	0,30-0,38 %

TABLE II.
PHYSICAL PROPERTIES OF SAFETY PIN MATERIAL

Type	1.0037 (S235JR)
Model	Isotropic Linear Elastic Analysis
Failure Criteria	Von Mises
Yield and Tensile Strength	2.35e+8 and 3.6e+8 N/m^2
Elastic Module	2.1e+011 N/m^2
Poisson Ratio	0.28
Mass Density	7800 kg/m^3
Thermal Expansion Coefficient	1.1e-005 /Kelvin

3. RESULT AND DISCUSSION

After using the snowplow equipment for a certain period of time, bending of the safety pin was observed as shown in Figure 2. After this stage, the use of the pin was not considered appropriate.

Figure 2. Bending condition of the safety pin after use

As shown in Figure 3, the safety pin was fixed during the analysis process. While loads are applied to the system as input data, supports are used to fix the system. In a three-dimensional system, each element has 6 degrees of freedom, 3 rotational and 3 translational. Supports are implemented by limiting these degrees of freedom belonging to the element. Boundary conditions must be chosen carefully. Minor errors in boundary conditions can drastically alter the result. The two intersecting surfaces of the safety pin and the other two models used in the snowplow equipment were used as fixed in the analysis phase. All bending analyzes were done with solidworks package program.

Figure 3. Surfaces fixed in bending analyzes

As can be seen in Figure 4 on the snowplow equipment, the load was acted in the middle of the safety pin. The force direction on which the load acts was unidirectional and was acted on a single surface. The force had a value of approximately 25000 N.

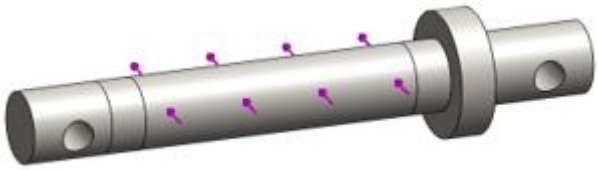

Figure 4. Forces applied in bending analyzes

The mesh view of the safety pin for which bending analyzes were made was given in Figure 5.

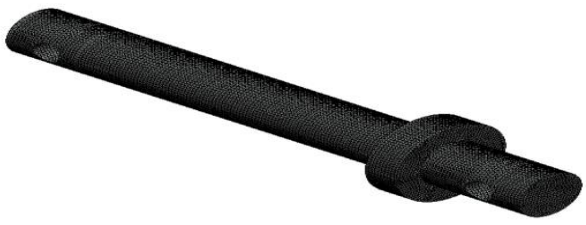

Figure 5. Safety pin mesh view

In the mesh structure given in Figure 5, there were 268365 mesh elements and 51298 nodes. Triangular meshes with good mesh quality with an element size of 1 mm were cast on the safety pin. Due to the fact that the safety pin did not have a complex geometry and the computer used was powerful, the completion time of the mesh was 53 seconds.

The reaction forces of the safety pin after the analysis performed were given in Table 3.

TABLE III.
THE REACTION FORCES OF THE GEAR

	X	Y	Z	Result
Reaction Forces (N)	-0.077755	-0.168421	24999.8	24999.8

As shown in Table 3, the safety pin was fixed during the analysis process. The two intersecting surfaces of the safety pin and the other two models used in the snowplow equipment were used as fixed in the analysis phase.

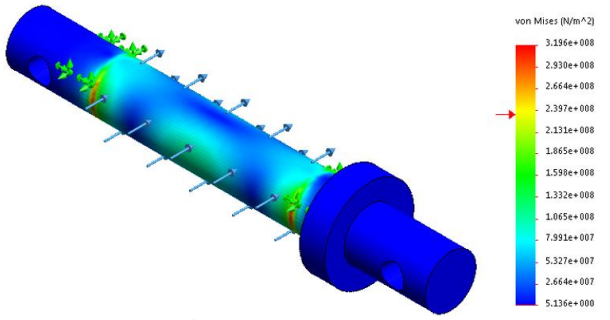

Figure 6. 20mm safety pin diameter - von mises stress value

When the pin diameter shown in Figure 6 was selected as 20 mm, Von Mises Stress values exceed the yield value of the material in the analysis. In the model seen in Figure 6, color changes occurred from blue to red. The colors corresponding to the numerical values on the right side of the graph showed the stresses that occur as a result of the analysis in geometry. Tensile values increased towards red color. The maximum stress value seen in the graph was 319.64 MPa. In geometry, two different support (fixing) locations were selected. The load was applied between the two supports. The maximum stress value occurred in the areas where the support points were. The stress values formed in the support areas exceeded the yield value of the material. The maximum stress value on the contact surface of the force increased up to 133 MPa. The stresses on these surfaces did not exceed the yield value of the material. The minimum stress (close to zero) occurred on the surfaces where the force was not applied and outside the support areas.

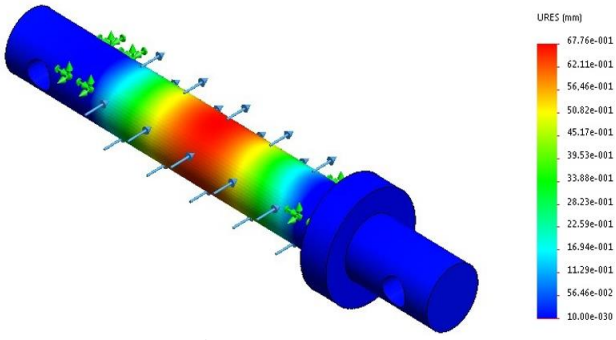

Figure 7. 20mm safety pin diameter - displacement values

When the pin diameter shown in Figure 7 was selected as 20 mm, the deflection values were seen in the analysis. In the model seen in Figure 7, there were changes in deflection values from blue to red. In the graph on the right, the maximum increase in deflection value was seen in red. The maximum deflection value seen in the graph was 6.77 mm. The deflection values at the support points increased up to 3 mm. The maximum deflection value was obtained by increasing the deflection value up to 6.77 mm on the surface where the force contacts. On the surfaces where the force did not come into contact, the deflection value was almost equal to zero.

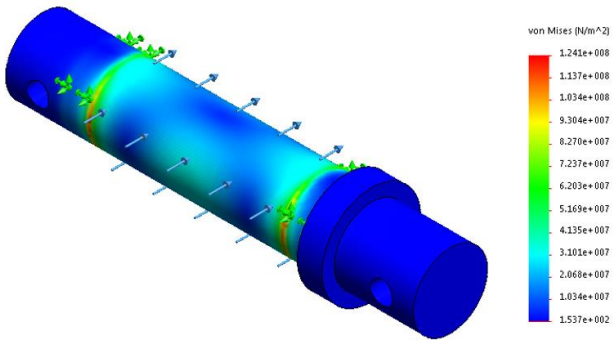

Figure 8. 30mm safety pin diameter - von mises stress value

In the analysis performed when the pin diameter shown in Figure 8 is 30 mm, Von Mises Stress values did not exceed the yield value of the material. In the model seen in Figure 8,

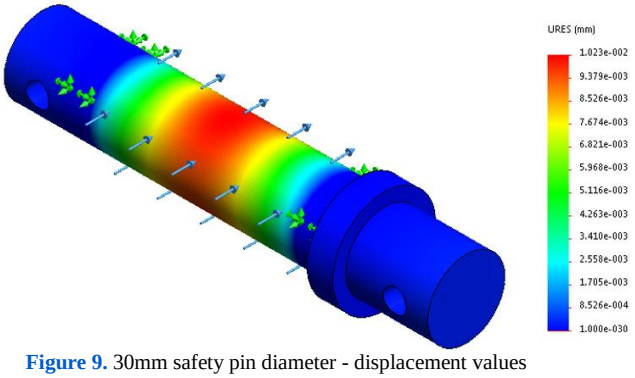

Figure 9. 30mm safety pin diameter - displacement values

When the pin diameter shown in Figure 9 was selected as 30 mm, the deflection values were seen in the analysis. In the model seen in Figure 9, there were changes in deflection values from blue to red. In the graph on the right, the maximum increase in deflection value was seen in red. The maximum deflection value seen in the graph was 0.01 mm. The deflection values at the support points increased up to 0.04 mm. The maximum deflection value was obtained by increasing the deflection value up to 0.01 mm on the surface where the force contacts. The deflection value on the surfaces where the force did not contact and on all surfaces of the geometry in general was almost equal to zero.

4. CONCLUSION

In this study, finite element analysis of the safety pin used in snowplow equipment was made using solidworks simulation program, and stress and deflection values were examined. In the analysis phase, attention was paid to

boundary conditions, mesh values and material properties. The analysis was carried out using the pin diameter of 20 mm in Figure 6 and Figure 7, which was seen in the results of the study. The safe yield value of St37 material was 235 MPa. In Figure 6, the maximum stress value was 319.64 MPa. The maximum stress value in the safety pin exceeded the safe yield value in the St37 material. The system was 1.36 times unsafe. In Figure 7, a deflection of 6.77 mm was observed. As the yield value and deflection value increased after the analysis, it was not considered appropriate to reuse the pin after this stage.

The diameter of the safety pin was increased from 20 mm to 30 mm and reanalyzed. The maximum stress value in Figure 8 was 124 MPa. Since the material did not exceed the safe yield value, the system was 1.89 times safe. In Figure 9, the deflection value was observed as 0.01 mm. As a result, the pin diameter increased to 30 mm and the safety pin became more durable. The deflection value also improved, reaching zero.

REFERENCES

[1] https://www.karba.com.tr/karla-mucadele-araclari.html

[2] F. C. Babalık, Makine elemanları ve konstrüksiyon örnekleri. Nobel Yayın Dağıtım, Ankara, TURKEY: 2006.

[3] V. L. Doughtie, A. Valence, Design of machine elements, McGraw Hill Book Company Inc, 1964, pp. 177-178.

[4] A. Taşkesen, Bilgisayar destekli mil tasarımı, Master Thesis, Gazi University Institute of Science and Technology, Ankara, 1997.

[5] Karabük Üniversitesi, Mühendislik Fakültesi, Ibrahim Cayiroglu, Makine Elemanlari Ders Notları

[6] F. Mendi, A. Taskesen, Y. Kisioglu, "Computer-Aided Shaft Design And Selection Of Rolling-Contact Bearings Using An Expert System," International Journal Of Modeling And Simulation In Engineering, Simulation, vol. 76, no. 3, pp. 151-159, 2001.

[7] A. Taskesen, F. Mendi, M. K. Kulekci, H. Basak, "Comprehensive Design Of Rotating Shafts And A Software For Designing And Selecting Of Rolling-Contact Bearings," Computer Applications In Engineering Education, vol. 15, no. 3, pp. 214-225, 2007.

[8] S. Nawate, Y. Terauchi, "Number of teeth in contact and loading capacity of gear type shaft caupling," Transactions of the Japan Society of Mechanical Engineers, vol. 11, no. 1, pp. 43-56, 2021.

[9] H. Adin, M.Ş. Adin, "Numerical Analysis of Damaged Helical Gear Wheel," Batman Üniversitesi Yaşam Bilimleri Dergisi, vol. 38, no. 1, pp. 106-111, 1995

[10] İ. Yavuz, M. Erdoğan, A. Erçetin, Otomobillerde Kullanılan Fren Diski Hasar Analizi, 7. Otomotiv Teknolojileri Kongresi, Bursa, TURKEY: 2014.

[11] M. Erdoğan, İ. Yavuz, A. Erçetin, Düz Dişli Çark Hasar Analizi, 7. Otomotiv Teknolojileri Kongresi, Bursa, TURKEY: 2014.

[12] M. Erdoğan, İ. Yavuz, A. Erçetin, Failure Analysis Of Differential Gear, 2. Uluslararası Demir Çelik Sempozyumu, Kongresi, TURKEY: 2015.

[13] https://celikfiyatlari.com/st-37-s235-kalite-celiklerin-ozellikleri/

BIOGRAPHIES

Mehmet Şükrü Adin Mehmet Şükrü Adin is a PhD candidate of the Department of Mechanical Engineering, University of Batman, Batman, Turkey. He received his master's degree in Mechanical Engineering from the University of Batman in 2016. His research interests include mechanical properties of materials, composite materials, adhesive, adhesion and solid metal forming.

Hamit Adin born in 1972, received his PhD degree from the University of Fırat, Elazığ, Turkey in 2007 and has been Associated Professor of Mechanical Engineering at the University of Batman, Turkey, since 2015. He has done research in the areas of mechanics, composite materials, adhesive, adhesion and finite element analysis. His research includes both theoretical and experimental studies.

Raşit Koray Ergün born in 1982, received his BSc degree from the Department of Mechanical Engineering at the University of Kahramanmaraş Sütçü İmam, Kahramanmaraş, Turkey, in 2014. Currently he is studying for his Ph.D. He is experienced in the areas of mechanics, composite materials, and theoretical and experimental studies.

European Journal of Technique

journal homepage: https://dergipark.org.tr/en/pub/ejt

Vol.12, No.1, 2022

An experimental study verification of production raw algae oil to biodiesel by industry 4.0

Fevzi Yaşar[1*], **Cemil Koyunoğlu**[2]

[1*] Department of Refinery and Petro-Chemistry Batman University, 72100 Batman, Turkey. (e-mail: fevzi.yasar@batman.edu.tr).
[2] Energy Systems Engineering Department, Yalova University, Cinarcik Campus, Yalova and 77200, Turkey. (e-mail: cemil.koyunoglu@yalova.edu.tr)

ARTICLE INFO

Received: Jan., 10. 2022
Revised: Apr., 11. 2022
Accepted: Jun, 26. 2022

Keywords:
Algae fuel
biodiesel production
Industry 4.0
Photobioreactors

Corresponding author: *Fevzi Yaşar*

ISSN: *2536-5010* | e-ISSN: *2536-5134*

DOI: https://doi.org/10.36222/ejt.1055633

ABSTRACT

As a result of the use of carbon dioxide in the flue gas of algae, it is generally known to use biofuel in photobioreactors or in bubble bed bioreactors and the principle of photosynthesis. During the algae growth, the extraction process should be terminated immediately after the esterification reaction of the algae oil. It is an inevitable fact that this biodiesel produced today is becoming widespread in many ways with traditional fuels. In this study, methanol was used experimentally in a reaction vessel to release triglyceride oils in algae. The interaction of the carbon dioxide gas combined with the transesterification reaction was modeled using computational fluid dynamics. We introduce the use of microbubbles to provide vapor-liquid-liquid phase equilibrium. The Ansys simulation program we use is an important tool for the biodiesel production rate calculation to stabilize the steps such as the decomposition of methanol in the triglyceride phase at low temperature and intermediate pressure values, but the mixing module helps us to find these processes easily. With this study, using the computational fluid dynamics of a simple experiment, it enables us to interpret the experimental and then the latest industrial plant modeling model under realistic and ideal conditions before real applications. The aim of this course is to make feasibility for application of the methodology that will shed light on industrial scale R & D studies. In addition, new reactor geometries can be tried in the continuation of this study in order to determine the ideal conditions and change the algae type.

1. INTRODUCTION

Microalgae can be used as raw material source for many types of biofuel. For example, by anaerobic degradation of microalgal biomass, it is possible to produce biohydrogen by methane, biodiesel from microalgal oils and photobiological reactions [1].

1.1. Oil content of microalgae and microalgal oil extraction

The basic structure of fatty acids consists of saturated and unsaturated fatty molecules. Saturated fatty acids do not have double bonds, while unsaturated fatty acids have at least one double bond in the structure. The oil content of microalgae may vary according to the species. In addition, the fatty acid profile of the species may vary according to cultivation conditions such as temperature, light and growth medium. The fatty acid profile of the microalgae is C_{12}-C_{22}. Microalgal oils are mostly neutral oils containing low levels of unsaturated fats. Mechanical and chemical methods are used in oil extraction processes from microalgae. Mechanical methods are microwave extraction, ultrasonic based extraction and extraction using mechanical compressors. Chemical methods are solvent extraction, supercritical CO_2 based extraction and extraction using ionic liquids ([Bmim] [CF_3SO_3], [Bmim] [$MeSO_4$], etc.). There are also improved methods that combine mechanical and chemical methods. For example, Teo and Idris [1] applied microwave heating in 4 different solvent extraction methods. With this method, they have achieved to increase oil extraction efficiency. In another study, Keris-Sen et al. [2] developed ultrasonic assisted solvent extraction method to increase oil extraction efficiency 1.5-2 times. Oil extraction efficiency may vary according to the method used in the oil extraction process [1-6]. In Table 1, advantages and disadvantages of different harvesting methods are shown. The most suitable method should be chosen considering the advantages and disadvantages of the methods used for oil extraction (see Table 2). These advantages and disadvantages are summarized in Table 3.

1.2. Computational Fluid Dynamics

In engineering calculations, it is very important to determine the fluid behavior correctly. In complex models that cannot be calculated directly by analytical methods, the determination of data such as heat transfer, pressure losses, flow rates by numerical methods while the part is in the design stage provides significant advantages to the manufacturer in terms of time and cost [7, 8].

Computational Fluid Dynamics (CFD) is a computer-based engineering method where detailed calculations can be made in the relevant field, flow area and other physical details can be displayed. The results of the CFD analysis provide significant

TABLE I. ADVANTAGES AND DISADVANTAGES OF DIFFERENT HARVESTING METHODS USED IN MICROALGAL BIOMASS HARVESTING [1-4]

Cultuvation method	Advantage	Disadvantage
Chemical coagulation/flocculation	It is a simple and fast method. No energy required	Chemical flocculants can be expensive and toxic to microalgal biomass. Re-use of the culture medium is limited.
Biofloculation	It is inexpensive. The culture medium can be reused. Toxic to microalgal biomass it is not	Change in cell concentration. Microbiological contamination can
Gravity precipitation	It is a simple and inexpensive method.	Time needs more. There is a possibility of biomass degradation. Algal cake concentration is low
Flotation	Low cost method. Space is minimal. Short operating time Applicable for many microalgae species.	Generally need chemical flocculant. Not suitable for harvesting marine microalgae
Electrical based processes	Additional chemical flocculant requirements It does not require. High recovery efficiency.	Filter clogging can increase operating costs
Filtration	Allows separation of sensitive species	Filter clogging can increase operating costs
Centrifuge	Fast method. High recovery efficiency. Applicable for almost all microalgae species	Energy requirement is high. Only suitable for recycling high value products. It may damage the cell structure.

benefits in simulating product operation in the Simulation Based Product Design process, simulating any problems in the computer environment and optimizing product performance [7, 8].

1.2.1. Steps in Computational Fluid Dynamics

1.2.1.1. Primary Steps

Solution Networks (Grids)

- Turbulence
- Computer Hardware
- Solution Methodologies [7, 8].

1.2.1.2. Secondary items

Solution networks (Complex Geometry Definitions)

- Pre- and Post- Processing (Pre- and Post- Tecplot, Fieldview, Ensight, ...)
- Algorithms [7, 8]

1.2.1.3. Where is computational fluid dynamics used and when is it preferred?

• Calculation and design studies

• Simulation based design

• CFD is more cost-effective than experimental fluid dynamics and results faster

• CFD provides data that can be examined and evaluated in more detail than the experimental in the flow zone of interest, and many data that cannot be measured or observed during the experiment can be accessed by computational fluid dynamics

• Modeling of physical events in which it is difficult or impossible to conduct experiments

• Full-scale simulations; for example, if it was necessary to examine the effect of the various tower positions on the actual submarine on the acoustic characteristics of the propeller, it would be almost impossible to obtain these data by experiment.

• Environmental impacts; for example, the effect of a predicted hurricane on the superstructure of the ship,

• Dangerous events; such as explosions, radiation, contamination

• Physics; star development, black holes etc.

• Developing new theories about fluid physics [7, 8].

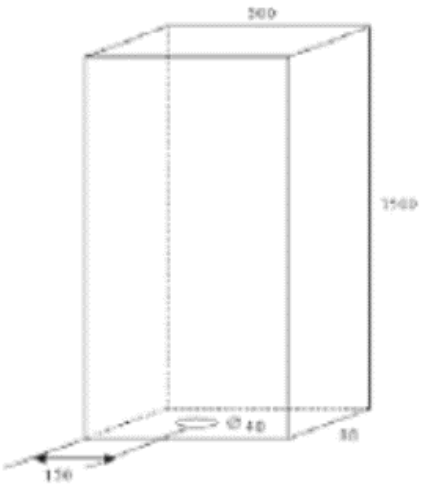

Figure 1. Schematic of the Gas-Liquid Bubble Column [7].

2. MATERIALS AND METHODS

This section will illustrate an exemplary application used in biotechnology and industrial processes, for example air-water bubble column, by modeling a biodiesel production according to a proposed reactor design.
The program to be used is ANSYS FLUENT. Eulerian multiphase model will be used [9].

2.1. Problem description

The sample reactor is shown in Figure 1. The boundary conditions of the geometry is shown in Table 2 [7].

TABLE II COMPARISON OF EXTRACTION METHODS [1-4]

Extraction method	Used solvent	Operating conditions	Used microalgae	Oil Yield (%)
Supercritical	CO_2 and ethanol, CO_2	40 ºC, 35 MPa, 30 min.	Shizochytrium limacinum	33,9
			Pavlova sp.	34
Soxhlet	n-Hexane	40 ºC, 0,1 MPa, 18 hours	Shizochytrium limacinum	45
	Diklоromethane		Nannochloropsis oculata	9
	n-Hexane		Nannochloropsis oculata	5,79
	Ethanol		Nannochloropsis oculata	40,90
	n-Hexane		Pavlova sp.	45,2
	Petroleum ether		Nannochloropsis oculata	8,2
	Ethanol			48
Mixed soxhlet extraction	Hexane/ethanol	200 ºC, 0,1 Mpa, 2 hours	Synechocystis PCC 6803	52
	Hexane/isopropanol		Synechocystis PCC 6803	36
	Cloroform/methanol		Synechocystis PCC 6803	40
	Cloroform/methanol water		Synechocystis PCC 6803	42
Pressurized liquid extraction	n-Hexane	60 ºC, 10-12 MPa, 10 min.	Nannochloropsis oculata	6,1
	n-Hexane/propan-2-ol (2:1 % volume)		Nannochloropsis oculata	20
	Ethanol %96 of volume			
Ultrasonic assisted extraction	Petroleum ether	Frequency 40 kHz, 1 hour	Nannochloropsis oculata	3,3
Wet extraction	Hexane	60 ºC, 0,1 MPa	Chlorella and Scenedesmus sp.	59,3

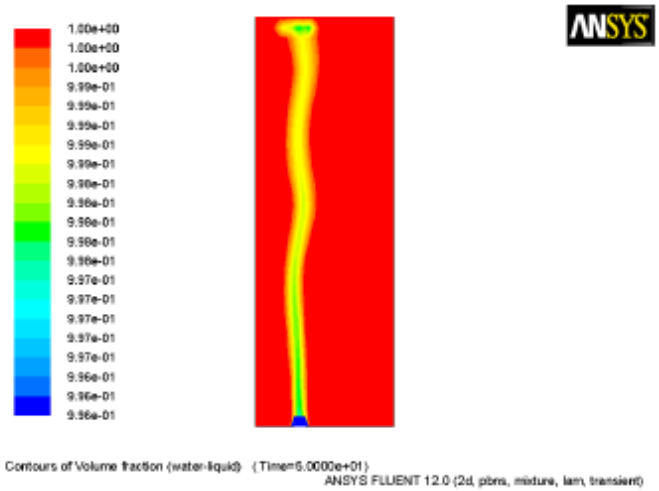

Figure 2. Contours of Volume Fraction of Water [7].

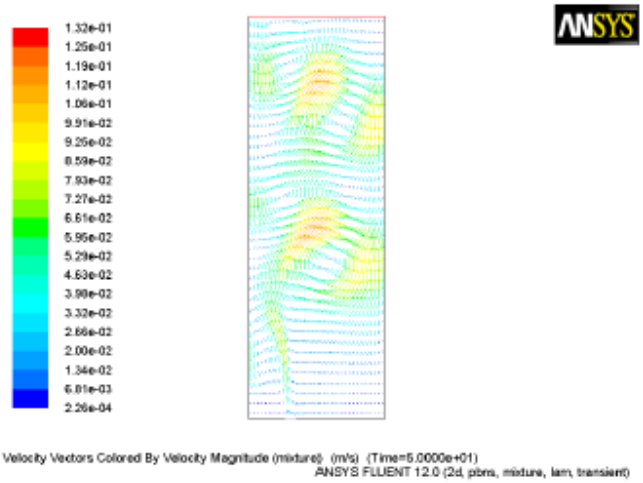

Figure 3. Velocity Vectors for the Bubble Column [7].

TABLE III ADVANTAGES AND DISADVANTAGES OF DIFFERENT OIL EXTRACTION METHODS [1-4]

Method	Advantages	Disadvantages
Mechanic pressuring	Easy to apply. No solvent required.	Large amounts of biomass are required. Application is slow
Ultrasonic assisted extraction	The extraction time is low. Solvent requirement is low. Since the solvent has better effect on the cells, the oil yield is high.	High energy consumption.
Microwave assisted extraction	Environmentally friendly. The extraction time is low. Solvent requirement is low. Oil extraction efficiency is high.	Microwave efficiency is low if non-polar and volatile components are present in the solution.
Solvent extraction	It is cheap and easy. It is good for small scale studies. High yield	Extraction time is long. Excess flammable and toxic solvent is required. Solvent recovery requires energy.
Supercritical extraction	Low solvent toxicity. Fluid diffusion / viscosity Suitable mass through properties transfer balance. Solvent-free extract.	Infrastructure and transaction costs are high.
Solvent-free extraction	Infrastructure and transaction costs are high. Wet extraction Biomass for drying process The required energy is conserved. Solvent requirement is low.	The quality of the extracted oil may be lower than the quality of the extracted oil from the dried biomass

TABLE IV BOUNDARY CONDITIONS FOR THE REACTOR

Velocity (m/s)	Operating density (kg/m^3)	Presure	Momentum	Volume fraction
0.66e-3	1.225	0.5	0.2	0.8

3. RESULTS and DISCUSSIONS

The key images showing the flow regimes and gas-liquid interactions are displayed in the following figures from Fig. 2 to 3.

In this study a transient bubble column set up and solved using the Multiphase-Mixture model. As can be seen in Figure 1 and 2 best seperation occurs at the top of the reactor and also the bottom. In the middle of the reactor there has no seperation ocur well. Volume fraction of water shows that the favorable seperation occurs at the top of the reactor due to the lower liquid density. Since oil has lower density than water.

ACKNOWLEDGEMENT

The study is partially presented in the “3rd world conference on technology, innovation and entrepreneurship”.

.

REFERENCES

[1] N. Moradi-kheibari, H. Ahmadzadeh, A. F. Talebi, M. Hosseini, and M. A. Murry, "Chapter 10 - Recent Advances in Lipid Extraction for Biodiesel Production," in Advances in Feedstock Conversion Technologies for Alternative Fuels and Bioproducts, M. Hosseini, Ed.: Woodhead Publishing, 2019, pp. 179-198.

[2] S. Dutta, F. Neto, and M. C. Coelho, "Microalgae biofuels: A comparative study on techno-economic analysis & life-cycle assessment," Algal Research, vol. 20, pp. 44-52, 2016/12/01/ 2016.

[3] D. Mu, R. Ruan, M. Addy, S. Mack, P. Chen, and Y. Zhou, "Life cycle assessment and nutrient analysis of various processing pathways in algal biofuel production," Bioresource Technology, vol. 230, pp. 33-42, 2017/04/01/ 2017.

[4] A. K. Pegallapati and E. D. Frank, "Energy use and greenhouse gas emissions from an algae fractionation process for producing renewable diesel," Algal Research, vol. 18, pp. 235-240, 2016/09/01/ 2016.

[5] C. L. Teo and A. Idris, "Enhancing the various solvent extraction method via microwave irradiation for extraction of lipids from marine microalgae in biodiesel production," Bioresource Technology, vol. 171, pp. 477-481, 2014/11/01/ 2014.

[6] U. D. Keris-Sen, U. Sen, G. Soydemir, and M. D. Gurol, "An investigation of ultrasound effect on microalgal cell integrity and lipid extraction efficiency," Bioresource Technology, vol. 152, pp. 407-413, 2014/01/01/ 2014.

[7] Y. Nakayama, "Chapter 15 - Computational Fluid Dynamics," in Introduction to Fluid Mechanics (Second Edition), Y. Nakayama, Ed.: Butterworth-Heinemann, 2018, pp. 293-327.

[8] B. Van Tran, S. I. Ngo, Y.-i. Lim, W. Kim, K.-S. Go, and N.-S. Nho, "Computational fluid dynamics of gas-liquid bubble column with hydrocracking reactions," in Computer Aided Chemical Engineering, vol. 44, M. R. Eden, M. G. Ierapetritou, and G. P. Towler, Eds.: Elsevier, 2018, pp. 313-318.

[9] ANSYS-FLUENT, "User's Guide," ed. USA: ANSYS Inc., 2014.

BIOGRAPHIES

Fevzi Yasar obtained his BSc degree in Chemical Engineering from Ataturk University in 2000. He received MSc. diploma in Chemical Engineering from the Firat University in 2005 and PhD degrees in Mechanical Engineering from Batman University in 2016. His research interests are energy, biodiesel, renewable energy, cambastion. He works at Batman University.

Cwmil Koyunoglu was born in Malatya in 1980. In the second grade of the school, his family settled in Antalya and completed his primary, secondary and high school education in Antalya. He graduated from İnönü University, Department of Chemical Engineering in 2007. Between 2007 and 2010, he was among the founders of the İnönü University petroleum research center financed by the Energy Market Regulatory Board. Starting his academic life in 2010 at Yalova University, Department of Energy Systems Engineering, Dr. Cemil Koyunoğlu, after completing his master's studies at İnönü University in Chemical Engineering, started his doctorate education at the energy institute, which he won in 2011. Continuing his doctoral studies in the USA for 1 year as a visiting lecturer during his doctorate. Cemil Koyunoğlu continued his studies by moving to Yalova University from his 4-year Istanbul technical university energy institute academic staff position. He still continues his academic studies at the same university.